Title

Roles for ATF6-Inducible Genes in Cardiac Physiology and Pathology

Author

Blackwood, Erik Alexander

Publication Date

2020

UNIVERSITY OF CALIFORNIA SAN DIEGO

SAN DIEGO STATE UNIVERSITY

Roles for ATF6-Inducible Genes in Cardiac Physiology and Pathology

A dissertation submitted in partial satisfaction of the
requirements for the degree Doctor of Philosophy

in

Biology

by

Erik Alexander Blackwood

Committee in charge:

San Diego State University

Professor Christopher C. Glembotski, Chair
Professor Sanford I. Bernstein
Professor Greg Harris

University of California San Diego

Professor Jeffrey Omens
Professor Nicholas Spitzer

2020

The Dissertation of Erik Alexander Blackwood is approved, and it is acceptable in quality and form for publication on microfilm and electronically:

Chair

University of California San Diego

San Diego State University

2020

Dedication

This dissertation is dedicated to my parents, Barry and Rebecca Blackwood for instilling in me the value of hard work, dedication and a healthy amount of stubbornness. Everything I am and become is a product of their love and support.

I would also like to dedicate this dissertation to my mentor, Dr. Christopher Glembotski, who has taught me many lessons over the years but none more important than the value of passion in every aspect of life.

Epigraph

The heart is a mystery and a miracle. It is more than just an ingenious pump – it is a metaphor of almost limitless profundity. It is an engine not just of blood but also of sublimity. We use it to signify our deepest thoughts and emotions when words alone do not suffice. It is the ultimate arbiter of our lives. And when it calls time, the game is over.

Stephen and Thomas Amidon

For science is more than the search for truth, more than a challenging game, more than a profession. It is a life that a diversity of people lead together, in the closest proximity, a school for social living. We are members one of another.

Oliver Smithies

Table of contents

Signature Page iii
Dedication iv
Epigraph v
Table of contents vi
List of figures ix
List of tables xii
Acknowledgements xiii
Curriculum vitae xvi
Abstract of the Dissertation xx
Chapter 1: General introduction 1
    1.1. Introduction 2
    1.2. Cardiac hypertrophy in health and disease 3
        1.2.1. Cardiac hypertrophy in health and disease 3
        1.2.2. Developmental and physiological cardiac hypertrophy 4
        1.2.3. Pathological cardiac hypertrophy 8
    1.3. The ER unfolded protein response in cardiac myocyte proteostasis 11
        1.3.1. The ER unfolded protein response in cardiac myocyte Proteostasis 11
        1.3.2. ER associated degradation 12
        1.3.3. ER UPR 13
    1.4. ATF6 and proteostasis in the heart 15
        1.4.1. ATF6 and proteostasis in the heart 15
        1.4.2. ATF6 activation 15
        1.4.3. Early findings of ATF6 in the heart 18
        1.4.4. ATF6 regulates and adaptive gene panel in the heart 19
    1.5. ATF6 is an adaptive responder to CVD via regulating non-canonical genes 20
        1.5.1. ATF6 is protective in models of acute myocardial infarction 20
        1.5.2. ATF6 is required for cardiac myocyte hypertrophy 22
        1.5.3. ATF6 enhances natriuretic peptide secretion and hemodynamic balance 25
        1.5.4. ATF6 induces stimulus-specific gene programs 26
    1.6. Small molecule ATF6-activators confer protection against cardiovascular disease 27
    1.7. References 31

Chapter 2: ATF6 decreases myocardial ischemia/reperfusion damage and links ER stress and oxidative stress signaling pathways in the heart..42
- 2.1. Introduction..43
- 2.2. Materials and methods 44
- 2.3. Results...62
- 2.4. Discussion 84
- 2.5. References 89

Chapter 3: ATF6 regulates cardiac hypertrophy by transcriptional induction of the mTORC1 activator, Rheb 92
- 3.1. Introduction..93
- 3.2. Materials and methods 94
- 3.3. Results...112
    - 3.3.1. ATF6 is required for cardiac myocyte hypertrophy in response to pressure overload 112
    - 3.3.2. ATF6 is required for cardiac myocyte hypertrophy in response to exercise...118
    - 3.3.3. Rheb is an ATF6-inducible gene in the heart 122
    - 3.3.4. RHEB induction during pressure-overload and exercise requires ATF6 127
    - 3.3.5. RHEB is required for PE- and IGF1-induced cardiac myocyte growth 129
    - 3.3.6. Mechanistic relationship between growth signaling and the UPR 140
    - 3.3.7. Stimulus-dependent differential induction of ATF6 target genes 146
    - 3.3.8. Ectopic expression of RHEB restores cardiac growth to ATF6 cKO mouse hearts 148
    - 3.3.9. ATF6 activation in response to growth requires mTORC1 activation, protein synthesis and protein misfolding...152
- 3.4. Discussion 159
- 3.5. References 162

Chapter 4: Pharmacologic ATF6 Activation Confers Global Protection in Widespread Disease Models by Reprograming Cellular Proteostasis 165
- 4.1. Introduction..166
- 4.2. Materials and methods 166
- 4.3. Results...181
    - 4.3.1. ATF6 in cardiac myocytes protects the heart from I/R injury 181
    - 4.3.2. 147 activates ATF6 and its target genes in cardiac myocytes.....192
    - 4.3.3. 147 improves ER proteostasis and decreases oxidative stress 197

4.3.4. 147 in vivo protects cardiac myocytes and hearts *in vitro* 200
4.3.5. 147 transiently activates ATF6 in the heart 200
4.3.6. 147 protects the heart from I/R injury *in vivo* 207
4.3.7. 147 is beneficial in a wide range of disease models *in vivo* 213
4.4. Discussion 220
4.5. References 225
Chapter 5: Conclusions 229
5.1. Conclusions 230

List of figures

Chapter 1: General introduction

Figure 1.1- Types of cardiac hypertrophy 7
Figure 1.2- ATF6 activation and gene program induction 17
Figure 1.3- Effect of cardiac myocyte-specific ATF6 deletion in mouse hearts subjected to acute pressure-overload 24
Figure 1.4- Approach to developing novel ATF6-based therapeutics 30

Chapter 2: ATF6 decreases myocardial ischemia/reperfusion damage and links ER stress and oxidative stress signaling pathways in the heart

Figure 2.1- Effects of ATF6 overexpression on ER- and oxidative stress in cultured cardiac myocytes 67
Figure 2.2- Effects of ATF6 knockdown on ER stress and oxidative stress in cultured cardiac myocytes 68
Figure 2.3- Effect of ATF6 gene deletion in hearts subjected to ischemia/reperfusion 70
Figure 2.4- Effect of I/R on GRP78 expression in WT and ATF6 KO mouse hearts as determined by immunocytofluorescence 71
Figure 2.5- Effect of I/R on markers of ER stress in WT and ATF6 KO mouse hearts as determined by immunoblotting 72
Figure 2.6- Effect of ATF6 deletion on GRP78 expression and cell viability of isolated adult mouse ventricular myocytes 74
Figure 2.7- Analysis of oxidative stress gene expression 76
Figure 2.8- Effect of TM on Catalase Expression in Cardiac Myocytes from WT and ATF6 KO Mouse Hearts 79
Figure 2.9- Effects of ATF6 deletion on catalase 80
Figure 2.10- Effect of I/R on Catalase expression in WT and ATF6 KO mouse hearts as determined by immunocytofluorescence and immunoblotting 81
Figure 2.11- Effects of ATF6 on the catalase promoter 83

Chapter 3: ATF6 regulates cardiac hypertrophy by transcriptional induction of the mTORC1 activator, Rheb

Figure 3.1- Effect of cardiac myocyte-specific ATF6 gene deletion in hearts of mice subjected to TAC 114
Figure 3.2- Effect of cardiac myocyte-specific *ATF6* gene deletion in mice subjected to TAC 116
Figure 3.3- Effect of cardiac myocyte-specific ATF6 gene deletion in hearts of mice subjected to free wheel exercise 119

Figure 3.4- Regulation of Rheb Expression by ATF6 124
Figure 3.5- ATF6-dependent induction of Rheb in mouse hearts 126
Figure 3.6- Effects of *ATF6* deletion on regulators of the mTORC1 pathway in hearts of mice subjected to TAC 128
Figure 3.7- Effects of *ATF6*- and *RHEB* knockdown and ectopic Rheb expression on phenylephrine-induced hypertrophy in cultured cardiac myocytes 131
Figure 3.8- Effect of *ATF6* and *RHEB* knockdown on the mTORC1 pathway at cardiac myocyte hypertrophy 133
Figure 3.9- Effects of *ATF6*- and *RHEB* knockdown and ectopic Rheb expression on insulin like growth factor 1-induced hypertrophy in cultured cardiac myocytes 135
Figure 3.10- Rheb-inhibitor, Lonafarnib, inhibition of cardiac myocyte hypertrophy ...137
Figure 3.11- Effect of ATF6 overexpression on cardiac myocyte hypertrophy....................139
Figure 3.12- mTORC1-dependent activation of the UPR during cardiac myocyte hypertrophy 141
Figure 3.13- Examination of Rheb Requirement for Growth-dependent but not Growth-independent Activation of the ATF6 144
Figure 3.14- Effect of cardiac myocyte-specific ectopic Rheb expression in ATF6 gene deleted mouse hearts subjected to TAC 149
Figure 3.15- Mechanism whereby ATF6 acts as a nodal regulator of both protein synthesis and protein folding during cardiac hypertrophy 154
Figure 3.16- Protein synthesis-dependent activation of the UPR during cardiac myocyte hypertrophy 157

Chapter 4: Pharmacologic ATF6 Activation Confers Global Protection in Widespread Disease Models by Reprograming Cellular Proteostasis

Figure 4.1– ATF6 in cardiac myocytes protects the heart from I/R injury 183
Figure 4.2– I/R activates the UPR....................185
Figure 4.3– Endogenous ATF6 is cardioprotective in a model of an acute AMI 188
Figure 4.4– Endogenous ATF6 is cardioprotective in a model of a chronic AMI....................190
Figure 4.5– 147 selectively activates ATF6 in the heart....................194
Figure 4.6– 147 is selectively activates ATF6 196
Fig. 4.7– 147 improves proteostasis and decreases oxidative stress in an ATF6-dependent manner 198
Figure 4.8– 147 acts transiently in vivo 203
Figure 4.9– 147 gene induction timecourse in vivo 204
Figure 4.10– 147 exhibits no deleterious effects, in vivo....................205
Figure 4.11– 147 improves cardiac performance 7d post-AMI 209
Figure 4.12– 147 decreases pathological remodeling 7d post-AMI 211
Figure 4.13– 147 exerts widespread protection in multiple organ systems....................215

Figure 4.14– 147 is protective in multiple models of myocardial damage 217
Figure 4.15– 147 mediates both ROS-dependent and ROS-independent protection globally 224

List of tables

Chapter 3: ATF6 regulates cardiac hypertrophy by transcriptional induction of the mTORC1 activator, Rheb

Table 3.1- 7-day TAC echocardiographic parameters for Con and ATF6 cKO mice ..117
Table 3.2- 4-week Free Wheel echocardiographic parameters for Con and ATF6 cKO mice 121
Table 3.3- 7-day TAC echocardiographic parameters 151
Table 3.4- TAC time course echocardiographic parameters 155
Table 3.5- 3-hour TAC echocardiographic parameters for Con and ATF6 cKO mice .156

Chapter 4: Pharmacologic ATF6 Activation Confers Global Protection in Widespread Disease Models by Reprograming Cellular Proteostasis

Table 4.1- 7-day I/R echocardiographic parameters 191
Table 4.2- Compound 147 7-day Time Course echocardiographic parameters 206
Table 4.3- Compound 147 7-day AMI echocardiographic parameters........................212
Table 4.4- Compound 147 24-hour AMI echocardiographic parameters 219

Acknowledgements

I'd like to first recognize and thank Dr. Christopher Glembotski for taking a risk on me at such a pivotal point in my career. At my first lab meeting Dr. Glembotski introduced me to the rest of his lab by saying, "Erik's an athlete, so he can run pretty fast. Well, he's going to have to run fast to keep up with us and the group of talented researchers in this room." I'd like to think he saw potential in me from the start, but in reality it was his mentorship that inspired me to work well beyond any such potential.

He has extended to me countless opportunities of which I have always tried to take advantage knowing he has such an incredible wealth of knowledge to share. What's more is being such a selfless person, he actively seeks opportunities to share it with his trainees. I am truly fortunate to have found such a compassionate and driven human being to serve as my mentor and now as a colleague and friend.

I would also like to thank that talented group of researchers that make up Team CCG. Jungkang Jin took me under his wing very early on and brought me into the world of small animal physiology research. Khalid Azizi expanded my horizons in that world and I owe many of the skills and training used in this dissertation to him. Donna Thuerauf is one of the most talented and brilliant molecular biologists I've ever had the pleasure of meeting and any success I have had during my doctoral studies is shared with her.

I've been incredibly fortunate to have mentored and worked with some amazing young researchers during my tenure in Dr. Glembotski's lab. Of which, I'd be remiss if I didn't directly acknowledge Alina Bilal. She joined the lab as a bright eyed yet reserved student and has grown into an extremely capable independent researcher. I couldn't imagine finding a better scientific teammate and I’m a better person for simply being around her.

I’d also like to thank our collaborators Dr. Luke Wiseman and Dr. Jeffery Kelly at The Scripps Research Institute for their mentorship and support both scientifically and professionally.

Chapter 1, in part, is a reprint of the material as it appears in Cells in 2020. Blackwood, E.A., Bilal, A.S., Stauffer, W.T., Arrieta, A., and Glembotski, C.C. Designing novel therapies to mend broken hearts: ATF6 and cardiac proteostasis. *Cells,* 2020; 9(3). The dissertation author was the primary author of this paper.

Chapter 2, in part, is a reprint of the material as it appears in Circulation Research in 2017. Jin, J-K., Blackwood, E.A., Azizi, K., Thuerauf, D.J., Fahem, A.G., Hofmann, C., Doroudgar, S., and Glembotski, C.C. ATF6 Decreases Myocardial Ischemia/reperfusion Damage and Links ER Stress and Oxidative Stress Signaling Pathways in the Heart. *Circ. Res.* 2017; 120(5):862-875. The dissertation author was a lead contributing investigator and author to the portions used in this text.

Chapter 3, in full, is a reprint of the material as it appears in Circulation Research in 2019. Blackwood, E.A., Hofmann, C., Santo Domingo, M., Bilal, A.S., Sarakki, A., Stauffer, W., Arrieta, A., Thuerauf, D.J., Kolkhorst, F., Muller, O.J., Jakobi, T., Dieterich, C., Katus, H.A., Doroudgar, S., and Glembotski, C.C. ATF6 regulates cardiac hypertrophy by transcriptional induction of the mTORC1 activator, Rheb. *Circ Res*. 2019; 124(1):79-93. The dissertation author was the primary investigator and author of this paper.

Chapter 4, in full, is a reprint of the material as it appears in Nature Communications in 2019. Blackwood, E.A., Azizi, K.M., Thuerauf, D.J., Paxman, R., Plate, L., Wiseman, L., Kelly, J., and Glembotski, C.C. Pharmacologic ATF6 activation confers global protection in widespread disease models by reprogramming cellular proteostasis. *Nat Commun*, 2019; 10:187. The dissertation author was the primary investigator and author of this paper.

This work was supported by an American Heart Association Predoctoral Fellowship, an NIH F31 Predoctoral Fellowship, a Rees-Stealy Research Foundation Phillips Gausewitz, M.D. Scholar of the SDSU Heart Institute Fellowship, a SDSU Inamori Fellowship, and a scholarship from the Achievement Rewards for College Scientists (ARCS) San Diego Chapter.

Curriculum vitae

Education:

- PhD., Joint Doctoral Program in Cell and Molecular Biology, San Diego State University and UC San Diego, 2016-June 2020
- B.S., PreProfessional Studies & Philosophy, University of Notre Dame, 2008-2012

Research positions:

- Graduate Researcher- PI: Dr. Christopher C. Glembotski, San Diego State University, 2015-present
- Undergraduate Researcher- PI: Dr. Kenneth Olson, University of Notre Dame, 2010-2012

Honors and Awards:

- Undergraduate Research Fellowship, University of Notre Dame, 2011
- Best Poster Award, Gordon Research Conference (GRC) on Cardiac Regulatory Mechanisms, New London, NH, 2016
- Rees-Stealy Research Fellowship, Rees-Stealy Research Foundation, 2016, 2017
- Abstract Travel Award, The Council on Basic Cardiovascular Sciences, American Heart Association, 2016
- Inamori Fellowship, Inamori Foundation, 2016
- UC San Diego Abstract Travel Grant, UCSD, La Jolla, CA, 2017
- Best Poster Award, International Society for Heart Research, New Orleans, LA, 2017
- American Heart Association Predoctoral Fellowship, June 2017
- ARCS Fellowship, August 2017
- Elected Early Career Investigator Committee Member, International Society for Heart Research, September 2017
- National Institutes of Health Predoctoral F31 Fellowship, September 2017
- Exemplary Participation Award, Gordon Research Conference (GRC) on Cardiac Regulatory Mechanisms, New London, NH, 2018
- Best Poster Award, Gordon Research Conference (GRC) on Cardiac Regulatory Mechanisms, New London, NH, 2018
- Abstract Travel Award, The Council on Basic Cardiovascular Sciences, American Heart Association, 2018
- Elected SDSU/UCSD Joint Doctoral Program Graduate Student Committee President, June 2019

Professional Memberships:

- American Heart Association, Basic Cardiovascular Sciences Council, 2015
- International Society for Heart Research, North American Division, 2017
- Sigma Xi, Scientific Research Honor Society, 2020

Publications and Manuscripts:

1. Gray, C.B., Suetomi, T., Xiang, S., **Blackwood, E.A.**, Glembotski, C.C., Miyamoto, S., Westenbrink, B.D., Mishra, S. and Brown, J.H. CaMKIIδ subtypes differentially regulate infarct formation following ex vivo myocardial ischemia/reperfusion through NF-κB and TNF-α. J Mol Cell Cardiol. 2017; 103:48-55.

2. Jin, J-K., **Blackwood, E.A.**, Azizi, K., Thuerauf, D.J., Fahem, A.G., Hofmann, C., Doroudgar, S., and Glembotski, C.C. ATF6 Decreases Myocardial Ischemia/reperfusion Damage and Links ER Stress and Oxidative Stress Signaling Pathways in the Heart. Circ. Res. 2017; 120(5):862-875.

3. Arrieta, A., **Blackwood, E.A.** and Glembotski, C.C. ER Protein Quality Control and the Unfolded Protein Response in the Heart. Curr. Top Microbiol Immunol. 2018; 414:193-213.

4. Paxman, R.J., Plate, L., **Blackwood, E.A.**, Glembotski, C.C., Powers, E.T., Wiseman, R.L., and Kelly, J.W. Pharmacologic ATF6 activating compounds are metabolically activated to selectively modify endoplasmic reticulum proteins. eLife. 2018; 7:e37168.

5. **Blackwood, E.A.**, Hofmann, C., Santo Domingo, M., Bilal, A.S., Sarakki, A., Stauffer, W., Arrieta, A., Thuerauf, D.J., Kolkhorst, F., Muller, O.J., Jakobi, T., Dieterich, C., Katus, H.A., Doroudgar, S., and Glembotski, C.C. ATF6 regulates cardiac hypertrophy by transcriptional induction of the mTORC1 activator, Rheb. Circ Res. 2019; 124(1):79-93.

6. **Blackwood, E.A.**, Azizi, K.M., Thuerauf, D.J., Paxman, R., Plate, L., Wiseman, L., Kelly, J., and Glembotski, C.C. Pharmacologic ATF6 activation confers global protection in widespread disease models by reprogramming cellular proteostasis. Nat Commun, 2019; 10:187.

7. Glembotski, C.C., Arrieta, A., and **Blackwood, E.A.** Unfolding the roles of mitochondria as therapeutic targets of heart disease. J Am Coll Cardiol. 2019; 73(14):1807-1810.

8. Palmer, J.E., Brietskem B.M., Bate, T.C., **Blackwood, E.A.**, Garg, M., Glembotski, C.C., Cooley, C.B. Reactive oxygen species (ROS)-activatable prodrug strategy for selective activation of ATF6 following ischemia-reperfusion injury. ACS Med Chem Lett, accepted for publication Nov 6, 2019.

9. Arrieta, A., **Blackwood, E.A.**, Stauffer, W.T., and Glembotski, C.C. Integrating ER and mitochondrial proteostasis in the healthy and diseased heart. Front Cardiovasc Med. 2020; 6:193.

10. Stauffer, W.T., Arrieta, A., **Blackwood, E.A.**, and Glembotski, C.C. Sledgehammer to scalpel: broad challenges to the heart and other tissues yield specific cellular responses via transcriptional regulation of the ER-stress master regulator ATF6. Int Journ of Mol Sci. 2020; 21(3).

11. Stauffer, W.T., **Blackwood, E.A.**, Azizi, K., Kaufman, R.J., and Glembotski, C.C. The ER unfolded protein response effector, ATF6, reduces cardiac fibrosis and moderates activation of cardiac fibroblasts. Int Journ of Mol Sci, 2020; 21(4).

12. **Blackwood, E.A.**, Bilal, A.S., Stauffer, W.T., Arrieta, A., and Glembotski, C.C. Designing novel therapies to mend broken hearts: ATF6 and cardiac proteostasis. Cells, 2020; 9(3).

13. **Blackwood, E.A.**, Azizi, K., Sarakki, A., Bilal, A.S., and Glembotski, C.C. Simultaneous isolation and culture of adult murine atrial myocytes, ventricular myocytes and non-myocytes for in vitro analysis from a single heart. Jove, accepted for publication February 21, 2020.

14. **Blackwood, E.A**., Thuerauf, D.J., Stastna, M., Stephens, H., Sand, S., Pentoney, A., Azizi, K., Van Eyke, J.E., Katus, K.A., Glembotski, C.C., and Doroudgar, S.D. (2020) Proteomic analysis of the ER stress secretome reveals extracellular functions for the ER stress response. *J Mol Cell Cardiol,* accepted for publication April 24, 2020.

15. Glembotski, C.C., Arrieta, A., **Blackwood, E.A.**, and Stauffer, W.T. ATF6 as a nodal regulator of proteostasis in the heart. *Front Physio,* 2020; 11:267.

16. Arrieta, A., **Blackwood, E.A**., Thuerauf, D.J., Santo Domingo, M., Doroudgar, S.D., and Glembotski, C.C. (2020) MANF is a novel ER chaperone that is required for ER-protein folding and the adaptive ER stress response in the ischemic heart. *JBC*, accepted for publication April 23, 2020.

17. **Blackwood, E.A**., Thuerauf, D.J., Bilal, A., Macdonnell, L., and Glembotski, C.C. (2020) The Selenoprotein, VIMP, modulates cardiac hypertrophy via dictating ERAD complex formation and substrate recognition. *Cell,* manuscript in preparation.

18. **Blackwood, E.A**., Thuerauf, D.J., Bilal, A., Yang, B., Plate, L., Wiseman, L., Patel, H., Sussman, M., and Glembotski, C.C. (2020) Role for ATF6 as a Gatekeeper of Regulated Hormonal Secretion. *Circ Res*, manuscript in preparation.

19. **Blackwood, E.A.**, Jin, J-K., Bilal, A.S., Sarakki, A., Jakobi, T., Dieterich, C., Katus, H.A., Doroudgar, S.D., and Glembotski, C.C. (2019) ATF6 signaling in cardiac myocytes propagates inflammasome activation in the heart via transcriptional regulation of and paracrine signaling by the cytokine, HMGB1. (2019) *eLife,* manuscript in preparation.

Professional Presentations:

International Society for Heart Research
- Denver, CO, August 2020

The Council on Basic Cardiovascular Sciences Conference
- Chicago, IL, July 2020

American Heart Association Scientific Sessions Conference
- Philadelphia, PA November 2019

The Council on Basic Cardiovascular Sciences Conference
- San Antonio, TX, July 2018

Gordon Research Seminar – *Innovative Answers to Classic Cardiac Questions*
- New London, NH, June 2018

Gordon Research Conference – *Cardiac Regulatory Mechanisms*
- New London, NH, June 2018

International Society for Heart Research
- Halifax, Nova Scotia, Canada, June 2018

Keystone Symposia on Heart Failure
- Keystone, CO January 2018

American Heart Association Scientific Sessions Conference
- Anaheim, CA November 2017

ER Stress Club
- La Jolla, CA September 2017

Alternative Muscle Club Symposium
- La Jolla, CA, September 2017

The Council on Basic Cardiovascular Sciences Conference
- Portland, OR July 2017

International Society for Heart Research
- New Orleans, LA, June 2017

Student Research Seminar
- San Diego, CA, March 2017

Alternative Muscle Club Symposium
- La Jolla, CA, September 2016

American Heart Association Scientific Sessions Conference
- New Orleans, LA, November 2016

The Council on Basic Cardiovascular Sciences Conference
- Phoenix, AZ, July 2016

Gordon Research Seminar – *Innovative Answers to Classic Cardiac Questions*
- New London, NH, June 2016

Gordon Research Conference – *Cardiac Regulatory Mechanisms*
- New London, NH, June 2016

Abstract of the Dissertation

Roles for ATF6-Inducible Genes in
Cardiac Physiology and Pathology

by

Erik Alexander Blackwood
Doctor of Philosophy in Biology
University of California San Diego, 2020
San Diego State University, 2020
Professor Christopher C. Glembotski, Chair

The heart exhibits incredible plasticity in response to both environmental and genetic alterations that affect workload. Over the course of development, or in response to physiological or pathological stimuli, the heart responds to fluctuations in workload by hypertrophic growth primarily by individual cardiac myocytes growing in size. Cardiac hypertrophy is associated with an increase in protein synthesis, which must coordinate with protein folding and degradation to allow for homeostatic growth without affecting the functional integrity of cardiac myocytes (i.e., proteostasis). This increase in the protein folding demand in the growing cardiac myocyte activates the transcription factor,

ATF6 (activating transcription factor 6α, an inducer of genes that restore proteostasis. Previously, ATF6 has been shown to induce ER-targeted proteins functioning primarily to enhance ER protein folding and degradation. More recent studies, however, have illuminated adaptive roles for ATF6 functioning outside of the ER by inducing non-canonical targets in a stimulus-specific manner. This unique ability of ATF6 to act as an initial adaptive responder has bolstered an enthusiasm for identifying small molecule activators of ATF6 and similar proteostasis-based therapeutics.

Chapter 1: General Introduction

1.1. Introduction

Cardiovascular disease (CVD) accounts for one in every three deaths in the US[1]. While various etiologies may contribute to the progression of CVD, they are generally associated with pathological left ventricular hypertrophy. Believed to be initially an adaptive compensatory response to maintain cardiac function and decrease ventricular wall tension, pathological cardiac hypertrophy can lead to a maladaptive remodeling of the heart during which there is thinning of the myocardium, chamber dilatation and a reduction in cardiac output and contractility, leading to eventual heart failure[2,3]. Despite improvements in clinical management, heart failure rates continue to represent the fastest-growing subcategory of CVD in an increasingly aging population[4–7], accounting for more than 500,000 deaths per year and resulting in an incredible economic impact of 100 billion USD per year[7–9]. While palliative measures are available and prescribed for patients to treat the symptoms associated with heart failure, aside from a heart transplant there is no clinically available curative therapy[3]. Furthermore, progress in therapeutic intervention is hindered by the lack of understanding of the molecular mechanisms underlying the pathophysiology of CVD and heart failure.

Cardiac hypertrophy requires an increase in protein synthesis in cardiac myocytes, much of which is responsible for the sarcomere growth necessary to maintain or improve global cardiac contractile function[10,11]. This net increase in protein is determined primarily by the rates of the synthesis, folding and degradation machinery to allow for homeostatic growth without affecting the functional integrity of cardiac myocytes, as misfolded proteins can be toxic[12–15]. Thus, the protein-folding load must equal that of the protein folding capacity to avoid toxic accumulation of misfolded proteins (proteostasis)[16–18]. Studies in both animal models and patients support imbalanced proteostasis as a primary driver of CVD and heart failure[11].

Proteostasis is maintained by intracellular pathways that coordinate protein synthesis and folding with the degradation of misfolded, potentially toxic proteins[19,20]. A majority of this protein synthesis occurs at the endoplasmic reticulum (ER), making it a major site of protein quality control[21]. Imbalances in proteostasis cause or exacerbate numerous pathologies, spawning interest in the exogenous manipulation of proteostasis as a therapeutic approach for such diseases[22]. ER proteostasis is regulated by the unfolded protein response (UPR), a stress-responsive signaling pathway comprising three sensors/effectors of protein misfolding, PERK (protein kinase R [PKR]-like ER kinase), IRE1 (inositol requiring enzyme 1), and ATF6 (activating transcription factor 6α)[23]. Considerable evidence supports ATF6, a transcriptional regulator of ER proteostasis, as a viable therapeutic target for exogenous manipulation of proteostasis[24–29]. This review focuses on the therapeutic potential of ATF6 in maintaining cardiac myocyte proteostasis by inducing canonical and non-canonical gene targets in CVD and, more specifically, cardiac hypertrophy.

1.2.1. Cardiac Hypertrophy in Health and Disease

Cardiac myocytes, which comprise 85% of the heart mass, are responsible for generating the contractile force necessary for maintaining systemic blood flow of oxygen and nutrients[30,31]. The force-generating units of cardiac myocytes are tightly aligned sarcomeres that, in response to an increase in workload, grow via addition of sequential nascent sarcomeres in length and/or width, depending upon the nature of the stimulus[31]. Cardiac myocytes are uniquely susceptible to damage associated with chronic increases in workload or stress, due to their limited potential to proliferate[31]. For this reason, hypertrophic growth via increased protein synthesis in cardiac myocytes is the primary mechanism whereby the heart reduces ventricular wall stress[10,32]. This hypertrophic growth was seen by physicians as initially a compensatory response mechanism, as it develops in accordance with Laplace's law, dictating that increases in pressure or volume load-induced tension in the heart must be offset by an increase in myocardial and ventricular wall thickness[33–36]. While ongoing studies are beginning to question this concept and the necessity for cardiac hypertrophy primarily in response to pathological stimuli[37], what is apparent is that the requisite increase in protein synthesis in any form of cardiac myocyte growth strains the protein-folding machinery in the heart. This strain must be abated for sustained cardiac function[12–15].

1.2.2. Developmental and Physiological Cardiac Hypertrophy

Despite the connotation, a number of physiological conditions can provoke cardiac hypertrophy and dramatic changes to cardiac myocyte number and size, beginning with development[31]. As depicted in **Fig. 1.1A**, the pre- and post-natal heart grows in cardiac myocyte number, or hyperplasia[38,39]. However, this replicative capacity is lost in as little as four days after birth[40], and continued increases in heart mass to meet an increasing circulatory demand are achieved through hypertrophic growth of preexisting cardiac myocytes[41,42]. This state of cell-cycle arrest of post-natal cardiac myocytes is associated with maturation of the gene programs governing isoforms of contractile proteins and calcium handling proteins, as well as a shift in the preferred energy source for cardiac myocytes, from anaerobic glycolysis to an oxygen-dependent mitochondrial oxidative phosphorylation[43]. While the mechanism is still unclear, this adaptation is greatly influenced by nutritional, hemodynamic, humoral, and even oxygen tension changes from the environment in utero[43]. Upon the cessation of hyperplastic growth, the heart hypertrophies in an eccentric manner characterized by an overall increase in cardiac mass, as well as chamber volume. Due to this abrupt dependence on hypertrophic growth of cardiac myocytes, it is imperative for the protein-folding machinery to meet the demands of increases in protein synthesis. In fact, neonatal and adolescent cardiac myocytes exhibit a robust adaptive UPR and ATF6 activity, as evidenced by the finding that the expression of many of the components of the canonical gene panel regulated by ATF6 is relatively high in the young heart, compared to the adult and aged heart[44,45].

Normal growth of the heart during adolescence and adulthood is driven by physiological cardiac hypertrophy, a reactive growth occurring as a direct response to extrinsic stimuli necessitating an increase in cardiac output **(Fig. 1.1B, Form 1)**[37,43,46]. Similar to postnatal hypertrophy, pregnancy, and prolonged exercise induce greater circulatory demands that inevitably drive a concentric growth of the heart, characterized by a relative increase in wall thickness and cardiac mass, but little or no change in chamber volume[43,46]. Coordinately, while physiological stimuli elicit a concentric manner of cardiac myocyte hypertrophy, the sarcomeric growth in diameter and length is nearly proportional. Ironically, in the 19th century, this form of cardiac hypertrophy was thought to be pathological in nature and a result of overexertion, even being coined as “athlete’s heart”[47]. Indeed, while well trained athletes can exhibit increases in cardiac mass by up to 60%, the transient nature of this form of heart growth, which can rapidly reverse upon hemodynamic unloading, was not conceived of until later on[48,49]. It is now known that growth of the myocardium as a result of pregnancy or exercise is not associated with heart failure progression and is adaptive in nature, due to the sustained or even increased cardiac output[43].

While adaptive, the increase in protein folding associated with physiological hypertrophy would be expected to strain the proteostasis network. However, studies have shown that not only is ATF6 activated to regulate an adaptive gene panel allowing for continued growth[50], but also, exercise can revert many of the age-related symptoms leading to CVD, such as attenuated accumulation of misfolded protein aggregates within cardiac myocytes[51].

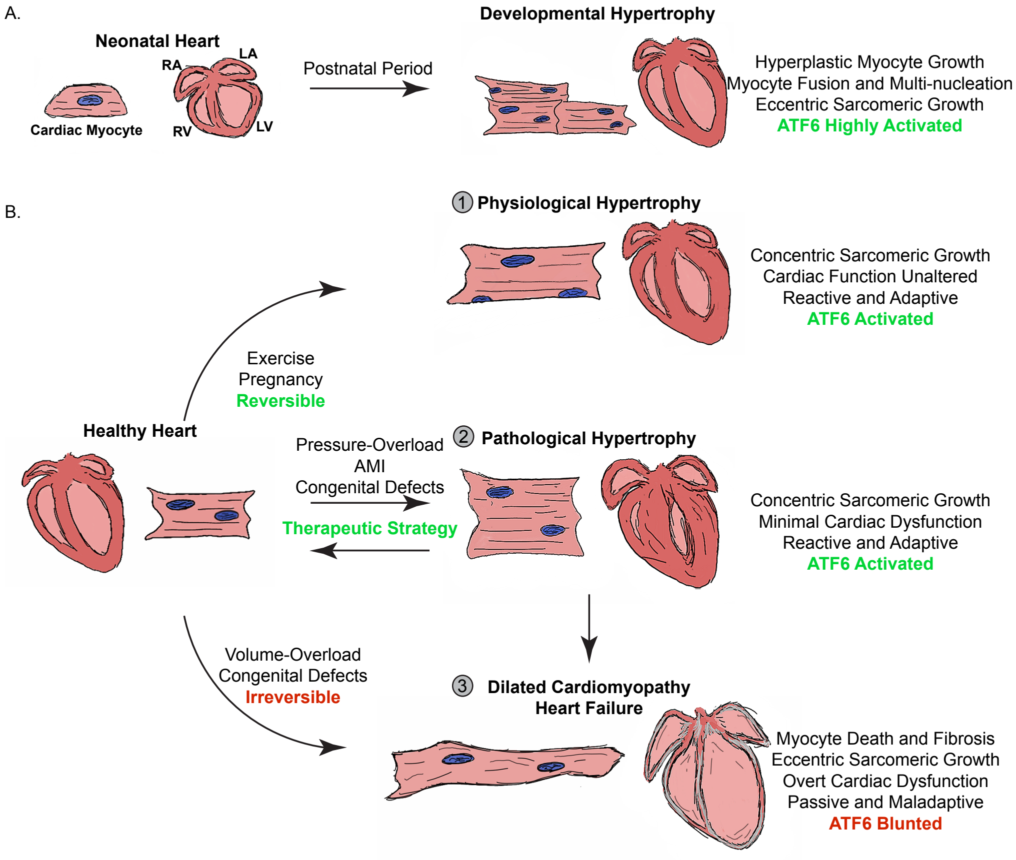

Figure 1.1- Types of cardiac hypertrophy.

(**A**) Cross-section drawings are shown to demonstrate the growth of the heart during pre- and postnatal development. This developmental hypertrophy is depicted showing increases in both atrial (RA and LA) and ventricular (RV and LV) chamber blood volume (pink) and wall thickness (red areas are myocardium). Developmental cardiac hypertrophy from the neonatal stage to adulthood is characterized by both hyperplasia and hypertrophy, and since ATF6 is expressed in robust quantities during this period of development, the ER protein folding machinery is sufficient to support the protein-folding load. (**B**) The adult healthy heart undergoes three main types of cardiac hypertrophy: 1. Physiological hypertrophy is an adaptive and reactive process of concentric growth in response to chronic exercise and pregnancy. ATF6 is robustly activated by this process, and the ER protein folding machinery is sufficient to support this form of hypertrophy. 2. Pathological hypertrophy is considered an adaptive and reactive process of concentric growth in response to pressure-overload or AMI. In the acute compensatory stages of this concentric growth, ATF6 is robustly activated by this process, and the ER protein folding machinery is sufficient to support this form of hypertrophy. This form of cardiac hypertrophy is reversible and a potential target of ATF6-based therapeutics. 3. Dilated cardiomyopathy and heart failure are either a result of chronic pathological hypertrophy or congenital defects. This is a passive process characterized by chamber dilatation and cardiac myocyte apoptosis and fibrosis. ATF6 and the protein folding machinery are not sufficient at this stage of maladaptive growth.

1.2.3. Pathological Cardiac Hypertrophy

Pathological cardiac hypertrophy is a reactive response to either genetic or environmental/habitual diseases that primarily affect cardiac myocytes[31,37]. The two major effectors of pathological cardiac hypertrophy are biomechanical stress and neurohumoral factors, both increasing cardiac workload. Subsequently, intracellular signaling cascades associated with an increase in protein synthesis are activated, and thus increase protein folding demand[37]. If proteostasis is not maintained throughout this growth, the integrity of the cardiac myocyte structure and contractile function is severely impaired, leading to eventual heart failure **(Fig. 1.1B, Forms 2 and 3)**. Hypertension and pressure-overload is the most important risk factor for heart failure, and data from the Framingham Heart Study demonstrated that the severity of hypertension and coordinate pathological cardiac hypertrophy is a prognostic indicator of heart failure risk[37,52,53]. Traditionally, hypertensive and pressure- or volume-induced cardiac hypertrophy is viewed as an adaptive response characterized by concentric growth of the heart and cardiac myocytes, as evidenced by a relative increase in wall thickness and mass without affecting chamber volume, as well as sarcomeric growth in diameter as opposed to length[31,37]. At this stage, there is minimal effect on cardiac output, and many of the symptoms are reversible, making it a prime target of therapeutic intervention. However, with prolonged stress, the heart undergoes an irreversible state of decompensation, characterized by chamber dilatation due to cardiac myocyte death, fibrotic remodeling, and immune cell infiltration, as well as a decreased cardiac output and compliance, leading to inevitable heart failure[37]. The dangers and pathogenesis of even early-stage concentric cardiac hypertrophy in response to hypertension have been noted as early as the 19th century by William Osler and physicians observing the broken nature of this compensatory phase of remodeling that is coordinate with degenerating myocardium[54]. Late-stage decompensation impairs excitation-contraction coupling, thus increasing the risk of malignant arrythmia and death[37]. Continued research efforts are aimed at dissecting the adaptive signaling mechanisms underlying the initial compensatory phases of cardiac hypertrophy that decrease ventricular wall stress in accordance with Laplace's law, while negating the maladaptive features associated with decompensation.

Pathological hypertrophy can also be secondary to chronic conditions not directly linked to hemodynamic stress, such as coronary artery disease (CAD) and ischemic heart disease or injury, including acute myocardial infarction (AMI), where thrombotic coronary artery occlusion causes rapid, irreparable ischemic injury to the heart[55–59]. Much of the damage associated with AMI occurs from reperfusion injury, which, ironically, results from the only treatment option, primary percutaneous coronary intervention, or coronary angioplasty[60]. While reperfusion limits ischemic injury, which would otherwise be fatal, coronary angioplasty causes a rapid generation of reactive oxygen species (ROS) leading to cardiac myocyte death, due mainly to impaired proteostasis[61,62]. Since cardiac myocytes in adults are incapable of regeneration, AMI damage is essentially permanent and can set in motion a pathological remodeling of the heart, culminating eventually in heart failure and arrhythmogenesis[3].

More recently, a less well-defined form of pathological cardiac hypertrophy, heart failure with preserved ejection fraction (HFpEF), has emerged as an important pathology due to its clinical prevalence and association with ever increasing metabolic diseases[63]. HFpEF is characterized by concentric cardiac hypertrophy without overt systolic impairment, and is associated with a patient population diagnosed with the comorbidities of obesity, type II diabetes mellitus and chronic hypertension[63–65]. While initially thought of as a form of diastolic heart failure, HFpEF is further characterized by impaired active myocardial relaxation and increased passive stiffness, as well as increased pulmonary capillary wedge pressures that can rise to levels above that of even hypertensive patients, or those with aortic stenosis[66,67]. However, underappreciated until more recently is the contribution of non-cardiac myocytes in the heart to the progression of HFpEF, namely endothelial cells, which lead to derangement of nitric oxide bioavailability, thus leading to cardiac myocyte hypertrophy subsequent to impaired Ca^{2+} handling[63]. HFpEF has also been directly linked to impaired proteostasis, as extracellular cardiac amyloid deposition and nitrosative stress strain the proteostasis network, resulting in protein damage that activates the adaptive UPR response pathway[68,69].

Given that the increase in the demands on the protein-folding machinery that is associated with cardiac hypertrophy, which has been shown to activate ATF6 and the adaptive UPR in order to maintain proteostasis and heart function, ATF6 becomes a potential therapeutic target for mitigation of the proteotoxicity associated with numerous models of CVD.

1.3.1. The ER Unfolded Protein Response in Cardiac Myocyte Proteostasis

The increase in protein folding demand associated with nascent protein synthesis occurring during cardiac hypertrophy puts a strain on the global cellular framework responsible for balancing proteostasis, which is necessary to allow for proper cardiac myocyte growth and is critical to maintaining cardiac function[10–15]. Proteostasis is maintained by cellular networks that balance protein synthesis with proper folding, trafficking, and degradation[15,70]. Imbalances in this cellular framework can lead to the accumulation of proteotoxic misfolded protein aggregates and proteinopathies, contributing to a multitude of systemic diseases including CVD and cardiomyopathies, eventually leading to heart failure[71–76]. In addition to CVD, impaired proteostasis has been intimately linked to aging-related diseases thought to be a result of genetic and environmental derailment of the integrity of the proteome, fundamental to the progression of many neuronal-based diseases such as Alzheimer’s, Parkinson’s, and Huntington’s disease[17].

While the proteostasis framework encompasses numerous proteins comprising chaperones, foldases, and scaffolds (assisting in the proper folding and refolding of proteins), the focus of many research efforts aimed at designing proteostasis-based therapeutics has been on the ubiquitin-proteasome system (UPS) responsible for the clearance of aggregation-prone misfolded proteins[30]. In fact, considering that as many as 30% of nascent proteins during cardiac hypertrophy never reach their final folded conformations, and therefore, must be degraded either concurrently or very soon after translation, emphasizes the critical nature of the UPS in maintaining proteostasis[77,78].

Furthermore, the majority of nascent proteins made during cardiac hypertrophy include sarcomeric proteins, calcium-handling proteins, or receptors destined for the sarcolemma, implicating the importance of not only the temporal kinetics of protein degradation, but also the spatial location of proteosomes relative to translational “hot-spots” for maintenance of proteostasis during cardiac myocyte growth.

1.3.2. ER Associated Degradation

As many as 40% of nascent proteins are translated on ER-associated ribosomes, including secreted and membrane proteins requiring transit across the ER membrane during translation in conjunction with either co- or post-translational folding prior to terminal trafficking[79]. Due to the high volume of protein translation associated with the ER, the ER maintains proteostasis in part by eliminating terminally misfolded or excess proteins via the evolutionarily conserved ER-associated degradation (ERAD) pathway[80]. ER luminal chaperones recognize these potentially proteotoxic hazards, and ERAD is initiated via retrotranslocation of polypeptides from the ER membrane or lumen to the cytosol, a process requiring the AAA+-type ATPase valosin-containing protein (VCP) to be recruited to the ER surface via a VCP-adaptor protein (e.g., Vimp)[81,82]. This ‘ratchet’ effect for extracting proteins from the ER then allows ER-transmembrane E3 ubiquitin ligases (e.g., Hrd1) to mark them for proteasome-mediated degradation[83,84]. ERAD complex constituents recognize a vast array of misfolded proteins and while the mechanism of substrate recognition is still unclear, it is known that the constituents of the complex dictate a degree of substrate specificity. Thus, specific VCP-adaptor proteins, such as Vimp, Derlin1, or Ufd1, that separately coordinate ERAD complex formation could recognize specific substrates.

1.3.3. ER UPR

Cardiac myocytes comprise the majority of the cellular mass of the myocardium and, within the ventricles, function primarily as the contractile unit required for pumping oxygenated blood into the circulation. Because of this dominant role, many studies have focused on sarcomeric and calcium-handling proteins as part of the contractile calcium handling process vital for cardiac myocyte contractility. However, the majority of sarcolemmal and secreted proteins integral to maintaining proper cardiac function via proper excitation-contraction coupling and endocrine/paracrine signaling under physiological conditions, as well as during cardiac hypertrophy, are made in the ER[85,86]. Furthermore, many post-translational modifications vital for proper protein function occur in the ER, namely glycosylation, disulfide bond formation, and proteolytic processing[87,88]. Thus, in the heart, etiologies related to CVD, including pressure- or volume-overload, and AMI place high demands on the ER protein folding machinery to maintain ER proteostasis.

Under conditions in which the protein folding demand outweighs the capacity of the ER protein folding machinery, such as during hypertrophic cardiac myocyte growth, the UPR is activated[14]. Acute activation of the UPR balances proteostasis and maintains viability and function of cardiac myocytes primarily via genetic modification. The PERK, IRE1, and ATF6 arms of the UPR overlap to an extent, however, they each confer individualistic downstream signaling cascades aimed at restoring proteostasis[23].

The PERK branch of the UPR functions primarily to phosphorylate the translation initiation factor, eIF2α on Ser-51 resulting in global arrest of 5′ cap-dependent protein translation in an attempt to acutely decrease the protein folding load[89]. Phosphorylation of eIF2α allows for the continued translation of a subset of mRNAs required for adaptive ER proteostasis. The role of PERK in CVD has been studied using a mouse model in which PERK has been selectively deleted in cardiac myocytes using a conditional gene targeting approach. These studies revealed that in a model of pressure overload-induced heart failure, PERK was critical for attenuating fibrotic remodeling associated with excessive cardiac myocyte apoptosis and immune cell infiltration[90].

IRE1 functions primarily as an endonuclease responsible for splicing the Xbp1 mRNA to a splice variant (Xbp1$_s$) encoding an active transcription factor[91]. The nuclease ability of IRE1 can contribute to decreasing the protein folding load of the ER via cleavage of mRNAs localized to the ER membrane that are not critical for the adaptive UPR. This process is called regulated Ire1-dependent decay (RIDD)[92]. For the most part, the gene program induced by XBP1$_s$ overlaps to an extent with ATF6, comprised mostly of chaperones and ERAD components. However, studies using a transgenic mouse model to overexpress XBP1$_s$ specifically in cardiac myocytes have demonstrated that XBP1$_s$ confers protection against AMI injury and post-AMI cardiac remodeling by transcriptionally regulating non-canonical targets that are key components of the hexosamine biosynthetic pathway[93]. More recently, it was shown that XBP1$_s$ is protective in a novel murine model of HFpEF via its ability to induce those same proteins involved in O-GlcNAcylation[69]. XBP1$_s$ has an additional role in regulating cardiac hypertrophy in response to pressure-overload via transcriptional induction of FKBP11, and thus regulating mTORC1 activity[94].

1.4.1. ATF6 and Proteostasis in the Heart

Upon sensing an increase in protein folding demand, ATF6 acts as the primary adaptive responder that is liberated from the ER to act as an active transcription factor regulating a gene program that fosters the maintenance of proteostasis in cardiac myocytes[95–97]. In response to CVD and various hypertrophic growth stimuli in the heart, ATF6 is activated, which allows for homeostatic growth and regulation of proteostasis via transcriptionally inducing gene targets that function to either temper protein synthesis, fold nascent proteins, or degrade misfolded and surplus proteins[50].

1.4.2. ATF6 Activation

The activation process of ATF6 is a tightly regulated process and, in the absence of proteostatic imbalance, exists as a 90 kD ER transmembrane protein **(Fig. 1.2, Step 1)**[98]. As a primary sensor/effector of the UPR, ATF6 recognizes an increase in protein folding demand brought about by stressors such as pressure- or volume-overload, or an accumulation of misfolded proteins as occurs during an AMI. While the mechanism by which stimulus-specific stressors are differentially recognized and integrated by ATF6 remains unclear, the primary activation process is mediated by the ER chaperone, GRP78, as well as protein disulfide isomerases (PDIs)[97,99]. ATF6 is kept inactive and retained in the ER via the binding of GRP78 to the ER-luminal domain of ATF6 cloaking a Golgi localization sequence[100,101]. Secondarily, inactive ATF6 exists in an oligomeric state via intermolecular disulfide bonding regulated by PDIs, such as PDIA5, and only upon the reduction of the disulfide bonds[97], and subsequent dissociation of GRP78[100,101], can ATF6 monomerize and translocate to the Golgi, where it is cleaved via regulated intramembrane proteolysis by S1 and S2 proteases **(Fig. 1.2, Step 2)**[102]. This proteolysis liberates an N-terminal 50 kD fragment of ATF6 that is able to freely translocate to the nucleus via a nuclear localization sequence **(Fig. 1.2, Step 3)**[98] where it recognizes and binds to promoter regions containing canonical ATF6 binding motifs, such as the ER stress element (ERSE)[95]. For the most part, ATF6 is known for regulating canonical gene targets as part of an adaptive panel destined for the ER and designed to regulate ER protein folding **(Fig. 1.2, Steps 4 and 5)** comprised of ER-resident chaperones (e.g., GRP78), PDIs, and ERAD components (e.g., HRD1)[11,14,16,18]. However, recent studies have illuminated a remarkable ability of ATF6 to induce non-canonical gene targets that were not previously known to be genes related to the UPR nor reside in the ER, but instead are induced by ATF6 in a stimulus-specific manner and localize to specific regions of cardiac myocytes including the lysosome[50], peroxisome[28] and sarcolemma **(Fig. 1.2, Step 6)**[103].

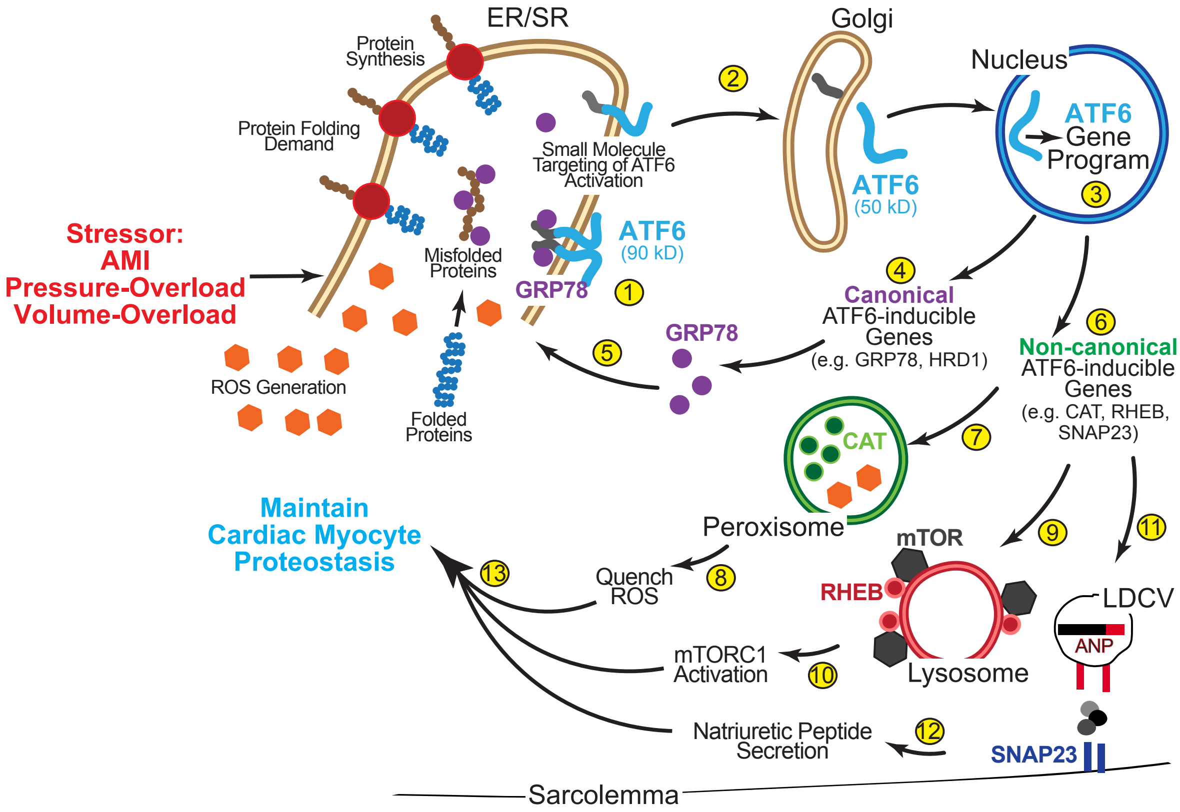

Figure 1.2- ATF6 activation and gene program induction.

(1) In its inactive state, ATF6 is a 90kD ER transmembrane protein that is anchored in the membrane in oligomers via GRP78 and intermolecular disulfide bonding. (2) Upon stressors, like cardiac hypertrophy that increases protein synthesis and the protein folding demand or AMI that elevates cellular levels of reactive oxygen species (ROS), GRP78 dissociates from the ER luminal domain of ATF6 and the disulfide bonds are reduced allowing monomerization of ATF6, which allows the 90 kD form of ATF6 to translocate to the Golgi, where it is cleaved by S1P and S2P to liberate the N-terminal approximately 400 amino acids (50 kD) of ATF6 from the ER membrane. It is this unique sequence of activation steps that open a window of small molecule targeting and discovery of ATF6-based therapeutics. (3) The clipped form of ATF6 has a nuclear localization sequence, which facilitates its movement to the nucleus where it binds to specific regulatory elements in ATF6-responsive genes, such as ER stress response elements (ERSEs), and induces the ATF6 gene program. (4) The canonical ATF6 gene program comprises genes that encode proteins that localize to the ER, such as the chaperone, GRP78, or components of ERAD, HRD1 (5), where they fortify ER protein folding. (6) The non-canonical ATF6 gene program comprises genes that encode proteins not typically categorized as ER stress-response proteins, many of which localize to regions of the cell outside the ER. (7) Catalase is a potent antioxidant that localizes to the lumen of peroxisomes where it functions to (8) quench ROS. (9) Rheb is a small GTPase located on the surface of lysosomes that when bound to mTOR, (10) promotes mTORC1 activation and sustains protein synthesis. (11) SNAP23 is a t-SNARE protein crucial for (12) secretion of natriuretic peptides via large dense-core vesicles (LDCV) in response to hemodynamic stress. (13) Both the canonical and non-canonical ATF6 gene programs coordinate to maintain cardiac myocyte proteostasis.

1.4.3. Early Findings of ATF6 in the Heart

The initial studies of ATF6 in the heart came about somewhat serendipitously. During the investigation of gene induction in response to hypertrophic stimuli, it was discovered that ATF6 was a requisite binding partner of Serum response factor (SRF) allowing for subsequent recognition and binding to canonical SRF promotor motifs, serum response elements (SREs) and thus allowing for proper cardiac myocyte growth. This was a bit of foreshadowing, and the first indication that ATF6 could be required for cardiac hypertrophy[104].

Following these initial discoveries in cultured cardiac myocytes, the fascinating biochemistry of ATF6 quickly attracted attention, which led to considerable continued investigation. While at this time, it was still unclear if pathophysiological stimuli activated ATF6, what was apparent was the transient nature of its activity. Once activated, ATF6 exhibits a robust influence on gene induction followed by its own rapid degradation[105]. In fact, the half-life of ATF6 was noted to be so short, it was actually an initial impediment for continued experimentation until proteasome inhibitors were used to decrease its degradation sufficiently to allow for detection. The rapid half-life was found to be directly correlated to its transcriptional induction capacity as domain mapping of ATF6 led to the identification of a unique 8 amino acid sequence shared with the rapidly-degraded viral transcription factor, VP16, and deletion of this motif not only attenuated transcriptional activity, but prolonged the half-life of ATF6[105–107]. Therefore, it appears that ATF6 was designed to be a rapid and transient adaptive response transcription factor, reasons for which are still unclear.

1.4.4. ATF6 Regulates an Adaptive Gene Panel in the Heart

In an attempt to delineate a functional role for ATF6 and proteostasis in the heart, the first ATF6 transgenic mice were generated. These mice were designed so that ATF6 could be selectively expressed and activated at will[27]. As researchers were keenly aware of the importance of the transient nature of ATF6 activity, this transgenic mouse was designed such that ATF6 could be conditionally activated by fusing activated ATF6 to the mutant mouse estrogen receptor (MER), unmasking of the ATF6 transactivation domain upon the introduction of tamoxifen. Upon initial study and characterization, it was discovered that similar to endogenous ATF6 in model cell lines, the ATF6-MER was rapidly degraded upon activation and was the first in vivo evidence of the "degraded-when-active" property of ATF6[27]. Subsequent microarray analysis of ventricular extracts identified approximately 400 genes to be regulated by ATF6 using this transgenic mouse, the majority of which make up a canonical adaptive gene profile of ER-targeted proteins to regulate ER-protein folding[108].

While at this time, it was becoming more apparent that a number of pathological conditions, including pressure-overload, ischemia, and AMI could cause an imbalance in proteostasis and activate the UPR, many studies emerged focusing on a role of downstream targets of ATF6 in CVD. Hrd1, a ubiquitin E3 ligase and integral for the ERAD system, was demonstrated to modulate cardiac hypertrophy and to restore cardiac function in a pressure-overload model of heart failure, presumably by enhancing the degradation of proteotoxic misfolded proteins and thus promoting cardiac myocyte viability[44]. A separate ATF6-inducible target that contributes to the translocation of misfolded proteins out of the ER in the ERAD system, Derlin3, was shown to be protective in cultured cardiac myocytes subjected to in vitro ischemia-reperfusion (I/R) and to enhance ERAD of terminally misfolded proteins in an ATF6-dependent manner[109]. Additional canonical targets of ATF6 identified in the ATF6-MER hearts included the protein disulfide isomerase, PDIA6[110], which was shown to confer protection against in vitro I/R, as well as ER-resident chaperones, MANF and GRP78[108,111,112]. MANF and GRP78 became interesting targets of ATF6, as they not only were known to enhance ER protein folding, but despite both having ER-retention motifs anchoring them inside the ER, were demonstrated to be actively secreted from cultured cardiac myocytes upon only select stimuli known to deplete ER Ca^{2+}.[112] Subsequent to their trafficking and secretion, MANF and GRP78 function adaptively in the extracellular matrix or at the sarcolemma via maintaining cardiac myocyte proteostasis[113]. Furthermore, GRP78 has drawn attention as a potential therapeutic target as an adaptive response protein conferring protection in the setting of AMI via activating the pro-survival kinase, Akt[114], and enhance the cardiac hypertrophic response by activating the pro-growth transcription factor, GATA-binding protein 4 (GATA4)[115].

1.5. ATF6 is an Adaptive Responder in CVD via Regulating Non-canonical Genes

1.5.1. ATF6 is Protective in Models of Acute Myocardial Infarction

Studies highlighting the protective roles of canonical gene targets of ATF6 have further fortified interest in pursuing ATF6-based therapeutics in clinically relevant disease models, namely AMI and pathological cardiac hypertrophy. Using the ATF6-MER model described above, it was discovered that ATF6 could confer protection against a model of I/R injury using an ex vivo Langendorff perfused heart system[27]. ATF6 activation blunted infarction and preserved cardiac contractile function in an acute injury model being the first report demonstrating activated ATF6 could exert widespread protective effects in any tissue, in vivo. Coordinately, additional studies demonstrated that using the ATF6-MER model in which the transgene was conditionally expressed in mouse forebrain neurons mitigated infarct size during an acute murine ischemic stroke model via occlusion of the middle cerebral artery (MCAO)[29].

Despite several studies demonstrating the efficacy of ATF6 in mitigating AMI injury, the mechanism of how ATF6, an ER-resident transcription factor, could protect from reperfusion damage associated with AMI or stroke, most of which is caused by oxidative stress and ROS generated by mitochondria, remained elusive. Accordingly, to address this mechanism, recent studies used either a mouse model where ATF6 had been globally deleted (ATF6 KO)[28] or generated a mouse model in which ATF6 is conditionally deleted only in cardiac myocytes (ATF6 cKO)[116]. Transcript profiling of ATF6 transgenic and ATF6 cKO mice revealed that in addition to genes encoding proteins that constitute the ER protein-folding machinery, ATF6 induces genes that encode proteins that do not even reside in the ER. One such group of genes encodes antioxidant proteins that reside outside the ER, including peroxisomal catalase **(Fig. 1.2, Step 7)**. This was a surprise because it was the first time antioxidant genes were shown to be induced by ATF6 in any cell or tissue type, and the first study to identify ATF6 as a direct transcriptional inducer of the catalase gene. This study demonstrated that it is through this non-canonical role that the scope of ATF6 action extends well beyond canonical UPR gene program to include proteostasis regulatory pathways, such as antioxidants, that can protect the heart from AMI damage **(Fig. 1.2, Step 8)**.

1.5.2. ATF6 is Required for Cardiac Myocyte Hypertrophy

In considering other possible non-canonical roles for ATF6, a recent study set out to test whether the increase in protein synthesis and protein folding demand that occur during cardiac hypertrophy poses a challenge to the protein folding machinery, resulting in ATF6 activation[50]. Indeed, ATF6 was activated in mouse hearts subjected to conditions that mimic not only pathological (pressure-overload), but also physiological (exercise) cardiac myocyte growth. Using ATF6 cKO mice, it was demonstrated that ATF6 is required for heart growth and for maintaining cardiac function under both conditions. Furthermore, ATF6 was necessary to prevent the accumulation of misfolded proteotoxic aggregates during pressure overload-induced pathological cardiac hypertrophy **(Fig. 1.3)**. The finding that ATF6 was required for exercise-induced physiological cardiac hypertrophy was surprising, as it’s a reactive growth process known to, if anything, decrease the accumulation of misfolded proteins, thus linking ATF6 activation primarily to the increase in protein synthesis. While many ATF6 regulated genes may contribute to this effect, RNAseq and ChIP analysis identified one gene that had not previously been shown to be regulated by ATF6, i.e., Rheb. Rheb is an activator of mTORC1, a major inducer of protein synthesis and subsequent myocyte growth during pathological and physiological hypertrophy[117]. While not previously studied in the heart, constitutive mTORC1 activation via inhibition of the tuberous sclerosis complex (TSC1/2), the negative regulator of Rheb, has been shown to activate the UPR in model cell lines[118]. Rheb expression increased and mTORC1 was activated during both physiological and pathological hypertrophy, but not in ATF6 cKO mouse hearts. AAV9-mediated ectopic expression of Rheb restored cardiac myocyte growth to ATF6 cKO hearts. Similar results were found in a more recent publication where blunted pressure overload-induced cardiac hypertrophy and an accelerated progression to heart failure in ATF6 cKO mice[119]. Thus, ATF6 plays a previously unappreciated role in cardiac hypertrophy via inducing the non-canonical target, Rheb **(Fig. 1.2, Steps 9 and 10)**.

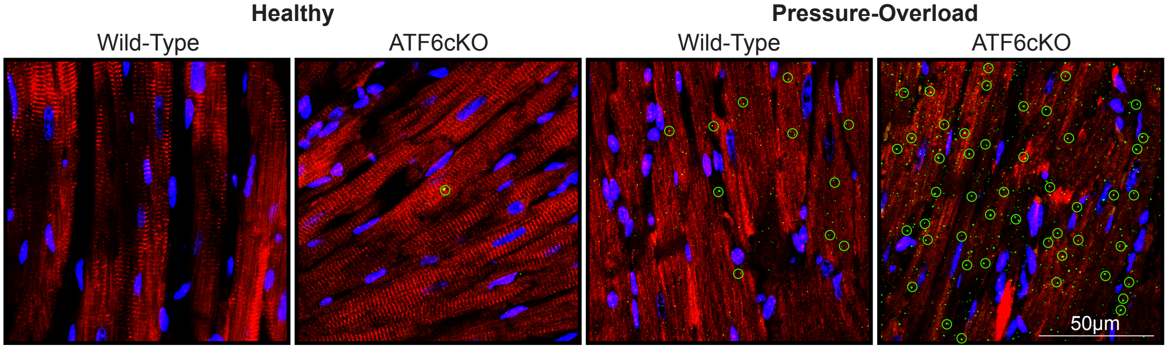

Figure 1.3- Effect of cardiac myocyte-specific ATF6 deletion in mouse hearts subjected to acute pressure-overload.

Mice in which ATF6 has been selectively deleted in cardiac myocytes were subjected to an acute model of pressure overload-induced cardiac hypertrophy. Confocal immunocytofluorescence microscopy analysis of mouse heart sections is shown for a cardiac myocyte marker, Cardiac troponin T (red), protein amyloid oligomers (green), and nuclei (blue). The accumulation of misfolded protein aggregates indicates the necessity of ATF6 to support the protein folding load during concentric cardiac hypertrophy.

1.5.3. ATF6 Enhances Natriuretic Peptide Secretion and Hemodynamic Balance

Recent unpublished work has found yet another non-canonical target of ATF6 in a model of volume overload-induced cardiac hypertrophy[103]. When mice were subjected to a high salt diet, which is known to increase cardiac afterload primarily via increased blood volume, ATF6 cKO mice displayed advanced cardiovascular pathology characterized by hemodynamic imbalance and decreased cardiac compliance. The heart responds to high salt-induced hypertension by increasing the secretion of atrial natriuretic peptide (ANP) from atrial myocytes. In this regard, ANP increases natriuresis and diuresis and thus, decreases blood pressure[120–122]. While it was found that ATF6 did not affect cellular levels of ANP in atrial myocytes, ATF6 was found to be required for the regulated secretion of ANP from cultured atrial myocytes, as well as from mouse hearts. Mechanistically, ATF6 was shown to induce genes encoding proteins required for secretory granule exocytosis, including the t-SNARE, Snap23[123,124]. Ectopic expression of Snap23 in the setting of ATF6 loss-of-function restored regulated ANP secretion, while Snap23 knockdown in culture and in vivo mimicked the effects of ATF6 deletion on ANP secretion. These results define a new ATF6-ANP molecular signaling axis whereby ATF6 induces a non-canonical gene program required for regulated secretion to maintain cardiac myocyte proteostasis **(Fig. 1.2, Steps 11 and 12)**. Moreover, since Snap23 is required for regulated secretion of other neurotransmitters and peptides[124], it is likely that ATF6 serves a more widespread, required role in the regulated secretion of neurotransmitters and peptides.

1.5.4. ATF6 Induces Stimulus-Specific Gene Programs

Over the course of studying ATF6 in various types of CVD, it was found that ATF6 can be activated by diverse stimuli, not just misfolded proteins in the ER. These diverse ATF6 activators include oxidative stress and growth stimuli, each of which impact global proteome integrity, not just the ER proteome. Remarkably, during these various pathophysiological maneuvers, ATF6 activates unique gene programs, depending on the stimulus, and these programs serve stress-specific adaptive effects[50]. For example, oxidative stress results in ATF6-dependent induction of antioxidants, e.g., catalase, but growth regulators, e.g., Rheb. In contrast, growth stimuli activate growth regulators, but antioxidants. ATF6 gene deletion ablated the capacity for stimulus-specific induction of these genes and promoter analysis demonstrated that ATF6 bound to consensus ERSEs in a stimulus-specific manner[27,50]. A series of studies have been published highlighting a novel role for the secreted extracellular matrix protein, Thrombospondin 4, in serving as an escort protein for ATF6 activation by competing with GRP78 for binding to ATF6′s luminal domain and facilitating its the trafficking and subsequent processing. Overexpression of Thrombospondin 4 leads to ATF6 activation and confers protection in models of AMI and pressure-overload via the adaptive gene panel induced by ATF6 consisting of genes involved in membrane expansion allowing for enhancing protein and vesicular trafficking[125]. This finding is further supported by work in model cell lines that demonstrate that ATF6 can be activated by sphingolipids (e.g., dihydrosphingosine and dihydroceramide) without evidence for increased protein folding demand or protein misfolding and activate a unique gene profile allowing for homeostatic membrane expansion[126]. A further surprising finding of this study was that the activation mechanism in response to lipid accumulation was by virtue of a separate domain than that required for activation in response to the accumulation of misfolded proteins implicating, for the first time, specific domains of ATF6 required to activate downstream stimulus-specific gene programs. These data suggest that ATF6 is uniquely suited as a rapid sensor and responder to specific stress stimuli and capable of dictating genetic cellular reprogramming aimed at maintaining global proteostasis.

1.6. Small Molecule ATF6-Activators Confer Protection Against Cardiovascular Disease

As described throughout this review, maintaining cardiac myocyte proteostasis is vital for cellular viability and function, and ATF6 has demonstrated efficacy as a therapeutic target for CVD and cardiac hypertrophy[27,50,116]. Thus, a conceptual framework with specific research approaches was designed in an attempt to identify key proteostasis regulatory pathways via discovering non-canonical gene targets of ATF6 using diverse animal models of various etiologies contributing to CVD. In coordination, lead candidate direct small molecule activators of ATF6 would be identified and validated for efficacy in small and large animal models of CVD and heart failure **(Fig. 1.4)**. However, small molecules, as regulators of transcription factors, have been an understudied topic of chemical biology, mainly due to fear of non-selectivity or lack of efficaciousness when interfering with transcriptional regulation[127]. Furthermore, targeting one of the three primary effectors of the ER UPR presents complications due to ambiguity concerning precise activation mechanisms and absence of known small molecule-binding sites[97]. However, recent studies identifying key methods of ATF6 activation have demonstrated the possibility of directing small molecule activators to these steps in the activation process **(Fig. 1.2, Steps 1 and 2)**.

Using a high throughput cell-based screen followed by medium-throughput transcriptional profiling and high-stringency filtering of a 644,971-compound small molecule library, several non-toxic molecules that activate ATF6 were found, one of which is named compound 147[128]. Compound 147 selectively activates ATF6, without effecting other UPR pathways, even in the absence of ER stress. An inhibitor of S1P, the Golgi protease that cleaves and activates ATF6, inhibited 147-mediated ATF6 target gene induction. Using “click” chemistry and forms of 147 with chemical handles, the 147 interactome was defined in an attempt to demonstrate the mechanism by which it activates ATF6[129]. It was discovered that 147 binds PDIs, which regulate disulfide bond formation in the ER. The mechanism of activation of ATF6 involves the dissociation of ATF6 oligomers in the ER to form ATF6 monomers that are able to relocate to the Golgi where S1P and S2P cleave ATF6, resulting in its activation. Compound 147 inhibits a unique group of PDIs that reside in a complex with ATF6 in the ER, where they maintain ATF6 in its inactive state. In this study, it was shown that 147 facilitates the movement of ATF6 out of the ER via PDI inhibition and subsequent dissociation from ATF6.

Given the robust protection, ATF6 confers during AMI and post-AMI remodeling, the effects of pharmacological activation of ATF6 with 147 in a mouse model of reperfusion damage was chosen for initial efficacy testing[116]. Intravenous administration of 147 concurrently with reperfusion robustly and selectively activated ATF6 and downstream genes of the ATF6 gene program, protected the heart from AMI injury, preserved cardiac function, and decreased infarct size when assessed 24 h after drug administration/reperfusion. However, this protection was lost in ATF6 cKO mouse hearts. Thus, one dose of 147 concurrent with reperfusion was sufficient to induce the adaptive ATF6 gene program and provide protection from reperfusion damage during the first 24 h after AMI. Cardioprotection and ameliorated post-AMI cardiac hypertrophy was also observed in a similar experiment where heart damage and function were examined seven days after drug/reperfusion. Moreover, 147 had no deleterious effects in the absence of pathology, or in other tissues that were unaffected by reperfusion injury, an indicator of its safety. In fact, in the absence of AMI, 147 improved cardiac basal performance. This improvement was associated with the ability of just one administration of 147 to increase SERCA2a expression, resulting in improved Ca^{2+} uptake. Remarkably, by activating ATF6, 147 protected other tissues, including the brain, kidney, and liver, when they were subjected to maneuvers that induced reperfusion damage and impaired proteostasis. Moreover, administration of 147 every two to three days over a two-week timeframe had no untoward toxic effects in the heart, brain, liver, and pancreas. Thus, 147 selectively activates the ATF6 arm of the UPR in vivo, exhibiting significant potential as a therapeutic approach for treating AMI and reperfusion damage in a wide range of tissues[116].

Chapter 1, in part, is a reprint of the material as it appears in Cells in 2020. Blackwood, E.A., Bilal, A.S., Stauffer, W.T., Arrieta, A., and Glembotski, C.C. Designing novel therapies to mend broken hearts: ATF6 and cardiac proteostasis. *Cells,* 2020; 9(3). The dissertation author was the primary author of this paper.

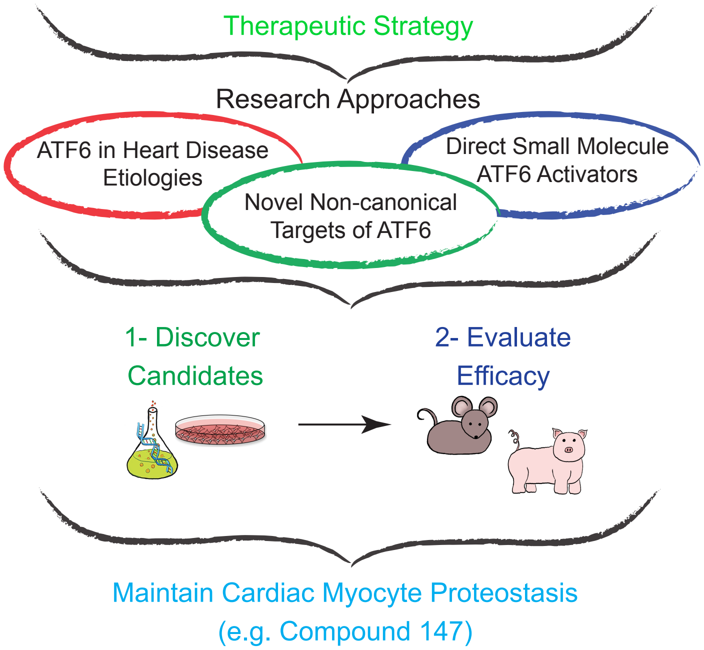

Figure 1.4- Approach to developing novel ATF6-based therapeutics.

The therapeutic framework for developing ATF6-based therapeutics is conceptually simple in design. Three main research approaches are prioritized: **1**) Expanding the scope of experimental animal models of various etiologies of heart disease in which ATF6 is studied. **2**) Discovering other non-canonical targets of ATF6. **3**) Using chemical biology to identify potent and specific small molecule activators of ATF6. Coordinately, these research approaches will converge into a streamlined experimental approach of **1**) preliminary testing of lead small molecule activators in cell models of disease, in vitro, and **2**) evaluating efficacy of these lead small molecule activators in small and large animal models, in vivo.

1.7. References

1. Benjamin, E.J.; Virani, S.S.; Callaway, C.W.; Chamberlain, A.M.; Chang, A.R.; Cheng, S.; Chiuve, S.E.; Cushman, M.; Delling, F.N.; Deo, R. American Heart Association Council on Prevention Statistics and Stroke Statistics Heart Disease and Stroke Statistics-2018 Update: A Report From the American Heart Association. *Circulation*. **2018**,*137*, 467–492.

2. Gheorghiade, M.; Braunwald, E. Hospitalizations for heart failure in the United States--a sign of hope. *JAMA* **2011**, *306*, 1705–1706.

3. Rosenzweig, A. Medicine. Cardiac regeneration. *Science*. **201**, *338*, 1549–1550.

4. Kannel, W.B. Vital epidemiologic clues in heart failure. *J. Clin. Epidemiology* **2000**, *53*, 229–235.

5. Hobbs, R.E. Guidelines for the Diagnosis and Management of Heart Failure. *Am. J. Ther.* **2004**, *11*, 467–472.

6. Levy, D.; Kenchaiah, S.; Larson, M.G.; Benjamin, E.J.; Kupka, M.J.; Ho, K.; Murabito, J.M.; Vasan, R.S. Long-Term Trends in the Incidence of and Survival with Heart Failure. *New Engl. J. Med.* **2002**, *347*, 1397–1402.

7. Zannad, F. Incidence, clinical and etiologic features, and outcomes of advanced chronic heart failure: The EPICAL study. Epidemiologie de l'Insuffisance Cardiaque Avancee en Lorraine. *J. Am. Coll. Cardiol*. **1999**, *33*, 734–742.

8. Haldeman, G.A.; Croft, J.B.; Giles, W.H.; Rashidee, A. Hospitalization of patients with heart failure: National Hospital Discharge Survey, 1985 to 1995. *Am. Hear. J.* **1999**, *137*, 352–360.

9. Malek, M. Health economics of heart failure. *Hear.* **1999**, *82*, IV11–IV13.

10. Frey, N.; Katus, H.A.; Olson, E.N.; Hill, J.A. Hypertrophy of the heart: A new therapeutic target? *Circulation* **2004**, *109*, 1580–1589.

11. Arrieta, A.; Blackwood, E.A.; Glembotski, C.C. ER Protein Quality Control and the Unfolded Protein Response in the Heart. *The Future of HIV-1 Therapeutics* **2017**, *414*, 193–213.

12. Razeghi, P.; Baskin, K.K.; Sharma, S.; Young, M.E.; Stepkowski, S.; Essop, M.F.; Taegtmeyer, H. Atrophy, hypertrophy, and hypoxemia induce transcriptional regulators of the ubiquitin proteasome system in the rat heart. *Biochem. Biophys. Res. Commun.* **2006**, *342*, 361–364.

13. Taegtmeyer, H.; Harinstein, M.E.; Gheorghiade, M. More Than Bricks and Mortar: Comments on Protein and Amino Acid Metabolism in the Heart. *Am. J. Cardiol.* **2008**, *101*, S3–S7.

14. Glembotski, C.C. Roles for the sarco-/endoplasmic reticulum in cardiac myocyte contraction, protein synthesis, and protein quality control. *Physiology.* **2012**, *27*, 343–350.

15. Balch, W.E.; Morimoto, R.I.; Dillin, A.; Kelly, J.W. Adapting Proteostasis for Disease Intervention. *Sci.* **2008**, *319*, 916–919.

16. Doroudgar, S.; Glembotski, C.C. New concepts of endoplasmic reticulum function in the heart: Programmed to conserve. *J. Mol. Cell. Cardiol.* **2012**, *55*, 85–91.

17. Hetz, C.; Glimcher, L.H. Protein homeostasis networks in physiology and disease. *Curr. Opin. Cell Boil.* **2011**, *23*, 123–125.

18. Glembotski, C.C. Clarifying the cardiac proteasome paradox: Protein quality control. *Circ. Res.* **2012**, *111*, 509–512.

19. Hartl, F.U.; Bracher, A.; Hayer-Hartl, M. Molecular chaperones in protein folding and proteostasis. *Nat.* **2011**, *475*, 324–332.

20. Labbadia, J.; Morimoto, R.I. The biology of proteostasis in aging and disease. *Annu. Rev. Biochem.* **2015**, *84*, 435–464.

21. Das, I.; Krzyzosiak, A.; Schneider, K.; Wrabetz, L.; D'Antonio, M.; Barry, N.; Sigurdardottir, A.; Bertolotti, A. Preventing proteostasis diseases by selective inhibition of a phosphatase regulatory subunit. *Sci.* **2015**, *348*, 239–242.

22. Roth, D.M.; Balch, W.E. Modeling general proteostasis: Proteome balance in health and disease. *Curr. Opin. Cell Boil.* **2010**, *23*, 126–134.

23. Walter, P.; Ron, D. The Unfolded Protein Response: From Stress Pathway to Homeostatic Regulation. *Sci.* **2011**, *334*, 1081–1086.

24. Smith, M.H.; Ploegh, H.L.; Weissman, J.S. Road to Ruin: Targeting Proteins for Degradation in the Endoplasmic Reticulum. *Sci.* **2011**, *334*, 1086–1090.

25. Chiang, W.-C.; Hiramatsu, N.; Messah, C.; Kroeger, H.; Lin, J.H. Selective Activation of ATF6 and PERK Endoplasmic Reticulum Stress Signaling Pathways Prevent Mutant Rhodopsin Accumulation. *Investig. Opthalmology Vis. Sci.* **2012**, *53*, 7159–7166.

26. Cooley, C.; Ryno, L.M.; Plate, L.; Morgan, G.; Hulleman, J.D.; Kelly, J.W.; Wiseman, R.L. Unfolded protein response activation reduces secretion and

extracellular aggregation of amyloidogenic immunoglobulin light chain. *Proc. Natl. Acad. Sci.* **2014**, *111*, 13046–13051.

27. Martindale, J.J.; Fernandez, R.; Thuerauf, D.; Whittaker, R.; Gude, N.; Sussman, M.; Glembotski, C.C. Endoplasmic Reticulum Stress Gene Induction and Protection From Ischemia/Reperfusion Injury in the Hearts of Transgenic Mice With a Tamoxifen-Regulated Form of ATF6. *Circ. Res.* **2006**, *98*, 1186–1193.

28. Jin, J.-K.; Blackwood, E.A.; Azizi, K.M.; Thuerauf, N.J.; Fahem, A.G.; Hofmann, C.; Kaufman, R.J.; Doroudgar, S.; Glembotski, C.C. ATF6 Decreases Myocardial Ischemia/Reperfusion Damage and Links ER Stress and Oxidative Stress Signaling Pathways in the Heart. *Circ. Res.* **2016**, *120*, 862–875.

29. Yu, Z.; Sheng, H.; Liu, S.; Zhao, S.; Glembotski, C.C.; Warner, D.S.; Paschen, W.; Yang, W. Activation of the ATF6 branch of the unfolded protein response in neurons improves stroke outcome. *Br. J. Pharmacol.* **2016**, *37*, 1069–1079.

30. Bernardo, B.C.; Weeks, K.; Pretorius, L.; McMullen, J.R. Molecular distinction between physiological and pathological cardiac hypertrophy: Experimental findings and therapeutic strategies. *Pharmacol. Ther.* **2010**, *128*, 191–227.

31. Heineke, J.; Molkentin, J.D. Regulation of cardiac hypertrophy by intracellular signalling pathways. *Nat. Rev. Mol. Cell Boil.* **2006**, *7*, 589–600.

32. Chien, K.R. Stress pathways and heart failure. *Cell* **1999**, *98*, 555–558.

33. Sandler, H.; Dodge, H.T. Left Ventricular Tension and Stress in Man. *Circ. Res.* **1963**, *13*, 91–104.

34. Hood, W.P.; Rackley, C.E.; Rolett, E.L. Wall stress in the normal and hypertrophied human left ventricle. *Am. J. Cardiol.* **1968**, *22*, 550–558.

35. Grossman, W.; Jones, D.; McLaurin, L.P. Wall stress and patterns of hypertrophy in the human left ventricle. *J. Clin. Investig.* **1975**, *56*, 56–64.

36. Meerson, F.Z. On the mechanism of compensatory hyperfunction and insufficiency of the heart. *Cor et Vasa* 1961, *3*, 161-77.

37. Hill, J.A.; Olson, E.N. Cardiac plasticity. *N Engl J. Med*. **2008**, *358*, 1370–1380.

38. Zak, R. Cell proliferation during cardiac growth. *Am. J. Cardiol.* **1973**, *31*, 211–219.

39. Zak, R. Development and proliferative capacity of cardiac muscle cells. *Circ. Res.* 1974, *35*, 17-26.

40. Li, F. Rapid Transition of Cardiac Myocytes from Hyperplasia to Hypertrophy During Postnatal Development. *J. Mol. Cell. Cardiol.* **1996**, *28*, 1737–1746.

41. Oparil, S.; Bishop, S.P.; Clubb, F.J. Myocardial cell hypertrophy or hyperplasia. *Hypertens.* **1984**, *6*, III38.

42. Bugaisky, L.; Zak, R. Cellular growth of cardiac muscle after birth. *Tex. Rep. Boil. Med.* 1979, *39* 123-38.

43. Maillet, M.; Van Berlo, J.; Molkentin, J.D. Molecular basis of physiological heart growth: Fundamental concepts and new players. *Nat. Rev. Mol. Cell Boil.* **2013**, *14*, 38–48.

44. Doroudgar, S.; Völkers, M.; Thuerauf, N.J.; Khan, M.; Mohsin, S.; Respress, J.L.; Wang, W.; Gude, N.; Müller, O.J.; Wehrens, X.H.; et al. Hrd1 and ER-Associated Protein Degradation, ERAD, are Critical Elements of the Adaptive ER Stress Response in Cardiac Myocytes. *Circ. Res.* **2015**, *117*, 536–546.

45. Taylor, R.C. Aging and the UPR(ER). *Brain Res.* **2016**, *1648*, 588–593.

46. Dorn, G.W. The Fuzzy Logic of Physiological Cardiac Hypertrophy. *Hypertens.* **2007**, *49*, 962–970.

47. Thompson, P.D. D. Bruce Dill Historical lecture. Historical concepts of the athlete's heart. *Med. Sci. Sports Exerc.* 2004, *36*, 363-70.

48. Milliken, M.C.; Stray-Gundersen, J.; Peshock, R.; Katz, J.; Mitchell, J.H. Left ventricular mass as determined by magnetic resonance imaging in male endurance athletes. *Am. J. Cardiol.* **1988**, *62*, 301–305.

49. Fagard, R. Athlete's heart. *Heart*. **2003**, *89*, 1455–1461.

50. Blackwood, E.A.; Hofmann, C.; Domingo, M.S.; Bilal, A.S.; Sarakki, A.; Stauffer, W.; Arrieta, A.; Thuerauf, N.J.; Kolkhorst, F.W.; Müller, O.; et al. ATF6 Regulates Cardiac Hypertrophy by Transcriptional Induction of the mTORC1 Activator, Rheb. *Circ. Res.* **2019**, *124*, 79–93.

51. Maloyan, A.; Gulick, J.; Glabe, C.G.; Kayed, R.; Robbins, J. Exercise reverses preamyloid oligomer and prolongs survival in αB-crystallin-based desmin-related cardiomyopathy. *PNAS*. **2007**, *14*, 5995–6000.

52. Levy, D.; Garrison, R.J.; Savage, D.D.; Kannel, W.B.; Castelli, W.P. Prognostic implications of echocardiographically determined left ventricular mass in the Framingham Heart Study. *N Engl J. Med*. **1990**, *322*, 1561–1566.

53. Koren, M.J.; Devereux, R.B.; Casale, P.N.; Savage, D.D.; Laragh, J.H. Relation of left ventricular mass and geometry to morbidity and mortality in uncomplicated essential hypertension. *Ann. Intern. Med*. **1991**, *114*, 345–352.

54. Osler, W. The principles and practice of medicine. *Appleton*: New York, NY, USA, **1892**.

55. Roth, G.A.; Global, Regional, and National Burden of Cardiovascular Diseases for 10 Causes, 1990 to 2015. *J. Am. Coll Cardiol*. **2017**, *70*, 1–25.

56. Frangogiannis, N.G. Pathophysiology of Myocardial Infarction. *Compr Physiol*. **2015**, *5*, 1841–1875.

57. Hausenloy, D.J.; Yellon, D.M. The evolving story of “conditioning” to protect against acute myocardial ischaemia-reperfusion injury. *Heart*. **2007**, *93*, 649–651.

58. Bulluck, H.; Yellon, D.M.; Hausenloy, D.J. Reducing myocardial infarct size: Challenges and future opportunities. *Heart*. **2016**, *102*, 341–348.

59. Hausenloy, D.J.; Yellon, D.M. Ischaemic conditioning and reperfusion injury. *Nat. Rev. Cardiol*. **2016**, *13*, 193–209.

60. Kalogeris, T.; Baines, C.P.; Krenz, M.; Korthuis, R.J. Ischemia/Reperfusion. *Compr Physiol*. **2016**, *7*, 113–170.

61. Murphy, E.; Steenbergen, C. Mechanisms underlying acute protection from cardiac ischemia-reperfusion injury. *Physiol Rev*. **2008**, *88*, 581–609.

62. Yellon, D.M.; Hausenloy, D.J. Myocardial reperfusion injury. *N Engl J. Med*. **2007**, *357*, 1121–1135.

63. Gevaert, A.B.; Boen, J.R.A.; Segers, V.F.; Van Craenenbroeck, E.M. Heart failure with preserved ejection fraction: A review of cardiac and noncardiac pathophysiology. *Front. Physiol*. **2019**, *10*, e638.

64. Lam, C.S.P.; Donal, E.; Kraigher-Krainer, E.; Vasan, R.S. Epidemiology and clinical course of heart failure with preserved ejection fraction. *Eur. J. Heart Fail.* **2011**, *13*, 18–28.

65. Lam, C.S.P.; Roger, V.L.; Rodeheffer, R.J.; Bursi, F.; Borlaug, B.A.; Ommen, S.R. Cardiac structure and ventricular-vascular function in persons with heart failure and preserved ejection fraction from Olmsted County, Minnesota. *Circulation.* **2007**, *115*, 1982–1990.

66. Zile, M.R.; Baicu, C.F.; Gaasch, W.H. Diastolic heart failure– abnormalities in active relaxation and passive stiffness of the left ventricle. *N. Engl. J. Med.* **2004**, *350*, 1953–1959.

67. Eisman, A.S.; Shah, R.V.; Dhakal, B.P.; Pappagianopoulos, P.P.; Wooster, L.; Bailey, C.; Cunningham, T.F.; Hardin, K.M.; Baggish, A.L.; Ho, J.E. Pulmonary

Capillary Wedge Pressure Patterns During Exercise Predict Exercise Capacity and Incident Heart Failure. *Circ Heart Fail*. **2018**, *11*, e004750.

68. Mohammed, S.F.; Mirzoyev, S.A.; Edwards, W.D.; Dogan, A.; Grogan, D.R.; Dunlay, S.M.; Roger, V.L.; Gertz, M.A.; Dispenzieri, A.; Zeldenrust, S.R. Left ventricular amyloid deposition in patients with heart failure and preserved ejection fraction. *JACC Heart Fail*. **2014**, *2*, 113–122.

69. Schiattarella, G.G.; Altamirano, F.; Tong, D.; French, K.M.; Villalobos, E.; Kim, S.Y.; Luo, X.; Jiang, N.; May, H.I.; Wang, Z.V. Nitrosative stress drives heart failure with preserved ejection fraction. *Nature.* **2019**, *568*, 351–356.

70. Sala, A.J.; Bott, L.C.; Morimoto, R.I. Shaping proteostasis at the cellular, tissue, and organismal level. *J. Cell Biol*. **2017**, *216*, 1231–1241.

71. Hightower, L.E. Heat shock, stress proteins, chaperones, and proteotoxicity. *Cell*. **1991**, *66*, 191–197.

72. Douglas, P.M.; Cyr, D.M. Interplay between protein homeostasis networks in protein aggregation and proteotoxicity. *Biopolymers*. **2010**, *93*, 229–236.

73. McLendon, P.M.; Robbins, J. Proteotoxicity and cardiac dysfunction. *Circ Res*. **2015**, *116*, 1863–1882.

74. Wang, X.; Robbins, J. Heart failure and protein quality control. *Circ Res*. **2006**, *99*, 1315–1328.

75. McLendon, P.M.; Robbins, J. Desmin-related cardiomyopathy: An unfolding story. *Am. J. Physiol Heart Circ Physiol*. **2011**, *301*, H1220–H1228.

76. Parry, T.L.; Melehani, J.H.; Ranek, M.J.; Willis, M.S. Functional Amyloid Signaling via the Inflammasome, Necrosome, and Signalosome: New Therapeutic Targets in Heart Failure. *Front. Cardiovasc Med*. **2015**, *2*, 25.

77. Choi, S.I.; Kwon, S.; Son, A.; Jeong, H.; Kim, K.H.; Seong, B.L. Protein folding in vivo revisited. *Curr Protein Pept Sci.* **2013**, *14*, 721–733.

78. Schubert, U.; Anton, L.C.; Gibbs, J.; Norbury, C.C.; Yewdell, J.W.; Bennink, J.R. Rapid degradation of a large fraction of newly synthesized proteins by proteasomes. *Nature*. **2000**, *404*, 770–774.

79. Fregno, I.; Molinari, M. Proteasomal and lysosomal clearance of faulty secretory proteins: ER-associated degradation (ERAD) and ER-to-lysosome-associated degradation (ERLAD) pathways. *Crit Rev. Biochem Mol Biol*. **2019**, *54*, 153–163.

80. Brodsky, J.L. Cleaning Up: ER-Associated Degradation to the Rescue. *Cell*. **2012**, *151*, 1163–1167.

81. Araki, K.; Nagata, K. Protein Folding and Quality Control in the ER. *Cold Spring Harb Perspect Biol*. **2011**, *3,* a007526.

82. Christianson, J.C.; Ye, Y. Cleaning up in the endoplasmic reticulum: Ubiquitin in charge. *Nature Structural and Molecular Biology.* **2014**, *21*, 325–335.

83. Ye, Y.; Tang, W.K.; Zhang, T.; Xia, D. A Mighty “Protein Extractor” of the Cell: Structure and Function of the p97/CDC48 ATPase. *Front. Mol Biosci*. **2017**, *4*, 39.

84. Olzmann, J.A.; Kopito, R.R.; Christianson, J.C. The mammalian endoplasmic reticulum-associated degradation system. *Cold Spring Harb Perspect Biol*. **2013**, *5*, a013185.

85. Reid, D.W.; Nicchitta, C.V. Primary role for endoplasmic reticulum-bound ribosomes in cellular translation identified by ribosome profiling. *J. Biol Chem*. **2012**, *287*, 5518–5527.

86. Reid, D.W.; Nicchitta, C.V. Diversity and selectivity in mRNA translation on the endoplasmic reticulum. *Nat. Rev. Mol Cell Biol*. **2015**, *16*, 221–231.

87. Steiner, D.F. On the discovery of precursor processing. *Methods Mol Biol*. **2011**, *768*, 3–11.

88. Braakman, I., Bulleid, N.J. Protein folding and modification in the mammalian endoplasmic reticulum. *Annu Rev. Biochem*. **2011**, *80*, 71–99.

89. Schroder, M.; Kaufman, R.J. Divergent roles of IRE1alpha and PERK in the unfolded protein response. *Curr Mol Med*. **2006**, *6*, 5–36.

90. Liu, X.; Kwak, D.; Lu, Z.; Xu, X.; Fassett, J.; Wang, H.; Wei, Y.; Cavener, D.R.; Hu, X.; Hall, J. Endoplasmic reticulum stress sensor protein kinase R-like endoplasmic reticulum kinase (PERK) protects against pressure overload-induced heart failure and lung remodeling. *Hypertension*. **2014**, *64*, 738–744.

91. Urano, F.; Bertolotti, A.; Ron, D. IRE1 and efferent signaling from the endoplasmic reticulum. *J. Cell Sci*. **2000**, *113*, 3697–3702.

92. Maurel, M.; Chevet, E.; Tavernier, J.; Gerlo, S. Getting RIDD of RNA: IRE1 in cell fate regulation. *Trends in Biochemical Sciences*, **2014**, *39*, 245–254.

93. Wang, Z.V.; Deng, Y.; Gao, N.; Pedrozo, Z.; Li, D.L.; Morales, C.R.; Criollo, A.; Luo, X.; Tan, W.; Jiang, N. Spliced X-box binding protein 1 couples the unfolded protein response to hexosamine biosynthetic pathway. *Cell*. **2014**, *156*, 1179–1192.

94. Wang, X.; Deng, Y.; Zhang, G.; Li, C.; Ding, G.; May, H.I. Spliced X-box binding protein 1 stimulates adaptive growth through activation of mTOR. *Circulation*. **2019**, *140*, 566–579.

95. Yamamoto, K.; Sato, T.; Matsui, T.; Sato, M.; Okada, T.; Yoshida, H.; Harada, A.; Mori, K. Transcriptional induction of mammalian ER quality control proteins is mediated by single or combined action of ATF6alpha and XBP1. *Dev Cell*. **2007**, *13*, 365–376.

96. Wu, J.; Rutkowski, D.T.; Dubois, M.; Swathirajan, J.; Saunders, T.; Wang, J.; Song, B.; Yau, G.D.; Kaufman, R.J. ATF6alpha optimizes long-term endoplasmic reticulum function to protect cells from chronic stress. *Dev Cell*. **2007**, *13*, 351–364.

97. Glembotski, C.C.; Rosarda, J.D.; Wiseman, R.L. Proteostasis and Beyond: ATF6 in Ischemic Disease. *Trends Mol Med*. **2019**, *25*, 538–550.

98. Haze, K.; Yoshida, H.; Yanagi, H.; Yura, T.; Mori, K. Mammalian transcription factor ATF6 is synthesized as a transmembrane protein and activated by proteolysis in response to endoplasmic reticulum stress. *Mol Biol Cell*. **1999**, *10*, 3787–3799.

99. Chen, X.; Shen, J.; Prywes, R. The luminal domain of ATF6 senses endoplasmic reticulum (ER) stress and causes translocation of ATF6 from the ER to the Golgi. *J. Biol Chem*. **2002**, *277*, 13045–13052.

100. Shen, J.; Snapp, E.L.; Lippincott-Schwartz, J.; Prywes, R. Stable binding of ATF6 to BiP in the endoplasmic reticulum stress response. *Mol Cell Biol*. **2005**, *25*, 921–932.

101. Shen, J.; Chen, X.; Hendershot, L.; Prywes, R. ER stress regulation of ATF6 localization by dissociation of BiP/GRP78 binding and unmasking of Golgi localization signals. *Dev Cell*. **2002**, *3*, 99–111.

102. Ye, J.; Rawson, R.B.; Komuro, R.; Chen, X.; Dave, U.P.; Prywes, R.; Brown, M.S.; Goldstein, J.L. ER stress induces cleavage of membrane-bound ATF6 by the same proteases that process SREBPs. *Mol Cell*. **2000**, *6*, 1355–1364.

103. Blackwood, E.A.; Jin, J.; Azizi, K.; Arrieta, A.;Thuerauf, D.J.; Glembotski, C.C. ATF6 is required for ANP secretion from the heart, American Heart Association Scientific Sessions, New Orleans, LA, United States of America, 2019; Abstract Number 19721, Avaliable online: www.ahajournals.org/doi/10.1161/circ.134.suppl_1.19721 (accessed on 1 Jan 2020).

104. Thuerauf, D.J.; Arnold, N.D.; Zechner, D.; Hanford, D.S.; DeMartin, K.M.; McDonough, P.M.; Prywes, R.; Glembotski, C.C. p38 Mitogen-activated protein kinase mediates the transcriptional induction of the atrial natriuretic factor gene

through a serum response element. A potential role for the transcription factor ATF6. *J. Biol Chem*. **1998**, *273*, 20636–20643.

105. Thuerauf, D.J.; Morrison, L.E.; Hoover, H.; Glembotski, C.C. Coordination of ATF6-mediated transcription and ATF6 degradation by a domain that is shared with the viral transcription factor, VP16. *J. Biol Chem*. **2002**, *277*, 20734–20739.

106. Geng, F.; Wenzel, S.; Tansey, W.P. Ubiquitin and proteasomes in transcription. *Annu Rev. Biochem*. **2012**, *81*, 177–201.

107. Tanaka, M. Modulation of promoter occupancy by cooperative DNA binding and activation-domain function is a major determinant of transcriptional regulation by activators in vivo. *Proc Natl Acad Sci*. **1996**, *93*, 4311–4315.

108. Belmont, P.J.; Tadimalla, A.; Chen, W.J.; Martindale, J.J.; Thuerauf, D.J.; Marcinko, M.; Gude, N.; Sussman, M.A.; Glembotski, C.C. Coordination of growth and endoplasmic reticulum stress signaling by regulator of calcineurin 1 (RCAN1), a novel ATF6-inducible gene. *J. Biol Chem*. **2008**, *283*, 14012–14021.

109. Belmont, P.J.; Chen, W.J.; San Pedro, M.N.; Thuerauf, D.J.; Gellings, L.N.; Gude, N.; Hilton, B.; Wolkowicz, R.; Sussman, M.A.; Glembotski, C.C. Roles for endoplasmic reticulum-associated degradation and the novel endoplasmic reticulum stress response gene Derlin-3 in the ischemic heart. *Circ Res*. **2010**, *106*, 307–316.

110. Vekich, J.A.; Belmont, P.J.; Thuerauf, D.J.; Glembotski, C.C. Protein disulfide isomerase-associated 6 is an ATF6-inducible ER stress response protein that protects cardiac myocytes from ischemia/reperfusion-mediated cell death. *J. Mol Cell Cardiol.* **2012**, *53*, 259–267.

111. Tadimalla, A.; Belmont, P.J.; Thuerauf, D.J.; Glassy, M.S.; Martindale, J.J.; Gude, N.; Sussman, M.A.; Glembotski, C.C. Mesencephalic Astrocyte-Derived Neurotrophic Factor Is an Ischemia-Inducible Secreted Endoplasmic Reticulum Stress Response Protein in the Heart. *Circ Res*. **2008**, *103*, 1249–1258.

112. Glembotski, C.C.; Thuerauf, D.J.; Huang, C.; Vekich, J.A.; Gottlieb, R.A.; Doroudgar, S. Mesencephalic astrocyte-derived neurotrophic factor protects the heart from ischemic damage and is selectively secreted upon sarco/endoplasmic reticulum calcium depletion. *J. Biol Chem.* **2012**, *287*, 25893–25904.

113. Shani, G.; Fischer, W.H.; Justice, N.J.; Kelber, J.A.; Vale, W.; Gray, P.C. GRP78 and Cripto Form a Complex at the Cell Surface and Collaborate To Inhibit Transforming Growth Factor β Signaling and Enhance Cell Growth. *Molecular and Cellular Biology.* **2008**, *28*, 666–677.

114. Bi, X.; Zhang, G.; Wang, X.; Nguyen, C.; May, H.I.; Li, X.; Al-Hashimi, A.A.; Austin, R.C.; Gillette, T.G.; Fu, G. Endoplasmic reticulum chaperone GRP78 protects heart from ischemia/reperfusion injury through Akt activation. *Circ Res*. **2018**, *122*, 1545–1554.

115. Zhang, G.; Wang, X.; Bi, X.; Li, C.; Deng, Y.; Al-Hashimi, A.A.; Luo, X.;Gillette, T.G.; Austin, R.C.; Wang, Y. GRP78 (glucose-regulated protein of 78 kDa) promotes cardiomyocyte growth through activation of GATA4 (GATA-binding protein 4). *Hypertension.* **2018**. *73*, 390-398.

116. Blackwood, E.A.; Azizi, K.; Thuerauf, D.J.; Paxman, R.J.; Plate, L.; Kelly, J.W.; Wiseman, R.L.; Glembotski, C.C. Pharmacologic ATF6 activation confers global protection in widespread disease models by reprograming cellular proteostasis. *Nat. Commun*. **2019**, *10*, 187.

117. Yamagata, K.; Sanders, L.K.; Kaufmann, W.E.; Yee, W.; Barnes, C.A.; Nathans, D.; Worley, P.F. Rheb, a growth factor- and synaptic activity-regulated gene, encodes a novel Ras-related protein. *J. Biol Chem*. **1994**, *269*, 16333–16339.

118. Ozcan, U.; Ozcan, L.; Yilmaz, E.; Duvel, K.; Sahin, M.; Manning, B.D.; Hotamisligil, G.S. Loss of tuberous sclerosis complex tumor suppressors triggers the unfolded protein response to regulate insulin signaling and apoptosis. *Mol Cell*. **2008**, *29*, 541–551.

119. Correll, R.N.; Grimes, K.M.; Prasad, V.; Lynch, J.M.; Khalil, H.; Molkentin, J.D. Overlapping and differential functions of ATF6alpha versus ATF6beta in the mouse heart. Sci Rep. **2019**, *9*, 2059.

120. Clerico, A.; Giannoni, A.; Vittorini, S.; Passino, C. Thirty years of the heart as an endocrine organ: Physiological role and clinical utility of cardiac natriuretic hormones. *Am. J. Physiol Heart Circ Physiol*. **2011**, *301*, H12–H20.

121. McGrath, M.F.; de Bold, M.L.; de Bold, A.J. The endocrine function of the heart. *Trends Endocrinol Metab*. **2005**, *16*, 469–477.

122. de Bold, A.J.; Borenstein, H.B.; Veress, A.T.; Sonnenberg, H. A rapid and potent natriuretic response to intravenous injection of atrial myocardial extract in rats. *Life Sci*. **1981**, *28*, 89–94.

123. Chao, C.C.; Mihic, A.; Tsushima, R.G.; Gaisano, H.Y. SNARE protein regulation of cardiac potassium channels and atrial natriuretic factor secretion. *J. Mol Cell Cardiol*. **2011**, *50*, 401–407.

124. Chieregatti, E.; Chicka, M.C.; Chapman, E.R.; Baldini, G. SNAP-23 functions in docking/fusion of granules at low Ca2+. *Mol Biol Cell*. **2004**, *15*, 1918–1930.

125. Lynch, J.M.; Maillet, M.; Vanhoutte, D.; Schloemer, A.; Sargent, M.A.; Blair, N.S.; Lynch, K.A.; Okada, T.; Aronow, B.J.; Osinska, H. A thrombospondin-

dependent pathway for a protective ER stress response. *Cell*. **2012**, *149*, 1257–1268.

126. Tam, A.B.; Roberts, L.S.; Chandra, V.; Rivera, I.G.; Nomura, D.K.; Forbes, D.J.; Niwa, M. The UPR Activator ATF6 Responds to Proteotoxic and Lipotoxic Stress by Distinct Mechanisms. *Dev Cell*. **2018**, *46*, 327–343 e7.

127. Butt, T.R.; Karathanasis, S.K. Transcription factors as drug targets: Opportunities for therapeutic selectivity. *Gene Expr*. **1995**, *4*, 319–336.

128. Plate, L.; Cooley, C.B.; Chen, J.J.; Paxman, R.J.; Gallagher, C.M.; Madoux, F.; Genereux, J.C.; Dobbs, W.; Garza, D.; Spicer, T.P. Small molecule proteostasis regulators that reprogram the ER to reduce extracellular protein aggregation. *Elife*. **2016**, *5*, e15550.

129. Paxman, R.; Plate, L.; Blackwood, E.A.; Glembotski, C.C.; Powers, E.T.; Wiseman, R.L.; Kelly, J.W. Pharmacologic ATF6 activating compounds are metabolically activated to selectively modify endoplasmic reticulum proteins. *Elife*. **2018**, *7*, e37168.

130. Wu, J.; Ruas, J.L.; Estall, J.L.; Rasbach, K.A.; Choi, J.H.; Ye, L.; Boström, P.; Tyra, H.M.; Crawford, R.W.; Campbell, K.P. The unfolded protein response mediates adaptation to exercise in skeletal muscle through a PGC-1α/ATF6α complex. Cell Metab. **2011**, *13*, 160–169.

131. Misra, J.; Kim, D.K.; Choi, W.; Koo, S.H.; Lee, C.H.; Back, S.H.; Kaufman, R.J.; Choi, H.S. Transcriptional cross talk between orphan nuclear receptor ERRγ and transmembrane transcription factor ATF6α coordinates endoplasmic reticulum stress response. *Nucleic Acids Res*. **2013**, *41*, 6960–6974.

Chapter 2: ATF6 Decreases Myocardial Ischemia/reperfusion Damage and Links ER Stress and Oxidative Stress Signaling Pathways in the Heart

2.1. Introduction

ER stress causes accumulation of misfolded proteins in the ER, activating the transcription factor, ATF6, which induces ER stress response genes. Myocardial ischemia induces the ER stress response; however, neither the function of this response nor whether it is mediated by ATF6 is known.

Here, we examined the effects of blocking the ATF6-mediated ER stress response on ischemia/reperfusion (I/R) in cardiac myocytes and mouse hearts.

Knockdown of ATF6 in cardiac myocytes subjected to I/R increased ROS and necrotic cell death, which were mitigated by ATF6 overexpression. Under non-stressed conditions, WT and ATF6 knockout (KO) mouse hearts were similar. However, compared to WT, ATF6 KO hearts showed increased damage and decreased function upon I/R. Mechanistically, gene array analysis showed that ATF6, which is known to induce genes encoding ER proteins that augment ER protein-folding, induced numerous oxidative stress response genes not previously known to be ATF6-inducible. Many of the proteins encoded by the ATF6-induced oxidative stress genes identified here reside outside the ER, including catalase, which is known to decrease damaging ROS in the heart. Catalase was induced by the canonical ER stressor, tunicamycin, and by I/R in cardiac myocytes from WT but not in cardiac myocytes from ATF6 KO mice. ER stress response elements were identified in the catalase gene and were shown to bind ATF6 in cardiac myocytes, which increased catalase promoter activity. Overexpression of catalase, *in vivo,* restored ATF6 KO mouse heart function to WT levels in a mouse model of I/R, as did AAV9-mediated ATF6 overexpression.

ATF6 serves as a previously unappreciated link between the ER stress and oxidative stress gene programs, supporting a novel mechanism by which ATF6 decreases myocardial I/R damage.

2.2. Materials and Methods

2.2.1. Cultured cardiac myocytes

Neonatal rat ventricular myocytes (NRVM) were isolated by enzymatic digestion of neonatal rat hearts and purified by Percoll density gradient centrifugation, as described[1]. Briefly, NRVM were prepared from 1 to 3 day-old Sprague-Dawley rat hearts using a neonatal cardiomyocyte isolation system (cat# LK003300, Worthington Biochemical Corp, Lakewood, NJ). Isolated cells were counted and collected by centrifugation at 250 xg for 5 min. Forty to 60 million cells were then resuspended in 2 ml of red (with phenol red) 1x ADS buffer (116 mM NaCl, 20 mM HEPES, 769 µM NaH_2PO_4, 5.55 mM glucose, 5.37 mM KCl, 831 µM $MgSO_4$, 0.002% phenol red, pH 7.35 ± 0.5). Stock Percoll was prepared by combining 9 parts of Percoll (cat# 17-0891-02, GE healthcare, Piscataway, NJ) with 1 part of clear (without phenol red) 10x ADS. The stock Percoll was used to make the Percoll gradient for the top (density= 1.059 g/ml; 1 part Percoll stock added to 1.2 parts clear 1x ADS) and bottom (density= 1.082 g/ml; 1 part Percoll stock added to 0.54 parts red 1x ADS) layers. The gradient, consisting of 4 ml top Percoll and 3 ml bottom Percoll, was set in a 15 ml conical tube by pipetting the top Percoll first, and layering the bottom Percoll gently underneath, and the cells (in 2 ml red 1x ADS buffer) were layered on the top. Subsequently, the Percoll gradient was centrifuged at 1500×g for 30 min with no deceleration brake at 4^{o}C. The isolated myocytes, which concentrated in the layer located between the lower red ADS layer and the middle clear ADS layer, were carefully collected and washed twice with 50 ml of 1x ADS, and were then resuspended in plating medium and counted. Following Percoll purification, myocytes were plated at the desired density on plastic culture plates that had been pre-treated with 5 μg/ml fibronectin for one hour. Cultures were then maintained in Dulbecco's modified Eagle's medium (DMEM)/F12 supplemented with 10% fetal calf serum (FCS) and antibiotics (100 units/ml penicillin and 100 μg/ml streptomycin).

2.2.2 Adenovirus

Construction of plasmid vectors encoding FLAG-tagged constitutively active ATF6 [ATF6α(1-373)], called form 1 in this paper, partially active ATF6 [ATF6α(39-373)], i.e. form 2, inactive ATF6 [ATF6α(94-373)], i.e. form 3, and empty vector AdV-control (AdV-Con) has been previously described[2]. The ATF6 vectors were used to generate recombinant adenovirus (AdV) expressing different forms of ATF6 using AdEasy system as previously described[3]. AdV-mito-Hyper containing a mitochondria-targeted Hyper protein was a generous gift from Dr. Junichi Sadoshima (New Jersey Medical School, NJ). Transduction was performed by incubating cultures overnight with the appropriate AdV at a multiplicity of infection of five.

2.2.3. Immunoblotting

NRVM were lysed in RIPA buffer comprising 20 mM Tris-HCl (pH 7.5), 150 mM NaCl, 0.1% SDS, 0.5% deoxycholic acid, 1% Triton X-100, protease inhibitor cocktail (Roche Diagnostics, Indianapolis, IN) and phosphatase inhibitor cocktail (Roche

Diagnostics). Mouse heart tissues were homogenized in modified RIPA buffer with 1 % SDS. Lysates were clarified by centrifugation at 15,000 x g for 15 min at 4°C, and the protein concentration was determined using DC protein assay (Bio-Rad, Hercules, CA). Samples usually comprising 40 µg of protein were mixed with Laemmli sample buffer, boiled for 5 min, then subjected to SDS-PAGE followed by transferring onto PVDF membrane for immunoblotting analysis. To detect HMGB1 released from cells as a result of necrosis, 20 µl of culture media were analyzed by SDS-PAGE followed by immunoblotting for HMGB1. For ATF6 antibody validation, antibodies raised against the N-terminal of ATF6 were purchased from Proteintech (1:1000, cat# 24169-1-AP, Rosemont, IL), Abcam (1:1000, cat# ab37149, Cambridge, MA), Novus Biologicals (1:1000, cat# NBP1-40256, Littleton, CO), and Santa Cruz Biotechnology (1:500, cat# sc-14250, Dallas, TX). An antibody raised against the C-terminal of ATF6 was purchased from Signalway (1:1000, cat# 32008, College Park, MD). An anti-KDEL antibody (1:8,000, cat# ADI-SPA-827 , Enzo Life Sciences, Farmingdale, NY) was used to detect GRP94, GRP78 and PDIA6, all of which have C-terminal KDEL sequences that cross-react with this antibody. Other antibodies used included anti-PARP (1:1000, cat# 9542, Cell Signaling, Danvers, MA), anti-catalase (1:1000, cat# ab16731, Abcam), anti-FLAG M2 (1:10,000, cat# F1804, Sigma-Aldrich, St. Louis, MO), anti-HMGB1 (1:1000, cat# ab18256 Abcam), anti-CHOP (1:1000, cat# 5554, Cell Signaling), anti-IRE1 (1:500, cat# sc-390960, Santa Cruz), anti-XBP1s (1:1000, cat# 619502, BioLegend, San Diego, CA), anti-phospho-PERK (1:1000, cat# 3179, Cell Signaling), anti-PERK (1:1000, cat# 3192, Cell Signaling), and anti-β-actin (1:1000, cat# sc-47778, Santa Cruz).

2.2.4. MTT and lactate dehydrogenase (LDH) assays

NRVM were plated in 96-well plates (1.5 x 10^4 cells/well) and treated with tunicamycin (TM) at 40 µg/ml for 48h, or with hydrogen peroxide (H_2O_2) at 37.5 µM for 8h. Dose response experiments were carried out to determine that these were the optimal doses of TM and H_2O_2 for measuring the effects of ATF6 gain- and loss-of-function on cell viability (MTT) and necrosis (medium LDH activity). Cell viability was measured using an MTT assay (Cell Proliferation Kit I, Roche Diagnostics), as previously described[1]. Media samples from H_2O_2-treated NRVM were collected for LDH activity assays, which were done using the CytoTox 96 Non-Radioactive Cytotoxicity Assay (Promega, Madison, WI), according to the manufacturer's instructions.

2.2.5. Isolation of adult mouse cardiac myocytes

Adult mouse ventricular myocytes (AMVM) were isolated essentially as previously described [4, 5]. Briefly, hearts were rapidly cannulated via the ascending aorta, mounted on a perfusion apparatus and retrograde perfused at 3 ml/min for 4 min at 37^{o}C with heart medium (Joklik Modified Minimum Essential Medium; cat# M-0518, Sigma-Aldrich, supplemented with 10 mM HEPES, 30 mM taurine, 2 mM D-L-carnitine, 20 mM creatine, 5 mM inosine, 5 mM adenosine, and 10 mM butanedione monoxime (BDM), pH 7.36). Collagenase digestion of hearts was performed by perfusing for 13 min with heart medium supplemented with type 2 collagenase (50-60 mg; ~320U/ml, cat# LS004176, Worthington) and 12.5 µM $CaCl_2$. Hearts were removed from the cannula and submerged in 2.5 ml of effluent collected off the heart during the collagenase digestion, and dissociated using forceps. Collagenase was neutralized by adding 2.5 ml of heart medium supplemented with 10% FCS, and the final concentration of $CaCl_2$ was adjusted to 12.5 μM. Cells were dissociated further by gently triturating for 4 min. The cell suspension was then filtered through a 100μm mesh filter and myocytes were allowed to sediment by gravity for 6 min at room temperature. The supernatant containing non-viable cells and non-myocytes was discarded and the remaining myocytes were resuspended in 5 ml of heart medium containing 5% FCS and 37.5 μM $CaCl_2$. The concentration of $CaCl_2$ in this suspension was slowly increased in a careful stepwise manner as follows: Step 1- add 50 μl of 10 mM $CaCl_2$, mix gently, allow to sit for 4 min; Step 2- repeat Step 1; Step 3- add 100 μl of 10 mM $CaCl_2$ and wait 4 min; Step 4- add 80 μl of 100 mM $CaCl_2$ and wait 4 min. Cells were resuspended in plating medium (MEM medium; cat# 12350-039, Thermo Fisher Scientific, Waltham, MA, 1x insulin-transferrin-selenium; cat# 41400-045, Thermo Fisher, 10 mM HEPES, 100 units/ml penicillin and 100 μg/ml streptomycin, 10 mM BDM and 4% FCS). Cells were plated at 5×10^4 cells per well in 12-well culture plates coated with laminin (10 μg/ml). After at least 2h, the medium was changed to maintaining medium (MEM medium, 1x insulin-transferrin-selenium, 10 mM HEPES, 1.2 mM $CaCl_2$ and 0.01% bovine serum albumin, 25 μM blebbistatin. Cells were used for experiments 12-18h later.

2.2.6. Simulated ischemia/reperfusion

NRVM or AMVM were subjected to simulated ischemia (sI) or simulated ischemia followed by simulated reperfusion (sI/R), as previously described[6]. Briefly, cells were placed into 12-well plates at 2×10^5 cells/well for NRVM, or 5×10^4 cells/well for AMVM. For sI of NRVM, medium was replaced with 0.5 ml of glucose-free DMEM containing 2% dialyzed FCS. Cells were incubated at 0.1% O_2 in a hypoxia chamber with an oxygen controller (ProOx P110 oxygen controller, Biospherix, Parish, NY). To simulate reperfusion, medium was replaced with medium containing 17.5 mM glucose and cells were incubated at 21% O_2. In some experiments, 5 mM N-acetyl cysteine (pH 7.5), a ROS scavenger, was added to the reperfusion medium. To examine the effects of sI/R on NRVM viability, cells were incubated in sI for 16h, followed by reperfusion for 24h. To examine the effects of sI/R on ROS generation in NRVM, cells were incubated in sI for 8h, followed by reperfusion for 1h. To examine the effects of sI/R on AMVM viability, cells were incubated in DMEM supplemented with 100 units/ml penicillin, 100 µg/ml streptomycin, and 292 µg/ml glutamine for 3h, followed by reperfusion with maintaining medium for 24h. To examine the effects of catalase on sI/R-mediated death of AMVM, cultures were pre-treated with 100U/mL of PEG (polyethylene glycol)-conjugated-Catalase, PEG-Catalase (Sigma cat# C4963) overnight, then PEG-Catalase was added into sI and sI/R media. Viable AMVM and were identified as calcein blue AM-positive (Thermo Fisher) and images were obtained using an IX70 fluorescence microscope (Olympus, Melville, NY). Numbers of viable, calcein blue AM-positive cells were counted using ImageJ or Image-Pro Plus software (Medium Cybernetics, Rockville, MD).

2.2.7. Reactive oxygen species (ROS) production

The levels of intracellular ROS were determined with the CellROX Orange fluorescent dye (Thermo Fisher). After sI/R, NRVM were incubated with 5 µM CellROX Orange for 20 min at 37°C, and then washed with PBS. Images were obtained using a fluorescence microscope at a magnification of 20X. Fluorescence intensity (absorbance units) was determined using Image-Pro Plus software. To detect intracellular H_2O_2, NRVM were permeabilized with 40 µM digitonin. The resulting media containing intracellular H_2O_2 were transferred to black 96-well plates. The levels of H_2O_2 were measured using Amplex Red Hydrogen Peroxide/peroxidase Assay Kit (Thermo Fisher) according to manufacturer's instructions. Mitochondrial-specific H_2O_2 production was detected through the expression of mitochondria-specific HyPer protein using AdV mito-Hyper as previously described[7].

2.2.8. Small interfering RNA (siRNA) transfection

Reverse transfection of siRNA duplexes into NRVM using TransMessenger Transfection Reagent (Qiagen, Valencia, CA) has been described previously[1]. Briefly, Percoll-purified NRVM (3×10^5 cells) were suspended in medium containing 2% FCS, incubated with 100 nM siRNA and transfection reagent followed by plating in 12-well plates for overnight. Medium was changed the next day. The sequence of siRNA targeting rat ATF6 was 5-GCUCUCUUUGUUGUUGCUUAGUGGA-3, and the sequence targeting rat catalase was 5-GGAACCCAAUAGGAGAUAAACUUAA-3 (cat# CatRSS302058, Stealth siRNA, Thermo Fisher). A non-targeting sequence (cat# 12935300, Thermo Fisher) was used as a control siRNA.

2.2.9. Malondialdehyde assay

Lipid peroxidation was determined by measuring the levels of malondialdehyde (MDA). Briefly, sI/R treated NRVM (6×10^5 cells) were scrapped into 0.5 ml of PBS, and sonicated on ice. MDA levels in cell lysates were measured using a TBARS assay kit (Cayman Chemical, Ann Arbor, MI) according to the manufacturer's instructions.

2.2.10. Immunocytofluorescence (ICF)

NRVM- NRVM were plated and on fibronectin-coated glass chamber slides (Nunc Lab-Tek II Chamber Slide) as previously described[1]. After treatment, cells were fixed with -20°C methanol for 10 min, then blocked for 1h with SuperBlock blocking buffer (Thermo Fisher). Slides were then incubated overnight with an anti-ATF6 antibody (1:50, cat# sc-166659, Santa Cruz)[8], and an anti-□-actinin antibody (1:50, cat# GTX103219, GeneTex, Irvine, CA). Slides were subsequently incubated at room temperature for 90 min with the appropriate fluorophore-conjugated a secondary antibody including: Cy3-conjugated anti-mouse IgG (1:100), FITC-conjugated anti-goat IgG (1:100), or FITC-conjugated anti-rabbit IgG (1:100, Jackson ImmunoResearch Laboratories, West Grove, PA). Nuclei were counterstained for 1 min with Topro-3 (1:1000, Thermo Fisher). Images were obtained using laser scanning confocal microscopy on an LSM 710 confocal laser scanning microscope (Carl Zeiss, Oberkochen, Germany).

AMVM- were plated in plating medium at 1.0x10^5 cells per chamber on laminin-coated 4-chamber glass slides (Falcon). After 3h, the medium was changed to maintaining medium containing 25 µM blebbistatin. After 16h, the medium was replaced with 0.5 ml of medium appropriate for sI/R for the appropriate times (see above), or with medium containing tunicamycin (10 µg/ml) for 24h. After each treatment, AMVM were washed with PBS, fixed for 15 min with 4% paraformaldehyde, followed by permeabilization for 10 min with 0.5% Triton-X. For ATF6 staining, AMVM were fixed for 10 min with -20°C methanol. Slides were blocked for 1h with SuperBlock, and then incubated with primary antibodies for 16h at 4^{o}C. Primary antibodies used for staining

AMVM were anti-α-actinin (1:200, cat# A7811, Sigma-Aldrich), anti-GRP78 (C-20, 1:30, cat# SC-1051, Santa Cruz), anti-catalase (1:100, Abcam), and anti-ATF6 (targeting to N-terminus of ATF6, 1:50, cat# sc-14250, Santa Cruz). Slides were incubated with appropriate fluorophore-conjugated secondary antibodies, followed by nuclei counter stain, as described above.

Adult mouse hearts were embedded and sectioned as previously described[11]. Briefly, mice were anesthetized and a catheter was inserted into the abdominal aorta. The aorta was retro-perfused with PBS followed by relaxation buffer containing $CdCl_2$ and KCl, fixed in neutral buffered 10% formalin. After 24h in formalin, the hearts were dehydrated in ethanol and embedded in paraffin. Five-μm sections of paraffin-embedded hearts were heated in antigen retrieval citrate buffer (10mM; pH 6.0). The heart sections were then treated with blocking buffer (Thermo Scientific, cat# 37528) for 1h at room temperature and then incubated with primary antibodies overnight at 4°C. Primary antibodies in this study included: anti-GRP78 (C-20, 1:30, cat# SC-1051, Santa Cruz), anti-catalase (1:50, Abcam), anti-ATF6 (targeting to N-terminus of ATF6, 1:50, cat# sc-14250, Santa Cruz), and anti-tropomyosin (1:200, cat# T9283, Sigma-Aldrich). Slides were incubated with appropriate fluorophore-conjugated secondary antibodies as described above for 90 min at room temperature (all at 1:100 dilutions). Nuclear marker counterstain, TO-PRO-3 (Thermo Fisher; 1:10000), was incubated for 15min at room temperature prior to application of coverslips fixed with Vectashield Hardset (Vector Labs, H1400).

2.2.11. Echocardiography

Echocardiography of WT and ATF6 KO mice was performed using an ultrasound imaging system (Vevo 2100 System, Fujifilm VisualSonics, Toronto, Ontario, Canada) as described[1].

2.2.12. *In Vivo* ischemia/reperfusion

Myocardial ischemia/reperfusion (I/R) was performed *in vivo* by 30 min of ligation of the left anterior descending coronary artery followed by 24h of reperfusion, as previously described[9]. Following I/R, 1% of Evans Blue was injected apically to determine the area at risk (AAR). Hearts were harvested and 1-mm sections of the hearts were stained with 1% triphenyl tetrazolium chloride (TTC) to measure infarcted area (INF) as previously described[9]. The AAR, INF and left ventricle area (LV) of digital images of heart sections were analyzed using ImageJ software.

2.2.13. *Ex vivo* ischemia/reperfusion

Mouse hearts were isolated and subjected to global I/R as previously described[10]. Briefly, isolated hearts were mounted onto a Langendorff perfused heart apparatus. Global no-flow ischemia was performed for 20 min followed by reperfusion for 1 h. Left ventricular developed pressure (LVDP) was measured using a pressure sensor balloon and analyzed using Powerlab software (ADInstruments, Colorado Springs, CO).

2.2.14. Intravenous Injections

For AAV9, C57/BL6 mice were anesthetized with 2% isoflurane and then injected via the lateral tail vein with 100 µl of AAV9-control or AAV9-3xFlag-ATF6α(1-373) containing 1×10^{11} viral particles, and then hearts were obtained after either 2 weeks for immunoblots (Fig. 6E), or after 2d for *ex vivo* I/R (Fig. 7J). In other experiments, C57/BL6 mice were anesthetized with 2% isoflurane and then injected via the lateral tail vein with 100 µl of 1000u/kg PEG-Catalase (Sigma cat# C4963), or vehicle 16h before hearts were obtained and subjected to *ex vivo* I/R (Fig. 7G).

2.2.15. Quantitative real-time PCR (qRT-PCR)

Total RNA was isolated from NRVM or hearts using Quick-RNA MiniPrep kit (Zymo Research, Irvine, CA) or RNeasy Mini kit (Qiagen), respectively. cDNA synthesis was performed using SuperScript III First-Strand Synthesis System (Thermo Fisher). qRT-PCR was performed using Maxima SYBR Green/ROX qPCR Master Mix in a StepOnePlus RT-PCR System (Thermo Fisher). The following primers were used:

Rat	Forward 5’ to 3’	Reverse 5’ to 3’
β-Actin	CTTCCTTCCTGGGTATGGAATC	CTGTGTTGGCATAGAGGTCTT
Cat	CTTTGAGGTCACCCACGATATT	GTGGGTTTCTCTTCTGGCTATG
Gpx1	TGAGAAGTGCGAGGTGAATG	CCAGATACCAGGAATGCCTTAG
Gpx3	CATTCGGCCTGGTCATTCT	CAGCGGATGTCATGGATCTT
Gpx4	GCAGGAGCCAGGAAGTAATC	ACGCAGCCGTTCTTATCAA
Prdx1	TGTAGCTCGACTCTGCTGATA	GTCCCAATCCTCCTTGTTTCT
Prdx2	ATGATGAGGGCATCGCTTAC	TCAGGCTCACCGATGTTTAC
Prdx3	CGCTCAGAGGTCTCTTCATTATT	GTACTGGTGCTATGTGCTACTT
Prdx4	GGGAAGGAACAGCTGTGATAA	GATCCAGGCCAAGTGAGTAAA
Prdx5	CAGAGCTGTTCAAGGACAAGA	CCCAAAGAGAGACACCAAAGA
Prdx6	CCTGGAGCAAGGACATCAAT	GGAGTCAACCACTCTGAGAATC

Sod1	TGGGTTCCATGTCCATCAATA	CAATCCCAATCACACCACAAG
Sod2	CTGACCTGCCTTACGACTATG	CTTGCAGTGGGTCCTGATTA
Vimp	GACCTTCTACTTCATCGGTCATC	TCAGAACAGAAATCAGCCCTAC
Mouse		
β-Actin	GACGGCCAGGTCATCACTAT	GTACTTGCGCTCAGGAGGAG
Cat	AACTGGGATCTTGTGGGAAAC	GTGGGTTTCTCTTCTGGCTATG
Grp78	CACGTCCAACCCCGAGAA	ATTCCAAGTGCGTCCGATG
Grp94	TCGTCAGAGCTGATGATGAAGT	GCGTTTAACCCATCCAACTGAAT
Pdia6	TGCCACCATGAATCAGGTTCT	TCGTCCGACCACCATCATAGT

For the RT-PCR array, total RNA was isolated from Ad-Con or Ad-ATF6 form 1 treated NRVM (5 x 10^5 cells) using miRNeasy Mini Kit (Qiagen). Synthesis of cDNA was performed using 500 ng of RNA and RT^2 First Strand Kit (Qiagen). Rat Oxidative Stress RT^2 Profiler PCR Arrays (Qiagen) were performed using RT^2 SYBR Green ROX qPCR Mastermix in a StepOnePlus RT-PCR System according to the manufacturer's instructions.

2.2.16. Adeno-Associated Virus Serotype 9 (AAV9)

AAV9 preparation was carried out essentially as previously described[1]. For generation of recombinant AAV9-control and AAV9-3xFlag-ATF6α(1-373), shuttle vectors for these recombinants were constructed and co-transfected with AAV9 helper, pDG-9 (a gift from Dr. Roger Hajjar) into HEK293T cells to produce virus. Two different expression constructs were prepared; AAV9-CMV-3xFlag-ATF6α(1-373) and AAV9-CMV_{enh}MLC800-3xFlag-ATF6α(1-373). Similar results were obtained with each vector, except the AAV9-CMV-3xFlag-ATF6α(1-373) results in more robust expression than AAV9-CMV$_{enh}$MLC800-3xFlag-ATF6α(1-373). Since the recombinant AAV9 were prepared using similar strategies, only the preparation of AAV9-CMV$_{enh}$MLC800-3xFlag-ATF6α(1-373) is described here. The shuttle vector, pTRUF-CMV$_{enh}$MLC800, was constructed by modifying pTRUF12 (a gift from Dr. Roger Hajjar) by first removing the region encoding GFP that was down-stream of the IRES. New restriction sites were inserted into the multiple cloning site to include Nhe1, Pme1, Xho1, and Mlu1. The CMV promoter was replaced with a composite promoter comprised of an 800bp fragment of the MLC2v promoter downstream of a minimal region of the CMV enhancer (a gift from Dr. Oliver J. Muller). AAV9 vectors with wild-type capsids were generated by co-transfection of the helper plasmid, pDG-9. pTRUF-CMV$_{enh}$MLC800-3xFlag-ATF6α(1-373) was created by sub-cloning the human 3xFlag-ATF6α(1-373) cDNA from pcDNA3.1-3xFlag-ATF6α(1-373). To prepare the recombinant AAV9, HEK293T cells were plated a density of $8x10^6$ per T-175 flask and maintained in DMEM/F12 containing 10%FBS, penicillin/streptomycin at 37°C and 5% CO_2. For each virus preparation, 48 flasks were used. Twenty-four hours after plating, cultures were transfected using Polyethylenimine “Max” (MW 40,000, Polysciences, cat# 24765) as follows: For each T-175 flask, 15µg of helper plasmid and 5µg of pTRUF plasmid were mixed with 1 ml of DMEM:F12 (no antibiotics) and 160 µl of polyethylenimine (0.517 mg/ml), vortexed for 30 seconds, and incubated for 15 min at room temperature. This was then mixed with 18 ml DMEM/F12 containing 2% FBS, penicillin/streptomycin then used to replace the media on the cultures. The cultures were then rocked intermittently for 15 minutes before incubation. Three days after transfection, the cells collected from six T-175 flasks were centrifuged at 500xg for 10 min, then resuspended in 10 ml of lysis buffer (150 mM NaCl, 50 mM Tris-HCL). The resuspended cells were then subjected to three rounds of freeze-thaw, followed by treatment with benzonase (1500 U of benzonase; Novagen) and 1 mM $MgCl_2$ at 37°C for 30 min. The cell debris was collected by centrifugation at 3,400 x g for 20 min. The supernatant obtained from six T-175 flasks containing the AAV9 was then purified on an iodixanol gradient comprised of the following four phases: 7.3 ml of 15%, 4.9 ml of 25%, 4 ml of 40%, and 4 ml of 60% iodixanol (Optiprep; Sigma-Aldrich) overlayed with 10 ml of cell supernatant. The gradients were centrifuged in a 70Ti rotor (Beckman Coulter) at 69,000 rpm for 1h using OptiSeal Polyallomer Tubes (Beckman Coulter). Virus was collected by inserting a needle 2 mm below the 40%-60% interface and collecting 4 or 5 fractions (~4ml) of this interface and most of the 40% layer. The fractions were analyzed for viral content and purity by examining 10 µl of each fraction on a 12% SDS-PAGE gel (BioRad), followed by staining with InstantBlue (Expedeon) to visualize the viral capsid proteins, VP1, VP2 and VP3. The virus was then collected from the fractions of several gradients and the buffer was exchanged with lactated Ringer’s using an ultrafiltration device, Vivaspin 20, 100kDa MWCO (GE Healthcare). The final viral preparation was then fractionated on a 12% SDS-PAGE gel, stained with InstantBlue, and then compared with a similarly stained gel of a virus of a known titer. Alternatively, a qPCR was performed using a forward primer (AAGTCTCCACCCCATTGACGT) and reverse primer (AGGAGCCTGAGCTTTGATTCC), which spans the CMV_{enh}MLC800 composite promoter. A pTRUF vector containing the CMV/MLC800 promoter was used as a standard to determine copy number. pTRUF-CMV_{enh}MLC-empty was used to generate an analogous control virus.

2.2.17. Cloning and mutagenesis

The promoter region of the rat catalase gene spanning nucleotides -1161 to +131 was amplified by PCR using ggaacgGGTACCTCACTGCCTTTATGGGCTTC as the forward primer, which introduced a Kpn1 site (lower case) just 5' of rat catalase -1161, and ggaacgCTCGAGGTGTAGGATTGCGGAGCTG as the reverse primer, which introduced an Xho1 site just 3' of rat catalase +131. Upper case nucleotides match those in the rat catalase gene. The amplified product was then cloned into pGL2p to generate rat-cat(-1161/+131)-Luc. Truncated versions of rat-cat luciferase were cloned into pGL2p using a similar strategy and the same reverse primer coupled with the following forward primers:

ggaacgGGTACCAAAGGAGCCATGAAGCTGAA (-689),
ggaacgGGTACCACAGTGGGCCAAGTGACAAG (-410), and
ggaacgGGTACCGTCCCCGAACTGTGACTCTC (-191)

to generate rat-cat(-689/+131)-Luc, rat-cat(-410/+131)-Luc and rat-cat(-191/+131)-Luc, respectively. The underlined regions of these primers correspond to rat catalase gene sequences. Informatics analyses identified putative ER stress response elements in the rat catalase gene at nucleotide positions -979 to -962 and -194 to -184 in the rat catalase gene, which we called ERSE-2 and ERSE-1, respectively. These elements in rat-cat(-1161/+131)-Luc were mutated by site-directed mutagenes in ways predicted to ablate ATF6 binding using cat-ERSE-2 mut sense primer, CCCAAGGGATTGCAAACTTACAATTTTACCccgCTCTGTTACCcacTCTTTGTCAAATCAAGAACAAGTTTTGGAGT

and cat-ERSE-2 mut antisense primer,

ACTCCAAAACTTGTTCTTGATTTGACAAAgagTGGGTAACAGAGcggGGTAAAATTGTAAGTTTTGCAATCCCTTGGG

cat-ERSE-1 mut sense primer,

CGTTGCACAGAGGAcggttTaaCagAACTGTGACTCTCAG, and

cat-ERSE-1 mut antisense primer,

CTGAGAGTCACAGTTctGttAaccgTCCTCTGTGCAACG.

PCR-based mutagenesis was performed using the QuikChange XL Site-Directed Mutagenesis Kit (Agilent Technologies, Santa Clara, CA). Lower case letters represent mutated nucleotides; upper case letters represent nucleotides that are identical to those in the rat catalase gene.

2.2.18. Luciferase reporter assay

Suspended NRVMs were co-transfected by electroporation with one of the above reporter constructs along with pCH110 plasmids encoding SV40-beta-galactosidase and pGL2B, as described previously.[5] NRVMs were plated overnight and then infected with different forms of AdV-ATF6, as described above. NRVMs were lysed after 48 h, and the activities of luciferase and beta-galactosidase were measured using an Optocompt II luminometer (MGM Instruments, Hamden, CT) as described previously[6].

2.2.19. Chromatin immunoprecipitation (ChIP)

ChIP assays were performed essentially as previously described[11]. Briefly, AdV-FLAG-ATF6 form 1-infected NRVM (2 x 10^6 cells) were treated with fixing buffer (50 mM HEPES-KOH, pH 7.5, 100 mM NaCl, 1 mM EDTA, 0.5 mM EGTA, and 1% formaldehyde) for 10 min, quenched with 125 mM glycine, and scraped into ice-cold PBS. Cells were centrifuged, resuspended in lysis buffer (50 mM HEPES, pH 7.9, 140 mM NaCl, 1 mM EDTA, 10% glycerol, 0.5% NP-40, 0.25% Triton X-100, and protease inhibitor cocktail), and incubated on ice for 10 min. After centrifugation at 1,800 x g for 10 min, the pellets were washed with buffer containing 10 mM Tris, pH 8.1, 200 mM NaCl, 1 mM EDTA, and 0.5 mM EGTA, resuspended in shearing buffer (0.1% SDS, 1 mM EDTA, and 10 mM Tris, pH 8.1), and then transferred to microTUBEs (Covaris, Woburn, MA). Chromatin was sheared by sonication for 15 min using an M220 focused-ultrasonicator (Covaris). Triton X-100 and NaCl were added to the final concentration of 1% Triton and 150 mM NaCl followed by centrifugation at 16,000 x g for 10 min. Immunoprecipitation was performed by incubated 140 µl of sheared chromatin with 5 µg of anti-FLAG antibody (cat# F1804, Sigma-Aldrich) and 260 µl of immunoprecipitation buffer (0.1% SDS, 1 mM EDTA, 10 mM Tris, pH 8.1, 1% Triton X-100, and 150 mM NaCl) at 4°C overnight. Protein A/G magnetic beads (5 µl, BcMag, Bioclone, San Diego, CA) were added to the mixtures and incubated at 4°C for 1.5 h. Magnetic beads were sequentially washed with low salt wash buffer (0.1% SDS, 1% Triton X-100, 2 mM EDTA, 20 mM HEPES-KOH, pH7.9, and 150 mM NaCl), high salt wash buffer with 500 mM NaCl, LiCl wash buffer (100 mM Tris-HCl, pH 7.5, 0.5 M LiCl, 1% NP-40, and 1% deoxycholate acid), and TE buffer (10 mM Tris-HCl, pH 8.0 and 0.1 mM EDTA).

Immune complexes were eluted by incubating beads with proteinase K digestion buffer (20 mM HEPES, pH 7.9, 1 mM EDTA, 0.5% SDS, and 0.4 mg/ml proteinase K) at 50°C for 15 min. Formaldehyde crosslinking was reversed by incubating with 0.3 M NaCl and 0.3 mg/ml RNase A at 65°C overnight. Samples were further incubated with 550 µg/ml proteinase K at 50°C for 1h. DNA was purified using NucleoSpin Gel and PCR Clean-up Kit (Macherey-Nagel, Bethlehem, PA) and eluted by 30 µl of water. Two µl of DNA was used for qRT-PCR analysis with primers targeting rat Cat ERSE-1 (5'-CTACCCACCAATTAGTACCAAATAA-3' and 5'-AGAAGGGACAGGATTGGAAG-3'), rat Cat ERSE-2 (5'-CACATTCTAGGGACAGTGTAGATG-3' and 5'-ACCTTGATTATGGGCTGTGG-3') or the rat Pdia6 ERSE (5'-CACATGAGCGAAATCCACAGA-3' and 5'-ACTAGTCGAGCCATGCTGAT-3'). Pdia6 served as a positive control for a known ATF6 target gene in cardiac myocytes[11]. ChIP signals obtained from the qRT-PCR were normalized to the input DNA.

2.2.20. References

1. Doroudgar S, Volkers M, Thuerauf DJ, Khan M, Mohsin S, Respress JL, Wang W, Gude N, Muller OJ, Wehrens XH, Sussman MA, Glembotski CC. Hrd1 and ER-Associated Protein Degradation, ERAD, are Critical Elements of the Adaptive ER Stress Response in Cardiac Myocytes. *Circ Res.* 2015;117(6):536-546.

2. Thuerauf DJ, Morrison LE, Hoover H, Glembotski CC. Coordination of ATF6-mediated transcription and ATF6 degradation by a domain that is shared with the viral transcription factor, VP16. *J Biol Chem.* 2002;277(23):20734-20739.

3. Thuerauf DJ, Marcinko M, Gude N, Rubio M, Sussman MA, Glembotski CC. Activation of the unfolded protein response in infarcted mouse heart and hypoxic cultured cardiac myocytes. *Circ Res.* 2006;99(3):275-282.

4. O'Connell TD, Rodrigo MC, Simpson PC. Isolation and culture of adult mouse cardiac myocytes. *Methods Mol Biol.* 2007;357:271-296.

5. Pinz I, Zhu M, Mende U, Ingwall JS. An improved isolation procedure for adult mouse cardiomyocytes. *Cell Biochem Biophys.* 2011;61(1):93-101.

6. Doroudgar S, Thuerauf DJ, Marcinko MC, Belmont PJ, Glembotski CC. Ischemia activates the ATF6 branch of the endoplasmic reticulum stress response. *J Biol Chem.* 2009;284(43):29735-29745.

7. Sciarretta S, Zhai P, Shao D, Zablocki D, Nagarajan N, Terada LS, Volpe M, Sadoshima J. Activation of NADPH oxidase 4 in the endoplasmic reticulum promotes cardiomyocyte autophagy and survival during energy stress through the protein kinase RNA-activated-like endoplasmic reticulum kinase/eukaryotic initiation factor 2alpha/activating transcription factor 4 pathway. *Circ Res.* 2013;113(11):1253-1264.

8. Lynch JM, Maillet M, Vanhoutte D, Schloemer A, Sargent MA, Blair NS, Lynch KA, Okada T, Aronow BJ, Osinska H, Prywes R, Lorenz JN, Mori K, Lawler J, Robbins J, Molkentin JD. A thrombospondin-dependent pathway for a protective ER stress response. *Cell.* 2012;149(6):1257-1268.

9. Glembotski CC, Thuerauf DJ, Huang C, Vekich JA, Gottlieb RA, Doroudgar S. Mesencephalic astrocyte-derived neurotrophic factor protects the heart from ischemic damage and is selectively secreted upon sarco/endoplasmic reticulum calcium depletion. *J Biol Chem.* 2012;287(31):25893-25904.

10. Jin JK, Whittaker R, Glassy MS, Barlow SB, Gottlieb RA, Glembotski CC. Localization of phosphorylated alphaB-crystallin to heart mitochondria during ischemia-reperfusion. *Am J Physiol Heart Circ Physiol.* 2008;294(1):H337-344.

11. Vekich JA, Belmont PJ, Thuerauf DJ, Glembotski CC. Protein disulfide isomerase-associated 6 is an ATF6-inducible ER stress response protein that protects cardiac myocytes from ischemia/reperfusion-mediated cell death. *J Mol Cell Cardiol.* 2012;53(2):259-267.

2.3. Results

Initial studies in neonatal rat ventricular myocytes (NRVM) showed that the three forms of ATF6 **(Fig. 2.1A)**, exhibited different abilities to increase expression of the well-known ATF6-induced proteins, GRP94 and GRP78. The native N-terminal fragment of ATF6, ATF6(1-373), called form 1 here, which was expressed at approximately similar levels as endogenous ATF6, mimics the cleaved form of ATF6 and was the most potent inducer, while ATF6(39-373), form 2, which has about half of the transcriptional activation domain missing, was partially active, and ATF6(94-373), form 3, which lacks all of the transcriptional activation domain was inactive **(Fig. 2.1B GRP94 and GRP78)**. None of the three forms of ATF6 affected the other two branches of the ER stress response, as they did not increase PERK phosphorylation, nor did they induce XBP1 splicing, an indicator of IRE1 activation. We also previously showed in HeLa cells that ATF6 exhibits a novel degraded-when-active property, such that the more transcriptionally active forms of ATF6 exhibit the shortest half-lifes[5, 6]. Consistent with those studies were our findings in NRVM showing that the transcriptional activity of ATF6 was inversely related to the expression level of ATF6 **(Fig. 2.1B FLAG)**.

Given the differential effects of these forms of ATF6 on ER stress gene induction, they are potentially valuable reagents with which to discover cardiac myocyte functions that are regulated by ATF6-induced genes. For example, if these forms of ATF6 affect a particular myocyte function, such as survival, with the same rank-order that they affect ATF6 target gene expression, then it is likely that at least some ATF6 target genes contribute to those functions. As an example, we showed that in NRVM treated with the prototypical ER stressor, tunicamycin (TM), which induces ER protein misfolding by inhibiting protein glycosylation, the three forms of ATF6 decreased ER stress-induced cell death with the same rank-order that they induce ER proteins that reduce ER protein misfolding, e.g. GRP94 and GRP78 **(Fig. 2.1C)**.

Next, we examined the effects of other stressors that are not typically considered to be inducers of ER protein misfolding and the canonical ER stress response, such as H_2O_2, which induces oxidative stress by increasing ROS levels. While ATF6 was expected to protect against ER stress-induced cell death, which is primarily apoptotic, we anticipated that it would be ineffective against oxidative stress-induced cell death, which is primarily necrotic. Surprisingly, form 1 of ATF6 protected myocytes from H_20_2-induced cell death **(Fig. 2.1D red)**, form 2 was without effect **(Fig. 2.1D blue)**, while form 3, which exerts dominant-negative effects on endogenous ATF6 signaling, actually increased H_2O_2-induced myocyte death **(Fig. 2.1D green)**. It is unclear why the relative effects of the three forms of ATF6 are somewhat different in response to TM vs H_2O_2, but one possibility is that the effects of ATF6 on H_2O_2-induced myocyte death might be due to induction of proteins that do not reside in the ER and do not directly affect ER protein folding, such as antioxidant proteins. Since ATF6 is not known for its ability to affect the expression of antioxidant genes, we focused on the antioxidant effects of ATF6 in more depth.

It has been shown that H_2O_2 kills myocytes by necrosis; accordingly, we examined the effects of the three forms of ATF6 on the media levels of LDH and HMGB1, which are measures of necrosis[7, 8]. Again, form 1 of ATF6 strongly decreased media levels of LDH and HMGB1, while the other forms had less of an effect **(Fig. 2.1E)**, indicating that activated ATF6 can inhibit H_2O_2-induced necrosis of cardiac myocytes. Since the deleterious effects of H_2O_2 are due to ROS, we tested the three forms of ATF6 in NRVM subjected to simulated ischemia/reperfusion (sI/R), a pathophysiological maneuver that increases mitochondrial-derived ROS . Similar to the findings with H_2O_2, form 1 of ATF6 exhibited the most significant ability to protect cardiac myocytes from sI/R-mediated death **(Fig. 2.1F)**, and to decrease ROS generation during sI/R **(Fig. 2.1G)**. Moreover, N-acetyl cysteine (NAC), a well-characterized ROS scavenger, mimicked the ability of form 1 of ATF6 to decrease ROS **(Fig. 2.1G)**, indicating that ATF6 acted functionally like a ROS scavenger.

These findings suggested that there might be a previously unappreciated link between ER stress signaling by ATF6 and ROS reduction; moreover, since the damaging ROS produced during reperfusion are mostly generated in mitochondria[11], the link could involve ATF6-mediated decreases in total cellular ROS. To examine whether this link also existed between endogenous ATF6 and ROS levels, NRVM were treated with siRNA to knockdown endogenous ATF6. Immunoblots showed that two different ATF6 siRNAs decreased the levels of full-length, p90 ATF6 and resulted in the absence of cleaved, p50 ATF6 upon TM treatment **(Fig. 2.2A, p90 and p50 ATF6 lanes 5-8)**. Importantly, siRNA-mediated ATF6 knockdown also blunted the induction of ATF6-inducible target genes, Grp94, Grp78 and PDIA6 **(Fig. 2.2A GRP94, GRP78, PDIA6, lanes 5-8),** but had no effect on activation of the other two branches of the ER stress response that are mediated by PERK and IRE-1. Endogenous ATF6 is difficult to detect by immunoblotting.

ATF6 knockdown decreased cell viability in NRVM treated with either TM **(Fig. 2.2B)** or H_2O_2 **(Fig. 2.2C)**. Moreover, ATF6 knockdown increased necrotic cell death in response to H_2O_2 treatment, as determined by increased media levels of LDH **(Fig. 2.2D)**. Simulated ischemia was shown to activate ATF6 and downstream genes in NRVM, as evidenced by the conversion of p90 ATF6 to p50 ATF6 and the increased levels of canonical ATF6 target proteins, GRP94, GRP78 and PDIA6 **(Fig. 2.2E sI)**. ATF6 activation appeared to persist during sI/R **(Fig. 2.2E sI/R)**. ATF6 knockdown decreased viability in NRVM subjected to I/R, increased media levels of LDH and

HMGB1, increased ROS levels and increased malondialdehyde (MDA), the latter of which is a measure of ROS-associated lipid peroxidation[12] **(Fig. 2.2F-I)**. Treatment with NAC verified that ROS were generated upon sI/R **(Fig. 2.2H)**. Thus, endogenous ATF6 protected NRVM from the maladaptive effects of prolonged ER protein misfolding and ER stress by TM, as well as from the damaging effects of oxidative stress induced by H_2O_2 and sI/R.

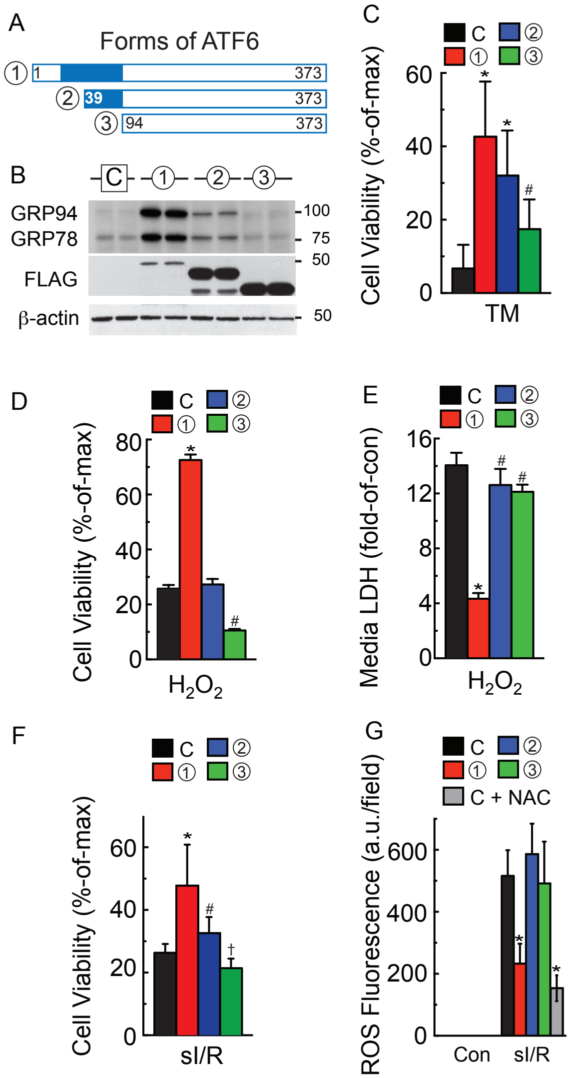

Figure 2.1- Effects of ATF6 overexpression on ER- and oxidative stress in cultured cardiac myocytes.

A, Diagram of the forms of ATF6 used in this study. **B,** Neonatal rat ventricular myocytes (NRVM) were infected with adenovirus (AdV) encoding either no protein (C), or one of the three forms of ATF6 shown, then immunoblotted using a FLAG antibody to detect the overexpressed ATF6, a KDEL antibody, which detects GRP94 and 78, or β-actin antibody. **C-G,** NRVM were infected with either control (C) or each of the ATF6-expressing AdV shown in A, then treated for 48h with TM (40 µg/ml) (C), 37.5 µM H_2O_2 for 8h (D, E), sI/R (F, G), and 5 mM N-acetyl cysteine (NAC) (G), followed by viability determination using an MTT assay, or by media enzyme assay to determine LDH activity, or ROS measurement with CellROX, as shown. * # † $p<0.05$ different than other values by ANOVA.

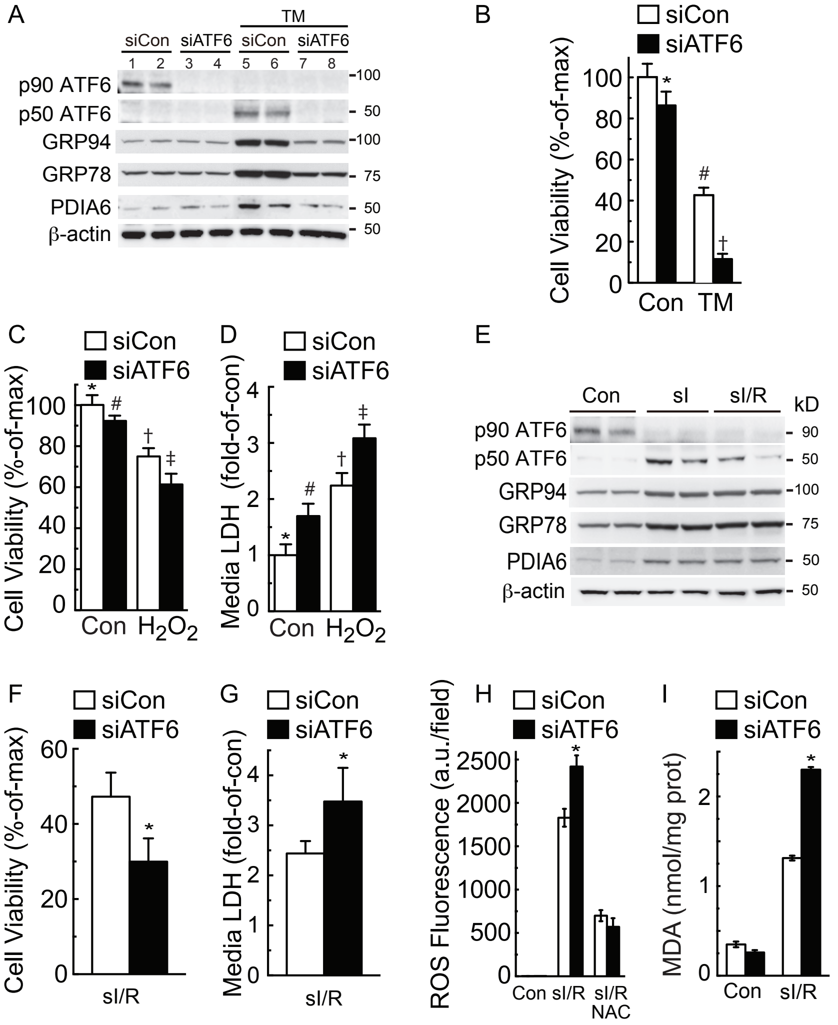

Figure 2.2- Effects of ATF6 knockdown on ER stress and oxidative stress in cultured cardiac myocytes.

A, NRVM were transfected with a non-targeted siRNA (siCon), or an siRNA targeted to rat ATF6 (siATF6), and then treated without or with TM (10 µg/ml) for 24h, then immunoblotted for endogenous ATF6 (p90 and p50 ATF6), GRP94, GRP78, PDIA6 and β-actin. NRVM were treated similarly with siCon or siATF6 for all subsequent experiments in this figure, except (E). **B,** NRVM were treated for 48h without or with TM (40 µg/ml) followed by MTT for cell viability. * # † $p<0.05$ different from other values by ANOVA. **C and D,** NRVM were treated for 8h with H_2O_2, then examined by MTT for cell viability (C), or media assayed for LDH activity (D). *#†‡ $p<0.05$ different than other values by ANOVA. **E,** NRVM were subjected to Con, sI or sI/R, then extracts were immunoblotted for the proteins shown. **F-I,** NRVM were treated with sI/R then examined by calcein blue AM for cell viability, media LDH activity, ROS using CellRox, and malondialdehyde (MDA). * $p<0.05$ different from siCon by t-test.

The effects of ATF6 deletion in the mouse heart have not been previously examined; therefore, to assess the effects of deleting ATF6, *in vivo,* ATF6 knockout mice (KO)[3] were used;. Immunoblots confirmed the absence of p90 ATF6 in ATF6 KO mouse hearts compared to wild type (WT) mouse hearts **(Fig. 2.3A)**. The ATF6 KO mice do not exhibit any overt phenotype under non-stressed conditions, developing normally through adulthood. Here, echocardiography confirmed that this was the case in the heart, demonstrating that all cardiac dimensions and contractile properties of the ATF6 KO mice were the same as WT mice. When mice were subjected to a model of surgical transient coronary artery occlusion, for 30 min followed by reperfusion for 24h, the area-at-risk was the same for both lines, however, infarct sizes were significantly larger in ATF6 KO mice following I/R **(Fig. 2.3B)**. Moreover, after I/R, plasma LDH levels and tissue MDA levels were greater in ATF6 KO mice than in WT mice **(Fig. 2.3C and 2.3D)**. Immunocytofluorescence and immunoblots of mouse heart tissue sections showed that I/R increased ATF6 and GRP78 in WT mice, but not in ATF6KO mice **(Fig. 2.4 and 2.5)**. Moreover, I/R did not activate PERK or IRE-1, as shown by the absence of phosphorylated PERK and spliced XBP1 **(Fig 2.5)**. Additionally, examination of heart extracts for transcript levels of canonical ATF6 regulated genes showed that, compared to WT mouse hearts, there was 50% or less Grp94, Grp78 and PDIA6 mRNA in ATF6 KO mouse hearts **(Fig. 2.3E)**.

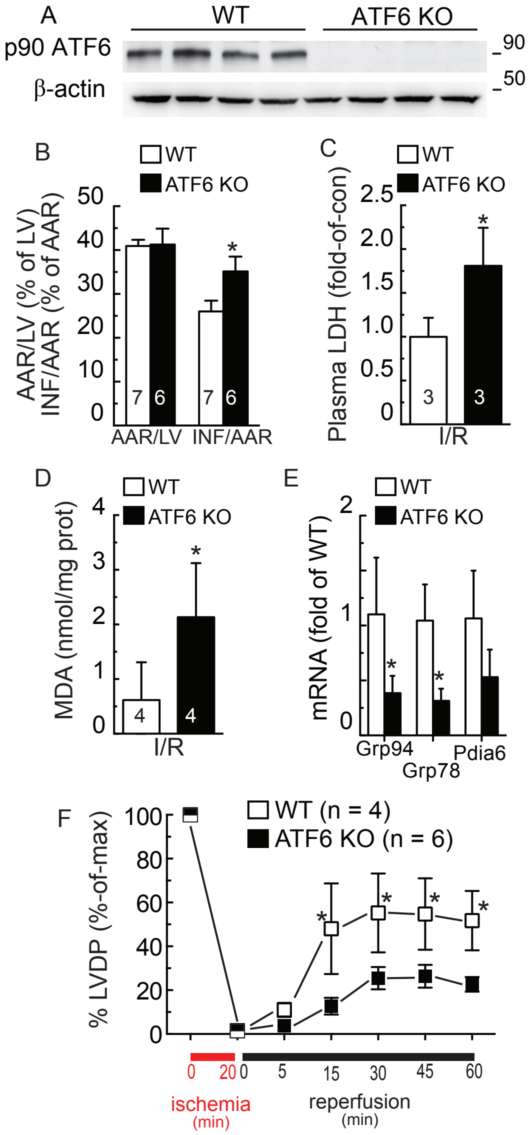

Figure 2.3- Effect of ATF6 gene deletion in hearts subjected to ischemia/reperfusion.

A, WT (n = 4) or ATF6 KO (n = 4) mouse heart extracts were examined for ATF6 and β-actin by immunoblotting. To detect p90 ATF6 in mouse heart extracts, the antibody raised against the C-terminal of ATF6 was used. **B,** WT (n = 7) or ATF6 KO (n = 6) mice were subjected to *in vivo* I/R, then hearts were assessed for damage; AAR = area at risk; LV = left ventricle; INF = infarcted area, * p<0.05 different than WT INF/AAR by t-test, **C,** plasma from WT (n = 3) and ATF6 KO (n = 3) mice assessed for LDH, * p<0.05 different than WT by t-test, or **D,** heart extracts from WT (n = 4) and ATF6 KO (n = 4) mice assessed for MDA ,* p<0.05 different than WT by t-test. **E,** WT (n = 3) and ATF6 KO (n = 4) mouse hearts were subjected to *in vivo* I/R after which heart extracts were analyzed for Grp94, Grp78, and Pdia6 mRNA levels, normalized to β-actin mRNA by qRT-PCR, * p<0.05 different than WT for each gene target by t-test. **F,** WT (n = 4) and ATF6 KO (n = 6) mouse hearts were subjected to *ex vivo* global ischemia/reperfusion and left ventricular developed pressure (LVDP) was determined before and after ischemia and presented as % of maximal function observed during equilibration for each mouse line, * p<0.05 different than ATF6 KO by t-test.

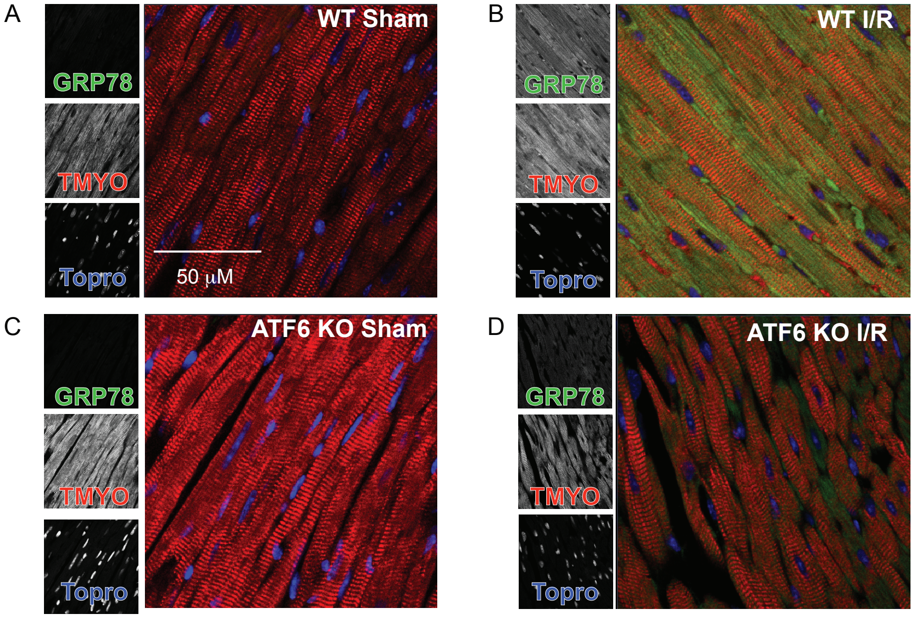

Figure 2.4- Effect of I/R on GRP78 expression in WT and ATF6 KO mouse hearts as determined by immunocytofluorescence.

A, B, WT or **C, D,** ATF6 KO mice were subjected to I/R in vivo, after which hearts were obtained and sections were stained for GRP78 (green), tropomyosin (red), or TOPRO (blue).

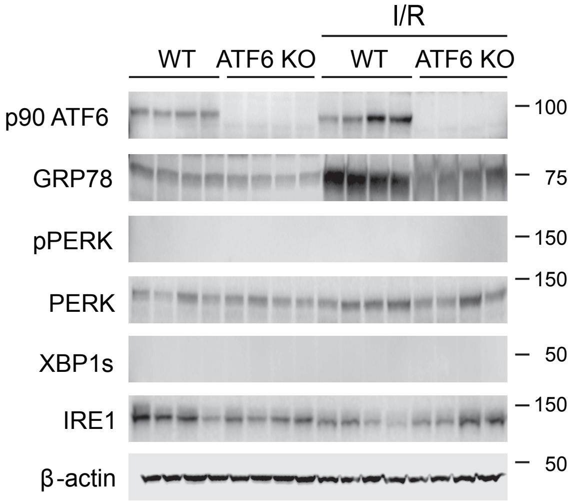

Figure 2.5- Effect of I/R on markers of ER stress in WT and ATF6 KO mouse hearts as determined by immunoblotting.

WT or ATF6KO mice were subjected to I/R in vivo, after which hearts were obtained and extracts were immunoblotted for p90 ATF6, GRP78, phospho-PERK (pPERK), total PERK (PERK), spliced XBP1 (XBP1s), IRE-1 and β-actin.

We also examined whether the effects of ATF6 deletion seen *in vivo* could be recapitulated in isolated hearts subjected to *ex vivo* I/R. Compared to WT mouse hearts, ATF6 KO mouse hearts were more susceptible to a loss of cardiac function following global ischemia, exhibiting a significantly reduced recovery of left ventricular developed pressure (LVDP) upon reperfusion **(Fig. 2.3F)**. Thus, the effects of global ATF6 deletion on I/R damage were autonomous to the heart.

Next we examined the effects of ATF6 deletion in cardiac myocytes isolated from ATF6 KO mouse hearts. Examination of the ATF6 target gene product, GRP78, was consistent with these results; in WT mouse myocytes, GRP78 levels increased upon treatment with TM or sI/R **(Fig. 2.6A and 5B)**. In contrast, myocytes isolated from ATF6 KO mouse hearts showed no induction of GRP78 in response to TM or sI/R **(Fig. 2.6C and D)**. Moreover, compared to myocytes from WT mouse hearts, myocytes from ATF6 KO mouse hearts exhibited greater death in response to sI/R **(Fig. 2.6E)**. Thus, the deleterious effects of ATF6 deletion on ATF6 target gene induction by TM or sI/R, as well as sI/R-mediated cell death, was observed in ATF6 KO mouse hearts *in vivo* and *ex vivo*, as well as in myocytes isolated from ATF6 KO mouse hearts.

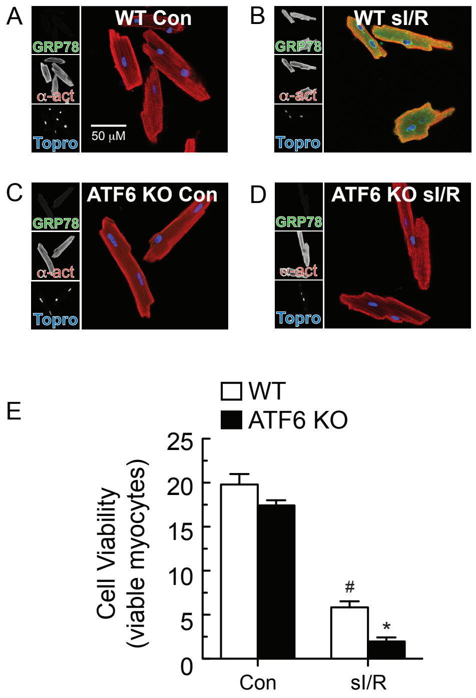

Figure 2.6- Effect of ATF6 deletion on GRP78 expression and cell viability of isolated adult mouse ventricular myocytes.

A-D, Myocytes were isolated from adult WT or ATF6 KO mice, subjected to sI/R, then fixed and examined by ICF for GRP78 (green), α-actinin (red) or TOPRO (blue). **E,** Myocytes were isolated from adult WT or ATF6 KO mice, then subjected to sI/R followed by determination of cell viability using calcein blue AM staining. n = 3 cultures for each treatment; shown is a representative experiment of three independent experiments, *# p<0.05 different than all other groups by ANOVA.

Since ATF6 reduced ROS levels and protected cardiac myocytes and hearts against oxidative stress, we examined whether ATF6 overexpression in NRVM affected the levels of typical oxidative stress response genes. An initial survey of expression levels of several typical antioxidant genes, i.e. superoxide dismutase 1 and 2 (SOD1/2), glutathione peroxidase 1, 3 and 4 (Gpx1/3/4), and peroxiredoxin 1-4 and 6 (Prdx1-4/6) showed that compared to control, ATF6 had a very small effect on the expression of any of these genes **(Fig. 2.7A)**. Accordingly, a wider range of oxidative stress response genes was assessed using a PCR gene array. Amongst the 84 genes represented in the array, ATF6 significantly changed the levels of 17 genes; eleven genes were increased by ATF6, including catalase (Cat), peroxiredoxin 5 (Prdx5) and Vimp **(Fig. 2.7B red)**, which encode antioxidant proteins, while 6 genes were decreased by ATF6 **(Fig. 2.7B green)**, most of which respond to oxidative stress, but do not encode antioxidants. PCR was used to examine the expression of several key genes in the array upon which ATF6 had the most robust induction effects, Cat, Prdx5 and Vimp. Form 1 of ATF6 was the strongest inducer of all three genes, with much less induction being observed for forms 2 and 3 **(Fig. 2.7C)**. These results suggested that ATF6 might directly transcriptionally induce these genes.

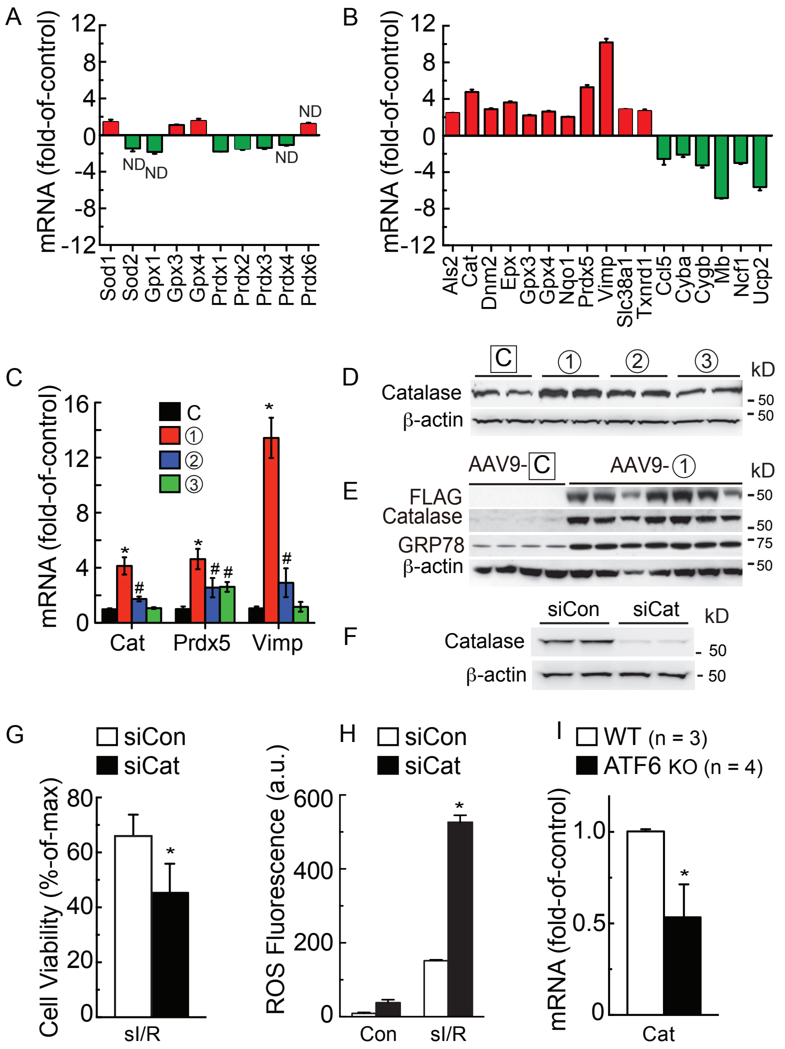

Figure 2.7- Analysis of oxidative stress gene expression.

A and B, NRVM were infected with AdV-Con or AdV-ATF6 (form 1), then RNA was subjected to qRT-PCR for the genes shown (A), or analyzed with an oxidative stress gene array (B). Shown are only genes that were increased (red) or decreased (green) by ATF6. In A and B all values were $p<0.05$ different than control by t-test, unless marked ND (no difference). **C and D,** NRVM were infected with the AdV-ATF6 shown, then RNA was isolated and analyzed for catalase (Cat), peroxiredoxin 5 (Prdx5), and Vimp mRNA by qRT-PCR (C), * # $p<0.05$ different than all other values for each target gene, and protein was analyzed for catalase levels by immunoblotting (D). **E,** WT mice were injected with AAV9-control or AAV9-CMV-FLAG-ATF6 form 1. Two weeks later, mice were sacrificed and hearts were analyzed for FLAG-ATF6, catalase, GRP78 and β-actin by immunoblotting. **F,** NRVM were transfected with siCon or siCat RNAs; 48h later, culture extracts were examined for catalase and β-actin. **G, H,** NRVM were transfected with siCon or siCat RNA, subjected to sI/R, then analyzed for cell viability by calcein blue AM staining (G), or for ROS by Amplex Red (H). **I,** following I/R, WT (n = 3) and ATF6 KO (n = 4) mouse heart extracts were analyzed for Cat mRNA levels, normalized to β-actin mRNA by qRT-PCR. * $p<0.05$ different from siCon (G, H) or WT (I) by t-test.

Since catalase is known to decrease I/R damage in the heart[13], we probed deeper into the mechanism by which ATF6 mediated the induction of catalase, which has not been studied before. Immunoblots of NRVM treated with the three forms of ATF6 showed that catalase protein levels were increased most by form 1, followed by form 2 and then not at all by form 3 **(Fig. 2.7D)**, consistent with the effects of these forms of ATF6 on catalase mRNA **(Fig. 2.7C)**. Moreover, when mice were injected with a recombinant AAV9 that expresses form 1 of ATF6 in cardiac myocytes **(Fig. 2.7E FLAG)**, immunoblots of heart extracts showed that catalase was robustly induced by ATF6 overexpression in the mouse heart, *in vivo* **(Fig. 2.7E Catalase)**. As a control, we showed that AAV9-ATF6 also induced the known ATF6 target gene, GRP78 **(Fig. 2.7E GRP78)**. Knocking down catalase in NRVM with siRNA **(Fig. 2.7F)** decreased cell viability and increased ROS generation in response to sI/R **(Fig. 2.7G and 2.7H)**. Quantitative RT-PCR of mouse hearts subjected to I/R showed that, compared to WT mouse hearts, catalase was about half in ATF6 KO mouse hearts **(Fig. 2.7I)**. While myocytes isolated from WT mouse hearts exhibited a strong induction of catalase by TM **(Fig. 2.8A and 2.8B)** or sI/R **(Fig. 2.9A and 2.9B)**, catalase did not increase in myocytes isolated from ATF6 KO mouse hearts treated with either TM **(Fig. 2.8C and Fig. 2.8D)** or sI/R **(Fig. 2.9C and 2.9D)**. ICF of mouse heart tissue sections showed that catalase increased in the hearts of WT mouse hearts subjected to I/R, *in vivo,* but not in ATF6 KO mouse hearts **(Fig. 2.10A-D)**. Immunoblots verified the impaired induction of catalase in the hearts of ATF6 KO mice subjected to I/R, *in vivo* **(Fig. 2.10E and 2.10F)**. In NRVM, catalase siRNA decreased the beneficial effects of ATF6 form 1, indicating that catalase is a major contributor of ATF6-mediated protection from I/R-induced cell death in cardiac myocytes **(Fig. 2.9E)**. Moreover, the increased susceptibility of ATF6 KO myocytes to death upon I/R was rescued by treating them with a cell-permeable form of catalase, PEG-catalase, as previously described[14], after which there was no difference in viability between myocytes from WT and ATF6 KO mouse hearts **(Fig. 2.9F)**. Treatment of mice with PEG-catalase *in vivo*, as previously described[15], resulted in a similar rescue of LVDP in ATF6 KO mouse hearts subjected to *ex vivo* I/R, such that the performance of WT and ATF6 KO mouse hearts was indistinguishable **(Fig. 2.9G)**. This catalase-mediated rescue was also seen when LDH release and infarct size were measured in WT vs ATF6 KO mouse hearts subjected to *ex vivo* I/R **(Fig. 2.9H and 2.9I)**. Moreover, the PEG-catalase rescue effect was recapitulated by AAV9-mediated ATF6 overexpression in ATF6 KO mouse hearts **(Fig. 2.9J)**.

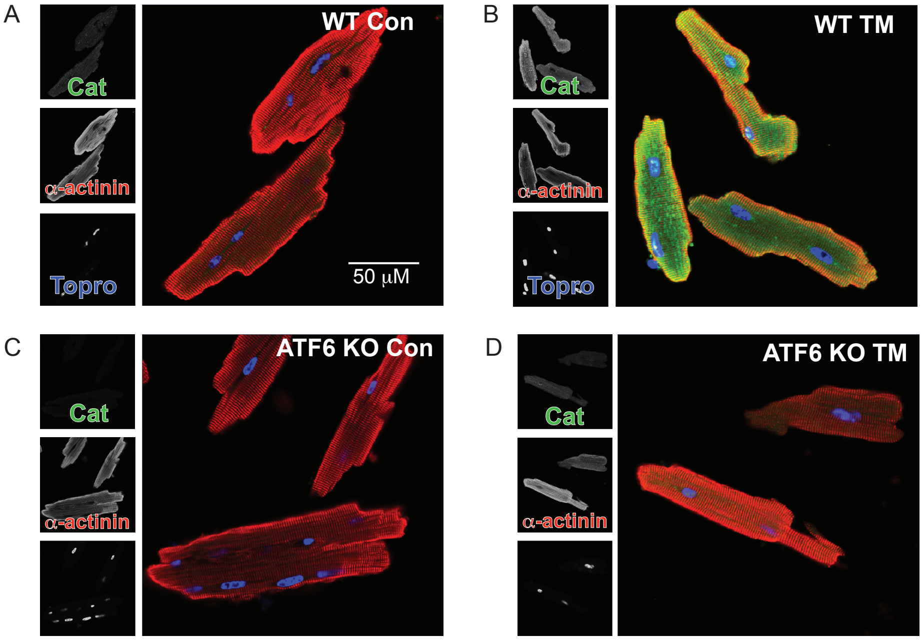

Figure 2.8- Effect of TM on Catalase Expression in Cardiac Myocytes from WT and ATF6 KO Mouse Hearts.

A, B, Myocytes were isolated from WT or **C, D,** ATF6 KO mouse hearts then treated without (A, C) or with TM (10 µg/ml; 24h; B, D), then fixed and stained for catalase (Cat; green), α-actinin (red) or TOPRO (blue).

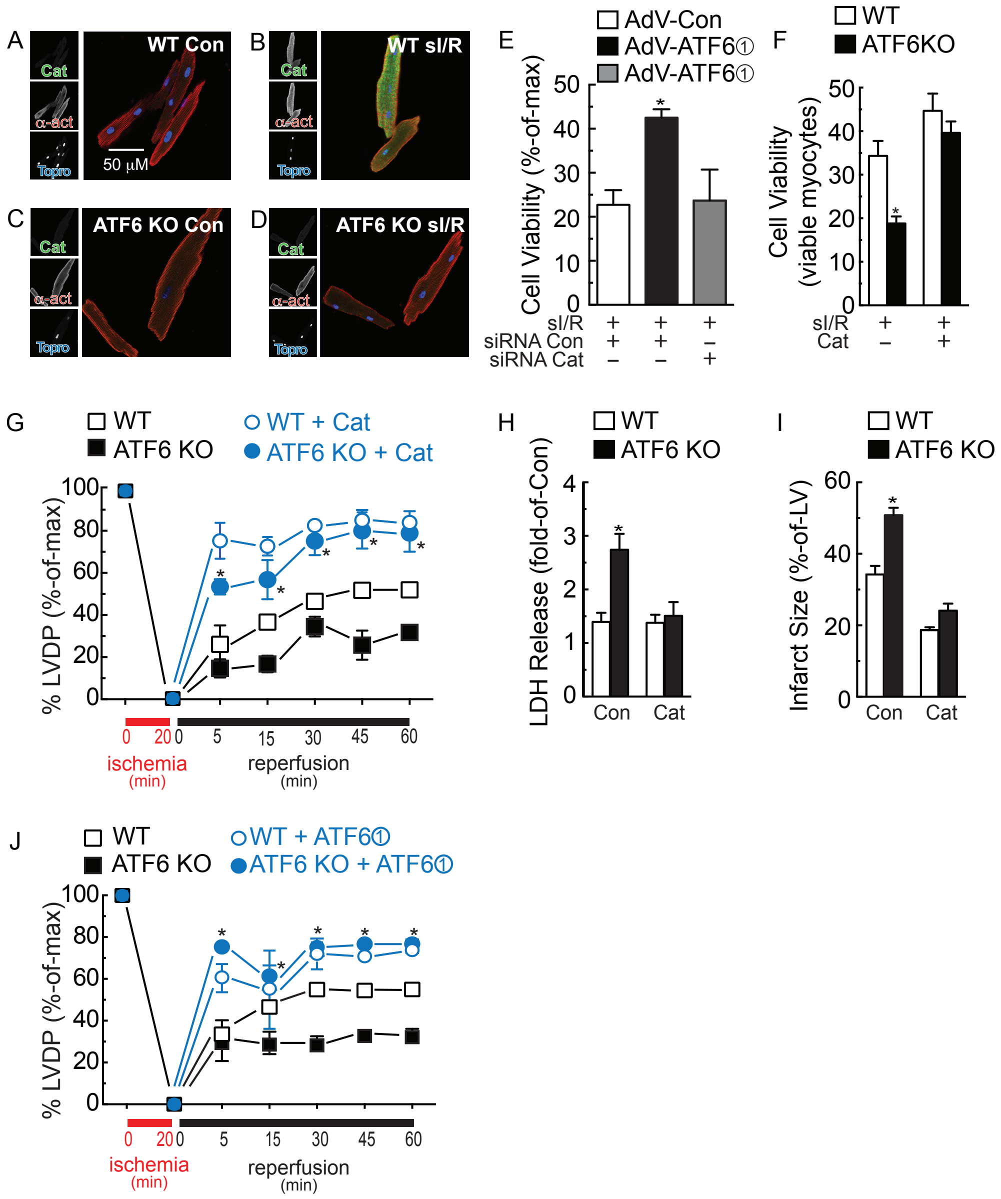

Figure 2.9- Effects of ATF6 deletion on catalase.

A-D, Myocytes were isolated from adult WT (A, B) or ATF6 KO (C, D) mice, subjected to sI/R, then fixed and examined by ICF for catalase (green), α-actinin (red) or TOPRO (blue). **E,** NRVM were treated with siCon or siCat RNAs, as well as infection with the AdVs shown, then subjected to sI/R followed by determination of cell viability by calein blue AM staining. * $p<0.05$ different from all other values by ANOVA. **F,** Myocytes isolated from WT or ATF6KO mouse hearts were treated with vehicle or PEG-catalase, followed by sI/R, the viability was determined by calein blue AM staining. * $p<0.05$ different from WT by t-test. **G-I,** Mice were injected with vehicle or PEG-Cat for 16h, then hearts were subjected to *ex vivo* I/R and LVDP, LDH release, and infarct size were measured. In G, * $p<0.001$ different from WT vehicle or ATF6 KO vehicle at a given reperfusion time by two-way ANOVA. In H and I, * $p<0.001$ different from WT Con, by t-test. **J,** Mice were injected with AAV9-Con or AAV9-CMV-FLAG-ATF6 form 1 for 2d, then hearts were subjected to *ex vivo* I/R and LVDP was measured. * $p<0.001$ different from WT AAV9-Con or ATF6 KO AAV9-Con at a given reperfusion time by two-way ANOVA.

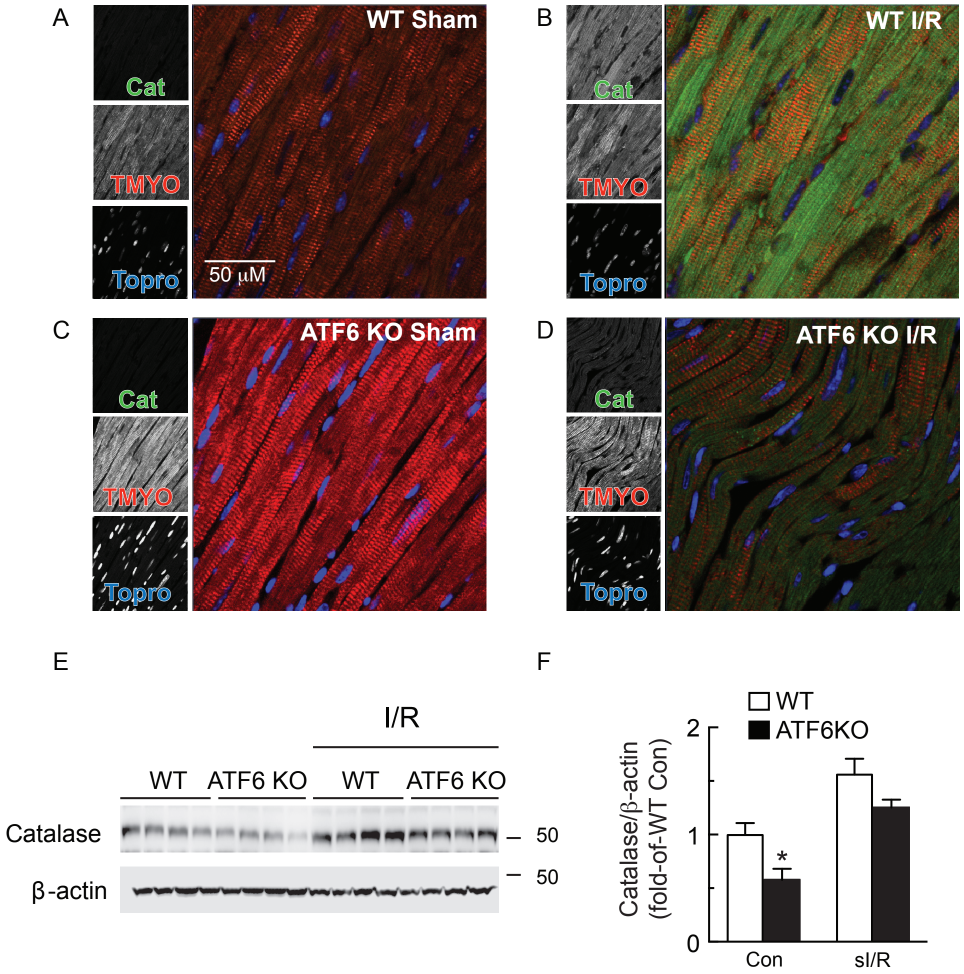

Figure 2.10- Effect of I/R on Catalase expression in WT and ATF6 KO mouse hearts as determined by immunocytofluorescence and immunoblotting.

A, B, WT or **C, D,** ATF6 KO mice were subjected to I/R in vivo, after which hearts were obtained and sections were stained for Catalase (green), tropomyosin (red), or TOPRO (blue). **E,** Hearts from WT or ATF6 KO subjected to I/R in vivo were extracted and analyzed for catalase and β-actin by immunoblotting (n =4 mice per treatment). **F,** The immunoblots shown in E were quantified by densitometry. * p<0.05 different from WT Con by t-test.

To further examine the mechanism by which ATF6 induces catalase, the 5’-flanking sequence (5’-FS) of the rat Cat gene was scanned for a DNA sequence that might bind ATF6, so called ER stress response element (ERSE). Two such elements were found within 1,000 nucleotides 5’ of the Cat mRNA start site; we named these ERSE-1 (-194 to -184) and ERSE-2 (-979 to -962)**.** To examine whether the rat Cat 5’-flanking sequences conferred transcriptional induction in response to ATF6, truncated versions of the rat Cat 5’-FS were cloned in front of firefly luciferase and the abilities of co-transfected ATF6 form 1 to induce luciferase were examined in NRVM. Truncating from -1161 to -689 and to -410, which removed ERSE-2, had little effect on ATF6 induction **(Fig. 2.11A, constructs 1 - 3)**. However, a truncated form of rat Cat that removed ERSE-1 resulted in a significant decrease in ATF6-mediated luciferase induction **(Fig. 2.11A, construct 4)**. In a second series of experiments, ERSE-1 and ERSE-2 were mutated in ways predicted to inhibit ATF6 binding **(Fig. 2.11B, M1 and M2)**. When these reporters were co-transfected with the various forms of ATF6 into NRVM, the mutation in ERSE-2, i.e. M2, moderately decreased Cat promoter activity, while the mutation in ERSE-1, i.e. M1, or in both ERSE-1 and ERSE-2, i.e. M1/M2, showed greater reductions of ATF6-meidated transcriptional induction **(Fig. 2.11C)**. Finally, a chromatin immunoprecipitation experiment showed that form 1 of ATF6 was able to bind to either ERSE-1 or ERSE-2 in myocytes **(Fig. 2.11D)**. Thus, activated ATF6 can bind to putative ERSEs in the rat Cat gene regulatory region and confer transcriptional induction, demonstrating one mechanism by which ATF6 could protect cardiac myocytes from oxidative stress during I/R.

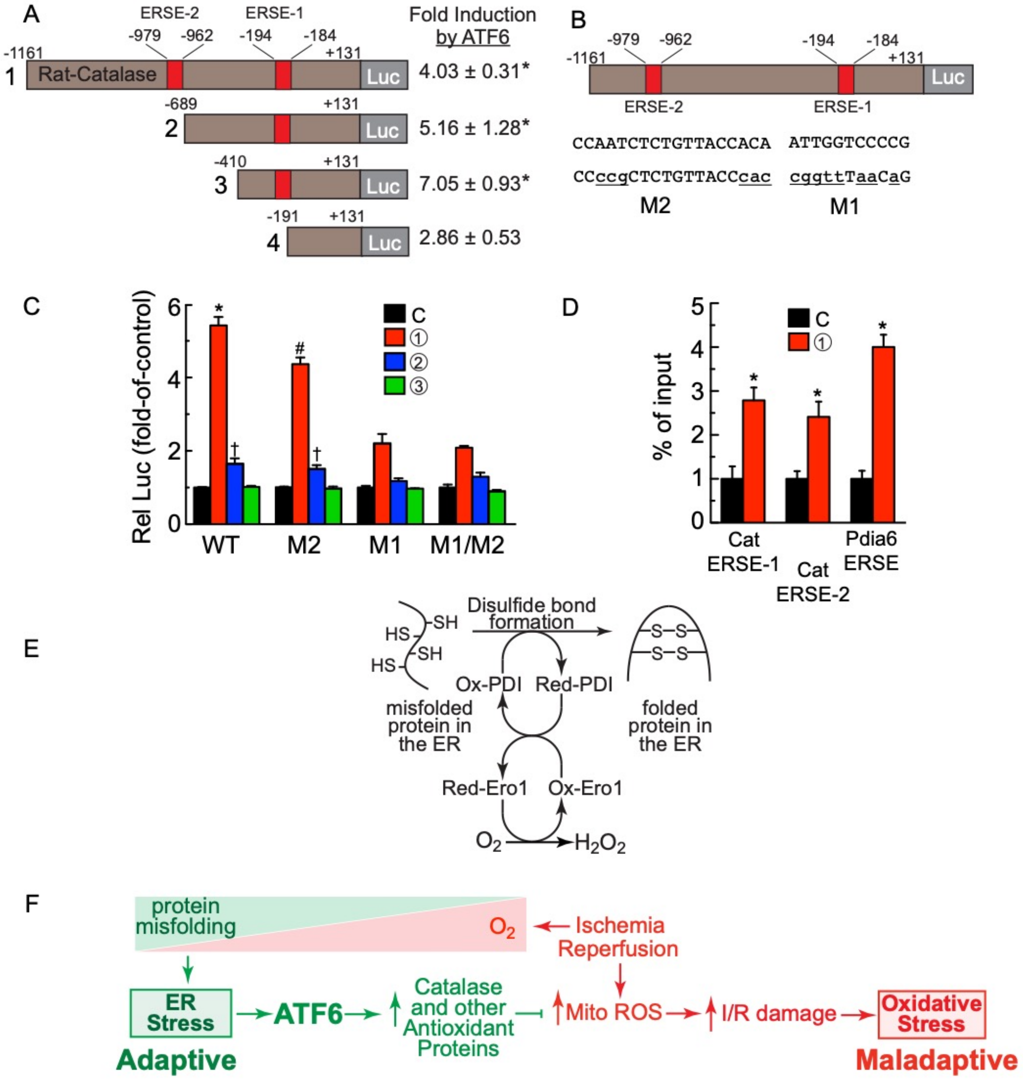

Figure 2.11- Effects of ATF6 on the catalase promoter.

A, Truncations of the catalase 5'-flanking sequence driving luciferase, as shown (left), i.e. rat-cat(-1161/+131)-Luc, rat-cat(-689/+131)-Luc, rat-cat(-410/+131)-Luc and rat-cat(-191/+131)-Luc were tramsfected into NRVM which were then infected with AdV encoding form 1 of ATF6 or with a control AdV. Luciferase enzyme activity in AdV-ATF6-infected cells was normalized to luciferase enzyme activity in AdV-Con-infected cells to determine the fold-induction by ATF6 (right), * $p<0.05$ different from control by t-test. **B,** Diagram of the locations of ERSE-2 and 1 in the catalase 5'-flanking region, their sequences (upper case), and the mutations to those sequences (lower case). **C,** NRVM were transfected with plasmids encoding rat-cat(-1161/+131)-Luc WT, M2, M1 or M1/M2 and then infected with the ATF6-expressing AdV, as shown; then, 48h later, luciferase levels were measured in extracts, *#† $p<0.05$ different than other values in WT or M2 by ANOVA. **D,** NRVM were infected with AdV encoding control or FLAG-ATF6 (form 1), and then ATF6 binding to endogenous ERSE-1 1 ERSE-2, as well as to the endogenous Pdia6 ERSE, previously studied and used here as a control, was examined by ChIP, * $p<0.05$ different than control by t-test. **E,** O_2 is required for protein disulfide bond formation and protein folding in the ER. **F,** ATF6 links the ER stress response with the oxidative stress response. As O_2 decreases during ischemia (red triangle), protein misfolding increases (green triangle), leading to adaptive ER stress, ATF6 activation and induction of catalase and other antioxidant proteins that decrease ROS generated in the mitochondria during reperfusion.

2.4. Discussion

2.4.1. ATF6 Links the ER Stress Response and the Oxidative Stress Response

This study provides evidence supporting a newly described role for ATF6 as a molecular link between the ER stress and oxidative stress gene programs. Initially, we thought this role for ATF6 fit well with a potential connection between ER stress and oxidative stress involving protein disulfide bond formation. Protein disulfide bond formation, which takes place only in the ER, requires oxygen to fuel the redox couple between ER oxidoreductase 1 (Ero1) and the final enzyme involved in protein disulfide bond formation, protein disulfide isomerase (PDI)[1, 16, 17] **(Fig. 2.11E)**. This ER redox system results in the conversion of molecular oxygen to H_2O_2, which contributes to total cellular ROS, although a very small amount compared to the ROS generated by mitochondria[18]. There are three ER proteins thought to be responsible for neutralizing the H_2O_2 generated during protein disulfide bond formation in the ER; peroxiredoxin 4 (Prx4), and glutathione perioxidases 7 and 8 (GPx7/8)[16]. Accordingly, when we first discovered that ATF6 had antioxidant activity, since ATF6 induces mostly ER proteins, we thought that ATF6 most likely exerted its antioxidant effects by inducing antioxidant proteins that reside in the ER, such as Prx4 and/or GPx7/8. However, our results showed that these genes were minimally affected by ATF6, and that ATF6 had more robust effects on expression of 11 other genes, all but one of which encode antioxidant proteins that reside outside of the ER **(Fig. 2.7)**. Thus, ATF6 can have widespread effects on antioxidant protein expression, even outside the ER, which increases the scope of the functional impact of ATF6 well beyond improving ER protein folding. It might be of clinical relevance to acutely activate ATF6 during reperfusion, in vivo, but this would likely require the development of new methods that do not depend on ATF6 overexpression. Although many of the antioxidant proteins induced by ATF6 may contribute in some way to reducing myocardial damage during I/R, we focused the mechanistic aspects of this study on catalase because of its ability to neutralize large quantities of ROS generated in various cellular locations, and because it has not previously been previously shown to be induced in an ATF6- and ER stress-dependent manner in any cell or tissue.

2.4.2. Catalase is an Example of how ATF6 Regulates Antioxidant Protein Expression

Catalase is a 527 amino acid protein (rat) that resides mainly in peroxisomes. Peroxisomes generate and utilize H_2O_2 for oxidative purposes, including peroxidative detoxification and β-oxidation of fatty acids. Catalase is an important component of peroxisomes, because it neutralizes H_2O_2 that remains after the required peroxidative reactions have taken place. Catalase can also oxidize peroxynitrate, nitric oxide and organic peroxides. In addition to peroxisomes, catalase has also been found in the cytosol and in cardiac mitochondria, however it has not been found in the ER. Moreover, it has been shown that in the heart, catalase overexpression in cardiac myocytes decreases I/R injury by reducing ROS levels[13].

Here, we showed that, in cardiac myocytes, ischemia, which impairs ER protein disulfide bond formation and increases misfolded proteins, activates ATF6, which binds to specific elements in the regulatory regions of the catalase gene and increases catalase transcription. We also showed that ATF6 can increase expression of other antioxidant proteins, supporting the hypothesis that, together with catalase these antioxidants decrease ROS and moderate myocardial damage during reperfusion **(Figure 2.11F)**. In further support of this hypothesis was our finding that, compared to WT mouse hearts, the induction of catalase during I/R was impaired in ATF6KO mouse hearts. To the best of our knowledge, this is the first demonstration that catalase is induced in the heart by I/R in an ATF6-dependent manner. Since we showed that ATF6 also induced two other antioxidant genes encoding proteins residing outside the ER, it appears that, during ER stress induced by ischemia, ATF6 is likely to be a direct transcriptional inducer of numerous antioxidant genes.

2.4.3. Catalase is an ATF6-inducible ER Stress Response Gene

Previous studies, mostly in non-cardiac myocytes, have shown that catalase expression is regulated by the transcription factors Sp1, NF-Y and Foxo3a[19]. However, there have been no studies examining whether ATF6 can regulate catalase transcription. Here, we showed that there are two sites in the catalase regulatory region to which ATF6 can bind, ERSE-1 and ERSE-2. Mutating ERSE-2 had less of an effect on catalase promoter activity than mutating ERSE-1, suggesting that ERSE-1, which lies proximal to the catalase promoter, is the major site through which ATF6 confers transcriptional induction in cardiac myocytes **(Fig. 2.11A-D)**. Moreover, since catalase is induced upon treatment with the prototypical ER stressor, TM, and by the pathological ER stress, I/R, and since the ER stress transcription factor, ATF6, binds to and induces catalase transcription, we posit that catalase should be categorized as an ER stress response gene. Consistent with the identification of catalase as an ER stress response gene is the apparent reduction of its expression as a function of development in the heart. We previously showed that the expression of several canonical ER stress response genes was much higher in neonatal rat cardiac myocytes than in adult rat cardiac myocytes[20]. The same appears to be true for catalase; here, immunoblotting showed relatively high levels of basal catalase in NRVM compared to adult mouse hearts **(Figs. 2.7D and 2.7E)**. Therefore, like some other ER stress response genes, catalase expression appears to be relatively low in the adult heart, compared to the neonatal heart. This is underscored further by our finding that the ATF6 dependence of catalase expression was quite evident when adult mouse cardiac myocytes isolated from WT and ATF6 KO mice were treated with TM or sI/R and then immunostained for catalase **(Fig. 2.8 and Fig. 2.9)**.

2.4.4. Global Effects of ATF6 on Antioxidant Protein Expression

The antioxidant genes that were induced the most by ATF6 in this study were catalase, peroxiredoxin 5 (Prdx5) and Vimp. ATF6-mediated induction of these genes was validated using the three forms of ATF6; each gene was induced with a profile consistent with the direct effects of ATF6 on transcription **(Fig. 2.7C)**. Like catalase, Prdx5 is not located in the ER lumen; however, it is unusual amongst other peroxiredoxins, in that it has been found in several cellular areas, including mitochondria, peroxisomes, cytosol and nucleus[21]. Prdx5 is a 213 amino acid protein (rat) that catalyzes the glutathione-mediated reduction of potentially damaging peroxides, providing a new mechanism by which the ATF6 branch of the ER stress response could contribute to decreasing ROS during myocardial reperfusion.

Vimp is a 189 amino acid ER-transmembrane protein (rat) configured with most of its structure, including its catalytic domain on the cytosolic face of the ER[22]. Vimp, also known as SelS, is believed to interact with Hrd1 and other ER stress, ATF6-regulated ER-transmembrane proteins that are involved in ER associated degradation, a process by which terminally misfolded proteins in the ER are degraded to mitigate their toxic effects. Vimp is one of only 24 selenoprotein genes in the mouse genome; in general, selenoproteins are known for their antioxidant roles as ROS scavengers[23]. However, the functions of selenoproteins and, in particular Vimp have not been studied in the heart. It is interesting to note that five of the 11 ATF6-inducible oxidative stress response genes identified in this study are selenoproteins. This is the first demonstration in any cell or tissue type that ATF6 has a global effect on selenoprotein expression, which provides even further linkage between the ATF6 branch of the ER stress response and the oxidative stress response.

In summary, previous studies showed that ectopic expression of activated ATF6 can decrease I/R damage in the heart. However, neither the mechanism of this effect, nor whether endogenous ATF6 plays a role in myocardial I/R damage had been examined. Here, we determined functions for endogenous ATF6 in the heart, and found evidence of a previously unappreciated role for ATF6 as an inducer of antioxidant genes, which establishes a mechanistic link by which ATF6 can decrease myocardial I/R damage **(Fig. 2.11F)**.

Chapter 2, in part, is a reprint of the material as it appears in Circulation Research in 2017. Jin, J-K., Blackwood, E.A., Azizi, K., Thuerauf, D.J., Fahem, A.G., Hofmann, C., Doroudgar, S., and Glembotski, C.C. ATF6 Decreases Myocardial

Ischemia/reperfusion Damage and Links ER Stress and Oxidative Stress Signaling Pathways in the Heart. *Circ. Res.* 2017; 120(5):862-875. The dissertation author was a lead contributing investigator and author to the portions used in this text.

2.5. References

1. Cao SS, Kaufman RJ. Endoplasmic reticulum stress and oxidative stress in cell fate decision and human disease. Antioxid Redox Signal. 2014;21(3):396-413.
2. Granger DN, Kvietys PR. Reperfusion injury and reactive oxygen species: The evolution of a concept. Redox Biol. 2015;6:524-551.
3. Wu J, Rutkowski DT, Dubois M, Swathirajan J, Saunders T, Wang J, Song B, Yau GD, Kaufman RJ. ATF6alpha optimizes long-term endoplasmic reticulum function to protect cells from chronic stress. Dev Cell. 2007;13(3):351-364.
4. Yoshida H, Okada T, Haze K, Yanagi H, Yura T, Negishi M, Mori K. ATF6 activated by proteolysis binds in the presence of NF-Y (CBF) directly to the cis-acting element responsible for the mammalian unfolded protein response. Mol Cell Biol. 2000;20(18):6755-6767.
5. Thuerauf DJ, Morrison LE, Hoover H, Glembotski CC. Coordination of ATF6-mediated transcription and ATF6 degradation by a domain that is shared with the viral transcription factor, VP16. J Biol Chem. 2002;277(23):20734-20739.
6. Thuerauf DJ, Morrison L, Glembotski CC. Opposing roles for ATF6alpha and ATF6beta in endoplasmic reticulum stress response gene induction. J Biol Chem. 2004;279(20):21078-21084.
7. Marshall KD, Edwards MA, Krenz M, Davis JW, Baines CP. Proteomic mapping of proteins released during necrosis and apoptosis from cultured neonatal cardiac myocytes. Am J Physiol Cell Physiol. 2014;306(7):C639-647.
8. Siman R, McIntosh TK, Soltesz KM, Chen Z, Neumar RW, Roberts VL. Proteins released from degenerating neurons are surrogate markers for acute brain damage. Neurobiol Dis. 2004;16(2):311-320.
9. van Wijk SJ, Hageman GJ. Poly(ADP-ribose) polymerase-1 mediated caspase-independent cell death after ischemia/reperfusion. Free Radic Biol Med. 2005;39(1):81-90.
10. Griendling KK, Touyz RM, Zweier JL, Dikalov S, Chilian W, Chen YR, Harrison DG, Bhatnagar A. Measurement of Reactive Oxygen Species, Reactive Nitrogen Species, and Redox-Dependent Signaling in the Cardiovascular System: A

Scientific Statement From the American Heart Association. Circ Res. 2016;119(5):e39-75.

11. Santos CX, Raza S, Shah AM. Redox signaling in the cardiomyocyte: From physiology to failure. Int J Biochem Cell Biol. 2016;74:145-151.

12. Pompella A, Maellaro E, Casini AF, Ferrali M, Ciccoli L, Comporti M. Measurement of lipid peroxidation in vivo: a comparison of different procedures. Lipids. 1987;22(3):206-211.

13. Li G, Chen Y, Saari JT, Kang YJ. Catalase-overexpressing transgenic mouse heart is resistant to ischemia-reperfusion injury. Am J Physiol. 1997;273(3 Pt 2):H1090-1095.

14. Nakagami H, Takemoto M, Liao JK. NADPH oxidase-derived superoxide anion mediates angiotensin II-induced cardiac hypertrophy. J Mol Cell Cardiol. 2003;35(7):851-859.

15. Schroder K, Zhang M, Benkhoff S, Mieth A, Pliquett R, Kosowski J, Kruse C, Luedike P, Michaelis UR, Weissmann N, Dimmeler S, Shah AM, Brandes RP. Nox4 is a protective reactive oxygen species generating vascular NADPH oxidase. Circ Res. 2012;110(9):1217-1225.

16. Delaunay-Moisan A, Appenzeller-Herzog C. The antioxidant machinery of the endoplasmic reticulum: Protection and signaling. Free Radic Biol Med. 2015;83:341-351.

17. Higa A, Chevet E. Redox signaling loops in the unfolded protein response. Cell Signal. 2012;24(8):1548-1555.

18. Tu BP, Weissman JS. Oxidative protein folding in eukaryotes: mechanisms and consequences. J Cell Biol. 2004;164(3):341-346.

19. Glorieux C, Zamocky M, Sandoval JM, Verrax J, Calderon PB. Regulation of catalase expression in healthy and cancerous cells. Free Radic Biol Med. 2015;87:84-97.

20. Doroudgar S, Volkers M, Thuerauf DJ, Khan M, Mohsin S, Respress JL, Wang W, Gude N, Muller OJ, Wehrens XH, Sussman MA, Glembotski CC. Hrd1 and ER-Associated Protein Degradation, ERAD, are Critical Elements of the Adaptive ER Stress Response in Cardiac Myocytes. Circ Res. 2015;117(6):536-546.

21. Knoops B, Goemaere J, Van der Eecken V, Declercq JP. Peroxiredoxin 5: structure, mechanism, and function of the mammalian atypical 2-Cys peroxiredoxin. Antioxid Redox Signal. 2011;15(3):817-829.

22. Liu J, Rozovsky S. Membrane-bound selenoproteins. Antioxid Redox Signal. 2015;23(10):795-813.

23. Reeves MA, Hoffmann PR. The human selenoproteome: recent insights into functions and regulation. Cell Mol Life Sci. 2009;66(15):2457-2478.

Chapter 3: ATF6 regulates cardiac hypertrophy by transcriptional induction of the mTORC1 activator, Rheb

3.1. Introduction

ER stress dysregulates ER proteostasis, which activates the transcription factor, ATF6, an inducer of genes that enhance protein folding and restore proteostasis. Due to increased protein synthesis, it is possible that protein folding and, thus, ER proteostasis are challenged during cardiac myocyte growth. However, it is not known whether ATF6 is activated, and if so, what its function is during hypertrophic growth of cardiac myocytes. Here we examined the activity and function of ATF6 during cardiac hypertrophy.

We found that ATF6 was activated and ATF6-target genes were induced in mice subjected to an acute model of trans-aortic constriction (TAC), or to free-wheel exercise, which promote adaptive cardiac myocyte hypertrophy with preserved cardiac function. Cardiac myocyte-specific deletion of *Atf6* (ATF6 cKO) blunted TAC- and exercise-induced cardiac myocyte hypertrophy and impaired cardiac function, demonstrating a role for ATF6 in compensatory myocyte growth. Transcript profiling and chromatin immunoprecipitation identified *RHEB* as an ATF6-target gene in the heart. RHEB is an activator of mTORC1, a major inducer of protein synthesis and subsequent cell growth. Both TAC and exercise upregulated *RHEB*, activated mTORC1, and induced cardiac hypertrophy in WT mouse hearts, but not in ATF6 cKO hearts. Mechanistically, knockdown of ATF6 in neonatal rat ventricular myocytes blocked phenylephrine (PE)-, and insulin-like growth factor 1 (IGF1)-mediated *Rheb* induction, mTORC1 activation, and myocyte growth, all of which were restored by ectopic RHEB expression. Moreover, AAV9-*RHEB* restored cardiac growth to ATF6 cKO mice subjected to TAC. Finally, ATF6 induced *RHEB* in response to growth factors, but not in response to other activators of ATF6 that do not induce growth, indicating that ATF6 target gene induction is stress-specific.

Compensatory cardiac hypertrophy activates ATF6, which induces *Rheb* and activates mTORC1. Thus, ATF6 is a previously unrecognized link between growth stimuli and mTORC1-mediated cardiac growth.

3.2. Materials and Methods

3.2.1. Laboratory animals

The research reported in this article has been reviewed and approved by the San Diego State University Institutional Animal Care and Use Committee (IACUC), and conforms to the Guide for the Care and Use of Laboratory Animals published by the National Research Council. ATF6-floxed (ATF6$^{fl/fl}$) mice were a generous gift from Dr. Gokhan S. Hotamisligil. Briefly, ATF6-floxed mice were generated with a targeting construct flanking exons 8 and 9 of ATF6 with LoxP sequences on a C57B/6J background, as previously described[1]. In previous, unpublished studies with the ATF6$^{fl/fl}$ mice using a recombinant AAV9 that encodes *Cre* under the control of the *cardiac troponin T* promoter, no gender differences could be detected in terms of baseline or pathological remodeling, cardiac function or survival. Due to this observation and in an attempt to decrease the total number of mice needed to adequately power the study, only male mice were used. For some experiments, the numbers of animals to use was based on a predictive power analysis to achieve 5% error and 80% power, or using the resource equation method. In other experiments, the numbers of animals to use were determined practically, based on previous experiments designed to determine, for example, surgery mortality rates and the approximate magnitude of changes in the measured parameters. Both the TAC and Free-Wheel exercise protocols were initially performed in our previously published global ATF6KO mice and all functional, morphological, and biochemical analysis performed in the manuscript were initially performed in these animals with large cohorts as a trial. Our previous experiments showed the surgical mortality rates to be <5%. For all experimentation, ATF6$^{fl/fl}$ or wild-type littermates were randomized in a 1:1 ratio and assigned a coded number independent of the investigator.

3.2.2. Animal numbers

A total of 184 mice were used for this study. ATF6$^{fl/fl}$ C57BL/6J mice injected with AAV9-Con (Con) (n=81) and their ATF6$^{fl/fl}$ littermates injected with AAV9-Cre (ATF6 cKO) (n=80); for certain experimental paradigms Con and ATF6 cKO mice were subsequently injected with either AAV9-Con (n=37), AAV9-Rheb (n=13) or AAV9-ATF6 (n=24); ATF6 TG C57BL/6J mice (n=4) and their non-transgenic littermates (n=3). Male wild-type C57BL/6J mice were purchased from Jackson Laboratories for the TAC time course experiment (n=16). All animals were fed *ad libitum* for all experimental purposes and kept on a traditional 12-hour light/dark cycle. All animal sacrifice and tissue harvest was consistently performed between the hours of 12pm-3pm when we have observed animals to be in a fasted and sedentary state.

3.2.3. Cultured cardiac myocytes (NRVM) and experimental design

Neonatal rat ventricular myocytes (NRVMs) were isolated via enzymatic digestion, purified by Percoll density gradient centrifugation, and maintained in Dulbecco's modified Eagle's medium (DMEM)/F12 supplemented with 10% fetal bovine serum (FBS) and antibiotics (100 units/ml penicillin and 100 µg/ml streptomycin) on plastic culture plates that had been pre-treated with 5 µg/ml fibronectin, as previously described[2]. For all NRVM experiments, plating density was maintained at 2.5 x 10^5 cells/well on 12-well plates. Sixteen hours after plating, NRVM were subjected to respective treatments. For stimulated *in vitro* hypertrophy in NRVM, an initial period of serum starvation was implemented by replacing all culture media with 0.5 ml of glucose-free DMEM for 48 hours. NRVM culture media was then replaced with DMEM/F12 supplemented with BSA (1 mg/ml) containing either control, phenylephrine (50 µM) or IGF1 (100ng/ml) for an additional 48 hours. Experiments in which Lonafarnib (2 µM; Cayman Chemical, Cas#193275-84-2), rapamycin (20nM; Sigma-Aldrich), cyclohexamide (100 µg/ml; Sigma-Aldrich, Cat#C1988) or 4-phenylbutyrate (100 µM; Sigma-Aldrich, Cat#SML0309) were administered was performed as previously described [3-6], treatment was performed after serum starvation in conjunction with respective phenylephrine or IGF1 administration. Images were obtained with an IX70 fluorescence microscope (Olympus, Melville, NY). For *in vitro* chemical UPR activation, sixteen hours after plating NRVM and AMVM were treated with tunicamycin (10 µg/ml) for 24 hours in DMEM/F12 supplemented with bovine serum albumin (BSA) (1 mg/ml) for NRVM. For *in vitro* ischemia/reperfusion (I/R), ischemia was simulated by replacing all culture media with 0.5 ml of glucose-free DMEM containing 2% dialyzed FBS, then incubated at 0.1% O_2 in a hypoxia chamber with an oxygen controller (ProOx P110 oxygen controller, Biospherix, Parish, NY) for 8 hours or 3 hours for NRVM or AMVM, respectively, as previously described[2]. Reperfusion was simulated by replacing culture media with DMEM/F12 supplemented with BSA (1 mg/ml) for NRVM or maintaining media for AMVM and incubating at 21% O_2 for an additional 24 hours.

3.2.4. Immunoblotting

NRVM were lysed and subjected to immunoblot analysis, as previously described[2]. In brief, cultures were lysed with VC lysis buffer made from 20 mM Tris-HCl (pH 7.5), 150 mM NaCl, 0.1% SDS, 1% Triton X-100, protease inhibitor cocktail (Roche Diagnostics, Indianapolis, IN) and phosphatase inhibitor cocktail (Roche Diagnostics). Mouse heart tissues were homogenized in modified RIPA buffer with 2% SDS. Lysates were clarified by centrifugation at 15,000xg for 15 min at 4°C, and the protein concentration was determined using DC protein assay (Bio-Rad, Hercules, CA). Samples comprising 15 µg of protein were mixed with Laemmli sample buffer, boiled, then subjected to SDS-PAGE followed by transfer onto PVDF membranes for immunoblotting. Full-length Atf6 (p90) was detected with an antibody from SAB Signalway Antibody (1:1000, cat# 32008, College Park, MD), while active Atf6 (p50) was detected with an antibody from Proteintech (1:1000, cat# 24169-1-AP, Rosemont, IL). Other antibodies used include: anti-KDEL antibody (1:8,000, cat# ADI-SPA-827 , Enzo Life Sciences, Farmingdale, NY), which was used to detect GRP78, anti-IRE1 (1:500, cat# sc-390960, Santa Cruz), anti-XBP1s (1:1000, cat# 619502, BioLegend, San Diego, CA), anti-phospho-PERK (1:1000, cat# 3179, Cell Signaling), anti-PERK

(1:1000, cat# 3192, Cell Signaling), anti-Gapdh (1:25000, cat# G109a, Fitzgerald Industries International Inc.), anti-β-actin (1:1000, cat# sc-47778, Santa Cruz), and anti-FLAG (1:3,000, cat#F1804, Sigma-Aldrich, St. Louis, MO). The following antibodies were purchased from Cell Signaling (Danvers, MA): anti-RHEB (1:1,000, cat#13879s), anti-Phospho-mTOR (Ser2448, 1:1,000, cat#2971s), anti-mTOR (1:1,1000, cat#2972s), anti-Phospho-AKT (Ser473, 1:1,000, cat#9271s), anti-Phospho-ATK (Thr308, 1:1000, cat#13038s), anti-AKT (1:1,000, cat#9272s), anti-Phospho-S6K (1:1,000, cat#9205s), anti-S6K (1:1,000, cat#9202s), anti-Phospho-4EBP (1:1,000, cat#2855s), anti-4EBP (1:1,000, cat#9452s), anti-Phospho-TSC2 (Thr1462, 1:1000, 3617s), anti-TSC2 (1:1000, 3990s), anti-Phospho-ERK1/2 (Thr202/Tyr204, 1:1000, 9101s), and anti-ERK1/2 (1:1000, 9102s).

3.2.5. Adenovirus

Recombinant adenoviruses (AdV) encoding 3XFLAG-tagged constitutively active ATF6, ATF6α(1-373), 3XFLAG-tagged transcriptionally dead ATF6, ATF6α(94-373), and 3XFLAG-tagged full-length inactive ATF6, ATF6α(1-670) were generated using AdEasy system essentially as previously described[7]. Transduction of NRVM was performed by incubating cultures for 5 hours with the appropriate AdV at a multiplicity of infection of one.

3.2.6. Plasmid transfection

Transfection of plasmids into NRVM was achieved using electroporation as previously described[8]. Briefly, 1 million NRVM were suspended in 300 µl DMEM/F12 supplemented with BSA (1 mg/ml) and mixed with 10 µg of CMV-Flag-Rheb (AddGene plasmid #19996), or a Rheb promoter-luciferase construct of choice (see below), or an empty vector control plasmid. Subsequently, each mixture was then electroporated in a Bio-Rad gene pulser at 500 V, 25 microfarads, 100 Ω in a 0.2 cm gap cuvette. Transfected NRVM viability is approximately 50% and were then plated into four-chamber Lab Tek chamber slides at 0.75x10^{5} NRVM per 2 cm^{2} chamber.

3.2.7. Rheb promoter-luciferase constructs

The promoter region of the rat RHEB gene spanning nucleotides -1067 to +123 was amplified by PCR using ggatcgacgcgtcagtacgcctgttgcagaaa as the forward primer, which introduced an MluI site (underlined) just 5' of rat RHEB -1067, and ggatcgctcgagcttggtagcCTgGTCAGC as the reverse primer, which introduced an Xho1 site (underlined) just 3' of rat RHEB +123. Upper case nucleotides match those in the rat RHEB gene. The amplified product was then cloned into pGL2p to generate rat-RHEB(-1067/+123)-Luc. Truncated versions of rat-RHEB luciferase were cloned into pGL2p using a similar strategy and the same reverse primer coupled with the following forward primers: ggaacgacgcgtTCACCACCCACACTAAGC (-723), and ggaacgacgcgtGAACAGTGTCTCTCCTTGGC (-390) to generate rat-RHEB(-723/+123)-Luc and rat-RHEB(-390/+123)-Luc, respectively. Upper case nucleotides of these primers correspond to rat RHEB gene sequences. Informatics analyses identified putative ER stress response elements in the rat RHEB gene at nucleotide positions -754 to -736 and -628 to -610 in the rat RHEB gene, which we called ERSE-2 and ERSE-1, respectively. These elements in rat-RHEB(-1067/+123)-Luc were mutated by site-directed mutagenesis in ways predicted to ablate ATF6 binding using RHEB-ERSE-2 mut sense primer,

CCCACAGTTCCTCAGaacatAATAAAGCTTAGTCAC

and RHEB-ERSE-2 mut antisense primer,

GTGACTAAGCTTTATTatgttCTGAGGAACTGTGGG

RHEB-ERSE-1 mut sense primer,

GCCCGTCAGCTAGGGaacatCGCCTCACGCC, and

RHEB-ERSE-1 mut antisense primer,

GGCGTGAGGCGatgttCCCTAGCTGACGGGC.

PCR-based mutagenesis was performed using the QuikChange XL Site-Directed Mutagenesis Kit (Agilent Technologies, Santa Clara, CA). Lower case letters represent mutated nucleotides; upper case letters represent nucleotides that are identical to those in the rat RHEB gene. Plasmids were transfected into NRVM and luciferase activity was determined as previously described[2].

3.2.8. Luciferase reporter assay

Luciferase reporter assays were performed as previously described[2]. Briefly, suspended NRVMs were co-transfected by electroporation with Rheb promoter-luciferase constructs described above, human-Hspa5(-284/+221), or rat-Catalase(-1161/+131) promoter-luciferase constructs previously described[2, 9] along with pCH110 plasmids encoding SV40-beta-galactosidase and pGL2B, as described previously[10]. NRVMs were plated overnight and then infected with different forms of AdV-ATF6 or subjected to respective experimental paradigms. NRVMs were lysed after 48 h, and the activities of luciferase and beta-galactosidase were measured using an Optocompt II luminometer (MGM Instruments, Hamden, CT).

3.2.9. Small interfering RNA (siRNA) transfection

Transfection of siRNA into NRVM was achieved using HiPerfect Transfection Reagent (Qiagen, Valencia, CA) following the vendor's protocol as previously described[2]. Briefly, NRVM culture medium was replaced with DMEM/F12 supplemented with 0.5% FBS without antibiotics, 120 nM siRNA, and 1.25 µl HiPerfect / 1 µl siRNA, then incubated for 16 hours, after which the culture medium was replaced with DMEM/F12 supplemented with BSA (1 mg/ml) for an additional 48 hours. The following targeting siRNAs were used: rat ATF6 (assay ID# RSS315363, Stealth siRNA, Thermo Fisher), rat RHEB (assay ID# RSS352522, Stealth siRNA, Thermo Fisher), rat PERK (assay ID# s132055, Silencer Select siRNA, Thermo Fisher), and rat IRE1 (assay ID# RSS363210, Stealth siRNA, Thermo Fisher). A non-targeting sequence (cat# 12935300, Thermo Fisher) was used as a control siRNA.

3.2.10. Immunocytofluorescence (ICF) and immunohistochemistry

NRVM were plated on fibronectin and laminin-coated glass chamber slides, respectively as previously described[2]. Briefly, cells were fixed with 4% paraformaldehyde, followed by permeabilization with 0.5% Triton-X. Adult mouse hearts were paraffin-embedded after fixation in neutral buffered 10% formalin via abdominal aorta retroperfusion as previously described[3]. Primary antibodies used were anti-α-actinin (1:200, cat# A7811, Sigma-Aldrich), anti-FLAG (1:200, cat#F1804, Sigma-Aldrich), and anti-laminin (1:30, cat# L9393, Sigma-Aldrich). Slides were incubated with appropriate fluorophore-conjugated secondary antibodies (1:100, Jackson ImmunoResearch Laboratories, West Grove, PA) followed by nuclei counter stain Topro-3 (1:1000, Thermo Fisher). To validate specificity of FLAG staining, NRVM were transfected with an empty vector plasmid and co-stained with the FLAG antibody as represented in the respective figures. Images were obtained using laser scanning confocal microscopy on an LSM 710 confocal laser scanning microscope (Carl Zeiss, Oberkochen, Germany).

3.2.11. Quantitative real-time PCR (qRT-PCR)

Total RNA was isolated from NRVM or mouse hearts as previously described[3] using Quick-RNA MiniPrep kit (Zymo Research, Irvine, CA) or RNeasy Mini kit (Qiagen), respectively. cDNA synthesis was performed using SuperScript III First-Strand Synthesis System (Thermo Fisher). qRT-PCR was performed using Maxima SYBR Green/ROX qPCR Master Mix in a StepOnePlus RT-PCR System (Thermo Fisher). All qPCR probes were obtained from Integrated DNA Technologies, as previously described[2, 6]. Rheb-specific qPCR primers are listed below:

Gene (rat)	Forward Primer	Reverse Primer
Rheb - 1	CAGCAGGGCAGGATGAATA	GCTTGCCGTGGATAACTTTAAT
Rheb - 2	AAGATGCCTCAGTCCAAGTC	GATCAGCTTGGTGAATGTGTTT
Gene (mouse)		
Rheb - 1	CCATGGCAAGTTGTTGGATATG	TCTTCATAGCTGATCACCCTTTC
Rheb - 2	ACGTCTGACTCTGTCCAAATG	TGCCAACAGGAGGCAATAA

3.2.12. Adeno-Associated virus serotype 9 (AAV9)

The plasmid encoding the human cardiac troponin T promoter driving Cre-recombinase was provided as a gift from Dr. Oliver Muller[9]. AAV9 preparation was carried out as previously described[2]. Non-anesthetized 8-week old ATF6$^{fl/fl}$ mice were injected with 100 μL of AAV9-control or AAV9-cTnT-Cre containing $1x10^{11}$ viral particles via the lateral tail vein using a 27-guage syringe and housed for 2 weeks before either sacrifice or experimental initiation. To generate AAV9-FLAG-Rheb, a plasmid encoding FLAG-Rheb was obtained from Addgene (Addgene 19996). The region of this construct containing FLAG-Rheb was excised with EcoR1 and Xho1, then, after addition of an EcoR1/Nhe1 linker, it was ligated into the Nhe1 and Xho1 sites of the AAV shuttle vector, pTRUF-CMVenhMLC800. AAV9 were then prepared and administered as previously described in accordance with the respective experimental paradigms[2].

3.2.13. Chromatin immunoprecipitation (ChIP)

ChIP assays were performed essentially as previously described[2, 11]. Briefly, AdV-Con, AdV-FLAG-ATF6(1-373), or AdV-FLAG-ATF6(1-670) infected NRVM were treated with fixing buffer (50 mM HEPES-KOH, pH 7.5, 100 mM NaCl, 1 mM EDTA, 0.5 mM EGTA, and 1% formaldehyde) for 10 min, quenched with 125 mM glycine, and scraped into ice-cold PBS. Cells were centrifuged, resuspended in lysis buffer (50 mM HEPES, pH 7.9, 140 mM NaCl, 1 mM EDTA, 10% glycerol, 0.5% NP-40, 0.25% Triton X-100, and protease inhibitor cocktail), and incubated on ice for 10 min. After centrifugation at 1,800 x g for 10 min, the pellets were washed with buffer containing 10 mM Tris, pH 8.1, 200 mM NaCl, 1 mM EDTA, and 0.5 mM EGTA, resuspended in shearing buffer (0.1% SDS, 1 mM EDTA, and 10 mM Tris, pH 8.1), and then transferred to microTUBEs (Covaris, Woburn, MA). Chromatin was sheared by sonication for 15 min using an M220 focused ultrasonicator (Covaris). Triton X-100 and NaCl were added to the final concentration of 1% Triton and 150 mM NaCl followed by centrifugation at 16,000 x g for 10 min. Immunoprecipitation was performed by incubated 140 μl of sheared chromatin with 5 μg of anti-FLAG antibody (cat# F1804, Sigma-Aldrich) and 260 μl of immunoprecipitation buffer (0.1% SDS, 1 mM EDTA, 10 mM Tris, pH 8.1, 1% Triton X-100, and 150 mM NaCl) at 4°C overnight. Protein A/G magnetic beads (5 μl, BcMag, Bioclone, San Diego, CA) were added to the mixtures and incubated at 4°C for 1.5 h. Magnetic beads were sequentially washed with low salt wash buffer (0.1% SDS, 1% Triton X-100, 2 mM EDTA, 20 mM HEPES-KOH, pH7.9, and 150 mM NaCl), high salt wash buffer with 500 mM NaCl, LiCl wash buffer (100 mM Tris-HCl, pH 7.5, 0.5 M LiCl, 1% NP-40, and 1% deoxycholate acid), and TE buffer (10 mM Tris-HCl, pH 8.0 and 0.1 mM EDTA). Immune complexes were eluted by incubating beads with proteinase K digestion buffer (20 mM HEPES, pH 7.9, 1 mM EDTA, 0.5% SDS, and 0.4 mg/ml proteinase K) at 50°C for 15 min. Formaldehyde crosslinking was reversed by incubating with 0.3 M NaCl and 0.3 mg/ml RNase A at 65°C overnight. Samples were further incubated with 550 μg/ml proteinase K at 50°C for 1h. DNA was purified using NucleoSpin Gel and PCR Clean-up Kit (Macherey-Nagel, Bethlehem, PA) and eluted by 30 μl of water. Two μl of DNA was used for qRT-PCR analysis with primers targeting rat Rheb ERSE-1 (5'-CTGCACAGATTCCATTCTTCCC-3' and 5'-TGTCTATACTTTAAATT-3'), rat Rheb ERSE-2 (5'-TGACAGCCAACCTACAGCC-3' and 5'-GAAGCGCGGTCATTGGTG-3'), rat Hspa5 (5'-GGTGGCATGAACCAACCAG-3' and 5'-GCTTATATATCCTCCCCGC-3'), rat Cat (5'-CTACCCACCAATTAGTACCAAATAA-3' and 5’-AGAAGGGACAGGATTGGAAG-3’), rat Pdia6 ERSE (5’-CACATGAGCGAAATCCACAGA-3’ and 5’-ACTAGTCGAGCCATGCTGAT-3’), rat HO-1 (5’-GGGCTACTCCCGTCTTCCTG-3’ and 5’-CCTTTCCAGAACCCTCTACTCTACTC-3’), or rat Gapdh (5’-ATGCGGTTTCTAGGTTCACG-3’ and 5’-ATGTTTTCTGGGGTGCAAAG-3’). Pdia6 served as a positive control for a known ATF6 target gene in cardiac myocytes while HO-1 and Gapdh served as negative controls. ChIP signals obtained from the qRT-PCR were normalized to the input DNA.

3.2.14. ^{3}H-Leucine incorporation and trichloroacetic acid precipitation of protein

NRVM ^{3}H-Leucine incorporation was performed as previously described[6]. Briefly, NRVM were plated at a density of 2.5 x 10^5 cells/well on 12-well plastic culture plates. After 48 hours of serum starvation in DMEM/F-12, NRVM culture media was replaced with DMEM/F12 supplemented with BSA (1 mg/ml) containing either control, phenylephrine (50 µM), IGF1 (100ng/ml), or Lonafarnib (2 µM) for an additional 48 hours. To this media was added 1 µCi of ^{3}H-Leucine (PerkinElmer NET460A001MC L-[3,4,5-^{3}H(N)]-Leucine, 100 to 150 Ci/mmol). After 48 hours, the media was removed, cultures were washed 3 times with 1 ml DMEM/F-12 and cells were subsequently scraped from culture dishes with 0.5 ml of 25% trichloroacetic acid and transferred to 1.5 ml microcentrifuge tubes. Protein precipitation was induced using 50 µl of a 10mg/ml solution of BSA and samples were allowed to freeze overnight. Upon thawing, precipitates were collected by centrifugation at 4˚C at ~20,000xg for 20 minutes. Supernatants were removed by manual aspiration and precipitated protein dissolved in 200 µl of base buffer (1% Triton X-100, 1M NaOH) at 37˚C for two hours. Radioactivity in solubilized material was quantified by scintillation counting in glass scintillation vials using 180 µl of solubilized protein into 10 ml of Ecoscint scintillation fluid. Each vial was counted for a minimum of 2 minutes with at least six separate myocyte cultures per treatment.

3.2.15. Cultured cardiac myocyte area

NRVM (minimum of n=3 cultures per treatment) were visualized by phase-contrast microscopy and images were obtained with an IX70 fluorescence microscope (Olympus, Melville, NY) as previously described[6]. Cell surface area was determined using NIH Image J software from a minimum of 100 cells per image using three separate fields from each cell culture.

3.2.16. Transverse aortic constriction

Transverse aortic constriction (TAC) was performed as previously described[6]. Briefly, adult male mice were anesthetized using a 2% isofluorane/O_2 mixture and intubated. Mice were treated with buprenorphine (0.1 mg/kg IP) and a partial trans-sternal thoracotomy performed using aseptic technique. An approximately 1.5 cm vertical left parasternal skin incision was made, underlying pectoralis muscle retracted, and the chest cavity entered through the fourth intercostal space. Using hooked retractors, adjacent ribs were retracted to expose the heart and aortic arch. The aorta was isolated from annexed tissue, and the artery partially ligated between the innominate and left common carotid arteries with 6-0 silk. The calibrated constriction of the aorta was performed by placing a dull 27-gauge needle to the side of the artery, the ligature tied firmly to both the needle and the artery, and, subsequently, the needle was removed leaving a calibrated stenosis of the aorta. Sham operated mice were exposed to the same procedure, except that the aorta was not constricted. The thoracic cavity was closed and the animals were allowed to recover. Animals were injected once with buprenorphine (0.1 mg/kg IP) about 12 h after recovery in order to reduce any post-operative discomfort. In case any animals displayed signs of pain or distress after this period, additional doses of buprenorphine were administered as needed. Immediately prior to sacrifice, animals were anesthetized and constriction levels were quantified by measuring alterations in Doppler velocities of the innominate and left carotid arteries 7 days post-TAC, as previously described[12]. Mean carotid peak blood flow velocities were determined using a 20 MHz Doppler probe (Indus Instruments, Houston, TX) and ratios of innominate (RC) to left carotid (LC) were determined to evaluate consistency across animals in both SHAM and TAC groups. Just prior to sacrifice, post-TAC, animals were anesthetized and 0.5 mL of arterial blood were obtained via inferior vena cava puncture. Blood was placed in heparin- and EDTA-coated vacutainer (BD Vacutainer) and centrifuged at 3000 rpm for 10 minutes and plasma samples were analyzed for cardiac troponin I with a Mouse cTnI High-Sensitivity ELISA kit (Life Diagnostics, Inc.). A calcineurin phosphatase activity assay was performed using a calcineurin tissue extract assay kit (cat#BML-AK816-0001, Enzo Life Sciences) according to the manufacturer’s protocol. Briefly, free phosphate was removed from LV tissue extracts by passing through a desalting column and calcineurin phosphatase activity was measured spectrophotometrically by detecting free phosphate released from the synthetic RII phosphopeptide.

3.2.17. Free-wheel exercise protocol

Free-wheel exercise protocol was performed as previously described[13]. Briefly, adult male mice were housed individually in cages containing rodent exercise wheels of a 5.356 in diameter (Model InnoWheel, BioServe) and provided with food and water *ad libitum*. The wheels were equipped with a digital magnetic counter to record revelations of the wheel during bouts of exercise. Sedentary mice were maximally house and provided with food and water *ad libitum* in cages not equipped with exercise wheels.

3.2.18. Transthoracic echocardiography

Transthoracic echocardiography was performed using an ultrasound imaging system (Vevo 2100 System, Fujifilm VisualSonics, Toronto, Ontario, Canada) as described[2].

3.2.19. Transcript profiling and bioinformatics

ATF6 TG and non-transgenic littermates were treated with tamoxifen (10 mg/kg IP) daily for 5 days as previously described[14]. Total RNA was isolated from mouse left ventricular extracts and RNA sequencing was carried out on Illumina Nextseq at CellNetworks Deep Sequencing Core Facility at Heidelberg University. Sequencing adapter residues and low quality bases were removed from raw sequencing reads prior to all other analysis steps using Flexbar version 3.0.3[15]. Subsequently, reads mapping to known ribosomal RNA species were excluded from further analyses using Bowtie2 version 2.3.0 with a custom rRNA-index and only keeping non-aligning reads[16]. Principal read mapping against the mouse reference genome (mm10, ENSEMBL build 85) was performed with the STAR aligner, version

2.5.3a[17]. The read-to-transcript assignment was carried out using the R package Rsubread version 1.24.2[18] and the ENSMBL gene annotation mm10/build85. The resulting count table was further processed with the edgeR R package[19] to construct the list of differentially expressed genes. The final heatmap was generated using the pheatmap R package version 1.0.10[20].

3.2.20. Statistics

For studies involving induction of myocardial hypertrophy through surgical TAC, cohort sizes were based on a predictive power analysis to achieve 5% error and 80% power using G*Power 3.1.9.3. Cell culture experiments were performed with at least three cultures for each treatment. Shapiro-Wilk tests were performed to examine data normality. Two-group comparisons were performed using Student's two-tailed t-test, and all multiple group comparisons were performed using a one-way ANOVA with a Newman-Keuls post-hoc analysis. All analyses were performed using Prism 7.0e. mRNA and protein expression levels were normalized to either glyceraldehyde 3-phosphate dehydrogenase (GAPDH) or β-Actin. Where appropriate, a linear transformation was performed to set the result of control group (usually Con Sham) to 1, by dividing each group with the average obtained for their control group. Data are represented as mean with all error bars indicating ± SEM. $^{*}P<0.05$, $^{**}P<0.01$, $^{\#}P<0.001$.

3.2.21. References

1. 1. Engin F, Yermalovich A, Nguyen T, Hummasti S, Fu W, Eizirik DL, Mathis D and Hotamisligil GS. Restoration of the unfolded protein response in pancreatic beta cells protects mice against type 1 diabetes. *Sci Transl Med*. 2013;5:211ra156.

2. 2. Jin JK, Blackwood EA, Azizi K, Thuerauf DJ, Fahem AG, Hofmann C, Kaufman RJ, Doroudgar S and Glembotski CC. ATF6 Decreases Myocardial

Ischemia/Reperfusion Damage and Links ER Stress and Oxidative Stress Signaling Pathways in the Heart. *Circ Res*. 2017;120:862-875.

3. 3. Niessner H, Beck D, Sinnberg T, Lasithiotakis K, Maczey E, Gogel J, Venturelli S, Berger A, Mauthe M, Toulany M, Flaherty K, Schaller M, Schadendorf D, Proikas-Cezanne T, Schittek B, Garbe C, Kulms D and Meier F. The farnesyl transferase inhibitor lonafarnib inhibits mTOR signaling and enforces sorafenib-induced apoptosis in melanoma cells. *J Invest Dermatol*. 2011;131:468-79.

4. 4. Volkers M, Toko H, Doroudgar S, Din S, Quijada P, Joyo AY, Ornelas L, Joyo E, Thuerauf DJ, Konstandin MH, Gude N, Glembotski CC and Sussman MA. Pathological hypertrophy amelioration by PRAS40-mediated inhibition of mTORC1. *Proc Natl Acad Sci U S A*. 2013;110:12661-6.

5. 5. Park CS, Cha H, Kwon EJ, Sreenivasaiah PK and Kim DH. The chemical chaperone 4-phenylbutyric acid attenuates pressure-overload cardiac hypertrophy by alleviating endoplasmic reticulum stress. *Biochem Biophys Res Commun*. 2012;421:578-84.

6. 6. Doroudgar S, Volkers M, Thuerauf DJ, Khan M, Mohsin S, Respress JL, Wang W, Gude N, Muller OJ, Wehrens XH, Sussman MA and Glembotski CC. Hrd1 and ER-Associated Protein Degradation, ERAD, are Critical Elements of the Adaptive ER Stress Response in Cardiac Myocytes. *Circ Res*. 2015;117:536-46.

7. 7. Thuerauf DJ, Hoover H, Meller J, Hernandez J, Su L, Andrews C, Dillmann WH, McDonough PM and Glembotski CC. Sarco/endoplasmic reticulum calcium ATPase-2 expression is regulated by ATF6 during the endoplasmic reticulum stress response: intracellular signaling of calcium stress in a cardiac myocyte model system. *J Biol Chem*. 2001;276:48309-17.

8. 8. Zechner D, Craig R, Hanford DS, McDonough PM, Sabbadini RA and Glembotski CC. MKK6 activates myocardial cell NF-kappa B and inhibits apoptosis in a p38 mitogen-activated protein kinase-dependent manner. *Journal of Biological Chemistry*. 1998;273:8232-8239.

9. 9. Doroudgar S, Thuerauf DJ, Marcinko MC, Belmont PJ and Glembotski CC. Ischemia activates the ATF6 branch of the endoplasmic reticulum stress response. *J Biol Chem*. 2009;284:29735-45.

10. 10. Thuerauf DJ, Hoover H, Meller J, Hernandez J, Su L, Andrews C, Dillmann WH, McDonough PM and Glembotski CC. Sarco/endoplasmic reticulum calcium ATPase-2 expression is regulated by ATF6 during the endoplasmic reticulum stress response - Intracellular signaling of calcium stress in a cardiac myocyte model system. *Journal of Biological Chemistry*. 2001;276:48309-48317.

11. 11. Vekich JA, Belmont PJ, Thuerauf DJ and Glembotski CC. Protein disulfide isomerase-associated 6 is an ATF6-inducible ER stress response protein that protects cardiac myocytes from ischemia/reperfusion-mediated cell death. *J Mol Cell Cardiol*. 2012;53:259-67.

12. 12. Reynolds JO, Quick AP, Wang Q, Beavers DL, Philippen LE, Showell J, Barreto-Torres G, Thuerauf DJ, Doroudgar S, Glembotski CC and Wehrens XH. Junctophilin-2 gene therapy rescues heart failure by normalizing RyR2-mediated Ca2+ release. *Int J Cardiol*. 2016;225:371-380.

13. 13. Volkers M, Toko H, Doroudgar S, Din S, Quijada P, Joyo AY, Ornelas L, Joyo E, Thuerauf DJ, Konstandin MH, Gude N, Glembotski CC and Sussman MA. Pathological hypertrophy amelioration by PRAS40-mediated inhibition of mTORC1. *Proc Natl Acad Sci U S A*. 110:12661-6.

14. 14. Martindale JJ, Fernandez R, Thuerauf D, Whittaker R, Gude N, Sussman MA and Glembotski CC. Endoplasmic reticulum stress gene induction and protection from ischemia/reperfusion injury in the hearts of transgenic mice with a tamoxifen-regulated form of ATF6. *Circ Res*. 2006;98:1186-93.

15. 15. Roehr JT, Dieterich C and Reinert K. Flexbar 3.0 - SIMD and multicore parallelization. *Bioinformatics*. 2017;33:2941-2942.

16. 16. Langmead B and Salzberg SL. Fast gapped-read alignment with Bowtie 2. *Nat Methods*. 2012;9:357-9.

17. 17. Dobin A, Davis CA, Schlesinger F, Drenkow J, Zaleski C, Jha S, Batut P, Chaisson M and Gingeras TR. STAR: ultrafast universal RNA-seq aligner. *Bioinformatics*. 2013;29:15-21.

18. 18. Liao Y, Smyth GK and Shi W. The Subread aligner: fast, accurate and scalable read mapping by seed-and-vote. *Nucleic Acids Res*. 2013;41:e108.

19. 19. Robinson MD, McCarthy DJ and Smyth GK. edgeR: a Bioconductor package for differential expression analysis of digital gene expression data. *Bioinformatics*. 2010;26:139-40.

20. 20. Kolde R. Pheatmap: pretty heatmaps. R Packag. version 61. 2012.

3.3. Results

3.3.1. ATF6 is required for cardiac myocyte hypertrophy in response to pressure overload

To examine the role of *Atf6* in cardiac myocytes on heart growth, we generated an *Atf6* conditional knockout mouse (ATF6 cKO) by injecting *Atf6*$^{fl/fl}$ mice with a recombinant AAV9 that encodes *Cre* under the control of the *cardiac troponin T* promoter **(Fig. 3.1A)**. Compared to *Atf6*$^{fl/fl}$ injected with AAV9-Con, injection with AAV9-CRE effectively reduced *Atf6* mRNA from cardiac myocytes isolated from *Atf6*$^{fl/fl}$ mice, but not non-cardiac myocytes, or liver **(Fig. 3.1B)**. *Atf6*$^{fl/fl}$ mice injected with AAV9-Con (Con) or AAV9-CRE (ATF6 cKO), were subjected to TAC and examined 7d later, when hypertrophic growth is maximal[4] and structural remodeling is compensatory[5, 6]. TAC activated ATF6 in Con mouse hearts, as evidenced by increased levels of the active, 50 kD form of ATF6 **(Fig. 3.1C)**. This was unexpected, since ATF6 is not known to be activated in cardiac myocytes by any growth stimulus. Coordinate with ATF6 activation, TAC increased expression of numerous canonical ATF6 target genes **(Fig. 3.1C-D; Fig. 3.2A)**. As expected, ATF6 was undetectable in ATF6 cKO mouse hearts **(Fig. 3.1C-D)**. TAC increased Con mouse heart weights, but, surprisingly, this growth effect was significantly blunted in ATF6 cKO mouse hearts **(Fig. 3.1E)**. TAC increased *Nppa and Nppb* expression to similar extents in both Con and ATF6 cKO mice, while the induction of *Myh7* and *Col1a1* was slightly greater in the ATF6 cKO mice **(Fig. 3.1F)**. This, coupled with the decrease in *Atp2a2* i.e. *SERCA2a* in ATF6 cKO mice, suggests a blunted compensatory response in the absence of ATF6. In Con mouse hearts, cardiac function, including fractional shortening was preserved, while chamber dimensions were unchanged after TAC **(Fig. 3.1G; Table 3.1)** and cardiac myocyte size was increased **(Fig. 3.1H)**, consistent with the compensatory nature of cardiac hypertrophy in mice at this time after pressure overload[7]. However, in contrast to Con, in ATF6 cKO mice subjected to TAC myocyte size was decreased compared to Con **(Fig. 3.1H)** and fractional shortening was impaired **(Fig. 3.1G)** with increased chamber dimensions, such as LVEDV and LVESV, despite high frequency Doppler measurements between right and left carotid arteries demonstrating consistent and identical pressure overload in TAC-operated Con and ATF6 cKO mice **(Table 3.I)**. Along with increased plasma levels of cTnI **(Fig. 3.2B)**, these results are consistent with the initial stages of chamber dilation, as well as myocardial damage and decompensation in the ATF6 cKO mice. Thus, ATF6 is activated by pressure overload and is required for hypertrophy.

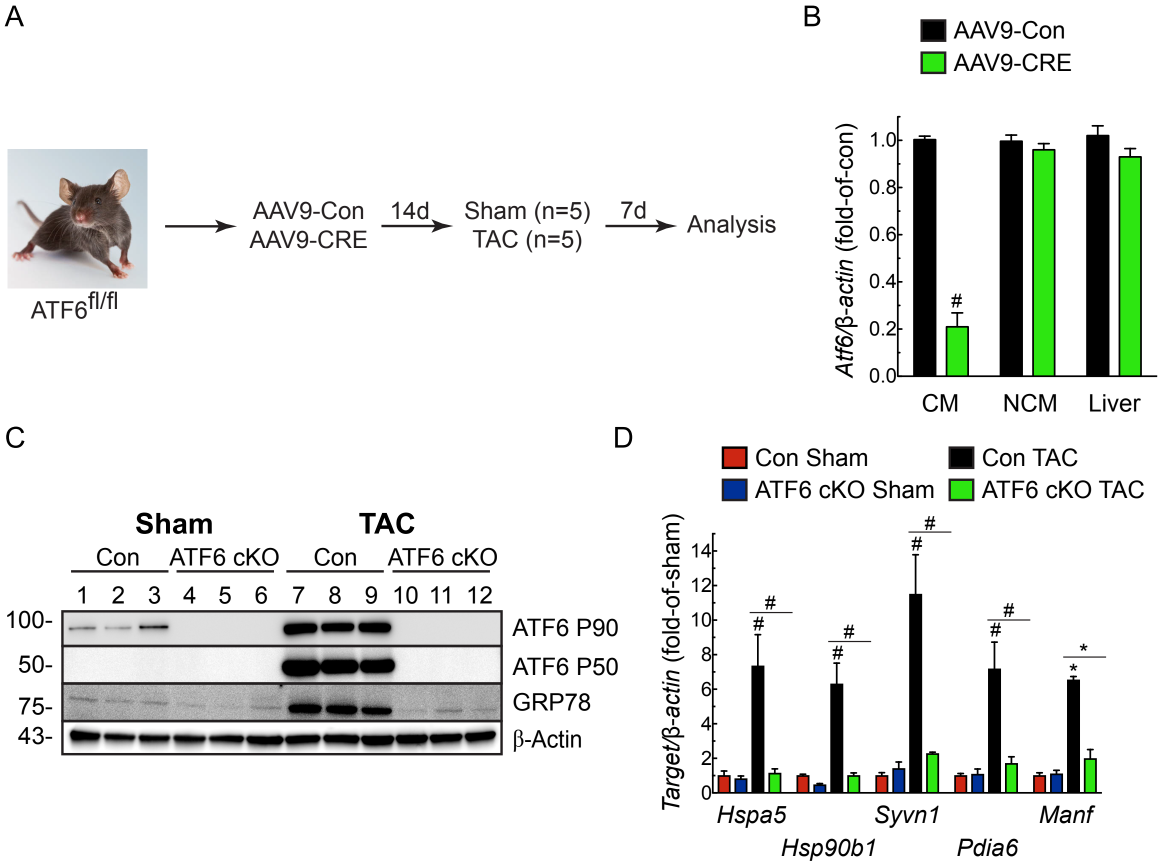

Figure 3.1- Effect of cardiac myocyte-specific ATF6 gene deletion in hearts of mice subjected to TAC.

A, Protocol for AAV9 administration to ATF6$^{fl/fl}$ mice and TAC. **B,** ATF6 mRNA levels determined by qRT-PCR on isolated cardiac myocytes (CM), non-cardiac myocytes (NCM), and liver extracts from ATF6$^{fl/fl}$ mice injected with AAV9-Con (Con) or AAV9-CRE (i.e. ATF6 cKO) n=3. **C,** Immunoblot of LV extracts from Con or ATF6 cKO mice. **D,** mRNA for ATF6 target genes determined by qRT-PCR. **E,** Heart weight/tibia lengths (HW/TL). **F,** mRNA levels for fetal genes determined by qRT-PCR. *Nppa* , natriuretic peptide A); *Nppb*, natriuretic peptide B); *Myh7*, β-myosin heavy chain; *Col1a1*, Collagen 1A1; *Atp2a2*, Serca2a. **G,** Fractional shortening (%), determined by echocardiography, see Online Table 3.1. **H,** Confocal immunocytofluorescence microscopy (ICF) analysis of mouse heart sections for laminin (green). Data are mean ± SEM. $^{*}P \leq 0.05$, $^{**}P \leq 0.01$, $^{\#}P \leq 0.001$ different from Con Sham, or from the value shown by the bar.

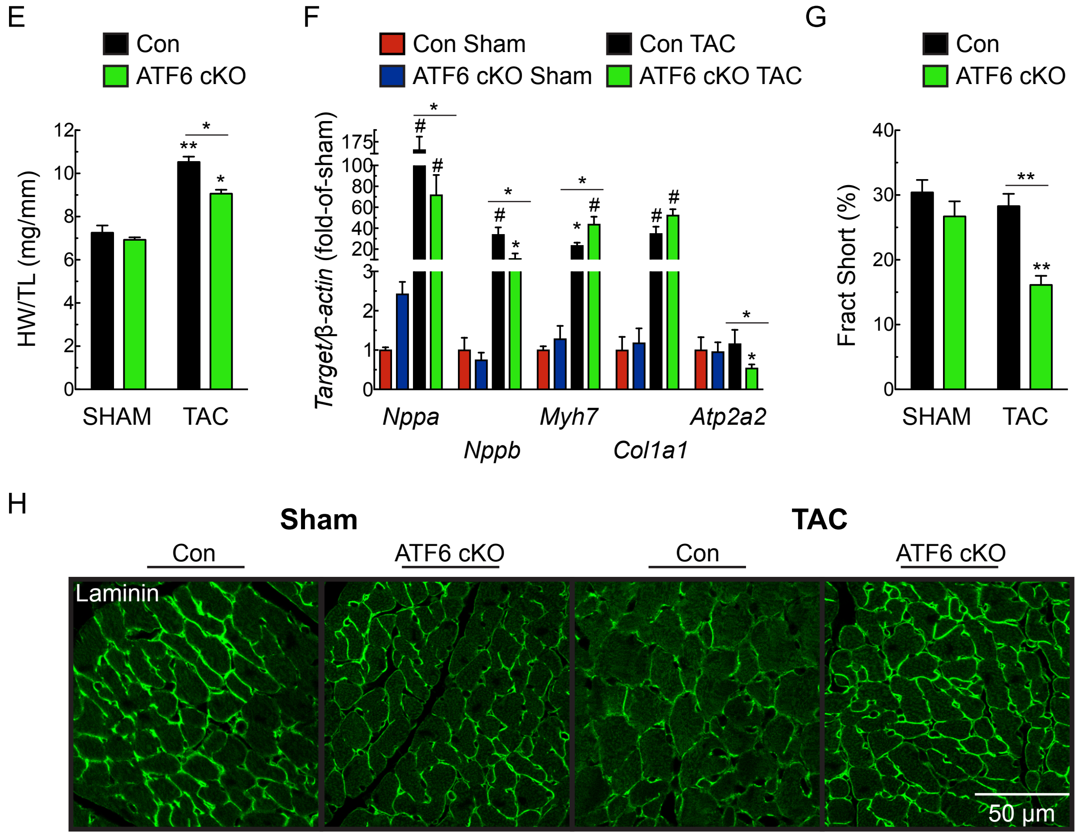

Figure 3.1 (continued)- Caption shown on previous page.

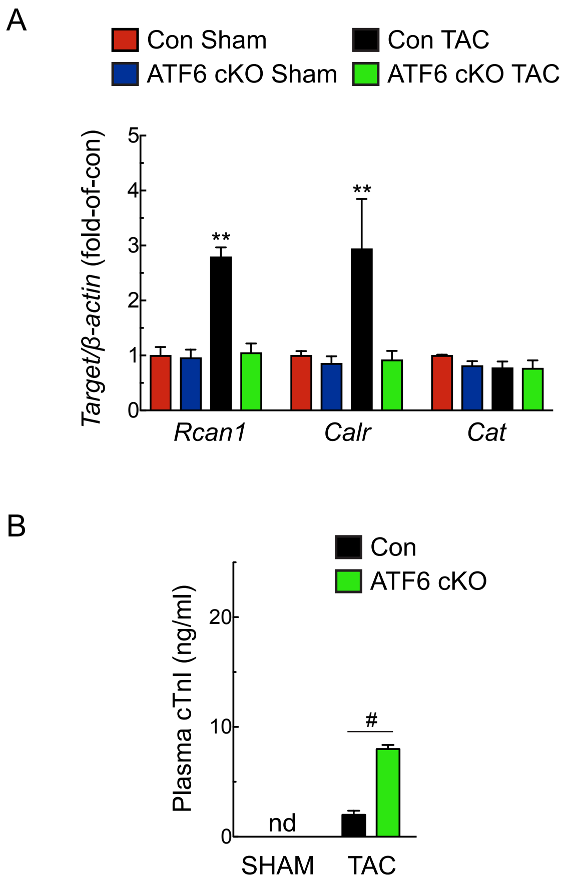

Figure 3.2- Effect of cardiac myocyte-specific *ATF6* gene deletion in mice subjected to TAC.

A, mRNA for ATF6 target genes was determined by qRT-PCR. **B,** Troponin I (cTnI) levels were measured in plasma samples collected from Con or ATF6 cKO mice. Data are represented as mean ± s.e.m. **P≤0.01, #P≤0.001.

Table 3.1- 7-day TAC echocardiographic parameters for Con and ATF6 cKO mice

	Con Sham (n = 5)	ATF6 cKO Sham (n = 5)	Con TAC (n = 5)	ATF6 cKO TAC (n = 6)
FS (%)	30.40±1.91	26.71±2.31	28.28±1.89	16.12±1.41[1,2]
EF (%)	58.60±2.72	52.64±3.72	55.46±2.86	34.30±2.74[1,2]
LVEDV (μl)	53.75±5.29	62.55±4.99	51.26±2.23	68.32±5.21[2]
LVESV (μl)	22.47±3.07	30.08±3.98	22.83±1.80	45.35±4.73[2]
LVIDD (mm)	3.56±0.15	3.80±0.13	3.51±0.06	3.95±0.13[2]
LVIDS (mm)	2.48±0.14	2.80±0.16	2.52±0.08	3.32±0.15[1,2]
PWTD (mm)	0.86±0.13	0.89±0.15	1.51±0.11[1]	1.01±0.10[2]
PWTS (mm)	1.17±0.10	1.04±0.12	1.76±0.10[1]	1.07±0.11[2]
AWTD (mm)	0.88±0.07	0.76±0.05	1.40±0.08[1]	0.97±0.07[1,2]
AWTS (mm)	1.08±0.04	1.02±0.08	1.72±0.03[1]	1.10±0.07[2]
HR (bpm)	519±13.27	540±2.63	524±3.71	523±13.47
DPLR (RC/LC)	0.91±0.05	1.11±0.08	4.56±0.25[1]	4.85±0.34[1]
HW (mg)	118.98±5.41	120.62±3.35	183.36±6.14[1]	154.08±3.09[1,2]
BW (g)	21.57±0.78	23.85±0.80	25.78±0.64[1]	24.43±0.59
TL (mm)	16.40±.0.24	17.40±0.24	17.40±0.24	17.00±0.00
HW/BW (mg/g)	5.53±0.27	5.06±0.08	7.12±0.20[1]	6.32±0.16[1,2]
HW/TL (mg/mm)	7.26±0.33	6.93±0.11	10.53±0.25[1]	9.06±0.18[1,2]

FS = fractional shortening
EF = ejection fraction
LVEDV = left ventricular end diastolic volume
LVESV = left ventricular end systolic volume
LVIDD = left ventricular inner diameter in diastole
LVIDS = left ventricular inner diameter in systole
PWTD = left ventricular posterior wall thickness in diastole
PWTS = left ventricular posterior wall thickness in systole
AWTD = left ventricular anterior wall thickness in diastole
AWTS = left ventricular anterior wall thickness in systole
HR = heart rate in beats per minute
DPLR = Doppler ratio of right carotid blood flow velocity to left carotid blood flow velocity
HW = heart weight
BW = body weight
TL = tibia length
HW/BW = heart weight/body weight
HW/TL = heart weight/tibia length

Statistical analyses used a one-way ANOVA with a Newman-Keuls post-hoc analysis.

[1] = $p \leq 0.05$ different from respective Sham

[2] = $p \leq 0.05$ different from Con TAC

3.3.2. ATF6 is required for cardiac myocyte hypertrophy in response to exercise

To assess the breadth of the impact of ATF6 on heart growth, we examined the effects of cardiac myocyte-specific ATF6 deletion in mice subjected to free-wheel exercise[8, 9] **(Fig. 3.3A)**. Similar to TAC, exercise surprisingly activated ATF6 and induced ATF6 target genes in Con, but not in ATF6 cKO mice **(Fig. 3.3B-C)**. As expected, compared to Con sedentary mice, Con mice subjected to exercise exhibited increased heart weights and LV wall thickness, as well as myocyte size **(Fig. 3.3D, 3.3F; Table 3.2)**. While *Nppa* and *Nppb* were mildly increased, *Atp2a2* was robustly increased by exercise in Con mouse hearts, and there was no change in *Myh7* or *Col1a1* **(Fig. 3.3E)**; this gene profile is typical of adaptive cardiac hypertrophy in exercising mice[7, 10]. In contrast to Con, in ATF6 cKO mice subjected to exercise there was no change in heart weights or LV wall thickness **(Fig. 3.3D; Table 3.2)**, reduced increases in myocyte size **(Fig. 3.3F)**, and reduced induction of ATF6 target genes **(Fig. 3.3C)**. Compared to exercised Con mice, exercised ATF6 cKO mice showed no increase in *Nppa*, and neither Con nor ATF6 cKO mice showed significant changes in *Nppb* or *Myh7*. Importantly, while Con mice exhibited decreased *Col1a1* and increased *Atp2a2* after exercise, which are beneficial genetic changes typical of this regime, the ATF6 cKO mice failed to adapt and had increased *Col1a1* and no change in *Atp2a2* **(Fig. 3.3E)**. Thus, ATF6 is activated by exercise and is required for compensatory hypertrophy in this exercise model.

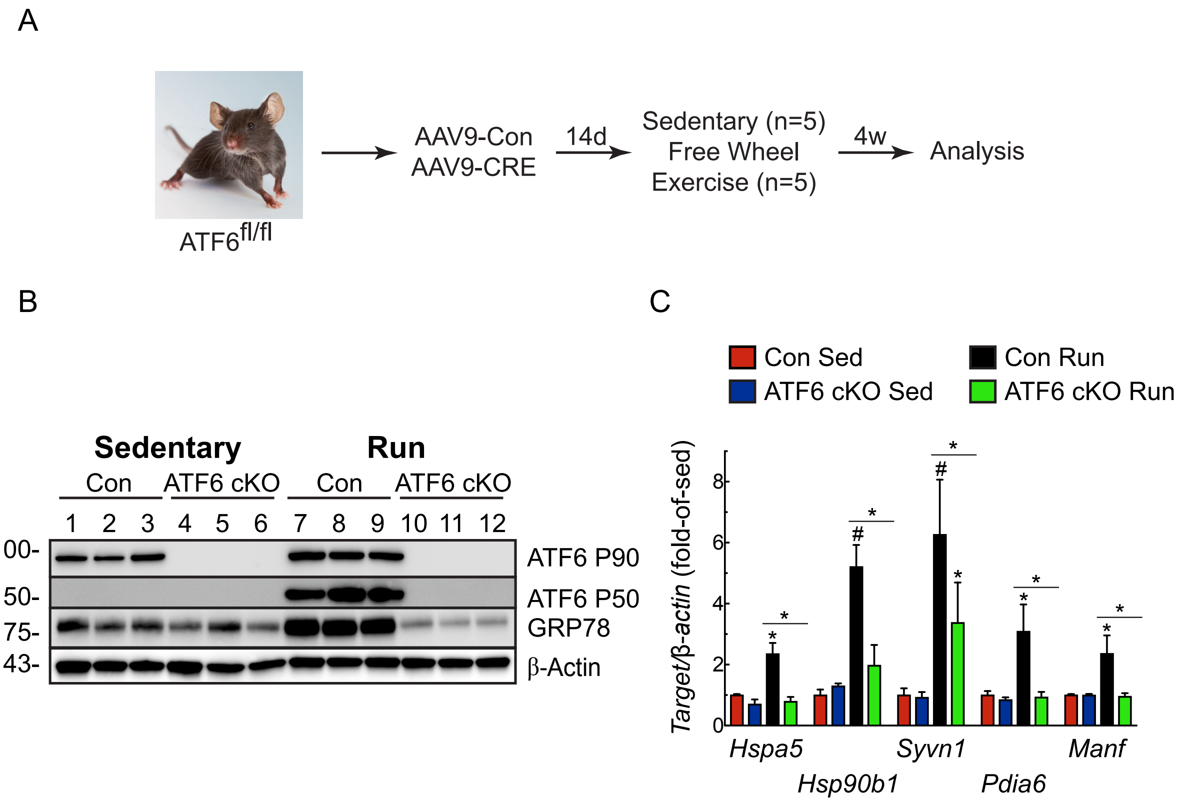

Figure 3.3- Effect of cardiac myocyte-specific ATF6 gene deletion in hearts of mice subjected to free wheel exercise.

A, Protocol for AAV9 administration to $ATF6^{fl/fl}$ mice and free wheel exercise. **B,** Immunoblot of LV extracts from Con or ATF6 cKO mice. **C,** mRNA levels for ATF6 target genes determined by qRT-PCR. **D,** Heart weights/tibia lengths (HW/TL). **E,** mRNA levels for fetal genes determined by qRT-PCR. **F,** ICF analysis of mouse heart sections for laminin (green). Data are mean ± SEM. $^{*}P \leq 0.05$, $^{**}P \leq 0.01$, $^{\#}P \leq 0.001$. Echocardiography details are in Table 3.2.

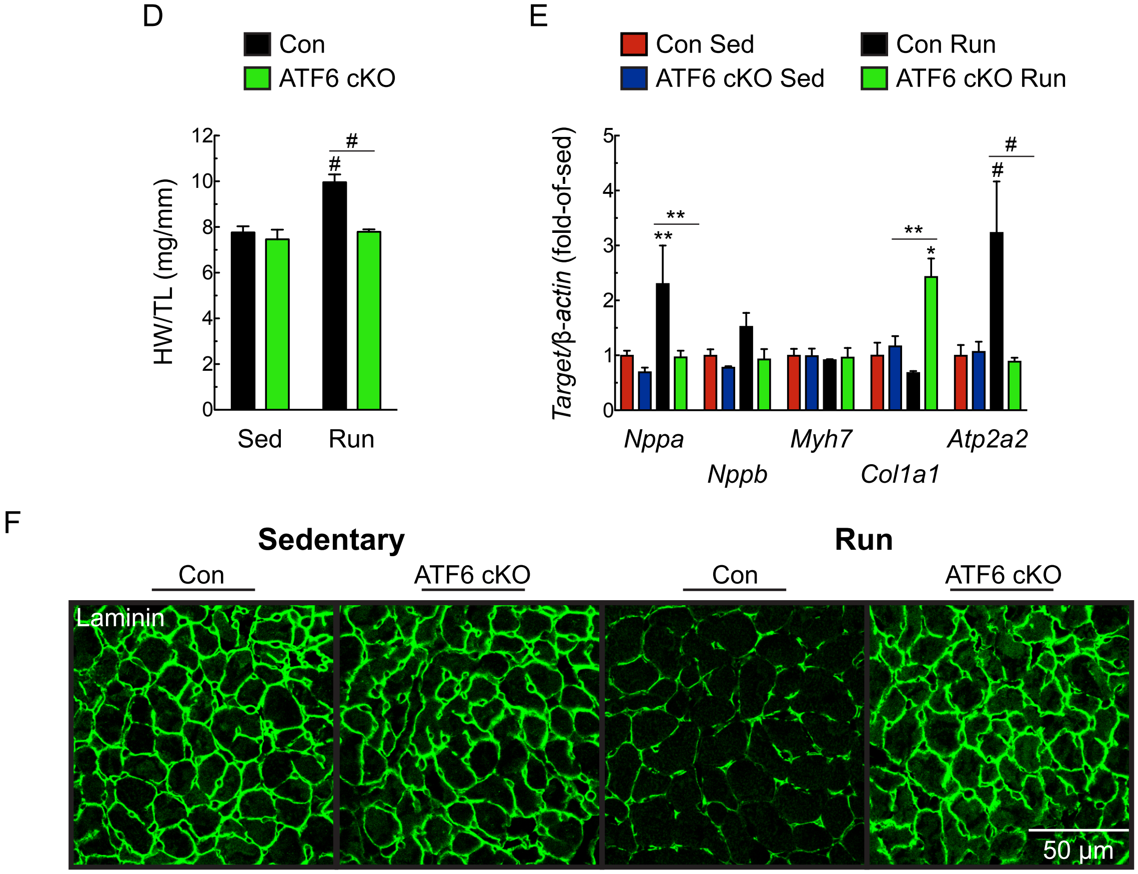

Figure 3.3 (continued)- Caption shown on previous page.

Table 3.2- 4-week Free Wheel echocardiographic parameters for Con and ATF6 cKO mice

	Con Sedentary (n = 5)	ATF6 cKO Sedentary (n = 5)	Con Run (n = 5)	ATF6 cKO Run (n = 5)
FS (%)	29.19±1.46	24.22±1.64	29.24±1.74	23.03±1.75[2]
EF (%)	56.42±2.33	48.55±2.70	57.06±2.74	46.53±3.00[2]
LVEDV (μl)	79.56±16.48	72.38±6.33	50.38±7.60	71.78±5.85[2]
LVESV (μl)	35.29±7.76	37.64±4.35	22.29±3.93	38.54±4.11[2]
LVIDD (mm)	4.13±0.40	4.04±0.15	3.44±0.24	4.03±0.14[2]
LVIDS (mm)	2.93±0.30	3.07±0.16	2.45±0.21	3.10±0.14[2]
PWTD (mm)	0.75±0.14	0.89±0.14	1.77±0.11[1]	0.79±0.03[2]
PWTS (mm)	1.08±0.08	1.21±0.15	2.06±0.08[1]	1.08±0.04[2]
AWTD (mm)	0.81±0.06	0.84±0.07	1.22±0.08[1]	0.96±0.09[2]
AWTS (mm)	1.11±0.03	1.14±0.05	1.48±0.07[1]	1.09±0.07[2]
HR (bpm)	491±9.28	500±9.36	506±9.11	556±8.70[1,2]
DIST (km/wk)	n/a	n/a	8.11±1.79	8.65±0.87
HW (mg)	132.02±4.51	128.32±7.28	171.16±5.24[1]	137.02±1.40[2]
BW (g)	27.23±0.51	25.14±0.90	24.80±0.66[1]	24.43±0.43
TL (mm)	17.00±0.00	17.20±0.20	17.20±0.20	17.60±0.24
HW/BW (mg/g)	4.85±0.14	5.09±0.16	6.90±0.13[1]	5.61±0.09[1,2]
HW/TL (mg/mm)	7.77±0.27	7.46±0.42	9.96±0.35[1]	7.79±0.11[2]

FS = fractional shortening
EF = ejection fraction
LVEDV = left ventricular end diastolic volume
LVESV = left ventricular end systolic volume
LVIDD = left ventricular inner diameter in diastole
LVIDS = left ventricular inner diameter in systole
PWTD = left ventricular posterior wall thickness in diastole
PWTS = left ventricular posterior wall thickness in systole
AWTD = left ventricular anterior wall thickness in diastole
AWTS = left ventricular anterior wall thickness in systole
HR = heart rate in beats per minute
DIST = average distance ran per week
HW = heart weight
BW = body weight
TL = tibia length
HW/BW = heart weight/body weight
HW/TL = heart weight/tibia length

Statistical analyses used a one-way ANOVA with a Newman-Keuls post-hoc analysis.

[1] = $p \leq 0.05$ different from respective Sedentary
[2] = $p \leq 0.05$ different from Con Run

3.3.3. Rheb is an ATF6-inducible gene in the heart

Since there are no known *Atf6*-inducible genes that are required for cardiac myocyte growth, we turned to transcript profiling for clues to the identities of such genes. RNA sequencing of the hearts of our previously published transgenic mice that express activated ATF6[11] revealed that ATF6 induced 51 genes in the gene ontology category, small GTPase mediated signal transduction; this category includes the ras-related small GTPase, Ras homologue enriched in brain (*RHEB*) **(Fig. 3.4A; Fig. 3.5A)**. Rheb is required for activation of mTORC1, however, only in the presence of a growth stimulus. Accordingly, we focused on *Rheb* as a candidate gene through which ATF6 might contribute to cardiac hypertrophy, pursuing the hypothesis that increased *Rheb* gene expression and subsequent mTORC1 activation under growth conditions are *Atf6*-dependent. The upregulation of *RHEB* by ATF6 in mouse hearts observed by RNA sequencing was confirmed by qRT-PCR **(Fig. 3.5B)**. Consistent with ATF6 as a possible transcriptional inducer of *Rheb* was our finding that the *Rheb* promoter has two potential ATF6 binding sites, which we call ER stress response elements (ERSEs)-1 and -2 **(Fig. 3.4B)**. Chromatin immunoprecipitation (ChIP) showed that ATF6 binds to both sites in the *RHEB* gene in neonatal rat ventricular myocytes (NRVM) **(Fig. 3.4C)**. The progressive decline in *RHEB* promoter activity in plasmids that encode 5’-truncation deletions of the rat *RHEB* promoter driving luciferase demonstrated the importance of these putative ERSEs in ATF6-mediated *RHEB* promoter activation **(Fig. 3.5C)**. To mechanistically investigate the functional involvement of these ERSEs further, we mutated either or both ERSE **(Fig. 3.4D)**. Mutating either ERSE decreased ATF6 *RHEB* promoter activation by ATF6, however, the promoter-proximal site, i.e. ERSE-1 appeared to have the largest effect **(Fig. 3.4E).** To determine whether ATF6 is sufficient to induce *Rheb* in the heart, *in vivo*, mice were injected with a recombinant AAV9 that encodes activated ATF6, i.e. ATF6(1-373). qRT-PCR and immunoblotting demonstrated that activated ATF6 increased *RHEB* mRNA and protein in the heart **(Fig. 3.5D-F)**. These results are the first demonstration in any cell type that ATF6 induces *RHEB,* implicating ATF6 as a critical link between growth stimuli and mTORC1 activation.

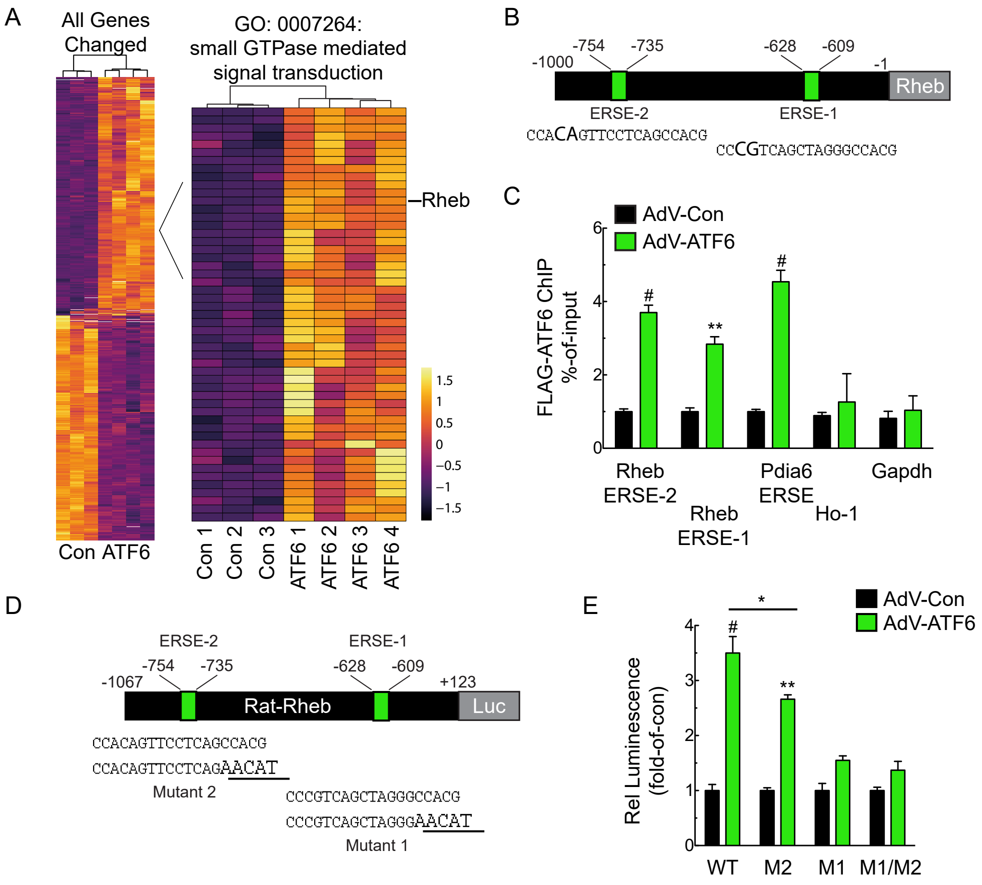

Figure 3.4- Regulation of Rheb Expression by ATF6.

A, Heat map of transcript profiling showing z-score-transformed RPKM values (Reads Per Kilobase per Million mapped reads) with hierarchical clustering of transcripts of control and ATF6 transgenic mouse hearts. Differentially expressed genes with *p* values and FDR ≤0.05 and a subset of genes annotated with term GO:0007264 are shown. **B,** Locations of consensus ATF6-binding motifs, i.e. ER stress response elements 1 and 2 (ERSE-1 and 2) and their sequences in the *RHEB* gene 5'-flanking region. Nucleotide differences from canonical ERSE elements are bold. **C,** Neonatal rat ventricular myocytes (NRVM) were infected with AdV encoding control or FLAG-ATF6(1-373) [active form], and then ATF6 binding to endogenous ERSE-1 or ERSE-2, as well as to the endogenous *PDIA6* ERSE, used here as a positive control, and the negative control targets heme oxygenase 1 (*ho-1*) and *gapdh* were examined by chromatin immunoprecipitation (ChIP) (n=3). **D,** Locations of ERSE-1 and 2 in the *RHEB* 5'-flanking region, their sequences (lower case), and the mutations that were made (bold and upper case). **E,** NRVM were transfected with rat-*rheb*(-1067/+123)-Luc WT, M2, M1 or M1/M2 then infected with AdV FLAG-ATF6(1-373). Then, 48h later, luciferase activity was measured in extracts (n=6). **F-H,** mRNA for *RHEB* determined by qRT-PCR **(F)** and Rheb protein and mTOR pathway components measured by immunoblots **(G)** and quantified by densitometry **(H)** from Con or ATF6 cKO mouse heart extracts after 7 days of Sham or TAC. **I-K,** mRNA for *RHEB* determined by qRT-PCR **(I)** and Rheb protein and mTOR pathway components immunoblots **(J)** and quantified by densitometry **(K)** from Con or ATF6 cKO mouse heart extracts after 4 weeks of sedentary or free wheel exercise (Run). Data are mean ± SEM. **P*≤0.05, ***P*≤0.01, $^{\#}$*P*≤0.001.

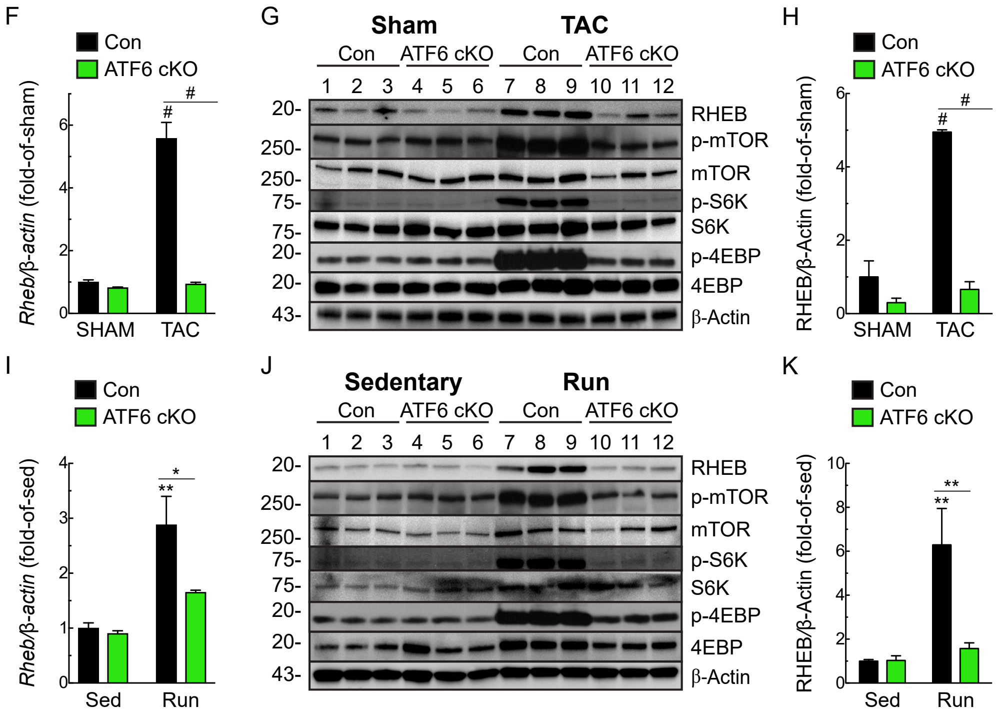

Figure 3.4 (continued)- Caption shown on previous page.

A GO:0007264: small GTPase mediated signal transduction

Rhoq	Arf2	Rheb	Tiam2	Rap1a	Pak4	Rap2b
Arhgap44	Rala	Mapkap1	Nckap1	Rhod	Farp1	Pak3
Ctnnal1	Arhgap12	Rhoa	Arhgap35	Arhgdia	Jun	Rnd1
Ralgps1	Map2k1	Arhgef10l	Spata13	Hras	Rap2a	Gpr35
Kras	Kpnb1	Rnd3	Shoc2	Git1	Kank1	Pdpn
Erbb2	Rhoc	Stmn1	Aif1	Sdcbp	Rras2	Dok2
Ralb	Hmox1	Net1	Cdc42	Itga3	Col3a1	Ect2
Arhgap1	Bcl6					

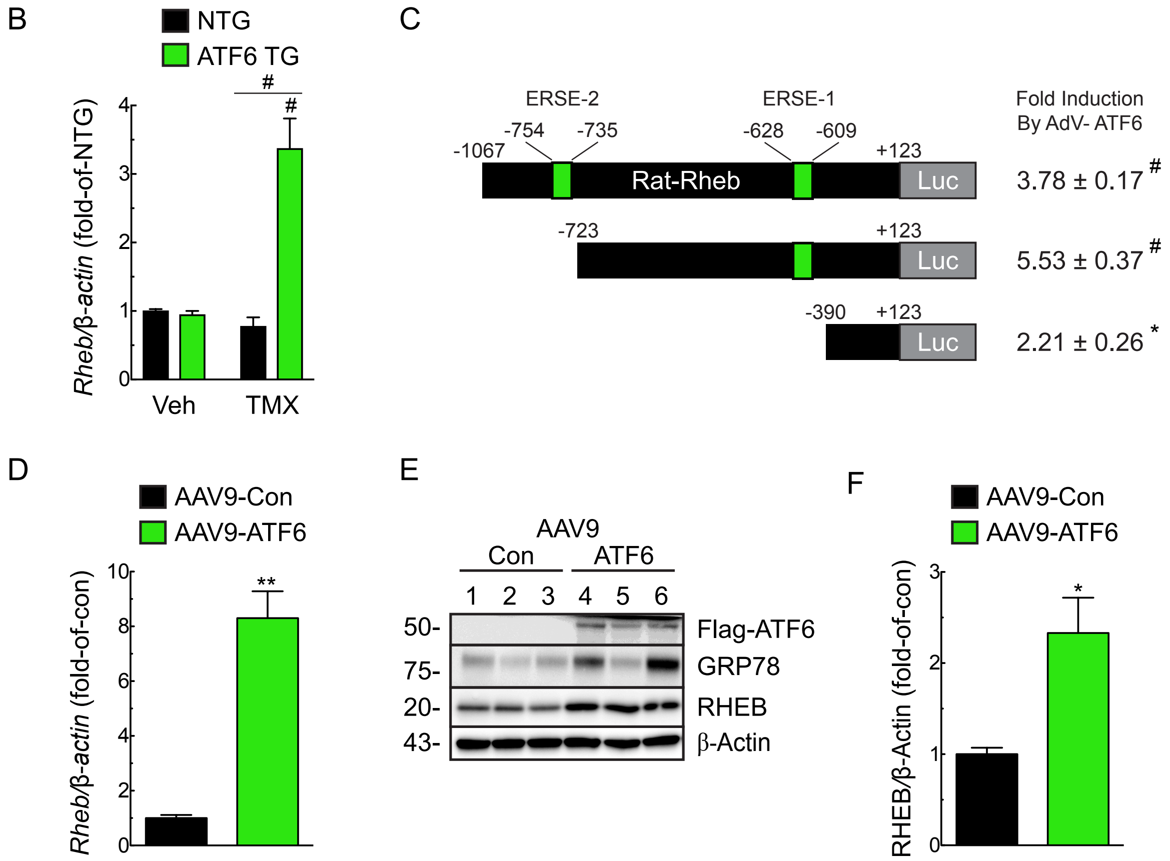

Figure 3.5- ATF6-dependent induction of Rheb in mouse hearts.

A, Table of a subset of induced genes represented by respective gene symbols in ATF6 TG mice with p values and FDR <0.05 annotated with ensemble biological process term GO:0007264. **B,** mRNA for Rheb was determined by qRT-PCR using LV extracts from ATF6-transgenic (ATF6 TG) and non-transgenic littermates after 5 days of tamoxifen administration (10mg/kg), which activates ATF6 in this mouse line. **C,** Diagram of constructs encoding different truncated forms of the rat *rheb* 5'-flanking sequence driving luciferase, as shown (left), i.e. rat-*rheb*(-1067/+123)-Luc, rat-*rheb*(-723/+123)-Luc, and rat-*rheb*(-390/+123)-Luc were transfected into NRVM which were then infected with AdV encoding ATF6(1-373) [active form], or with a control AdV. Luciferase enzyme activity in AdV-ATF6-infected cells was normalized to luciferase enzyme activity in AdV-Con-infected cells to determine the fold-induction by ATF6 (right). **D,** mRNA for *Rheb* was determined by qRT-PCR from LV extracts from mice treated 4 weeks with AAV9-Con or AAV9-ATF6. **E, F,** Immunoblot (**E**) and densitometry quantification (**F**) of RHEB protein expression AAV9-Con or AAV9-ATF6 mouse heart extracts. Data are represented as mean ± s.e.m. $*P \leq 0.05$, $**P \leq 0.01$, $\#P \leq 0.001$.

3.3.4. RHEB induction during pressure-overload and exercise requires ATF6

We found that *RHEB* was strongly induced in Con mice after either TAC or exercise, but not in ATF6 cKO mouse hearts **(Fig. 3.4F-K)**. Thus, ATF6 is necessary for the upregulation of RHEB in these models of cardiac hypertrophy, *in vivo*. Since RHEB is required for mTORC1 activation in response to a growth stimulus, we assessed mTORC1 pathway activation. As expected, pressure-overload and exercise both activated mTORC1, as shown by increased phosphorylation of mTORC1 (Ser2448), p70 ribosomal S6 kinase (S6K; Thr389), and eukaryotic translation initiation factor 4E-binding protein 1 (4E-BP1; Thr37/46); however, mTORC1 activation was blunted in ATF6 cKO mouse hearts **(Fig. 3.4G, J)**, consistent with the key role for ATF6 in mTORC1 activation by growth stimuli. To examine whether ATF6 might affect other signaling pathways leading to mTORC1 activation, we assessed the phosphorylation of Akt on Ser308 and the phosphorylation of TSC2, both of which lie upstream of Rheb in the mTORC1 signaling pathway. We found that pressure overload increased phosphorylation of Akt (Thr308) and TSC2 (Thr1462), as expected; however, in contrast to Rheb expression, neither of these phosphorylation events were affected by *ATF6* deletion **(Fig. 3.6A)**. Thus, the deficit in mTORC1 activation in ATF6 cKO mice must reside downstream of Akt and TSC2, i.e. Rheb. We also examined whether ATF6 deletion affected other well known canonical hypertrophy signaling pathways, but found that neither phosphorylation of Akt on Ser473, Erk phosphorylation **(Fig. 3.6A)** or calcineurin activation **(Fig. 3.6B)** were affected by ATF6 deletion. These results pinpoint the growth deficit in the ATF6 cKO mouse hearts to the inability to upregulate Rheb.

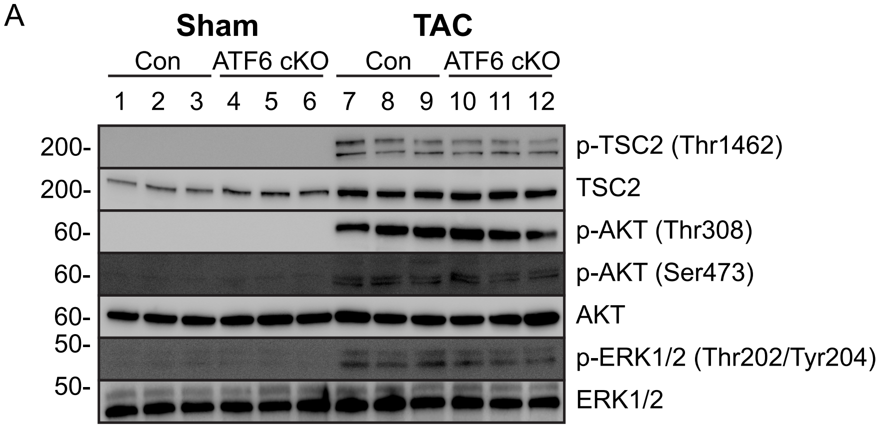

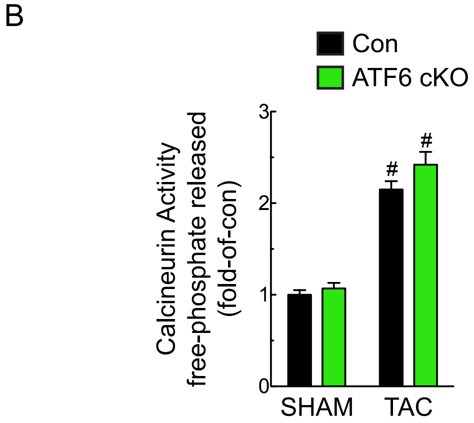

Figure 3.6- Effects of *ATF6* deletion on regulators of the mTORC1 pathway in hearts of mice subjected to TAC.

A, Immunoblot of TSC2, AKT, and ERK1/2 protein phosphorylation and expression in LV extracts from Con or ATF6 cKO mice after 7 days of Sham or TAC. **B,** Calcineurin activity as measured by free-phosphate release in LV extracts from Con or ATF6 cKO mice after 7 days of Sham or TAC. Data are represented as mean ± s.e.m. #P≤0.001.

3.3.5. RHEB is required for PE- and IGF1-induced cardiac myocyte growth

To explore the mechanistic relationship between *ATF6* and *RHEB* we used *RHEB* and *ATF6* loss-of-function approaches in NRVM treated with the α_1-adrenergenic receptor agonist, phenylephrine (PE) or insulin-like growth factor 1 (IGF1), which recapitulate much of the intracellular signaling during pressure-overload or exercise-induced hypertrophy, respecitvely[12]. Knocking down either *ATF6* or *RHEB* abrogated the effects of PE or IGF1 on cardiac myocyte hypertrophy, fetal gene induction, ATF6 target gene induction and mTORC1 signaling **(Fig. 3.7A-E; Fig. 3.8A, 3.8C; Fig. 3.9A-E; Fig. 3.8B)**, but had no effect on mTORC2 signaling, as assessed by phosphorylation of Akt on Ser-473 **(Fig. 3.8D-E)**. To further substantiate the results with *Rheb* siRNA, we used a different Rheb loss-of-function approach involving the Rheb inhibitor, Lonafarnib[13]. Lonafarnib mimicked the effects of *Rheb* siRNA on PE- and IGF1-mediated ATF6 activation, mTORC1 signaling, ATF6 gene induction and growth in NRVM **(Fig. 3.10)**.

To complement *ATF6* loss-of-function approach, we used a gain-of-function approach, examining the effects of ectopic expression of *ATF6* and *RHEB*. In the absence of a growth stimulus, ectopic expression of *ATF6* did not increase myocyte growth, as expected, due to the absence of mTORC1 activation under these conditions **(Fig. 3.11A Con)**. Either PE or IGF1 increased myocyte growth, which was completely blocked by the mTORC1 inhibitor, rapamycin, as expected **(Fig. 3.11A, PE and IGF1, red vs blue)**. Ectopic ATF6 augmented the growth-promoting effects of PE and IGF1, which were also completely blocked by rapamycin **(Fig. 3.11A, PE and IGF1, black and green)**. Moreover, ectopic ATF6 slightly augmented PE- and IGF1-stimulated NRVM growth, however, it was not able to restore growth in cells treated with either *RHEB* siRNA or Lonafarnib **(Fig. 3.11B-C)**. As expected, ectopic expression of *RHEB* had no effect in the absence of a growth stimulus; however, upon a growth stimulus, the loss of growth and mTORC1 activation seen with *ATF6* siRNA were completely restored by ectopically expressed *RHEB* **(Fig. 3.7F-H; Fig. 3.9F-H)**.

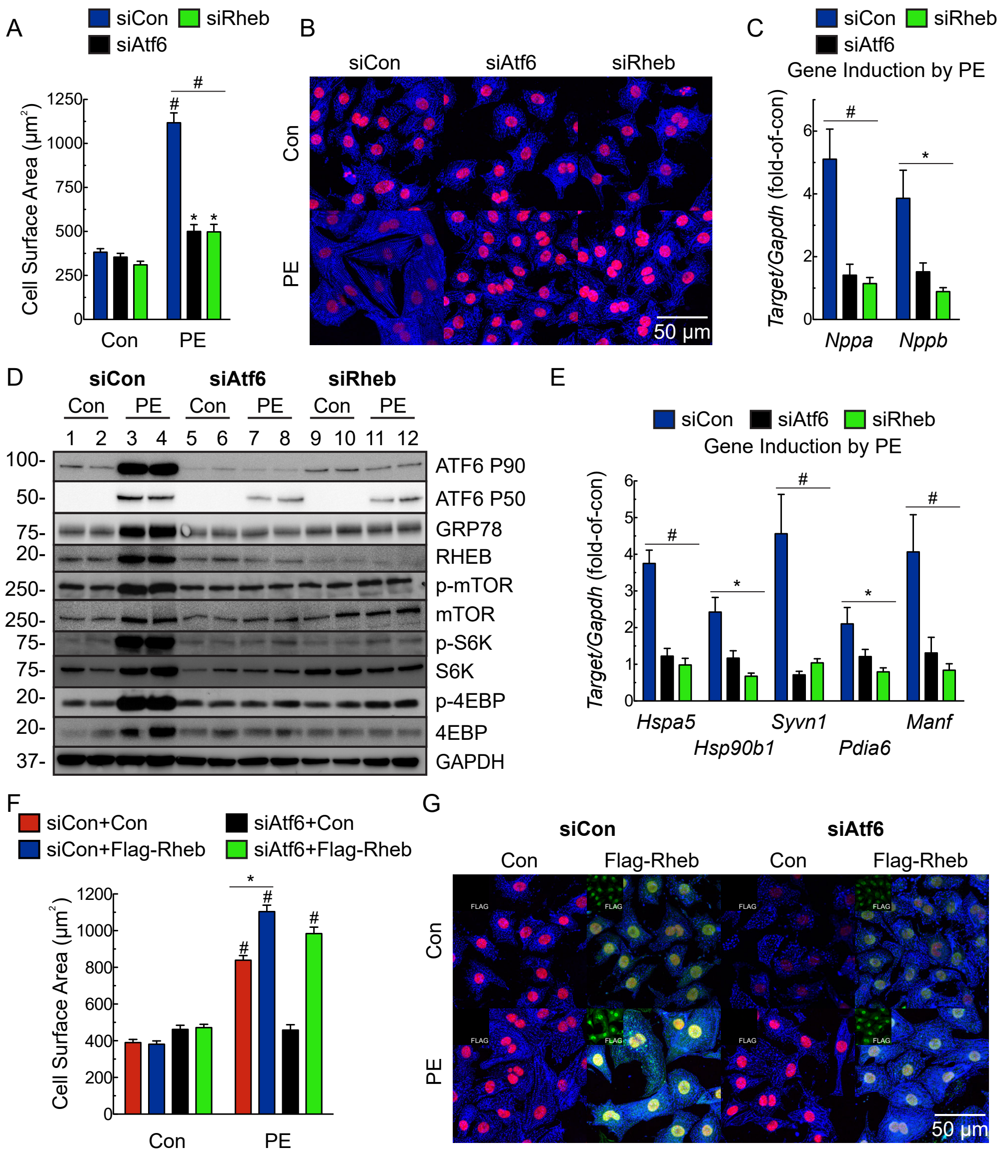

Figure 3.7- Effects of *ATF6*- and *RHEB* knockdown and ectopic Rheb expression on phenylephrine-induced hypertrophy in cultured cardiac myocytes.

A-E, NRVM were transfected with a nontargeted siRNA (siCon) or with siRNAs targeted to either rat *ATF6* (siAtf6) or *RHEB* (siRheb), and then treated ± phenylephrine (PE; 50μM) for 48 hours. **A,** Cell surface area was determined by photomicroscopy and morphometry (n=6). **B,** ICF of NRVM for α-actinin (blue) and TOPRO-3 (red). Bar = 50μm. **C,** qRT-PCR examination of *Nppa* and *Nppb*. Values are expressed as fold-of-control cardiac myocytes in the absence of PE (n=6). **D,** Immunoblot of NRVM. **E,** mRNA for ATF6 target genes determined by qRT-PCR. Values are expressed as fold-of-control myocytes in the absence of PE (n=3). **F-H,** NRVM were transfected with a control plasmid or a plasmid encoding Flag-Rheb and either siCon or siAtf6, followed by treatment ± PE for 48 hours. Cell surface area (**F**) was determined by morphometry after ICF (**G**). NRVM were stained for FLAG (green; isolated channel displayed in inset), α-actinin (blue), and TOPRO-3 (red). Bar = 50μm. Only FLAG-positive cells were used for cell surface area analysis (n=3). **H,** Immunoblot of NRVM. Data are mean ± SEM. *$P \leq 0.05$, **$P \leq 0.01$, $^{\#}P \leq 0.001$.

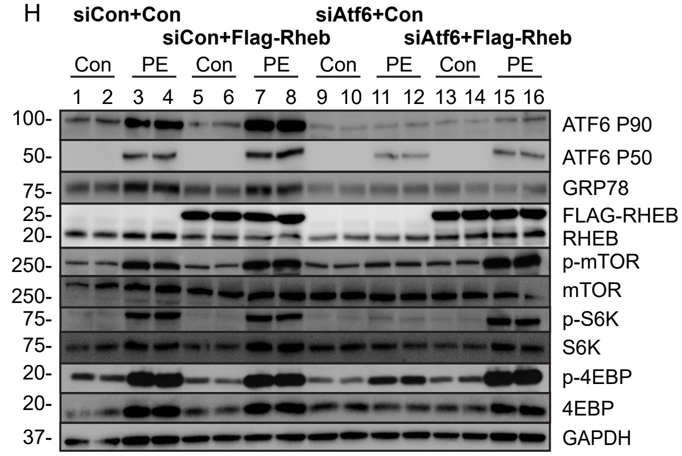

Figure 3.7 (continued)- Caption shown on previous page.

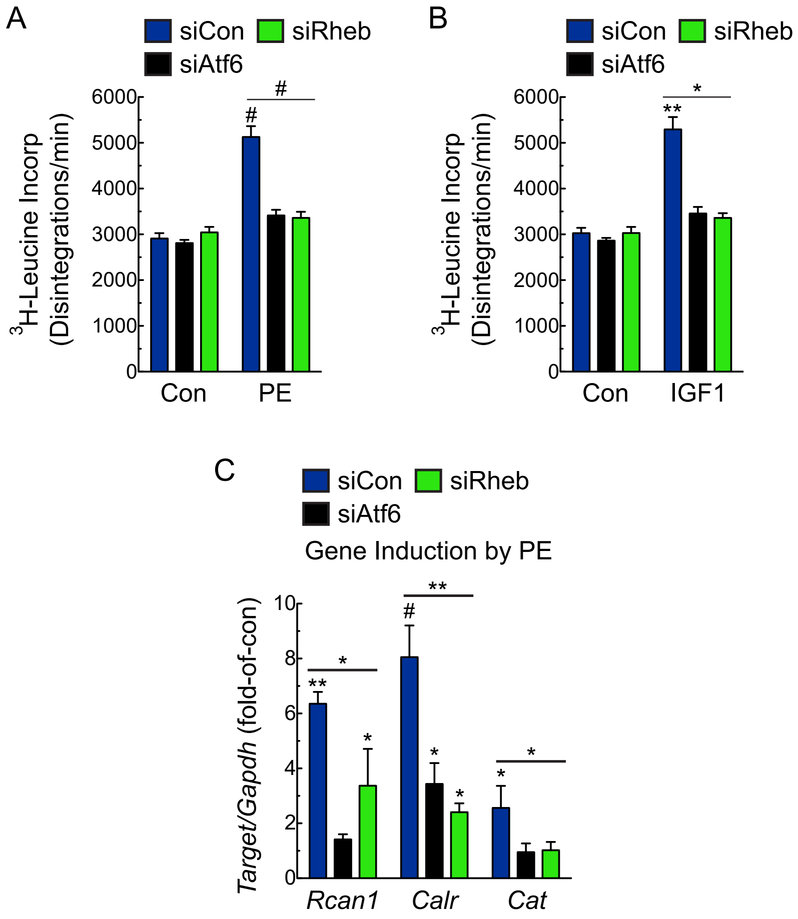

Figure 3.8- Effect of *ATF6* and *RHEB* knockdown on the mTORC1 pathway at cardiac myocyte hypertrophy.

A, C, NRVM were transfected with a nontargeted siRNA (siCon) or siRNAs targeted to rat *ATF6* (siAtf6) or *RHEB* (siRheb), and then treated with or without phenylephrine (PE; 50µM) **(A)** or IGF1 (100ng/ml) **(C)** for 48 hours. **A, B,** Incorporation of ^{3}H-leucine into TCA-precipitable protein in NRVM extracts was measured by scintillation counting. **C, D,** Immunoblot of NRVM. Phosphorylation of AKT on Ser473 is indicative of mTORC2 activity. **E,** mRNA for ATF6 target genes was determined by qRT-PCR in coordination with target genes presented in Figure 4E. Data are represented as mean ± s.e.m. *P≤0.05, **P≤0.01, #P≤0.001.

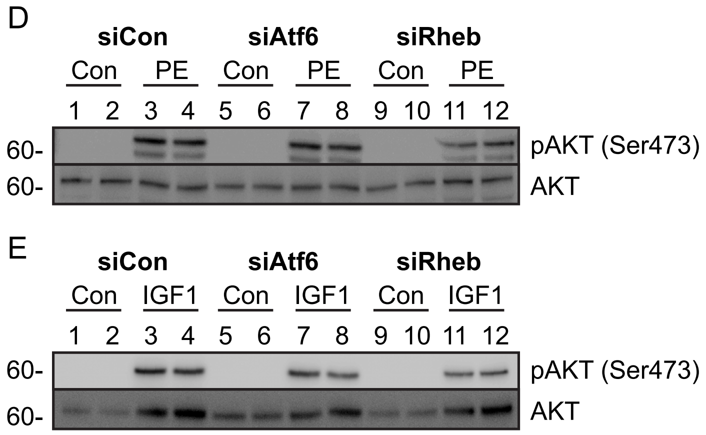

Figure 3.8 (continued)- Caption shown on previous page.

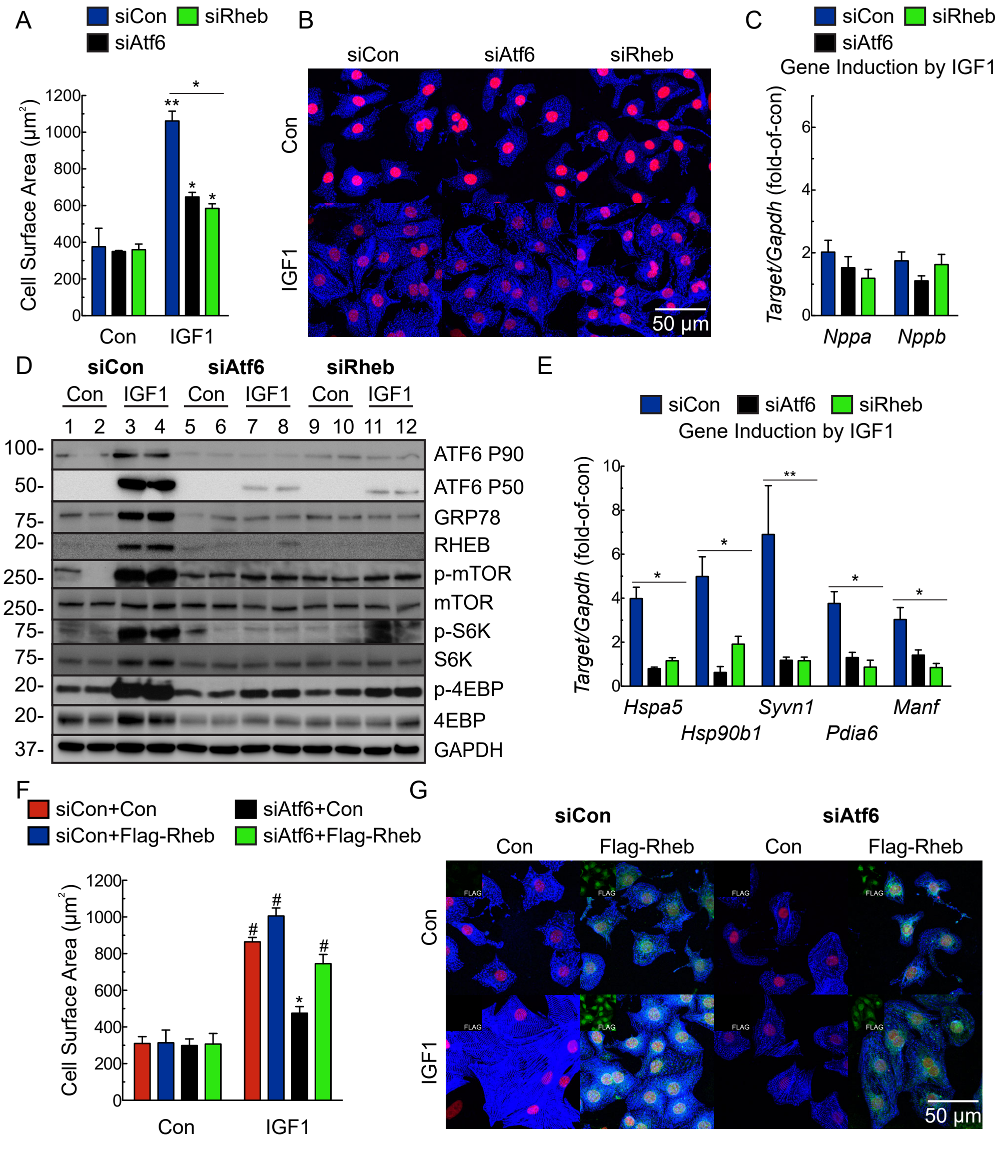

Figure 3.9- Effects of *ATF6*- and *RHEB* knockdown and ectopic Rheb expression on insulin like growth factor 1-induced hypertrophy in cultured cardiac myocytes.

A-E, NRVM were transfected with siCon, siAtf6 or siRheb, then treated ± IGF1 (100ng/ml) for 48 hours. **A,** Cell surface area was determined by morphometry after ICF (n=6). **B,** ICF of NRVM for α-actinin (blue) and TOPRO-3 (red). Bar = 50μm. **C,** qRT-PCR for *Nppa* and *Nppb*. Values are fold-of-control myocytes in the absence of IGF1 (n=6). **D,** Immunoblot of NRVM. **E,** mRNA levels of ATF6 target genes determined by qRT-PCR. Values are fold-of-control myocytes in the absence of IGF1 (n=3). **F-H,** NRVM were transfected with a control plasmid or a plasmid encoding Flag-Rheb and then either siCon or siAtf6, followed by treatment ± IGF1 for 48 hours. Cell surface area **(F)** was determined by morphometry after ICF **(G)**. NRVM were stained for FLAG (green; isolated channel displayed in inset), α-actinin (blue) and TOPRO-3 (red). Bar = 50μm. Only FLAG-positive cells were used for cell surface area analysis (n=3). **H,** Immunoblot of NRVM. Data are mean ± SEM. *$P≤0.05$, **$P≤0.01$, $^{\#}P≤0.001$.

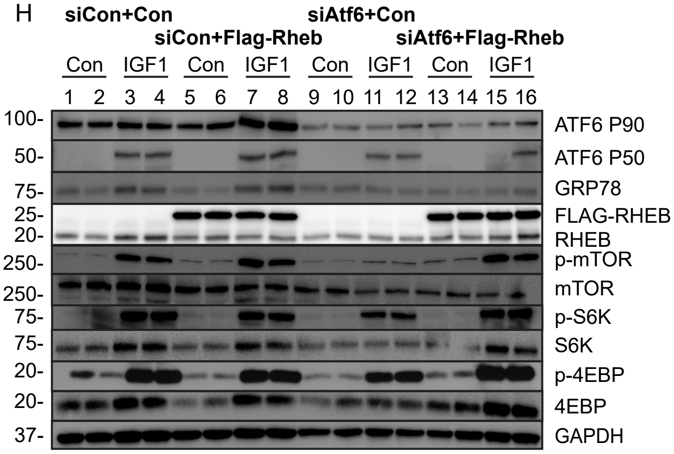

Figure 3.9 (continued)- Caption shown on previous page.

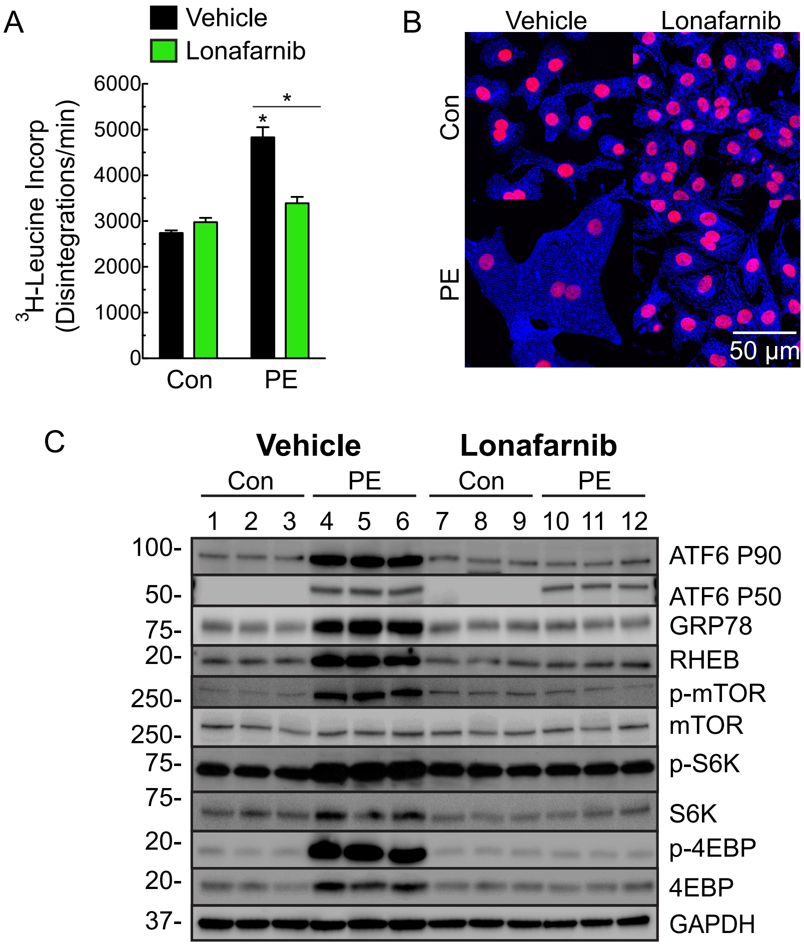

Figure 3.10- Rheb-inhibitor, Lonafarnib, inhibition of cardiac myocyte hypertrophy.

A-C, NRVM were treated with or without PE (50µM) for 48 hours in the presence or absence of the Rheb inhibitor, Lonafarnib (2µM). **A,** Incorporation of ^{3}H-leucine into TCA-precipitable protein in NRVM extracts was measured by scintillation counting. **B,** ICF of NRVM stained for α-actinin (blue) and TOPRO-3 (red). Bar = 50µm. **C,** Immunoblot of NRVM. **D-E,** NRVM were treated with or without IGF1 (100ng/ml) for 48 hours in the presence or absence of the Rheb inhibitor, Lonafarnib (2µM). **D,** Incorporation of ^{3}H-leucine into TCA-precipitable protein in NRVM extracts was measured by scintillation counting. **E,** ICF of NRVM stained for α-actinin (blue) and TOPRO-3 (red). Bar = 50µm. Data are represented as mean ± s.e.m. *P≤0.05, **P≤0.01.

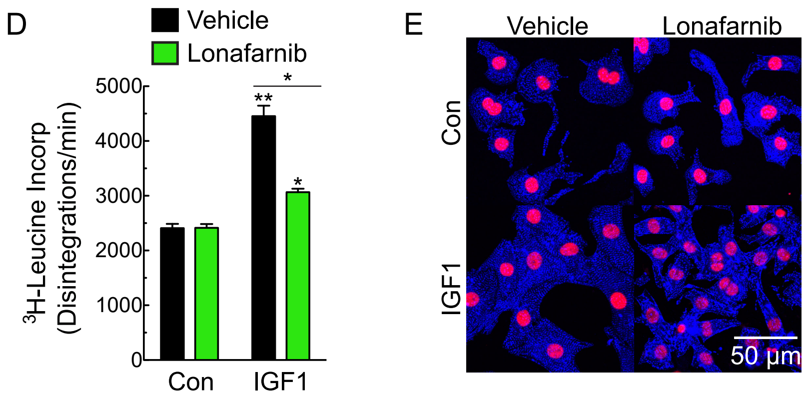

Figure 3.10 (continued)- Caption shown on previous page.

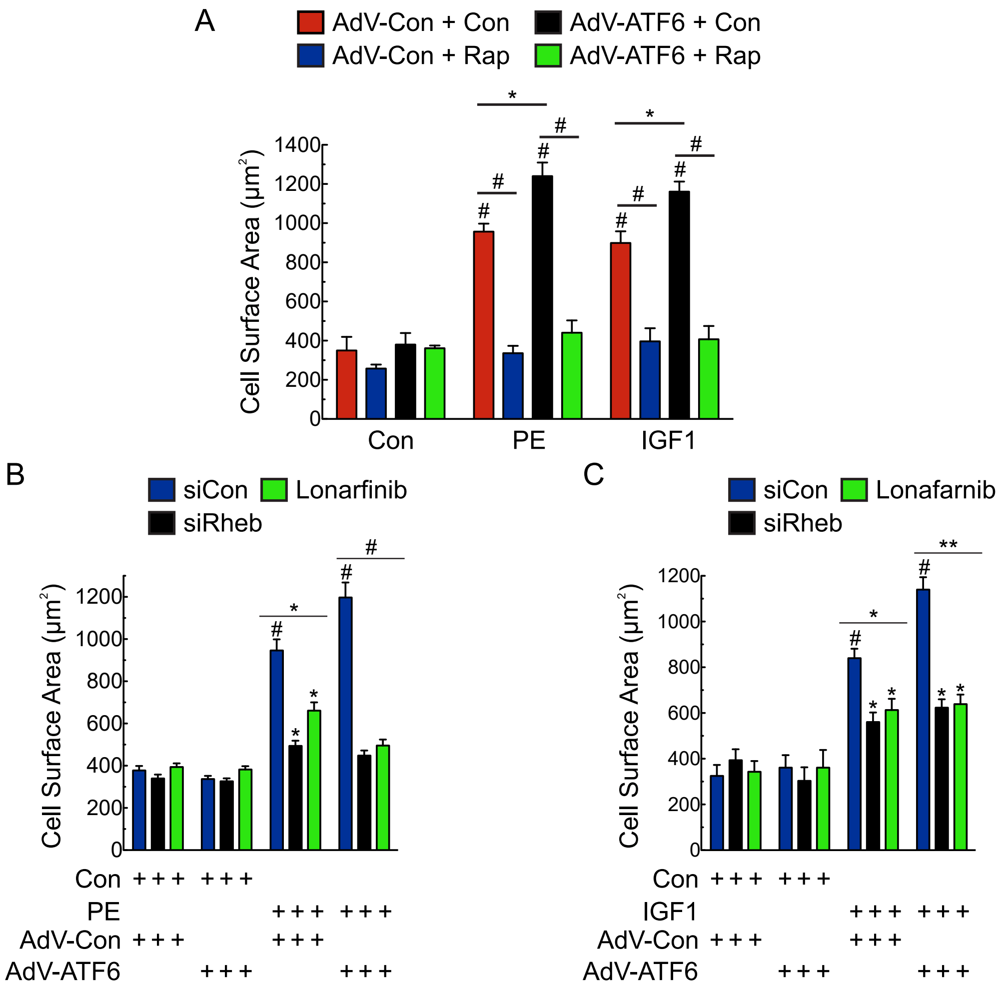

Figure 3.11- Effect of ATF6 overexpression on cardiac myocyte hypertrophy.

A, NRVM were infected with AdV encoding control or FLAG-ATF6(1-373) [active form] and then treated with or without phenylephrine (PE; 50µM) or IGF1 (100ng/ml), with or without rapamycin (20nM) for 48 hours, as shown. Cell surface area was determined by photomicroscopy and morphometry, then expressed as mean ± s.e.m after analyzing at least 100 cells per treatment per experiment. **B-C,** NRVM were transfected with a non-targeted siRNA (siCon) or siRNA targeted to rat RHEB (siRheb), and then infected with AdV encoding control or FLAG-ATF6(1-373) [active form]. NRVM were then treated with or without phenylephrine (PE; 50µM) (**B**) or IGF1 (100ng/ml) (**C**) with or without Lonafarnib (2µM) for 48 hours, as shown. Data are represented as mean ± s.e.m. *P≤0.05, **P≤0.01, #P≤0.001.

3.3.6. Mechanistic Relationship between Growth Signaling and the UPR

The unfolded protein response (UPR), which in addition to ATF6, is mediated by PERK and IRE1, is activated by the misfolding of proteins induced by a variety of chemical and pathophysiological treatments, most of these do not promote growth. In fact, the UPR is not widely considered to be growth-promoting. Accordingly, since we found here that ATF6 can be activated during growth, we assessed how growth affected the other arms of the UPR. We found that PE and IGF1 activated all three arms of the UPR in a rapamycin-sensitive manner **(Fig. 3.12A)**, indicating that mTORC1 activation is required for UPR activation during growth. We then individually knocked down *ATF6, PERK* and *IRE1*, and found that only ATF6 knockdown blunted growth **(Fig. 3.12B-C)**. To ensure that the effects of ATF6 on growth are dependent on the transcriptional effects of ATF6, we showed that NRVM infected with AdV-ATF6(1-373) [active] exhibited increased growth in response to PE, especially when endogenous ATF6 was knocked down, however AdV-ATF6(94-373) [trancriptionally inactive] did not **(Fig. 3.12D)**.

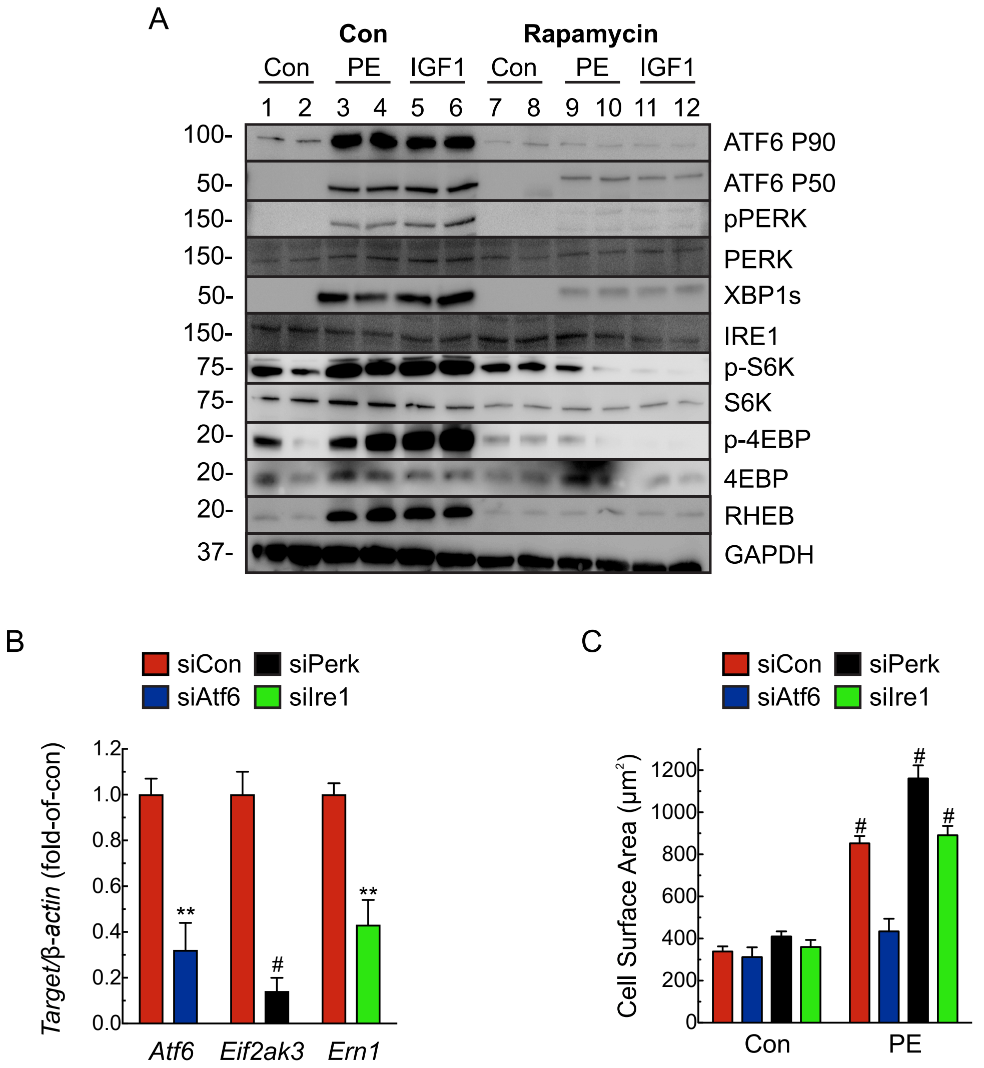

Figure 3.12- mTORC1-dependent activation of the UPR during cardiac myocyte hypertrophy.

A, Immunoblot of NRVM after treatment with or without phenylephrine (PE; 50µM) or IGF1 (100ng/ml), with or without rapamycin (20nM) for 48 hours, as shown. **B, C,** NRVM were transfected with siCon or siRNAs targeted to rat ATF6 (siAtf6), PERK (siPerk), or IRE1 (siIre1) and then treated with or without phenylephrine (PE; 50µM) for 48 hours. Atf6, Perk (Eif2ak3) and Ire1 (Ern1) mRNA levels were determined by qRT-PCR (**B**), and cell surface area was determined by photomicroscopy and morphometry (**C**). **D,** NRVM were transfected with a nontargeted siRNA (siCon) or siRNA targeted to rat ATF6 (siAtf6) and were then infected with AdV encoding control, FLAG-ATF6(1-373) [active] or FLAG-ATF6(94-373) [inactive due to deletion of transcriptional activation domain], then treated with or without phenylephrine (PE; 50µM) for 48 hours. Cell surface area was determined by photomicroscopy and morphometry, then expressed as mean ± s.e.m after analyzing at least 100 cells per treatment per experiment. Data are represented as mean ± s.e.m. $*P \leq 0.05$, $**P \leq 0.01$, $\#P \leq 0.001$.

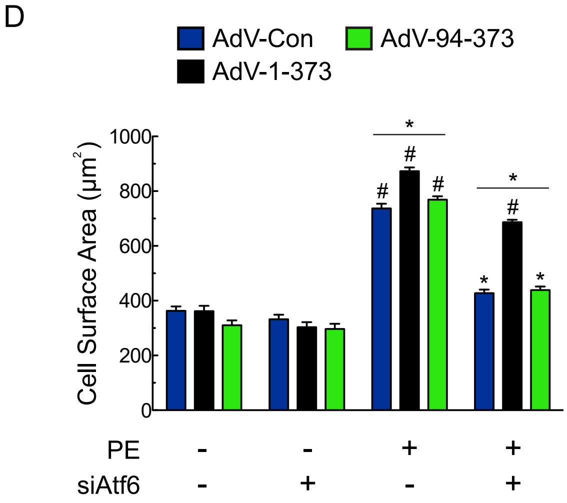

Figure 3.12 (continued)- Caption shown on previous page.

Next, we examined the effect on mTORC1 signaling of other UPR stimulators that do not affect growth, such as tunicamycin (TM), which increases ER protein misfolding by inhibiting protein glycosylation in the ER. In contrast to PE, activation of ATF6 by TM was not dependent on *RHEB* **(Fig. 3.13A-B)**. Additionally, while *RHEB* knockdown blocked PE- and IGF1-mediated induction of ATF6 target genes, **(Fig. 3.7E, 5E)**, it had no effect on TM-mediated induction of ATF6 target genes **(Fig. 3.13C)**. Thus, there are RHEB/growth-dependent and RHEB/growth-independent pathways that lead to ATF6 activation and induction of ATF6 target genes.

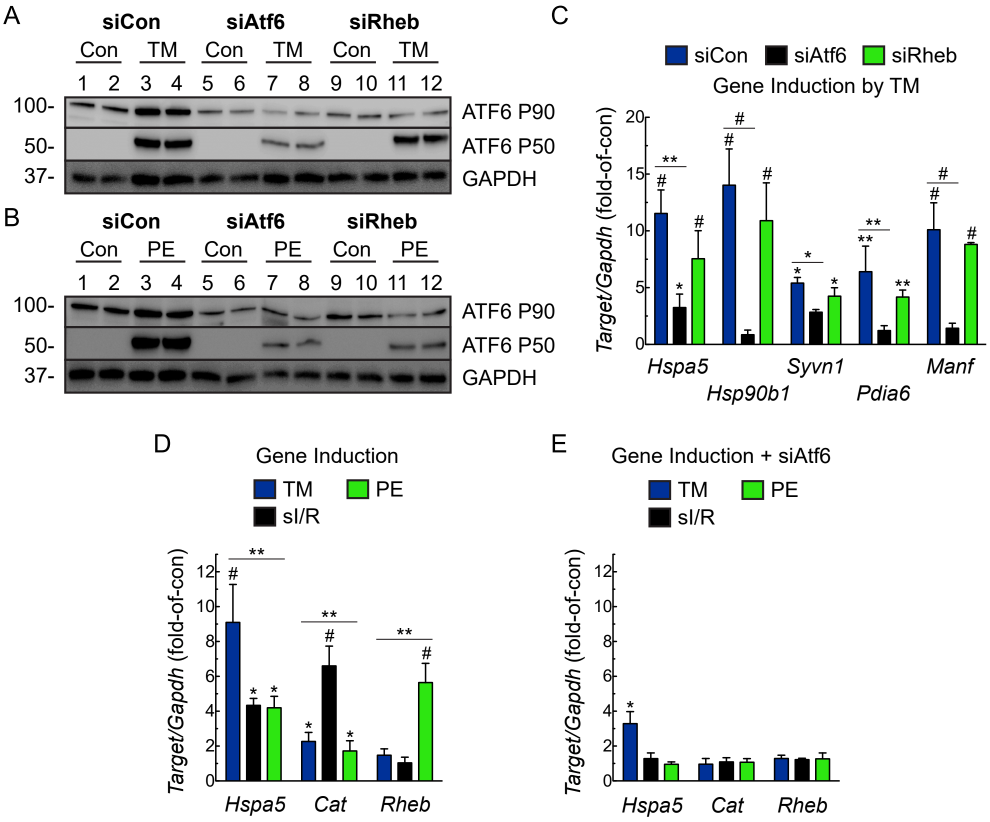

Figure 3.13- Examination of Rheb Requirement for Growth-dependent but not Growth-independent Activation of the ATF6.

A-B, NRVM were transfected with siCon, siAtf6 or siRheb then treated ± tunicamycin (TM; 10µg/mL) **(A)** or PE (50µM) **(B)** for 24 hours, then analyzed for ATF6 activation by immunoblotting. **C,** mRNA levels for ATF6 target genes determined by qRT-PCR. Values are fold-of-control, i.e. not treated with TM (n=6). **D, E,** NRVM were transfected with siCon (D) or siAtf6 (E), then treated ± TM (10µg/mL), or PE (50µM) for 24 hours, or subjected to simulated ischemia/reperfusion (sI/R; 8 hours of sI, followed by 24 hours of reperfusion) and mRNA for ATF6 target genes determined by qRT-PCR (n=6). **F,** Diagram of constructs that encode luciferase driven by the *grp78*, *catalase*, and *rheb* 5'-flanking region. **G, H,** NRVM were transfected with human-*grp78*(-284/+221)-Luc WT, rat-*catalase*(-1161/+131)-Luc WT, or rat-*rheb*(-1067/+123)-Luc WT and then transfected with siCon **(G)** or siAtf6 **(H)**, then treated ± TM (10µg/mL), or PE (50µM) for 24 hours, or subjected to sI/R and luciferase activity measured in extracts (n=6). **I, J,** NRVM infected with AdV FLAG-ATF6(1-670) **(I)** or control **(J)**, and then ATF6 binding to the endogenous *grp78*, *catalase*, or *rheb* genes, as well as to the negative control gene, *gapdh,* examined by ChIP under the same experimental conditions described above (n=3). Data are mean ± SEM. *P≤0.05, **P≤0.01, $^{\#}$P≤0.001.

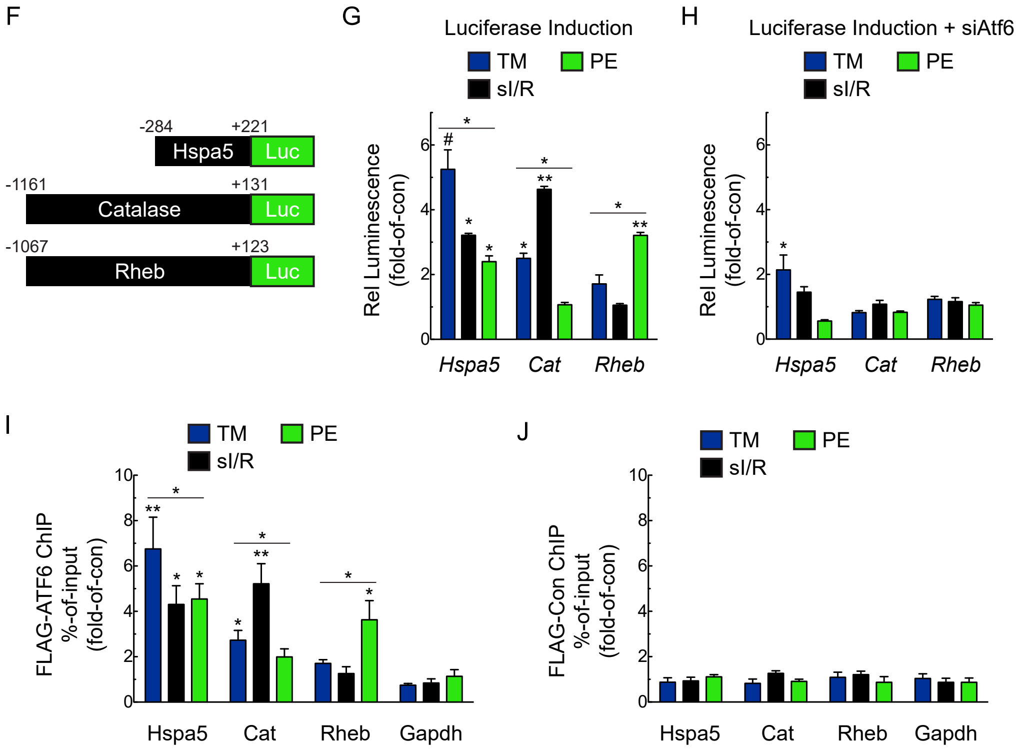

Figure 3.13 (continued)- Caption shown on previous page.

3.3.7. Stimulus-dependent Differential Induction of ATF6 Target Genes

We dived deeper into the mechanism of RHEB/growth-dependent and RHEB/growth-independent pathways of ATF6 activation. We previously showed that ATF6 induces some proteins targeted to the ER, where they enhance protein folding (e.g. *HSPA5*/*GRP78*), and others located outside the ER, where they serve other functions. One example of the latter is our finding that I/R activates ATF6-dependent induction of *catalase (CAT)***,** which resides in peroxisomes and neutralizes damaging ROS. Here, we provide an additional example of an ATF6-inducible gene, *RHEB*, that encodes a protein that resides outside the ER. Because of the differences in the locations and functions of Hspa5, Cat, and Rheb, we posited that they might be differentially induced by treatments that cause ER protein misfolding (TM), or oxidative stress (I/R) but do not induce growth, or to a treatment that induces growth (PE). While, for the most part, the mRNA levels for all three genes were increased by all the treatments, the quantitative nature of induction differed depending on the treatments, such that TM, sI/R, and PE had the greatest effects on induction of *Hspa5, Cat,* and *Rheb,* respectively **(Fig. 3.13D)**. Notably, *CAT* induction was highly selective, showing an approximate 6-fold induction by sI/R, and much less induction by either TM or PE **(Fig. 3.13D, *Cat*)**. Remarkably, *RHEB* induction was also highly selective, showing the least induction by TM or sI/R, while being induced by over 5-fold by PE **(Fig. 3.13D, *Rheb*)**. Importantly, all of these effects depended on ATF6 **(Fig. 3.13E)**.

To dissect this stimulus-dependent differential gene induction further, we showed that promoter/luciferase reporter constructs for *Hspa5, Cat,* and *Rheb* **(Fig. 3.13F)** were also differentially induced by TM, sI/R and PE, mimicking mRNA induction **(Fig. 3.13G)**. Importantly, as with the mRNA, all of these effects depended upon ATF6 **(Fig. 3.13H)**.

These stimulus-specific effects of ATF6 on *Hspa5, Cat,* and *Rheb* could be due to the stimulus-dependent binding of ATF6 to the ERSEs in these genes. To test this, we developed a new method for measuring ATF6 binding to the *HSPA5, CAT,* and *RHEB* promoters in cells treated with TM, sI/R or PE. To this end we generated a recombinant AdV FLAG full-length p90 ATF6, i.e. ATF6(1-670), which remains in the ER in the absence of ER stress, and, therefore, can not bind to ERSEs. NRVM expressing FLAG-ATF6(1-670) were treated with TM, sI/R or PE, each of which induce the formation of the FLAG-tagged N-terminal, active p50 form of ATF6, so it can bind to ERSEs. ChIP demonstrated that the binding of ATF6 to these genes differed, depending on the stimulus, mimicking the mRNA induction and promoter activation **(Fig. 3.13I)**. These effects were not seen with AdV encoding only FLAG, verifying ATF6-specificity **(Fig. 3.13J)**. This shows, for the first time in any cell type, that ATF6 can be activated by a broad spectrum of conditions that affect proteostasis in a variety of ways, yet the relative induction of ATF6 targets differs in a condition-dependent manner.

3.3.8. Ectopic Expression of RHEB Restores Cardiac Growth to ATF6 cKO Mouse Hearts

Next, we assessed the effects of ectopic expression of *RHEB* in the heart, *in vivo* using a new recombinant AAV9-RHEB **(Fig. 3.14A)**. In ATF6 cKO mice, AAV9-RHEB effectively restored the loss of mTORC1 signaling, hypertrophic growth and cardiac function, as well as the hypertrophic and ATF6 gene programs in response to TAC **(Fig. 3.14B-F; Table 3.3)**. Thus, it is by increasing RHEB that ATF6 influences mTORC1 signaling and subsequent cardiac myocyte growth, fetal gene expression and ATF6-target gene expression.

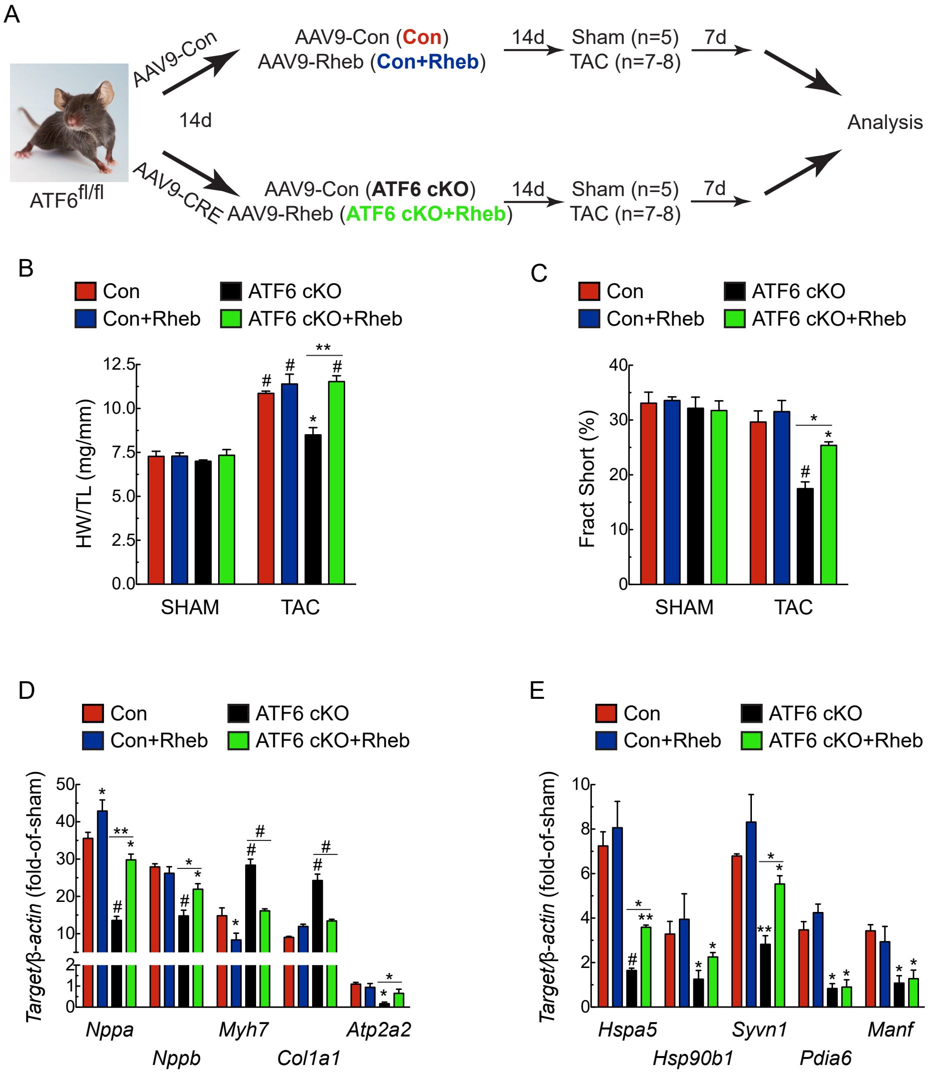

Figure 3.14- Effect of cardiac myocyte-specific ectopic Rheb expression in ATF6 gene deleted mouse hearts subjected to TAC.

A, Experimental protocol for AAV9 administration to ATF6$^{fl/fl}$ mice and TAC. **B,** Heart weights/tibia lengths (HW/TL). **C,** Fractional shortening (%), as determined by echocardiography, see Table 3.3. **D,** mRNA for fetal genes determined by qRT-PCR. **E,** mRNA for ATF6 target genes determined by qRT-PCR. **F,** Immunoblots of LV extracts. Data are mean ± SEM. *$P \leq 0.05$, **$P \leq 0.01$, $^{\#}P \leq 0.001$.

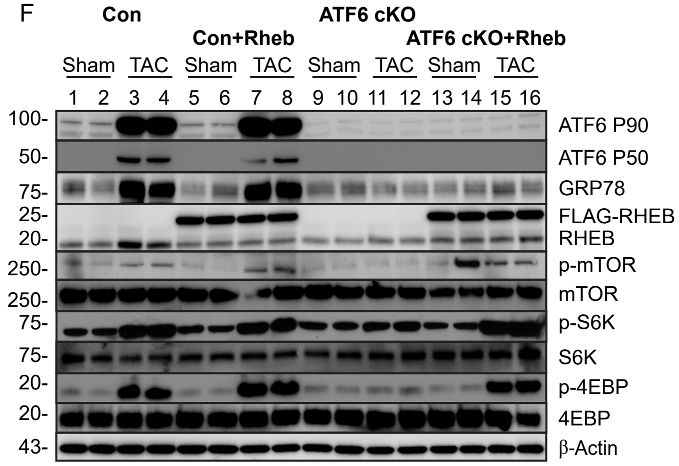

Figure 3.14 (continued)- Caption shown on previous page.

Table 3.3- 7-day TAC echocardiographic parameters

	Con Sham (n = 5)	Con+Rheb Sham (n = 5)	ATF6 cKO Sham (n = 5)	ATF6 cKO+Rheb Sham (n = 5)
FS (%)	31.47±4.07	33.63±1.68	28.61±2.54	28.28±1.67
EF (%)	59.40±5.61	63.18±2.30	55.60±4.07	54.94±2.72
LVEDV (μl)	55.61±9.30	56.30±2.97	59.41±3.99	75.90±6.83
LVESV (μl)	23.61±2.83	20.84±2.03	26.91±4.19	34.54±4.42
LVIDD (mm)	3.59±0.24	3.65±0.08	3.73±0.10	4.12±0.16
LVIDS (mm)	2.48±0.27	2.42±0.10	2.67±0.16	2.96±0.15
PWTD (mm)	0.72±0.06	0.68±0.05	0.93±0.08	0.72±0.08
PWTS (mm)	1.03±0.11	1.02±0.06	1.15±0.14	0.94±0.08
AWTD (mm)	0.91±0.07	0.87±0.02	0.92±0.08	0.83±0.03
AWTS (mm)	1.21±0.05	1.16±0.08	1.21±0.08	1.12±0.05
HR (bpm)	488±18.43	516±16.48	464±33.55	504±35.34
HW (mg)	138.60±7.91	134.75±2.55	137.73±3.05	161.60±8.84
BW (g)	26.14±0.97	26.64±0.43	27.13±0.26	28.05±0.65
TL (mm)	19.00±0.37	18.50±0.26	19.67±0.26	22.00±0.37
HW/BW (mg/g)	5.29±0.13	5.07±0.15	5.08±0.13	5.75±0.21
HW/TL (mg/mm)	7.28±0.29	7.29±0.19	7.00±0.07	7.34±0.32

	Con TAC (n = 7)	Con+Rheb TAC (n = 8)	ATF6 cKO TAC (n = 7)	ATF6 cKO+Rheb TAC (n = 8)
FS (%)	29.73±2.25	31.60±1.08	17.71±2.20^{1,2}	26.25±1.07
EF (%)	57.77±1.54	60.57±1.54	37.25±4.15^{1,2}	52.41±1.88
LVEDV (μl)	46.54±4.61	50.55±2.03	61.26±4.53^{2}	52.73±5.77^{1}
LVESV (μl)	19.71±1.81	19.92±1.08	38.91±4.66^{1,2}	25.46±3.78^{2}
LVIDD (mm)	3.36±0.15	3.49±0.06^{1}	3.77±0.12^{2}	3.53±0.16^{1}
LVIDS (mm)	2.36±0.13	2.39±0.05	3.11±0.16^{1,2}	2.61±0.15^{1}
PWTD (mm)	1.78±0.12^{1}	1.54±0.08^{1}	1.03±0.04^{2}	1.45±0.14^{1}
PWTS (mm)	1.99±0.11^{1}	1.66±0.14^{1}	1.07±0.08^{2}	1.68±0.13^{1}
AWTD (mm)	1.28±0.05^{1}	1.23±0.08^{1}	0.91±0.12^{2}	1.27±0.13^{1}
AWTS (mm)	1.49±0.09^{1}	1.61±0.06^{1}	1.28±0.13^{2}	1.62±0.13^{1}
HR (bpm)	523±9.02	519±13.29	505±13.20	514±22.54
HW (mg)	212.44±3.89^{1}	217.20±14.08^{1}	176.89±7.44^{1,2}	232.95±9.99^{1,2}
BW (g)	24.34±0.66	23.99±0.51^{1}	25.63±0.47	25.52±0.73^{1}
TL (mm)	19.60±0.40	19.00±0.31	20.86±0.32	20.17±0.44
HW/BW (mg/g)	8.75±0.24^{1}	9.10±0.69^{1}	6.90±0.27^{1,2}	9.15±0.39^{1}
HW/TL (mg/mm)	10.86±0.22^{1}	11.39±0.56^{1}	8.50±0.41^{1,2}	11.54±0.33^{1}

3.3.9. ATF6 Activation in Response to Growth Requires mTORC1 Activation, Protein Synthesis and Protein Misfolding

To this point, mTORC1 and ATF6 activation were shown to be dependent on each other under the growth conditions examined. To account for this interdependence, we posited a temporal sequence of events, wherein the initial event is mTORC1 activation, which depends on basal levels of Rheb **(Fig. 3.15A, Step 1)**. This initial mTORC1 activation precedes, but drives initial increases in protein synthesis that place demands on the protein-folding machinery **(Fig. 3.15A, Step 2)**, which activates ATF6. Then, ATF6 serves canonical- and non-canonical roles **(Fig. 3.15A, Steps 3, 4)**, the latter of which includes *RHEB* induction **(Fig. 3.15A, Step 5)**, which is necessary to sustain mTORC1 activation **(Fig. 3.15A, Step 6)** and the continued increases in protein synthesis that required for growth and cardiac myocyte hypertrophy **(Fig. 3.15A, Step 7)**. To examine this hypothesis, a TAC time course was carried out. At 3h of TAC, a time when mTORC1 is activated, but protein synthesis has not yet increased, mTORC1 signaling was activated, but ATF6 was not activated and *RHEB* was not induced **(Fig. 3.15B, 3h)**. However, at both 2 and 7d of TAC, when protein synthesis is increased, mTORC1 signaling and ATF6 were activated, and *RHEB* was induced **(Fig. 3.15B, 2d and 7d)**. As expected, heart weights increased as a function of TAC time from 3h to 7d **(Fig. 3.15C; Table 3.4)**. Thus, mTORC1 activation occurred soon after TAC and preceded ATF6 activation. Further supporting our hypothesis that initially, mTORC1 activation precedes ATF6 activation were results of a 3h TAC experiment in ATF6 cKO mice, where, in contrast to longer times of TAC **(i.e. 7d - Fig. 3.4G)**, the deletion of

ATF6 did not affect mTORC1 activation **(Fig. 3.15D)**. As expected, heart weights did not change under these conditions **(Fig. 3.15E; Table 3.5)**.

Consistent with these results, when examining the effect of PE and IGF1 at the earliest time points, just prior to when protein synthesis is greatest in NRVM, knocking down *ATF6* did not affect mTORC1 activation **(Fig. 3.16A)**, but again, ATF6 activation was rapamycin-dependent **(Fig. 3.16B)**. Moreover, inhibiting protein synthesis with cycloheximide had no effect on mTORC1 activation at these short times of PE or IGF1 treatment, but impaired ATF6 activation and *RHEB* induction, indicating that protein synthesis is required for ATF6 activation and subsequent *RHEB* induction **(Fig. 3.16C)**. Finally, in NRVM treated with the chemical chaperone, 4PBA, PE and IGF1 activated mTORC1 however, ATF6 was not activated and *RHEB* was not induced **(Fig. 3.16D)**, indicating the increase in protein folding demand driven by increases in protein synthesis are responsible for activating ATF6.

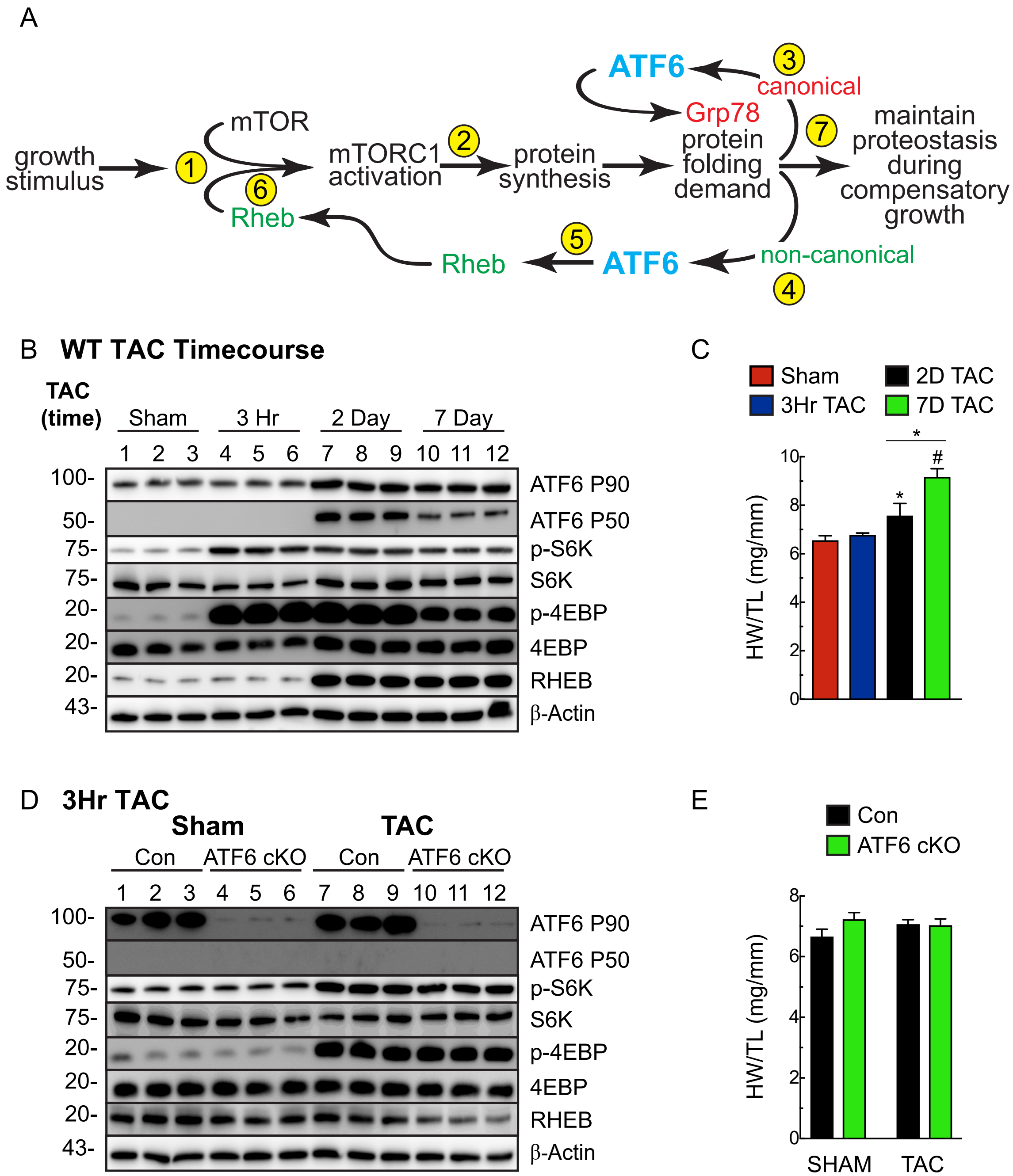

Figure 3.15- Mechanism whereby ATF6 acts as a nodal regulator of both protein synthesis and protein folding during cardiac hypertrophy.

A, Shown are the temporal sequence of steps involved in mediating the initial (Steps 1-4) and sustained (Steps 5-7) aspects of growth and the interdependent roles of mTORC1 and ATF6. **B, C,** Immunoblot of LV extracts (**B**) and heart weights/tibia lengths (HW/TL) (**C**) from WT mice subjected to TAC for 3 hours, 2 days, or 7 days. Echocardiography details in Table 3.4. **D, E,** Immunoblot of LV extracts (**D**) and heart weights/tibia lengths (HW/TL) (**E**) from Con or ATF6 cKO mice subjected to 3 hours of TAC. Echocardiography details in Table 3.5. Data are mean ± SEM. **P*≤0.05, $^{\#}$*P*≤0.001.

Table 3.4- TAC time course echocardiographic parameters for Wild-Type mice

	Sham (n = 4)	3-Hours TAC (n = 4)	2-Days TAC (n = 4)	7-Days TAC (n = 4)
FS (%)	30.76±1.69	32.27±1.83	28.32±3.21	25.36±1.85
EF (%)	59.11±2.58	61.40±2.64	54.95±4.98	50.51±3.00[1]
LVEDV (μl)	55.18±3.16	50.76±3.82	58.16±1.60	62.66±1.32[1]
LVESV (μl)	22.82±2.74	19.94±2.60	26.38±3.44	30.87±1.67[1]
LVIDD (mm)	3.62±0.08	3.49±0.11	3.70±0.04	3.82±0.03[1]
LVIDS (mm)	2.51±0.11	2.37±0.13	2.65±0.14	2.85±0.06[1]
PWTD (mm)	0.70±0.04	0.78±0.03	0.91±0.12	1.30±0.05[1]
PWTS (mm)	1.03±0.04	1.12±0.06	1.22±0.09	1.69±0.06[1]
AWTD (mm)	0.79±0.04	0.93±0.05	1.03±0.05[1]	1.50±0.04[1]
AWTS (mm)	1.10±0.04	1.22±0.06	1.25±0.04	1.78±0.05[1]
HR (bpm)	517±11.32	503±13.78	509±11.75	517±7.18
HW (mg)	121.05±5.23	158.95±4.05[1]	162.90±3.39[1]	208.50±10.04[1]
BW (g)	23.09±0.28	31.00±0.85[1]	27.94±1.56[1]	29.06±0.37[1]
TL (mm)	18.50±.0.29	23.50±0.29[1]	21.50±0.50[1]	22.75±0.25[1]
HW/BW (mg/g)	5.24±0.22	5.13±0.06	5.85±0.43	7.19±0.42[1]
HW/TL (mg/mm)	6.54±0.21	6.76±0.10	7.56±0.51[1]	9.15±0.35[1]

FS = fractional shortening
EF = ejection fraction
LVEDV = left ventricular end diastolic volume
LVESV = left ventricular end systolic volume
LVIDD = left ventricular inner diameter in diastole
LVIDS = left ventricular inner diameter in systole
PWTD = left ventricular posterior wall thickness in diastole
PWTS = left ventricular posterior wall thickness in systole
AWTD = left ventricular anterior wall thickness in diastole
AWTS = left ventricular anterior wall thickness in systole
HR = heart rate in beats per minute
HW = heart weight
BW = body weight
TL = tibia length
HW/BW = heart weight/body weight
HW/TL = heart weight/tibia length

Statistical analyses used a one-way ANOVA with a Newman-Keuls post-hoc analysis.

[1] = $p \leq 0.05$ different from Sham

Table 3.5- 3-hour TAC echocardiographic parameters for Con and ATF6 cKO mice

	Con Sham (n = 5)	ATF6 cKO Sham (n = 4)	Con TAC (n = 5)	ATF6 cKO TAC (n = 4)
FS (%)	34.06±2.95	33.88±3.13	31.91±1.57	31.59±3.66
EF (%)	63.57±3.78	63.18±4.30	60.66±2.26	59.72±5.30
LVEDV (µl)	51.52±3.83	58.55±2.44	61.47±4.92	63.15±5.20
LVESV (µl)	18.28±1.23	21.79±3.28	24.33±2.86	26.21±5.31
LVIDD (mm)	3.51±0.11	3.71±0.07	3.78±0.12	3.82±0.13
LVIDS (mm)	2.30±0.06	2.46±0.15	2.57±0.12	2.63±0.23
PWTD (mm)	0.84±0.08	0.76±0.07	0.72±0.05	0.81±0.06
PWTS (mm)	0.90±0.23	1.16±0.18	1.08±0.05	1.16±0.07
AWTD (mm)	0.86±0.10	0.90±0.09	0.88±0.04	0.93±0.04
AWTS (mm)	1.77±0.16	1.24±0.08	1.21±0.04	1.22±0.04
HR (bpm)	493±19.31	517±10.09	510±10.16	512±14.34
HW (mg)	128.88±5.32	137.30±6.35	148.00±2.16[1]	152.78±6.37[1]
BW (g)	24.58±0.88	25.88±1.04	26.58±0.40	28.16±0.65[1]
TL (mm)	19.40±.0.51	19.00±0.41	21.00±0.32	21.75±0.48[1]
HW/BW (mg/g)	5.24±0.11	5.31±0.16	5.58±0.15	5.42±0.14
HW/TL (mg/mm)	6.65±0.25	7.23±0.23	7.06±0.16	7.02±0.22

FS = fractional shortening
EF = ejection fraction
LVEDV = left ventricular end diastolic volume
LVESV = left ventricular end systolic volume
LVIDD = left ventricular inner diameter in diastole
LVIDS = left ventricular inner diameter in systole
PWTD = left ventricular posterior wall thickness in diastole
PWTS = left ventricular posterior wall thickness in systole
AWTD = left ventricular anterior wall thickness in diastole
AWTS = left ventricular anterior wall thickness in systole
HR = heart rate in beats per minute
HW = heart weight
BW = body weight
TL = tibia length
HW/BW = heart weight/body weight
HW/TL = heart weight/tibia length

Statistical analyses used a one-way ANOVA with a Newman-Keuls post-hoc analysis.

[1] = $p \leq 0.05$ different from respective Sham
[2] = $p \leq 0.05$ different from Con TAC

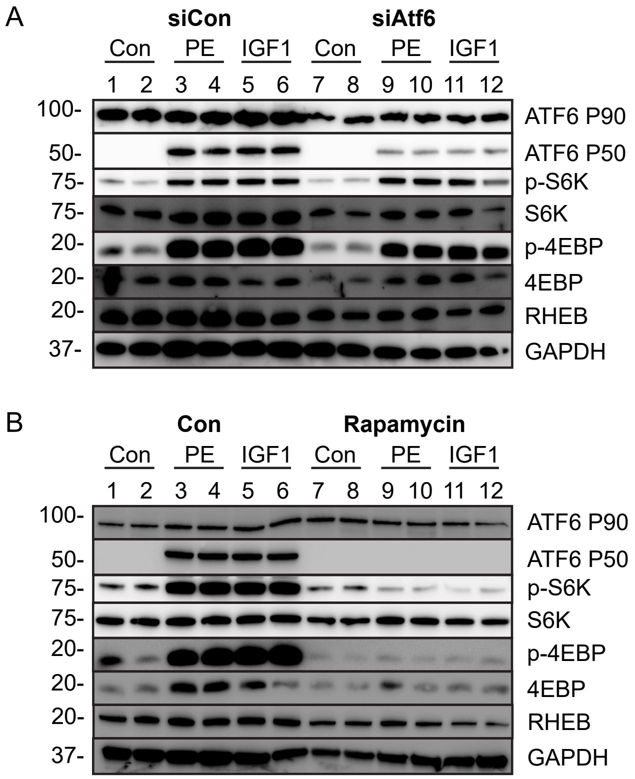

Figure 3.16- Protein synthesis-dependent activation of the UPR during cardiac myocyte hypertrophy.

A, Immunoblot of NRVM transfected with a nontargeted siRNA (siCon) or with siRNA targeted to rat ATF6 (siAtf6) and then treated with or without phenylephrine (PE; 50µM) or IGF1 (100ng/ml) for 6 hours. **B,** Immunoblot of NRVM after treatment with or without phenylephrine (PE; 50µM) or IGF1 (100ng/ml), with or without rapamycin (20nM) for 6 hours, as shown. **C,** Immunoblot of NRVM after co-treatment with or without cyclohexamide (CHX; 100µg/ml) and either phenylephrine (PE; 50µM) or IGF1 (100ng/ml) for 6 hours. **D,** Immunoblot of NRVM after pretreatment with 4-phenylbutyrate (4-PBA; 100µM) for 24 hours and subsequent co-treatment with or without 4-PBA (100µM) and either phenylephrine (PE; 50µM) or IGF1 (100ng/ml) for an additional 6 hours.

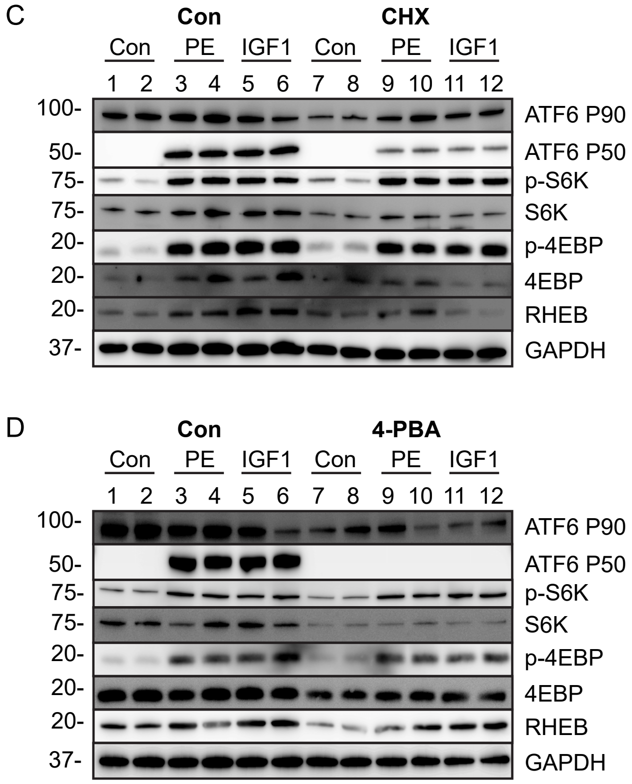

Figure 3.16 (continued)- Caption shown on previous page.

3.4. Discussion

3.4.1. ATF6 is Required for Growth of the Heart

While previous studies reported increased expression of a few ER stress genes in mouse models of pressure overload, implicating ER protein misfolding[14-17], prior to our study here, neither the activation nor the roles for ATF6 in cardiac myocytes during cardiac growth had been examined. Here, we showed, for the first time that ATF6, a major mediator of the UPR, is activated by diverse growth stimuli and that ATF6 is required for growth of the heart in response to these stimuli. We determined that the mechanism of this effect involves ATF6-mediated induction of *RHEB* **(Fig. 3.15A)**. It was surprising to find that ATF6 is required for heart growth, considering the UPR is not widely known to be involved in growth processes. However, this non-canonical role for ATF6 complements its canonical role as a sensor of misfolded proteins in the ER and, as such, a sensor of increases in protein folding demand, which occur during growth. Thus, ATF6 maintains proteostasis and proteome integrity when the heart is stimulated to grow in a compensatory manner.

We also found that, depending on the stimulus, ATF6 target genes are differentially expressed due to the unique effects that the stresses have on ATF6 binding to, and thus, transcriptional activation of ATF6 target genes. Such differential ATF6 target gene induction by treatments that all activate ATF6 suggests that there are yet-to-be-described regulatory layers that fine-tune the ATF6 gene program to best adapt to the conditions. Some possible mechanisms that could contribute to this differential expression are beginning to emerge, as it has been shown that ATF6 can interact with other transcription factors, such as Nrf1, PGC1α and β, and ERRγ,[18-20] which changes the transcriptional programming in ways that fine-tune ATF6 target gene induction.

3.4.2. Rheb in the Heart

Rheb was originally documented as an mTORC1 activator in the brain[21], this role has been demonstrated in numerous other tissues and organs[2, 22, 23]. Global deletion of *Rheb* is embryonic lethal, in part due to cardiac defects[24], demonstrating the importance of Rheb-mediated mTORC1 activation in heart growth and development. The growth-promoting effect of *Rheb* gain-of-function was demonstrated in adult rat ventricular myocytes transfected with adenovirus encoding *Rheb*[25]. However, overexpression of *Rheb* in transgenic mice increased infarct size, in part because Rheb inappropriately decreased autophagy, which is adaptive in this disease setting[26]. Pharmacological inhibition of Rheb in mice subjected to TAC for three weeks was cardioprotective[2]. These findings differ from our study, perhaps because different times after TAC were studied, or different approaches to decreasing Rheb. It is also possible that Rheb induction and mTORC1 activation have different roles in a severe afterload-induced hypertrophy model, such that acute activation works in a compensatory manner, but chronic activation drives decompensation. The αMHC-CRE-dependent conditional deletion of *Rheb* from mouse cardiac myocytes resulted in atrophic hearts, heart failure, and death within 1-2 weeks after birth, a timeframe that aligns with the time of αMHC expression after birth[1, 27]. Although there have been no studies prior to ours mechanistically connecting *Atf6* with *Rheb* induction, one study in tumor cells[28], and another in the setting of Huntington's disease[29], have implicated such a connection and, therefore, support the findings reported here.

3.4.3. Feedback Regulation of ATF6-mediated Growth

Our study describes a mechanism whereby ATF6 matches protein synthesis with folding in times of increased growth; since this constitutes a positive feedback mechanism, we reason that there must also be mechanisms that interrupt this feedback, thereby limiting the rate of growth driven by the ATF6-Rheb-mTORC1 axis. One such mechanism might involve Rheb itself, which has been shown to activate PERK[30]. Mechanisms such as this underscore the complexities of proteostasis, raising questions about how Rheb switches from protein synthesis activator to inhibitor.

3.4.4. Conclusions

The results of our study firmly place ATF6 in a critical position as a determinant of cardiac growth **(Fig. 3.15A)**. Moreover, since ATF6 is ubiquitously expressed, our findings underscore the widespread importance of the ATF6-Rheb-mTORC1-growth signaling axis described here in non-cardiac cells and tissues in addition to the heart.

Chapter 3, in full, is a reprint of the material as it appears in Circulation Research in 2019. Blackwood, E.A., Hofmann, C., Santo Domingo, M., Bilal, A.S., Sarakki, A., Stauffer, W., Arrieta, A., Thuerauf, D.J., Kolkhorst, F., Muller, O.J., Jakobi, T., Dieterich, C., Katus, H.A., Doroudgar, S., and Glembotski, C.C. ATF6 regulates cardiac hypertrophy by transcriptional induction of the mTORC1 activator, Rheb. *Circ Res*. 2019; 124(1):79-93. The dissertation author was the primary investigator and author of this paper.

3.5. References

1. Tamai T, Yamaguchi O, Hikoso S, Takeda T, Taneike M, Oka T, Oyabu J, Murakawa T, Nakayama H, Uno Y, Horie K, Nishida K, Sonenberg N, Shah AM, Takeda J, Komuro I and Otsu K. Rheb (Ras homologue enriched in brain)-dependent mammalian target of rapamycin complex 1 (mTORC1) activation becomes indispensable for cardiac hypertrophic growth after early postnatal period. *J Biol Chem*. 2013;288:10176-87.

2. Wu X, Cao Y, Nie J, Liu H, Lu S, Hu X, Zhu J, Zhao X, Chen J, Chen X, Yang Z and Li X. Genetic and pharmacological inhibition of Rheb1-mTORC1 signaling exerts cardioprotection against adverse cardiac remodeling in mice. *Am J Pathol*. 2013;182:2005-14.

3. Duran RV and Hall MN. Regulation of TOR by small GTPases. *EMBO Rep*. 2012;13:121-8.

4. Wang Y, Zhang Y, Ding G, May HI, Xu J, Gillette TG, Wang H and Wang ZV. Temporal dynamics of cardiac hypertrophic growth in response to pressure overload. *Am J Physiol Heart Circ Physiol*. 2017;313:H1119-H1129.

5. Nakamura A, Rokosh DG, Paccanaro M, Yee RR, Simpson PC, Grossman W and Foster E. LV systolic performance improves with development of hypertrophy after transverse aortic constriction in mice. *Am J Physiol Heart Circ Physiol*. 2001;281:H1104-12.

6. Takaoka H, Esposito G, Mao L, Suga H and Rockman HA. Heart size-independent analysis of myocardial function in murine pressure overload hypertrophy. *Am J Physiol Heart Circ Physiol*. 2002;282:H2190-7.

7. Harvey PA and Leinwand LA. The cell biology of disease: cellular mechanisms of cardiomyopathy. *J Cell Biol*. 2011;194:355-65.

8. Allen DL, Harrison BC, Maass A, Bell ML, Byrnes WC and Leinwand LA. Cardiac and skeletal muscle adaptations to voluntary wheel running in the mouse. *J Appl Physiol (1985)*. 2001;90:1900-8.

9. Chung E, Heimiller J and Leinwand LA. Distinct cardiac transcriptional profiles defining pregnancy and exercise. *PLoS One*. 2012;7:e42297.

10. Bernardo BC, Weeks KL, Pretorius L and McMullen JR. Molecular distinction between physiological and pathological cardiac hypertrophy: experimental findings and therapeutic strategies. *Pharmacol Ther*. 2010;128:191-227.

11. Martindale JJ, Fernandez R, Thuerauf D, Whittaker R, Gude N, Sussman MA and Glembotski CC. Endoplasmic reticulum stress gene induction and

protection from ischemia/reperfusion injury in the hearts of transgenic mice with a tamoxifen-regulated form of ATF6. *Circ Res*. 2006;98:1186-93.

12. Simpson P. Stimulation of hypertrophy of cultured neonatal rat heart cells through an alpha 1-adrenergic receptor and induction of beating through an alpha 1- and beta 1-adrenergic receptor interaction. Evidence for independent regulation of growth and beating. *Circ Res*. 1985;56:884-94.

13. Basso AD, Mirza A, Liu G, Long BJ, Bishop WR and Kirschmeier P. The farnesyl transferase inhibitor (FTI) SCH66336 (lonafarnib) inhibits Rheb farnesylation and mTOR signaling. Role in FTI enhancement of taxane and tamoxifen anti-tumor activity. *J Biol Chem*. 2005;280:31101-8.

14. Okada K, Minamino T, Tsukamoto Y, Liao Y, Tsukamoto O, Takashima S, Hirata A, Fujita M, Nagamachi Y, Nakatani T, Yutani C, Ozawa K, Ogawa S, Tomoike H, Hori M and Kitakaze M. Prolonged endoplasmic reticulum stress in hypertrophic and failing heart after aortic constriction: possible contribution of endoplasmic reticulum stress to cardiac myocyte apoptosis. *Circulation*. 2004;110:705-12.

15. Sari FR, Widyantoro B, Thandavarayan RA, Harima M, Lakshmanan AP, Zhang S, Muslin AJ, Suzuki K, Kodama M and Watanabe K. Attenuation of CHOP-mediated myocardial apoptosis in pressure-overloaded dominant negative p38alpha mitogen-activated protein kinase mice. *Cell Physiol Biochem*. 2011;27:487-96.

16. Park CS, Cha H, Kwon EJ, Sreenivasaiah PK and Kim DH. The chemical chaperone 4-phenylbutyric acid attenuates pressure-overload cardiac hypertrophy by alleviating endoplasmic reticulum stress. *Biochem Biophys Res Commun*. 2012;421:578-84.

17. Liu X, Kwak D, Lu Z, Xu X, Fassett J, Wang H, Wei Y, Cavener DR, Hu X, Hall J, Bache RJ and Chen Y. Endoplasmic reticulum stress sensor protein kinase R-like endoplasmic reticulum kinase (PERK) protects against pressure overload-induced heart failure and lung remodeling. *Hypertension*. 2014;64:738-44.

18. Vekich JA, Belmont PJ, Thuerauf DJ and Glembotski CC. Protein disulfide isomerase-associated 6 is an ATF6-inducible ER stress response protein that protects cardiac myocytes from ischemia/reperfusion-mediated cell death. *J Mol Cell Cardiol*. 2012;53:259-67.

19. Wu J, Ruas JL, Estall JL, Rasbach KA, Choi JH, Ye L, Bostrom P, Tyra HM, Crawford RW, Campbell KP, Rutkowski DT, Kaufman RJ and Spiegelman BM. The unfolded protein response mediates adaptation to exercise in skeletal muscle through a PGC-1alpha/ATF6alpha complex. *Cell Metab*. 2011;13:160-9.

20. Misra J, Kim DK, Choi W, Koo SH, Lee CH, Back SH, Kaufman RJ and Choi HS. Transcriptional cross talk between orphan nuclear receptor ERRgamma and transmembrane transcription factor ATF6alpha coordinates endoplasmic reticulum stress response. *Nucleic Acids Res*. 2013;41:6960-74.

21. Yamagata K, Sanders LK, Kaufmann WE, Yee W, Barnes CA, Nathans D and Worley PF. rheb, a growth factor- and synaptic activity-regulated gene, encodes a novel Ras-related protein. *J Biol Chem*. 1994;269:16333-9.

22. Potheraveedu VN, Schopel M, Stoll R and Heumann R. Rheb in neuronal degeneration, regeneration, and connectivity. *Biol Chem*. 2017;398:589-606.

23. Heard JJ, Fong V, Bathaie SZ and Tamanoi F. Recent progress in the study of the Rheb family GTPases. *Cell Signal*. 2014;26:1950-7.

24. Goorden SM, Hoogeveen-Westerveld M, Cheng C, van Woerden GM, Mozaffari M, Post L, Duckers HJ, Nellist M and Elgersma Y. Rheb is essential for murine development. *Mol Cell Biol*. 2011;31:1672-8.

25. Wang Y, Huang BP, Luciani DS, Wang X, Johnson JD and Proud CG. Rheb activates protein synthesis and growth in adult rat ventricular cardiomyocytes. *J Mol Cell Cardiol*. 2008;45:812-20.

26. Sciarretta S, Zhai P, Shao D, Maejima Y, Robbins J, Volpe M, Condorelli G and Sadoshima J. Rheb is a critical regulator of autophagy during myocardial ischemia: pathophysiological implications in obesity and metabolic syndrome. *Circulation*. 2012;125:1134-46.

27. Cao Y, Tao L, Shen S, Xiao J, Wu H, Li B, Wu X, Luo W, Xiao Q, Hu X, Liu H, Nie J, Lu S, Yuan B, Han Z, Xiao B, Yang Z and Li X. Cardiac ablation of Rheb1 induces impaired heart growth, endoplasmic reticulum-associated apoptosis and heart failure in infant mice. *Int J Mol Sci*. 2013;14:24380-98.

28. Schewe DM and Aguirre-Ghiso JA. ATF6alpha-Rheb-mTOR signaling promotes survival of dormant tumor cells in vivo. *Proc Natl Acad Sci U S A*. 2008;105:10519-24.

29. Fernandez-Fernandez MR, Ferrer I and Lucas JJ. Impaired ATF6alpha processing, decreased Rheb and neuronal cell cycle re-entry in Huntington's disease. *Neurobiol Dis*. 2011;41:23-32.

30. Tyagi R, Shahani N, Gorgen L, Ferretti M, Pryor W, Chen PY, Swarnkar S, Worley PF, Karbstein K, Snyder SH and Subramaniam S. Rheb Inhibits Protein Synthesis by Activating the PERK-eIF2alpha Signaling Cascade. *Cell Rep*. 2015.

Chapter 4: Pharmacologic ATF6 Activation Confers Global Protection in Widespread Disease Models by Reprograming Cellular Proteostasis

4.1. Introduction

Pharmacologic activation of stress-responsive signaling pathways provides a promising approach for ameliorating imbalances in proteostasis associated with diverse diseases. However, this approach has not been employed *in vivo*. Here we show, using a mouse model of myocardial ischemia/reperfusion, that selective pharmacologic activation of the ATF6 arm of the unfolded protein response (UPR) during reperfusion, a typical clinical intervention point after myocardial infarction, transcriptionally reprograms proteostasis, ameliorates damage and preserves heart function. These effects were lost upon cardiac myocyte-specific *Atf6* deletion in the heart, demonstrating the critical role played by ATF6 in mediating pharmacologically activated proteostasis-based protection of the heart. Pharmacological activation of ATF6 is also protective in renal and cerebral ischemia/reperfusion models, demonstrating its widespread utility. Thus, pharmacologic activation of ATF6 represents a proteostasis-based therapeutic strategy for ameliorating ischemia/reperfusion damage, underscoring its unique translational potential for treating a wide range of pathologies caused by imbalanced proteostasis.

4.2. Materials and Methods

4.2.1.Laboratory animals

The research reported in this article complies with all relevant ethical regulations and has been reviewed and approved by the San Diego State University Institutional Animal Care and Use Committee (IACUC), and conforms to the Guide for the Care and Use of Laboratory Animals published by the National Research Council. ATF6-floxed mice were a generous gift from Gokhan S. Hotamisligil. Briefly, ATF6-floxed mice were generated with a targeting construct flanking exons 8 and 9 of ATF6 with LoxP sequences on a C57B/6J background, as previously described[32]. For preclinical efficacy testing of experimental compounds, wild-type (WT) 10-week old male or female C57B/6J mice were used (The Jackson Laboratory; Bar Harbor, ME). For some experiments we determined the numbers of animals to use based on a predictive power analysis to achieve 5% error and 80% power, or using the resource equation method[33]. In other experiments, the numbers of animals to use were determined practically, based on previous experiments designed to determine, for example, surgery mortality rates and the approximate magnitude of changes in the measured parameters. This was the case in experiments using ATF6 cKO mice. Our previous experiments showed that the variation in infarct size between litermates post-in vivo I/R surgeries was low, amounting to $\leq$ 5%[10]. All animal work was performed at the same time of the circadian rhythm typical of animals housed on a 12-hour light-dark cycle with ad libitum feeding. All studies in which compound 147 was administered to mice were conducted such that the surgeon and data analyst were blinded to the group assignments. Prior to all experiments, animals were assigned codes by one investigator, while investigator #2 was blinded to animal codes and nature of the treatments, e.g. control vs compound 147, performed the surgeries and echocardiographic analysis. Investigator #3 analyzed the areas at risk and infarct regions for all cardiac, renal, and cerebral ischemia reperfusion injury models; as with investigator #2, this investigator was also blinded to the animal codes and treatments. Animals were not decoded until after all surgical, functional and histological analyses were fully analyzed and relevant statistical assessments had been calculated for all parameters measured. For all animal experiments involving conditional knockout of ATF6, ATF6-floxed littermates were randomly assigned to receive AAV-control or AAV-Cre (1:1 ratio) to minimize mouse-to-mouse variability. Animals involved in I/R experiments involving administration of either the control compound, or compound 147, wild-type 10-week old male or female C57B/6J littermates. Consistency and, therefore, minimal variability of infarct sizes following ex vivo and in vivo I/R studies was ensured through blinded measurements of areas at risk relative to total left ventricular areas, as described above. As a result, we observe a variation in AAR/LV within experimental groups of $\leq$ 5%. For ex vivo I/R studies, mechanical error and variability were maintained as low as possible by minimizing the time between animal sacrifice and initiation of retroperfusion; our criteria is that this process must take less than 60 seconds. We find that this results in a relatively rapid progression to equilibration of heart function during ex vivo perfusion; our criteria for reaching equilibration of LVDP is < 15 min after initiation or retroperfusion on the Langendorff apparatus.

4.2.2. Patient samples

Human heart explants were obtained from ventricular myocardium of patients with advanced ischemic heart failure. Control patient ventricular explants were obtained from non-failing donor hearts deemed unsuitable for transplantation for non-cardiac reasons. Samples were collected with informed consent and complying with all relevant ethical regulations as previously described[34]. All study procedures were approved by the University of Pennsylvania Hospital Institutional Review Board.

4.2.3. Adeno-associated virus serotype 9 (AAV9)

The plasmid encoding the human cardiac troponin T promoter driving Cre-recombinase was provided as a gift from Dr. Oliver Muller[35]. AAV9 preparation and injection were carried out as previously described[10,24]. Non-anesthetized 8-week old ATF6-floxed mice were injected with 100 μL of AAV9-control or AAV9-cTnT-Cre containing $1x10^{11}$ viral particles via the lateral tail vein using a 27-guage syringe and housed for 2 weeks before either sacrifice or experimental initiation.

4.2.4. Adenovirus

Construction of plasmid vectors encoding FLAG-tagged full length inactive ATF6 [ATF6(1-670)], TCR-α-HA, and empty vector (AdV-Con) has been previously described[10,24].

4.2.5. Cardiomyocyte isolation, culture and experimental design

Neonatal rat ventricular myocytes (NRVM) were isolated via enzymatic digestion, purified by Percoll density gradient centrifugation, and maintained in Dulbecco's modified Eagle's medium (DMEM)/F12 supplemented with 10% fetal bovine serum (FBS) and antibiotics (100 units/ml penicillin and 100 µg/ml streptomycin) on plastic culture plates that had been pre-treated with 5 µg/ml fibronectin, as previously described[10,24]. For all NRVM experiments, plating density was maintained at 4.5×10^5 cells/well on 12-well plates. Adult mouse ventricular myocytes (AMVM) were isolated from WT or ATF6 cKO mice 24 hours after IV injection of control compound (2mg/kg) or compound 147 (2mg/kg). AMVM isolation was performed by cannulating the ascending aorta, followed by retroperfusion and collagenase digestion, as previously described[10].

For all experiments, AMVM were plated at a density of 5.0 x 10^5 cells/well on 24-well plates that had been pre-treated with laminin (10 µg/ml) and incubated in maintaining medium (MEM medium, 1x insulin-transferrin-selenium, 10 mM HEPES, 1.2 mM $CaCl_2$ and 0.01% bovine serum albumin, 25 µM blebbistatin) for 16 hours before initiating experiments as previously described[10]. Sixteen hours after plating NRVM and AMVM were treated with control compound (10 µM), compound 147 (10 µM) or tunicamycin (10 µg/ml) for 24 hours in DMEM/F12 supplemented with bovine serum albumin (BSA) (1 mg/ml) for NRVM, or maintaining media for AMVM. For *in vitro* ischemia/reperfusion (I/R), ischemia was simulated by replacing all culture media with 0.5 ml of glucose-free DMEM containing 2% dialyzed FBS with either the control compound (10 µM), or compound 147 (10 µM), then incubated at 0.1% O_2 in a hypoxia chamber with an oxygen controller (ProOx P110 oxygen controller, Biospherix, Parish, NY) for 8 hours or 3 hours for NRVM or AMVM, respectively, as previously described[10]. Reperfusion was simulated by replacing culture media with DMEM/F12 supplemented with BSA (1 mg/ml) for NRVM or maintaining media for AMVM and incubating at 21% O_2 for an additional 24 hours. NRVM and AMVM reperfusion media were supplemented with control compound (10 µM), compound 147 (10 µM) throughout the duration of the reperfusion period. Viability was determined as numbers of calcein-AM-labeled NRVM or rod-shaped calcein-AM-labeled AMVM, using calcein-AM green (Thermo Fisher). Images were obtained with an IX70 fluorescence microscope (Olympus, Melville, NY). Numbers of viable, calcein-AM green-positive cells were counted using ImageJ or Image-Pro Plus software (Medium Cybernetics, Rockville, MD).

4.2.6. Small interfering RNA (siRNA) transfection

Transfection of siRNA into NRVM was achieved using HiPerfect Transfection Reagent (Qiagen, Valencia, CA) following the vendor's protocol. Briefly, NRVM culture medium was replaced with DMEM/F12 supplemented with 0.5% FBS without antibiotics, 120 nM siRNA, and 1.25 µl HiPerfect / 1 µl siRNA, then incubated for 16 hours, after which the culture medium was replaced with DMEM/F12 supplemented with BSA (1 mg/ml) for an additional 48 hours. The sequence of siRNA targeting rat ATF6 was 5-GCUCUCUUUGUUGUUGCUUAGUGGA-3, the sequence targeting rat catalase was 5-GGAACCCAAUAGGAGAUAAACUUAA-3 (cat# CatRSS302058, Stealth siRNA, Thermo Fisher), and the sequence targeting rat grp78 was 5-AGUGUUGGAAGAUUCUGA-3 (cat# 4390771, Stealth siRNA, Thermo Fisher) as previously described[10]. A non-targeting sequence (cat# 12935300, Thermo Fisher) was used as a control siRNA.

4.2.7. Immunoblot analysis

NRVM were lysed and subjected to immunoblot analysis, as previously described[10]. In brief, cultures were lysed with VC lysis buffer made from 20 mM Tris-HCl (pH 7.5), 150 mM NaCl, 0.1% SDS, 1% Triton X-100, protease inhibitor cocktail (Roche Diagnostics, Indianapolis, IN) and phosphatase inhibitor cocktail (Roche Diagnostics). Samples comprising 10 µg of protein were mixed with Laemmli sample buffer, boiled, then subjected to SDS-PAGE followed by transfer onto PVDF membranes for immunoblotting. Full-length Atf6 (p90) was detected with an antibody from SAB Signalway Antibody (1:1000, cat# 32008, College Park, MD), while active Atf6 (p50) was detected with an antibody from Proteintech (1:1000, cat# 24169-1-AP, Rosemont, IL). Other antibodies used include: anti-KDEL antibody (1:8,000, cat# ADI-SPA-827 , Enzo Life Sciences, Farmingdale, NY), which was used to detect GRP78, anti-catalase (1:1000, cat# ab16731, Abcam), anti-IRE1 (1:500, cat# sc-390960, Santa Cruz), anti-XBP1s (1:1000, cat# 619502, BioLegend, San Diego, CA), anti-phospho-PERK (1:1000, cat# 3179, Cell Signaling), anti-PERK (1:1000, cat# 3192, Cell Signaling), anti-Anp (1:4000, cat# T-4014 , Peninsula), anti-Gapdh (1:25000, cat# G109a, Fitzgerald Industries International Inc.), HA-probe F-7 (Santa Cruz, SC-7392; 1:1,000) and anti-FLAG (1:3,000, cat#F1804, Sigma-Aldrich, St. Louis, MO). The oxidation state of ATF6 in NRVM treated with 147 was analyzed by gel-shift essentially as previously described[32]. Briefly, cells were lysed in low-stringency lysis buffer comprising 20 mM Tris-HCl (pH 7.5), 150 mM NaCl, 1% Triton X-100, protease inhibitor cocktail (Roche Diagnostics, Indianapolis, IN) and phosphatase inhibitor cocktail (Roche Diagnostics) and 20 µM 4-Acetamido-4'-Maleimidylstilbene-2,2'-Disulfonic Acid, Disodium Salt (AMS) (Thermo Fisher, cat# A485). AMS binds covalently to reduced thiols, typically on cysteine residues, and increases their molecular mass in SDS-PAGE. Thus, proteins that exhibit an upward shift when analyzed under non-reducing conditions compared to reducing are considered to have reduced thiols.

4.2.8. RT-qPCR

Total RNA was extracted from left ventricular extract using the RNeasy Mini kit (Qiagen) as previously described[10].

4.2.9. Immunocyto- and immunohistochemistry

NRVM and AMVM were plated on fibronectin and laminin-coated glass chamber slides, respectively as previously described[10]. In brief, cells were fixed with 4%

paraformaldehyde, followed by permeabilization with 0.5% Triton-X. Adult mouse hearts were paraffin-embedded after fixation in neutral buffered 10% formalin via abdominal aorta retroperfusion as previously described[10]. The infarct border zone was imaged in hearts subjected to surgical I/R. The infarct border zone was identified as an area that stained positively for the cardiac muscle protein, tropomyosin that was adjacent to an area that did not stain for tropomysin (infarct zone) due to the absence of viable myocytes. The left ventricular free wall was imaged in sham and non-injured hearts. Primary antibodies used were anti-α-actinin (1:200, cat# A7811, Sigma-Aldrich), anti-tropomyosin (1:200, cat# T9283, Sigma-Aldrich), anti-GRP78 (C-20, 1:30, cat# SC-1051, Santa Cruz), anti-catalase (1:100, Abcam), anti-ATF6 (targeting to N-terminus of ATF6, 1:50, cat# sc-14250, Santa Cruz), and anti-cleaved caspase-3 (1:100, cat# D175, Cell Signaling). Slides were incubated with appropriate fluorophore-conjugated secondary antibodies (1:100, Jackson ImmunoResearch Laboratories, West Grove, PA) followed by nuclei counter stain Topro-3 (1:2000, Thermo Fisher). Images were obtained using laser scanning confocal microscopy on an LSM 710 confocal laser scanning microscope (Carl Zeiss, Oberkochen, Germany).

4.2.10. ERAD Assay

ER-associated degradation (ERAD) was determined using a C-terminal HA-tagged version of the model chronic misfolded substrate, TCR-α-HA as previously described[24].

4.2.11. Luciferase Secretion Assay

Secretory capacity of cardiac myocytes was determined essentially as described[36]. Briefly, NRVM were cotransfected with pcDNA plasmid as well as p-SV-β-

galactosidase control vector and pCMV-GLuc plasmid (NEB, N8081S) using FuGENE6 (2 μg cDNA, 2:1, FuGENE:cDNA).

4.2.12. Chromatin immunoprecipitation (ChIP)

ChIP assays were performed essentially as previously described[10]. Briefly, AdV-FLAG-ATF6(1-670) infected NRVM were treated with fixing buffer (50 mM HEPES-KOH, pH 7.5, 100 mM NaCl, 1 mM EDTA, 0.5 mM EGTA, and 1% formaldehyde) for 10 min, quenched with 125 mM glycine, and scraped into ice-cold PBS. Cells were centrifuged, resuspended in lysis buffer (50 mM HEPES, pH 7.9, 140 mM NaCl, 1 mM EDTA, 10% glycerol, 0.5% NP-40, 0.25% Triton X-100, and protease inhibitor cocktail), and incubated on ice for 10 min. After centrifugation at 1,800 x g for 10 min, the pellets were washed with buffer containing 10 mM Tris, pH 8.1, 200 mM NaCl, 1 mM EDTA, and 0.5 mM EGTA, resuspended in shearing buffer (0.1% SDS, 1 mM EDTA, and 10 mM Tris, pH 8.1), and then transferred to microTUBEs (Covaris, Woburn, MA). Chromatin was sheared by sonication for 15 min using an M220 focused ultrasonicator (Covaris). Triton X-100 and NaCl were added to the final concentration of 1% Triton and 150 mM NaCl followed by centrifugation at 16,000 x g for 10 min. Immunoprecipitation was performed by incubated 140 μl of sheared chromatin with 5 μg of anti-FLAG antibody (cat# F1804, Sigma-Aldrich) and 260 μl of immunoprecipitation buffer (0.1% SDS, 1 mM EDTA, 10 mM Tris, pH 8.1, 1% Triton X-100, and 150 mM NaCl) at 4°C overnight. Protein A/G magnetic beads (5 μl, BcMag, Bioclone, San Diego, CA) were added to the mixtures and incubated at 4°C for 1.5 h. Magnetic beads were sequentially washed with low salt wash buffer (0.1% SDS, 1% Triton X-100, 2 mM EDTA, 20 mM HEPES-KOH, pH7.9, and 150 mM NaCl), high salt wash buffer with 500 mM NaCl, LiCl wash buffer (100 mM Tris-HCl, pH 7.5, 0.5 M LiCl, 1% NP-40, and 1% deoxycholate acid), and TE buffer (10 mM Tris-HCl, pH 8.0 and 0.1 mM EDTA). Immune complexes were eluted by incubating beads with proteinase K digestion buffer (20 mM HEPES, pH 7.9, 1 mM EDTA, 0.5% SDS, and 0.4 mg/ml proteinase K) at 50°C for 15 min. Formaldehyde crosslinking was reversed by incubating with 0.3 M NaCl and 0.3 mg/ml RNase A at 65°C overnight. Samples were further incubated with 550 μg/ml proteinase K at 50°C for 1h. DNA was purified using NucleoSpin Gel and PCR Clean-up Kit (Macherey-Nagel, Bethlehem, PA) and eluted by 30 μl of water. Two μl of DNA was used for qRT-PCR analysis with primers targeting rat Hspa5 (5’-GGTGGCATGAACCAACCAG-3’ and 5’-GCTTATATATCCTCCCCGC-3’), rat Cat ERSE-1 (5’-CTACCCACCAATTAGTACCAAATAA-3’ and 5’-AGAAGGGACAGGATTGGAAG-3’), rat Cat ERSE-2 (5’-CACATTCTAGGGACAGTGTAGATG-3’ and 5’-ACCTTGATTATGGGCTGTGG-3’), rat Pdia6 ERSE (5’-CACATGAGCGAAATCCACAGA-3’ and 5’-ACTAGTCGAGCCATGCTGAT-3’), rat HO-1 (5’-GGGCTACTCCCGTCTTCCTG-3’ and 5’-CCTTTCCAGAACCCTCTACTCTACTC-3’), or rat Gapdh (5’-ATGCGGTTTCTAGGTTCACG-3’ and 5’-ATGTTTTCTGGGGTGCAAAG-3’). Pdia6 served as a positive control for a known ATF6 target gene in cardiac myocytes while HO-1 and Gapdh served as negative controls as previously described[37]. ChIP signals obtained from the qRT-PCR were normalized to the input DNA.

4.2.13. *Ex vivo* ischemia/reperfusion

Hearts from WT or ATF6 cKO mice that had previously received 2 mg/kg IV administration of control compound or compound 147 were rapidly excised and cannulated via the ascending aorta and subjected to global I/R, as previously described[38]. Here, the hearts were subjected to 20 minutes global no-flow ischemia followed by reperfusion for 1 hour. Left ventricular developed pressure (LVDP) was measured using a pressure sensor balloon placed into the left ventricle and analyzed using Powerlab software (ADInstruments, Colorado Springs, CO).

4.2.14. *In vivo* myocardial ischemia/reperfusion

Surgical myocardial I/R was performed as previously described[10]. Briefly, mice were anesthetized with 2% isoflurane and a thoracotomy was performed to isolate the heart, after which the left anterior descending coronary artery (LAD) was ligated with a 6-0 Prolene suture for 30 minutes, followed by suture removal and either 24 hours or 7 days of reperfusion. Regional ischemia was confirmed by visual inspection of the discoloration of the myocardium distal of the ligation, which is characteristic of impaired blood flow. Animals assigned as shams underwent the thoracotomy surgical procedure, but weren’t subjected to LAD ligation. Animals were randomly assigned to experimental groups prior to outset of the experiment by a single investigator, while the surgeon and data analyst were blinded to group assignments. Animals designated to receive either control compound or compound 147 at the time of reperfusion received 2 mg/kg of respective compounds via IV injection 5 minutes prior to release of the ligation. Twenty-four hours after reperfusion, 1% of Evans Blue was injected apically to determine the area at risk (AAR). Hearts were harvested and 1-mm sections of the hearts were stained with 1% 2,3,5-triphenyltetrazolium chloride (TTC) to measure the infarcted area (INF) as previously described[36]. The AAR, INF and left ventricle area (LV) from digitized images of heart sections were analyzed using ImageJ software. For all infarct data presented, respective AAR was normalized to total LV area and all compared experiments displayed the same AAR/LV ratios. A separate investigator analyzed the AAR, INF, and LV and was blinded to the animal assignments. Just prior to sacrifice, post-I/R, animals were anesthetized and 0.5 mL of arterial blood were obtained via inferior vena cava puncture as previously described[33]. Blood was placed in heparin- and EDTA-coated vacutainer (BD Vacutainer) and centrifuged at 1800 x g for 10 minutes and plasma samples were analyzed for cardiac troponin I with a Mouse cTnI High-Sensitivity ELISA kit (Life Diagnostics, Inc.).

4.2.15. *In vivo* renal ischemia/reperfusion

Surgical renal I/R was performed as previously described[39]. Briefly, mice were anesthetized with 2% isoflurane and a 3cm incision was made upon the abdominal midline and the abdominal cavity entered via an incision along the linea alba. The right kidney was visualized and separated from surrounding connective tissue. The right ureter and right renal portal system was permanently ligated and a right unilateral nephrectomy performed. Subsequently, the left kidney was visualized and separated from surrounding connective tissue. A Bulldog Clamp (Fine Science Tools, Foster City, CA) was applied temporarily ligating the left renal portal system for a period of 30 minutes. Global ischemia was confirmed by visual inspection of the discoloration of the kidney of the ligation, which is characteristic of impaired blood flow. After that duration, the Bulldog Clamp was removed and the abdomen closed with instant tissue adhesive. Animals were randomly assigned to experimental groups prior to outset of the experiment by a single investigator, while the data analyst was blinded to experiment assignments. Animals designated to receive either control compound or compound 147 at the time of reperfusion received 2 mg/kg of respective compounds via IV injection 5 minutes prior to release of the ligation. Twenty-four hours after reperfusion, kidneys were harvested and 1-mm sections of the kidneys were stained with 1% TTC to measure the infarcted area (INF) as previously described[39]. Just prior to sacrifice, post-I/R, animals were anesthetized and 0.5 mL of arterial blood were obtained via inferior vena cava puncture as previously described[40]. Blood was placed in heparin- and EDTA-coated vacutainer (BD Vacutainer) and centrifuged at 1800 x g for 10 minutes and plasma samples were analyzed for creatinine as a measure of glomerular filtration rate and renal functional output with a Creatinine Assay kit (Abcam).

4.2.16. *In vivo* cerebral ischemia/reperfusion

Surgical cerebral I/R was performed as previously described[11]. Briefly, mice were anesthetized with 2% isoflurane and a 3 cm incision was made along the midline of the ventral surface of the neck along the left side of the trachea. The left external and internal carotid arteries were visualized and dissected from surrounding connective tissue without disturbing tangential nerves. An 8-0 catheter filament 10mm in length (Doccol Corporation) was inserted into the middle cerebral artery (MCA) via the internal carotid artery. This occluded blood flow to the MCA and was left in position for a period of 30 minutes. After that duration, the catheter was removed and the neck closed with instant tissue adhesive. Animals were randomly assigned to experimental groups prior to outset of the experiment by a single investigator, while the data analyst was blinded to experimentalassignments. Animals designated to receive either control compound or compound 147 at the time of reperfusion received 2 mg/kg of respective compounds via IV injection 5 minutes prior to release of the ligation. Twenty-four hours after reperfusion, brains were harvested and 1-mm sections of the brains were stained with 1% TTC to measure the infarcted area (INF) as previously described[41]. Just prior to sacrifice animals were assigned a behavioral score to assess the severity of neurological function and deficit as a result of the cerebral ischemia. The scoring was performed based on the Bederson Neurological Examination Grading System[42], where a grade of 0 corresponded to a normal function with no observable deficit, grade 1 to a moderate deficit with animals exhibiting forearm flexion, grade 2 to a severe deficit with decreased resistance to a lateral push when suspended by the tail and lethargy, and grade 3 to a severe deficit with extreme lethargy and circling behavior in the cage.

4.2.17. Hepatic triglyceride assay

Hepatic triglyceride assay was performed as previously described[43]. Briefly, livers were harvested and 10mg extracts were homogenized and analyzed for triglyceride content using the EnzyChrom Triglyceride Assay Kit (BioAssay Systems).

4.2.18. Transthoracic echocardiography

Transthoracic echocardiography was performed using an ultrasound imaging system (Vevo 2100 System, Fujifilm VisualSonics, Toronto, Ontario, Canada) as described[24]. Diastolic function was determined as previously described[40]. Briefly, echocardiography coupled with pulse-wave Doppler was used to visualize trans-mitral flow velocities and were recorded by imaging the mitral orifice at the point of the mitral leaflets. Waveforms were recorded and analyzed for peak early- and late-diastolic transmitral flow velocities corresponding to E and A waves, respectively.

4.2.19. Acute isoproterenol myocardial damage

Myocardial damage was induced by administering high-dose (200 mg/kg) isoproterenol via intraperitoneal injection in mice as previously described[40].

4.2.20. Malondialdehyde assay

Lipid peroxidation was determined by measuring the levels of malondialdehyde (MDA) using a TBARS assay kit (Cayman Chemical, Ann Arbor, MI) according to the manufacturer's instructions as previously described[10].

4.2.21. *In vivo* experimental compound administration

Control compound and compound 147 were suspended to a final concentration of 0.2 mg/mL in 10% DMSO. Mice were weighed prior to administration of compounds and, subsequently, non-anesthetized 10-week old WT or ATF6 cKO mice were injected with ~250 µL of stock compounds via the lateral tail vein depending upon body mass to ensure accurate administration of 2 mg/kg. This dose was established in preliminary experiments with the control compound or compound 147 where it was shown to activate Atf6 *in vivo*; the prototypical UPR inducer, tunicamycin, which was also administered to mice at 2 mg/kg, as previously shown[44] was used as a control. Since compound 147 and tunicamycin have similar molecular weights, this dose of 147 is near the molar equivalent of the typical dose of tunicamycin. It is relevant to note that for compound 147, a dose of 2 mg/kg is similar to FDA-approved cardiovascular drugs, such as many angiotensin-converting enzyme (ACE) inhibitors, which are used in small-animal models at 2 mg/kg[45].

4.2.22. Statistics

For studies involving induction of myocardial damage, either through surgical I/R or isoproterenol administration, cohort sizes were based on a predictive power analysis to achieve 5% error and 80% power. All acute *in vivo* I/R studies in which compound 147 were conducted such that the surgeon and data analyst was blinded to the group assignments. Two-group comparisons were performed using Student's two-tailed t-test, and all multiple group comparisons were performed using a one-way ANOVA with a Newman-Keuls post-hoc analysis. Data are represented as mean with all error bars indicating ± s.e.m. $^{*}P \leq 0.05$, $^{**}P \leq 0.01$, $^{***}P \leq 0.001$.

4.3. Results

4.3.1. ATF6 in cardiac myocytes protects the heart from I/R injury

Given their roles in contraction, the viability of cardiac myocytes is crucial for heart function, and cardiac myocyte death during I/R leads to impairment of this function[17]. Accordingly, we examined the effects of I/R on proteostasis in isolated cardiac myocytes and in the mouse heart, positing that I/R disrupts proteostasis, leading to activation of all three arms of the UPR, and that the ATF6 arm induces genes that adaptively reprogram proteostasis, decrease myocyte death and provide cardioprotection from I/R damage **(Fig. 4.1a)**. Consistent with this hypothesis was our finding that I/R activated ATF6, as well as the IRE1 and PERK arms of the UPR in cultured cardiac myocytes, albeit to a lesser extent than the chemical activator of the UPR, tunicamycin (TM) **(Fig 4.2a-d)**. As a measure of ATF6 activation, we examined the expression of two known ATF6 target genes, glucose regulated protein 78 kDa

(*Grp78*), a well-studied ER HSP70 chaperone, also known as BiP[21], which participates in ER protein folding, and catalase (*Cat*), a prominent member of a novel antioxidant gene program recently shown to be induced by ATF6[10]. In accordance with the increased activity of ATF6 in response to I/R, both *Grp78* and *Cat* were induced in cultured cardiac myocytes **(Fig 4.2a, e, f, g)**.

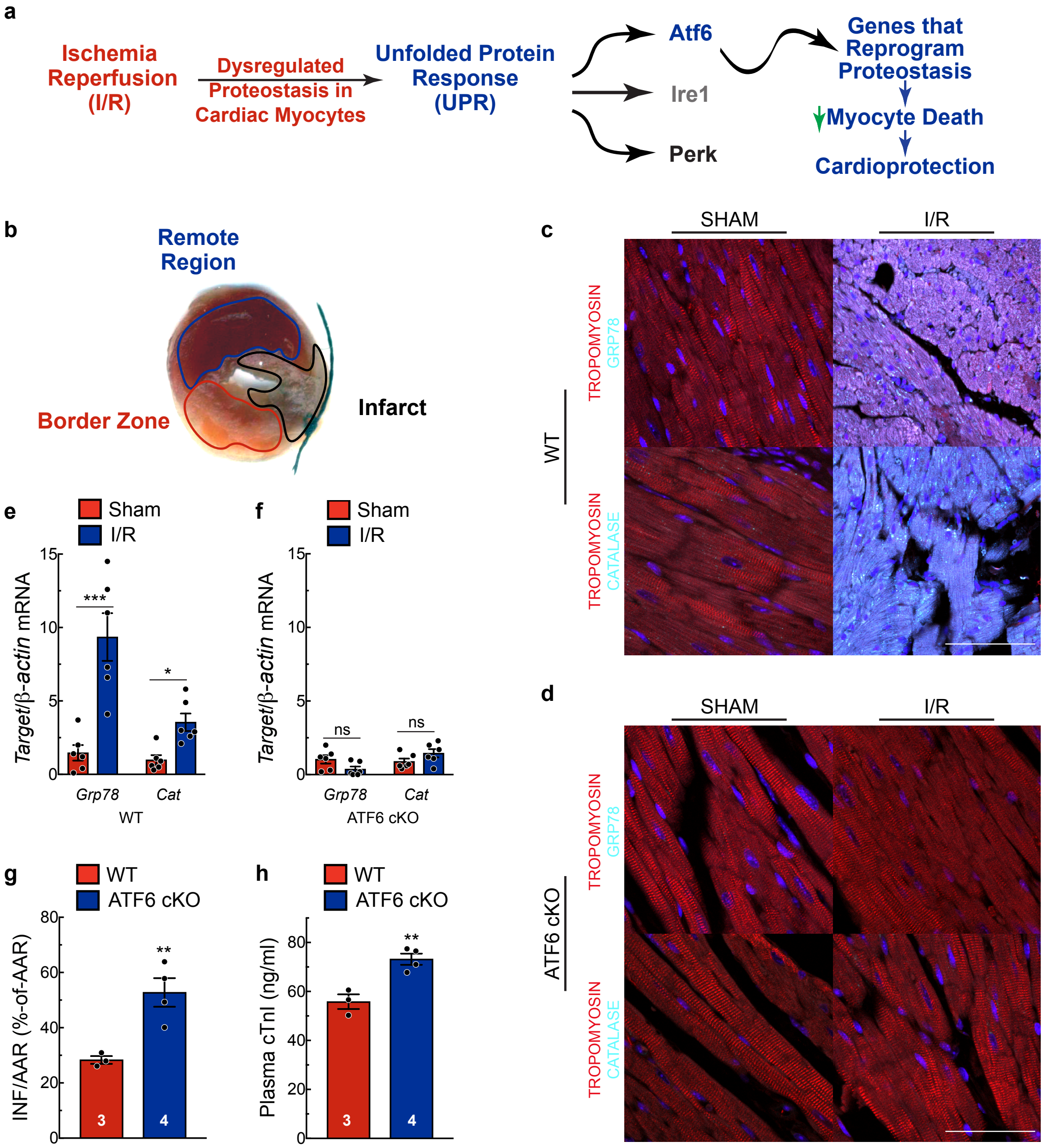

Figure 4.1– ATF6 in cardiac myocytes protects the heart from I/R injury.

a, Activation of the unfolded protein response (UPR) by ischemia/reperfusion (I/R) in the heart. **b,** Post-AMI cross section of the left ventricle of a mouse heart after I/R and TTC staining to identify the infarct region (black), border zone (red) CAT (cyan), tropomyosin (red), and nuclei (TOPRO-3) in the border zone of wild-type (WT) (**c**) or ATF6 cKO (**d**) hearts subjected to either sham or I/R surgery with 24h of reperfusion. Tissue sections are representative images from one mouse per condition. Scale bar represents 50µm. **e,f,** Quantitative real-time PCR (qPCR) for *Grp78* or *Cat* in sham or border zone of post-I/R hearts in WT (n=6) (**e**), ATF6 cKO (n=6) (**f**). **g,h,** Infarct sizes (**h**) and plasma cardiac troponin I (cTnI) (**i**) in WT (n=3) and ATF6 cKO (n=4) mice post-I/R. **i,j,** Left ventricular developed pressure (LVDP) (**i**) and relative infarct sizes (**j**) post-*ex vivo* I/R (n=3). Data are represented as mean ± s.e.m. Two-group comparisons were performed using Student's two-tailed t-test, and all multiple group comparisons were performed using a one-way ANOVA with a Newman-Keuls post-hoc analysis. *$P \leq 0.05$, **$P \leq 0.01$, ***$P \leq 0.001$.

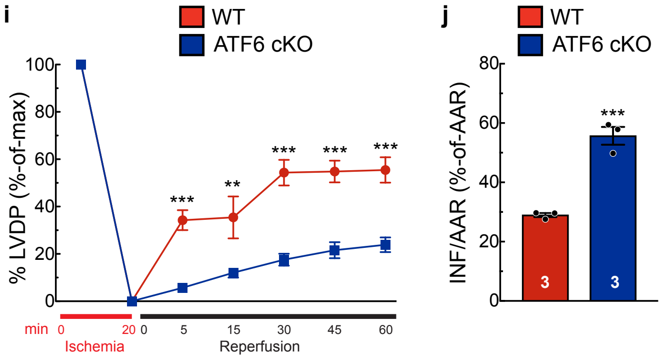

Figure 4.1 (continued)- Caption shown on previous page.

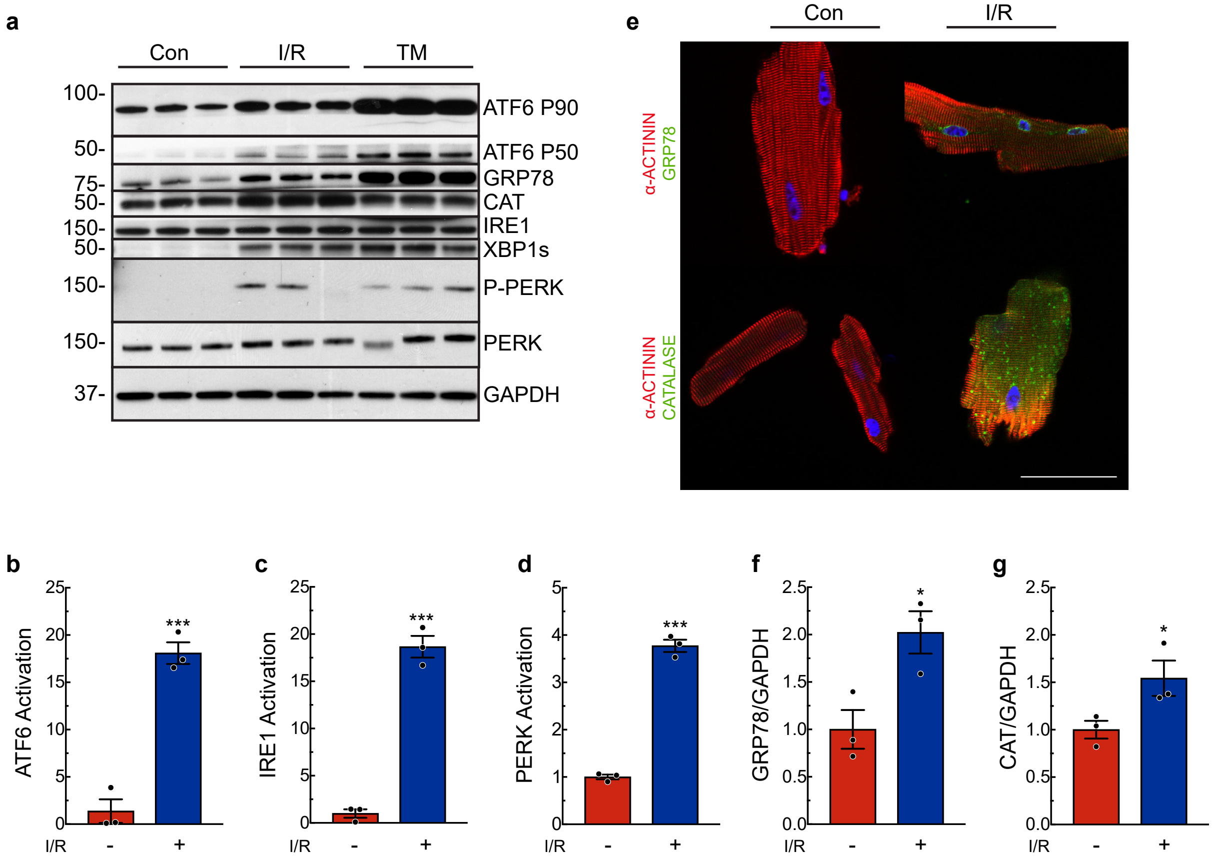

Figure 4.2– I/R activates the UPR.

a, Immunoblots of neonatal rat ventricular myocytes (NRVM) for the proteins shown after I/R or tunicamycin (TM). **b-d,** Quantification of immunoblots from NRVM subjected to normoxia or I/R. ATF6, IRE1, and PERK activation are displayed as ratios of active fragment ATF6 (50kd), spliced-XBP1 and phospho-PERK relative to ATF6 (90kd), IRE1, and PERK, respectively (n=3). **e,** Immunocytofluorescence (ICF) for GRP78 or CAT (green), alpha-actinin (red) and nuclei (TOPRO-3) in isolated adult cardiomyocytes (AMVM) post-I/R. Scale bar represents 50μm. **f, g,** Quantification of immunoblots for Grp78 **(f)** or Cat **(g)** from NRVM subjected to normoxia or I/R. Data are represented as mean ± s.e.m. Two-group comparisons were performed using Student's two-tailed t-test, and all multiple group comparisons were performed using a one-way ANOVA with a Newman-Keuls post-hoc analysis. $^{*}P \leq 0.05$, $^{***}P \leq 0.001$.

To examine the effects of deleting ATF6 specifically from cardiac myocytes, *in vivo*, we made an ATF6 conditional knockout mouse (ATF6 cKO) in which *Atf6* was selectively deleted in cardiac myocytes of ATF6$^{fl/fl}$ mice using AAV9-cTnT-CRE **(Fig 4.3a, b)**. ATF6 cKO and wild type (WT) mice, the latter of which retain ATF6, were subjected to 30 min of surgical coronary artery ligation, followed by 24 hours of reperfusion (I/R), which mimics the reperfusion injury in AMI patients that occurs acutely, a time during which the extent of reperfusion injury is progressive[22]. In this model, I/R causes cardiac myocyte death and irreparable damage in the infarct zone **(Fig. 4.1b, black)**, where blood flow has been completely occluded. However, cardiac myocytes adjacent to the infarct, in the border zone **(Fig. 4.1b, red)**, are exposed to sub-lethal I/R and mount protective stress responses, such as the UPR, while the remote region **(Fig. 4.1b, blue)** is relatively unaffected[13,23]. Thus, protective stress responses in border zone myocytes conserve their viability, thereby reducing the size of the infarct. WT mice exhibited a robust activation of ATF6 in response to I/R, as evidenced by induction of the ATF6 target genes, *Grp78* and *Cat* in the border zone of hearts subjected to acute I/R **(Fig. 4.1c, e)**; however, this induction was lost in ATF6 cKO mice **(Fig. 4.1d, f)**. In contrast, the IRE1 target gene, *Erdj4,* and PERK target gene, *Atf4*, were similarly induced by I/R in WT and ATF6 cKO mouse hearts **(Fig 4.3c, d)**. However, compared to WT, ATF6 cKO mice had increased infarct sizes and plasma cardiac troponin I (cTnI) **(Fig. 4.1g, h)**, canonical indicators of cardiac injury, and exhibited increased lipid peroxidation **(Fig 4.3e)**, a measure of ROS-mediated damage. Cardiac hemodynamics were also assessed in an *ex vivo* isolated perfused heart model that enables the precise measurement of the strength of cardiac pump function, i.e., left ventricular developed pressure (LVDP), with each contraction in response to I/R injury[10]. ATF6 cKO mouse hearts exhibited significantly lower recovery of LVDP and larger infarcts than WT hearts **(Fig. 4.1i, j)**. Collectively, these results show that ATF6 in cardiac myocytes protects the heart from I/R injury. Thus, while all three arms of the UPR were activated in the ischemic mouse heart, cardiac specific deletion of *Atf6* significantly increased heart damage in response to I/R, demonstrating the importance of the ATF6 arm of the UPR in mitigating I/R injury in the heart.

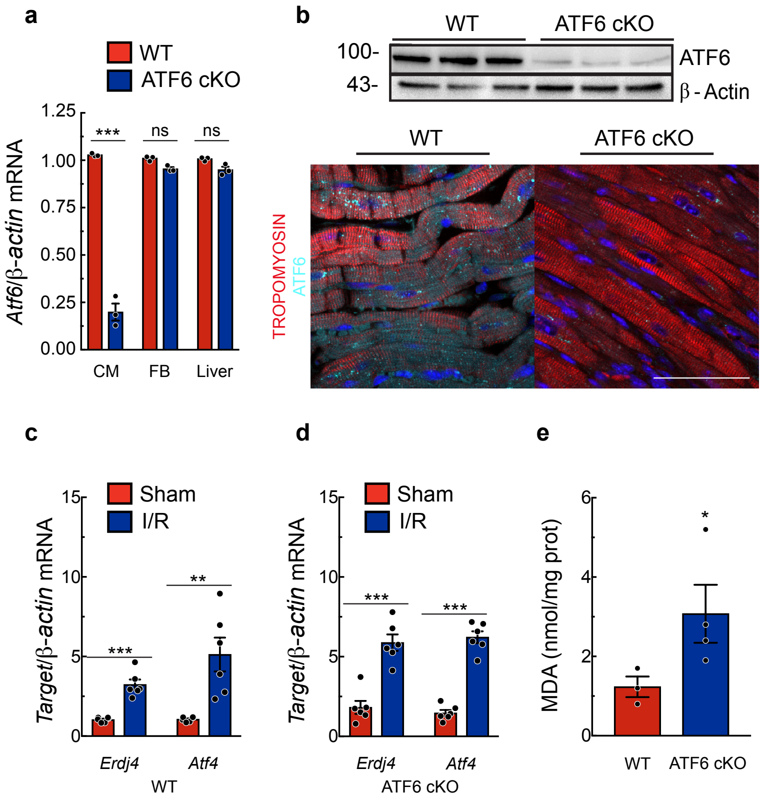

Figure 4.3– Endogenous ATF6 is cardioprotective in a model of an acute AMI.

a, qPCR for atf6 in isolated adult mouse ventricular myocytes (AMVM), isolated cardiac fibroblasts, or liver extracts from WT (n=3) or ATF6 cKO (n=3) mice. **b,** Immunoblot for Atf6 and loading control, β-actin, and IHC staining for ATF6 (cyan), tropomyosin (red), and nuclei (TOPRO-3) in LV of WT or ATF6 cKO mice. Scale bar represents 50μm. **c, d,** qPCR for IRE1 downstream target, Erdj4, or PERK downstream target, Atf4 in the border zone of WT **(c)** (n=6) or ATF6 cKO (n=6) **(d)** hearts 24-hours after I/R. **e,** Malondialdehyde (MDA) in WT (n=3) and ATF6 cKO (n=3) mice 24-hours post-I/R. Data are represented as mean ± s.e.m. Two-group comparisons were performed using Student's two-tailed t-test, and all multiple group comparisons were performed using a one-way ANOVA with a Newman-Keuls post-hoc analysis. *P≤0.05, **P≤0.01, ***P≤0.001.

In the days following AMI, the infarct continues to expand and remodels to become a fibrotic scar, so the detrimental effects of I/R on cardiac function and performance are often more pronounced a week after infarction[13]. Therefore, to examine the effect of *Atf6* deletion on cardiac function and performance, mice were analyzed 7d after AMI. ATF6 cKO mice exhibited significantly reduced fractional shortening compared to WT, despite being aphenotypic at baseline **(Fig. 4.4a; Table 4.1)**. ATF6 cKO mice also exhibited exaggerated pathological cardiac hypertrophy and plasma cTnI **(Fig. 4.4b, c)**. Notably, the levels of *Grp78* and *Cat* were lower in ATF6 cKO than WT mice at 7 days **(Fig. 4.4d, e)**. When gene expression was examined at 1 and 7d after MI, the induction of *Atf6* and its target genes remained increased through 7d post MI, although the level of induction was reduced compared to 1d post MI **(Fig. 4.4f)**, indicating that the adaptive effects of ATF6-induced genes are likely exerted for at least the first week following MI. *Grp78* and *Cat* were also increased in hearts from patients with ischemic heart disease **(Fig. 4.4g)**, supporting the relevance of the ATF6 adaptive arm of the UPR in human pathology and validating the phenotypes observed in this mouse model of AMI.

Interestingly, I/R activated ATF6 less than tunicamycin, the latter of which is a strong, chemical inducer of ER protein misfolding and activator of the UPR **(Fig 4.2a)**. Importantly, this result suggests that during I/R there is a reserve of inactive ATF6 that has the potential to be activated. Accordingly, we hypothesized that selective pharmacologic activation of ATF6 could supplement the modest ATF6 activation achieved upon I/R, and this supplemental ATF6 activation might enhance cardioprotection.

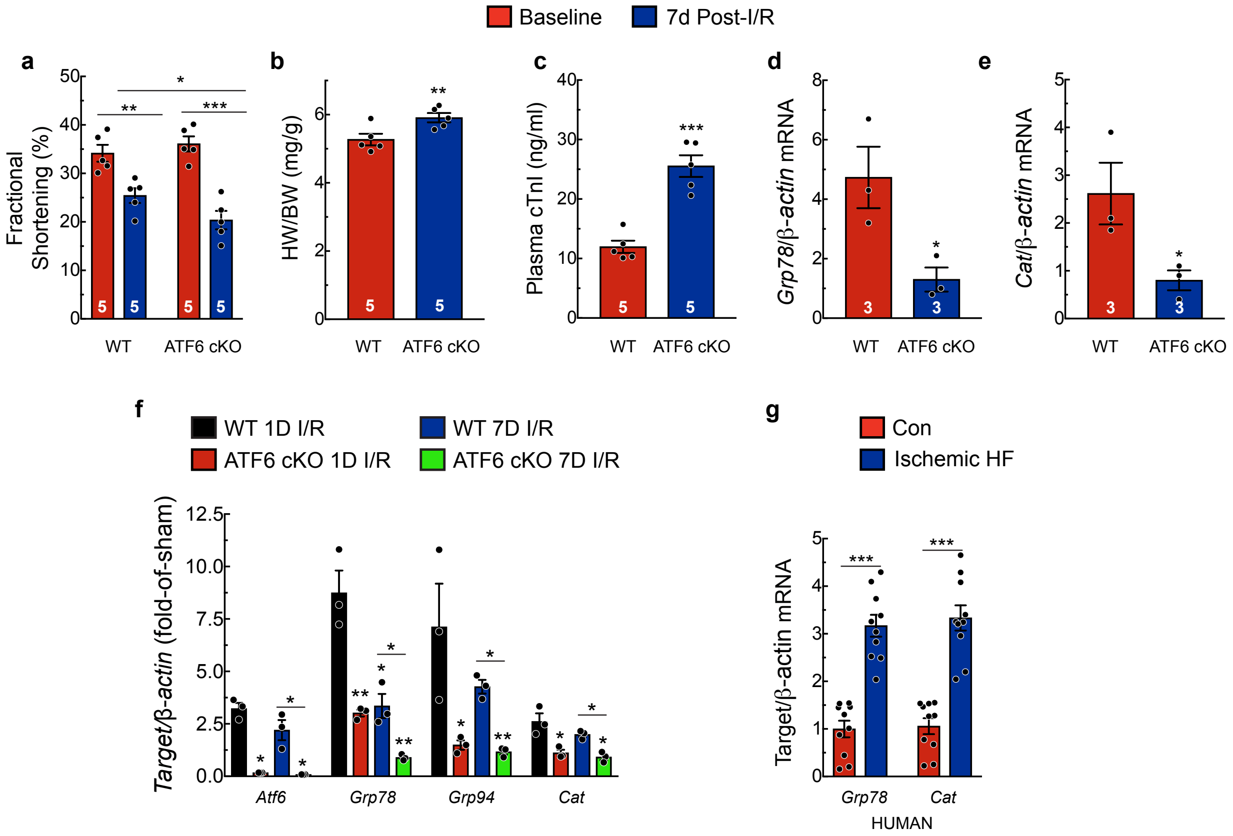

Figure 4.4– Endogenous ATF6 is cardioprotective in a model of a chronic AMI.

a-e, Parameters from mice 7-days post I/R. **a,** Fractional shortening. Detailed analyses of echocardiography parameters are in Table 4.1 (n=5). **b,** Ratio of heart weight to body weight. **c,** Plasma cTnI. **d, e,** qPCR for Grp78 **(d)** or Cat **(e)** in border zone of mice (n=3). **f,** qPCR for Atf6 and ATF6 target genes Grp78, Grp94, and Cat in WT (n=3) and ATF6 cKO (n=3) mice either 1-day or 7-days after I/R. **g,** Quantitative real-time PCR (qPCR) for Grp78 or Cat in ventricular explants from control (n=10) or ischemic heart failure (n=10) patients. Data are represented as mean ± s.e.m. Two-group comparisons were performed using Student's two-tailed t-test, and all multiple group comparisons were performed using a one-way ANOVA with a Newman-Keuls post-hoc analysis. $^{*}P \leq 0.05$, $^{**}P \leq 0.01$, $^{***}P \leq 0.001$.

Table 4.1- 7-day I/R echocardiographic parameters

	WT Baseline (n = 5)	ATF6 cKO Baseline (n = 5)	WT Post-I/R (n = 5)	ATF6 cKO Post-I/R (n = 5)
FS (%)	34.17±1.74	36.09±1.55	25.43±1.38[1]	21.36±1.09[1,2]
EF (%)	64.37±2.38	67.22±1.88	51.07±2.52[1]	44.10±3.51[1,2]
LVEDV (μl)	41.46±2.83	36.03±3.95	43.69±4.34	55.36±4.78[1,2]
LVESV (μl)	14.86±1.62	11.59±1.06	17.61±4.42	32.22±3.51[1,2]
LVIDD (mm)	3.21±0.09	3.02±0.15	3.49±0.16[1]	3.77±0.27[1,2]
LVIDS (mm)	2.11±0.09	1.92±0.07	2.60±0.12[1]	2.83±0.27[1]
PWTD (mm)	1.47±0.13	1.43±0.10	0.97±0.15[1]	1.03±0.13[1]
PWTS (mm)	1.56±0.13	1.63±0.15	1.21±0.19[1]	1.17±0.14[1]
AWTD (mm)	0.90±0.05	0.92±0.08	0.72±0.04[1]	0.73±0.06[1]
AWTS (mm)	1.26±0.06	1.22±0.07	1.14±0.06	1.10±0.05[1]
LV mass (mg)	102.70±7.81	91.73±7.45	106.53±6.30	115.43±4.29[1,2]
HR (bpm)	504±9.96	540±9.99	543±7.54	546±6.24

FS = fractional shortening
EF = ejection fraction
LVEDV = left ventricular end diastolic volume
LVESV = left ventricular end systolic volume
LVIDD = left ventricular inner diameter in diastole
LVIDS = left ventricular inner diameter in systole
PWTD = left ventricular posterior wall thickness in diastole
PWTS = left ventricular posterior wall thickness in systole
AWTD = left ventricular anterior wall thickness in diastole
AWTS = left ventricular anterior wall thickness in systole
LV mass = left ventricular mass
HR = heart rate in beats per minute

Statistical analyses used a one-way ANOVA with a Newman-Keuls post-hoc analysis.

[1] = $p \leq 0.05$ different from respective Baseline
[2] = $p \leq 0.05$ different from WT Post-I/R

4.3.2. 147 activates ATF6 and its target genes in cardiac myocytes

The compound **147** was previously shown to specifically activate ATF6 in HEK293 cells through a canonical mechanism involving translocation of ATF6 from the ER to the Golgi, where it is cleaved by S1 and S2 proteases to release the active ATF6 transcription factor[20] **(Fig. 4.5a)**. The translocation of ATF6 out of the ER during protein misfolding is known to require a reduction of the inter- and intramolecular disulfide bonds in ATF6; however, neither the effects of **147** on ATF6, nor its mechanism of action have been studied in cardiac myocytes. Here, in cultured cardiac myocytes, a control compound that closely resembles **147 (Fig. 4.5b)**, but does not activate ATF6, did not affect the disulfide bond status of ATF6, while **147** reduced intramolecular disulfide bonds in ATF6 **(Fig. 4.5c, lanes 7-10)**. Moreover, while the control compound did not activate any of the UPR pathways, **147** activated ATF6, but not PERK or IRE1 **(Fig 4.6a-d)**. Thus**,** in cardiac myocytes, **147** induced the canonical reduction of disulfide bonds in ATF6, which is associated with ATF6 translocation to the Golgi. Coordinate with the generation of the active, nuclear form of ATF6 in the Golgi was our finding that **147** increased the nuclear translocation of ATF6 in cardiac myocytes **(Fig. 4.5d)** and increased the specific cleavage and activation of ATF6 **(Fig 4.6a, b, g)**. Mechanistically, **147** increased the association of ATF6 with known ATF6 binding sites in the *Grp78* and *Cat* promoters **(Fig. 4.5e)**, and **147** increased GRP78 and CAT **(Fig 4.6a, e, f)**. Intravenous administration of **147** activated ATF6 and increased *Grp78* and *Cat* expression in WT mouse hearts; however, this effect was completely absent in ATF6 cKO mice **(Fig. 4.5g-j; Fig 4.6h).** As a testament to the ability of **147** to activate only the ATF6 arm of the UPR was our finding that **147** had no effect on the expression levels of the IRE1 or PERK targets, *Erdj4* or *Atf4* in either WT or ATF6 cKO mouse hearts **(Fig 4.6i, j)**. Thus, **147** selectively activates the ATF6 arm of the UPR in the heart, *in vivo*, as it does in cultured cardiac myocytes.

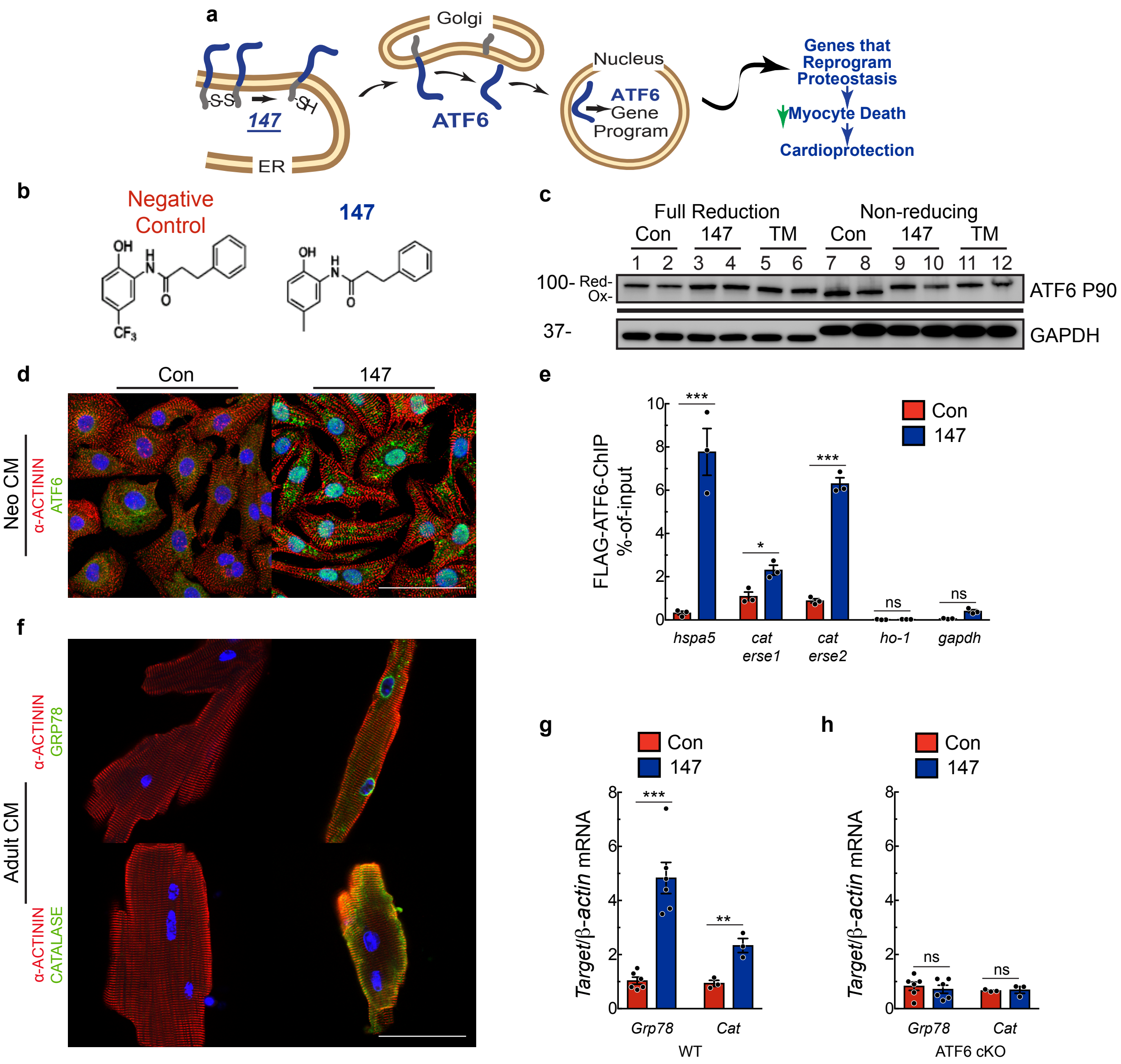

Figure 4.5– 147 selectively activates ATF6 in the heart.

a, Diagram of hypothetical mechanism of ATF6 activation by 147. **b,** Chemical structure of synthetic control compound and compound 147. **c,** Immunoblot of ATF6 and GAPDH in NRVM 24-hours after treatment with compound 147 or TM in fully-reducing condition (lanes 1-6) or non-reducing conditions (lanes 7-12). Shift exhibited in Atf6 in TM-treated cells in full-reducing conditions is typical of de-glycosylated ATF6. **d,** Immunocytofluorescence (ICF) of ATF6 (green), alpha-actinin (red) and nuclei (TOPRO-3) in NRVM 24-hours after treatment with compound 147. Scale bar represents 50µm. **e,** Chromatin immunoprecipitation (ChIP-qPCR) of known ATF6 target promoter binding elements (ERSE) for Grp78 (hspa5), cat, and negative control targets Heme oxygenase 1 (ho-1) and gapdh NRVM infected with AdV encoding Flag-ATF6 (1-670) 24-hours after treatment with compound 147(n=3). **f,** ICF of GRP78 and CAT (green), alpha-actinin (red) and nuclei (TOPRO-3) in AMVM 24-hours after treatment with compound 147. **g, h,** qPCR for Grp78 (n=6) or Cat (n=3) in LV of WT **(g)** or ATF6 cKO **(h)** hearts 24-hours post-treatment with control or 147. **i,j,** IHC staining of GRP78 or CAT (cyan), tropomyosin (red), and nuclei (TOPRO-3) in left ventricle (LV) of WT **(i)** or ATF6 cKO **(j)** hearts 24-hours post-treatment with control or 147. Tissue sections are representative images from one mouse per condition. Scale bar represents 50µm. Data are represented as mean ± s.e.m. Two-group comparisons were performed using Student's two-tailed t-test, and all multiple group comparisons were performed using a one-way ANOVA with a Newman-Keuls post-hoc analysis. *P≤0.05, **P≤0.01, ***P≤0.001.

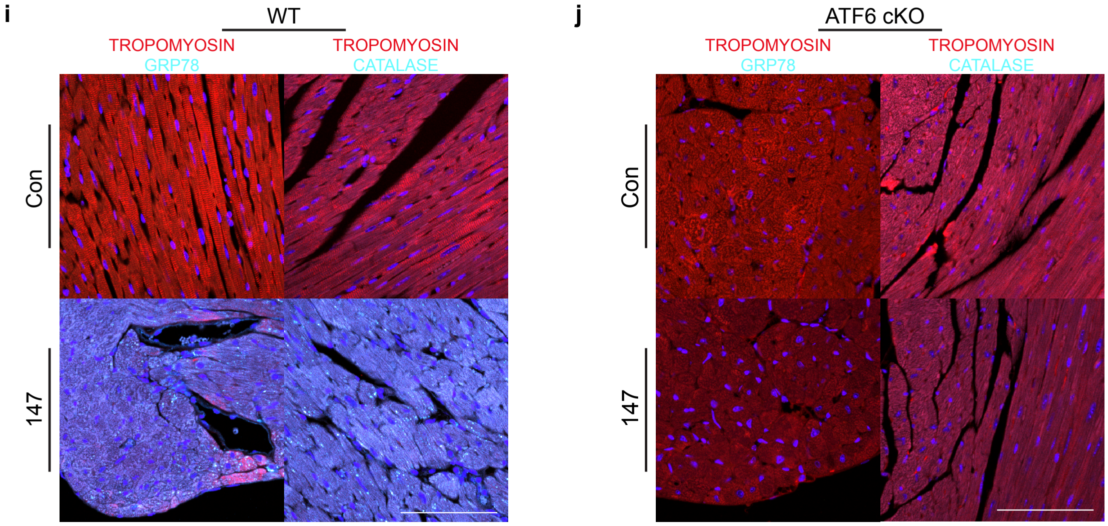

Figure 4.5 (continued)- Caption shown on previous page.

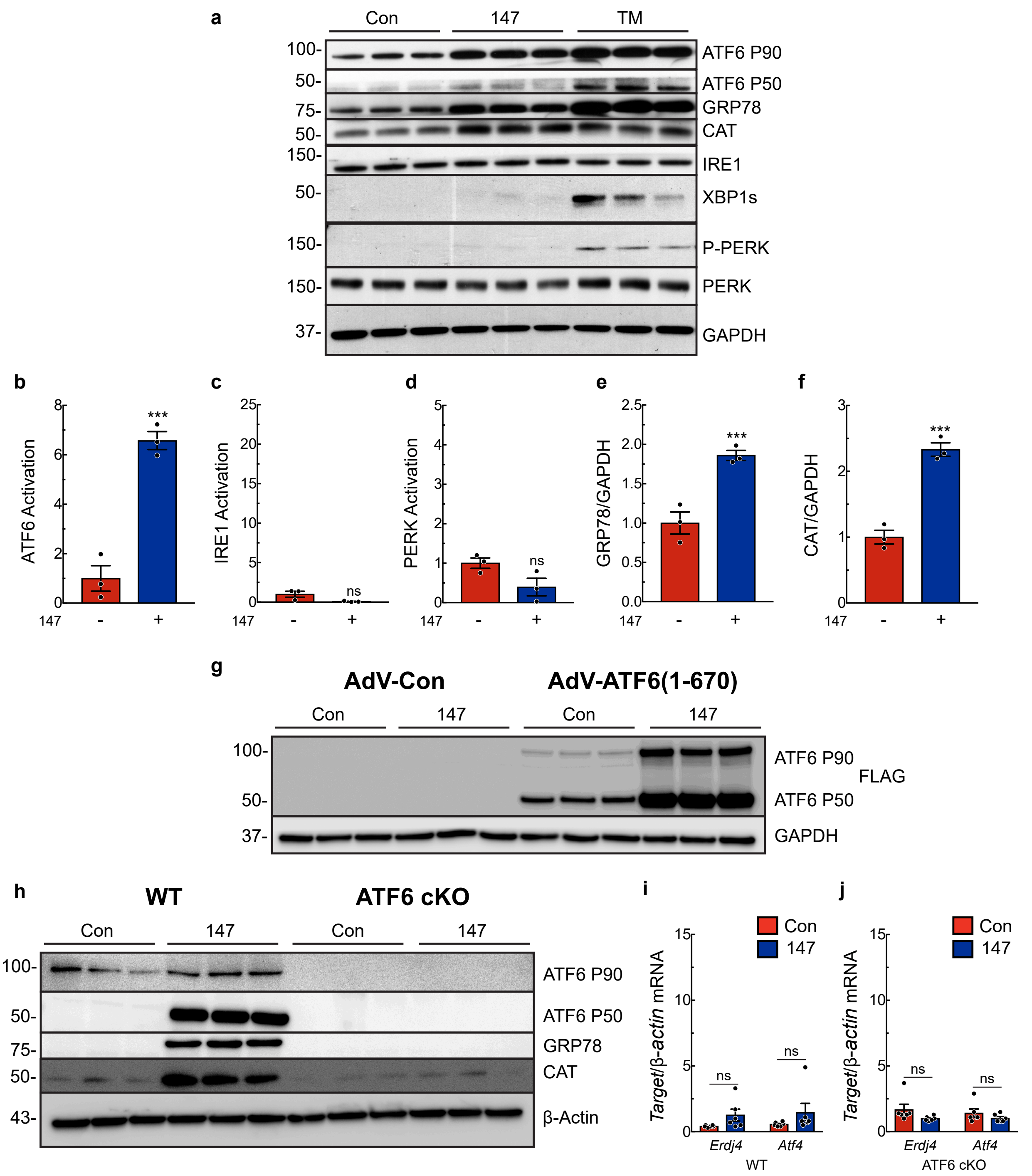

Figure 4.6– 147 is selectively activates ATF6.

a, Immunoblots of UPR target proteins from NRVM 24-hours after treatment with compound 147 or tunicamycin (TM). **b-f,** Quantification of immunoblots of NRVM treated with control or 147 (n=3). **g,** Immunoblot of NRVM infected with AdV encoding Flag-ATF6 (1-670) 24-hours after treatment with control or compound 147. Samples were performed in coordination with ChIP in Fig. 3e. **h,** Immunoblots of UPR target proteins from LV of WT (n=6) or ATF6 cKO (n=6) hearts 24-hours after treatment with control or 147. **i, j,** qPCR for Erdj4 or Atf4 in LV of WT **(i)** or ATF6 cKO **(j)** hearts 24-hours after treatment with control or 147. Data are represented as mean ± s.e.m. Two-group comparisons were performed using Student's two-tailed t-test, and all multiple group comparisons were performed using a one-way ANOVA with a Newman-Keuls post-hoc analysis. *P≤0.05, **P≤0.01, ***P≤0.001.

4.3.3. 147 improves ER proteostasis and decreases oxidative stress

Mechanistically, we examined whether **147** could replicate the breadth of adaptive effects of ATF6 on ER proteostasis, such as increasing ER associated protein degradation (ERAD), which removes potentially toxic terminally misfolded proteins, increasing folding and subsequent secretion of proteins made in the ER, and enhancing protection against ER protein misfolding. **147** increased ERAD, as measured by the rate of degradation of ectopically expressed TCRα[24] **(Fig. 4.7a, b)**, increased the folding and secretion of protein from the ER pathway **(Fig. 4.7c)**, and protected cells from death in response to ER protein misfolding induced by tunicamycin **(Fig. 4.7d)**; importantly, all of these effects were lost upon knockdown of *Atf6*. Next we explored whether **147** could replicate the adaptive effects of ATF6 against oxidative stress, *in vitro*. **147** significantly improved the survival of cardiac myocytes subjected to I/R **(Fig. 4.7e)** and decreased ROS-mediated damage **(Fig. 4.7f)**. Importantly, these effects of **147** were lost upon knockdown of *Atf6*. Thus, **147** replicated a broad spectrum of the adaptive effects of ATF6 on proteostasis and oxidative stress. Moreover, all of these effects required endogenous ATF6, demonstrating the ATF6-dependent mechanism of action of **147**.

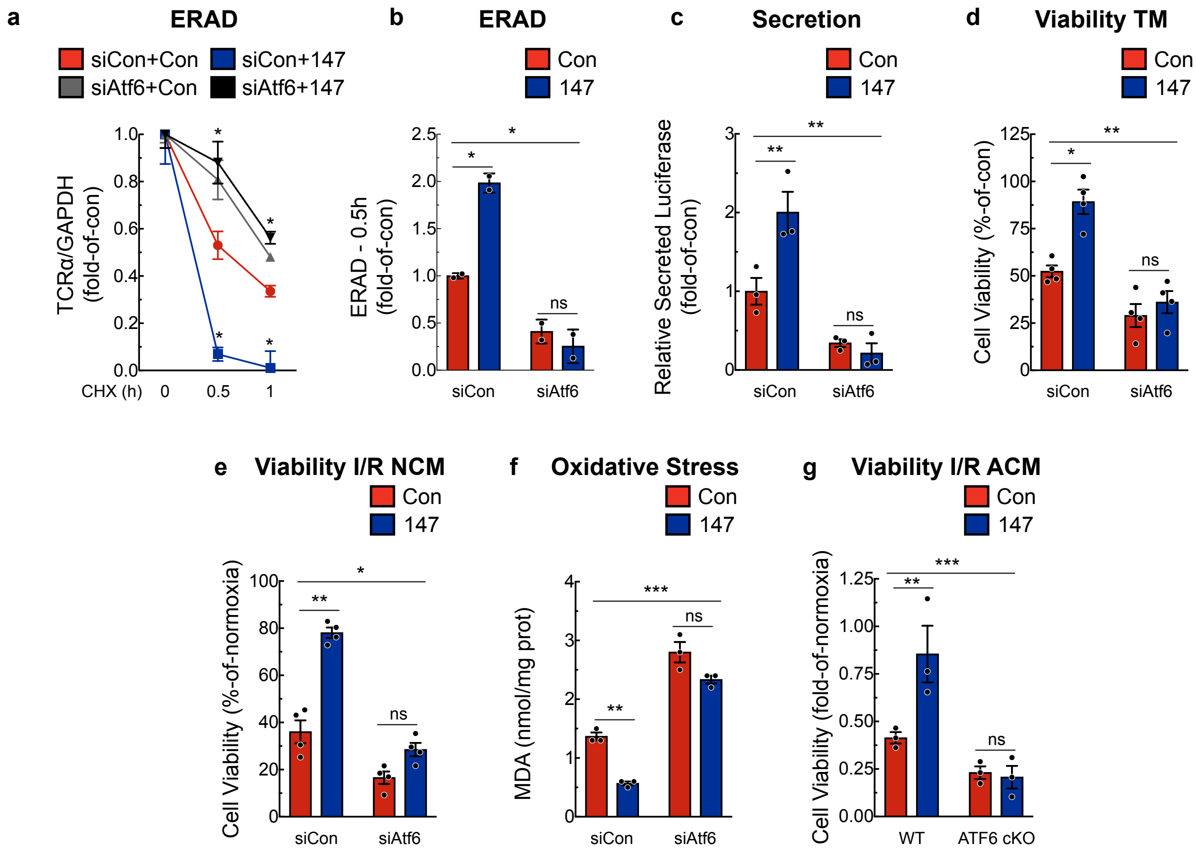

Figure 4.7– 147 improves proteostasis and decreases oxidative stress in an ATF6-dependent manner.

a, b, NRVM were infected with AdV-HA-T-cell antigen receptor alpha-chain (TCRα; an ER-transmembrane protein that is chronically misfolded and degraded by ERAD), treated with siCon or siAtf6 and either control or 147 for 24-hours prior to cyclohexamide for 0, 0.5 or 1h. Densitometry of the HA-TCRα immunoblots at the respective times **(a)** and ERAD at the 0.5-hour time point **(b)** are shown (n=2). **c,** Secretory proteostasis assayed in NRVM when transfected with Gaussia luciferase and treated with siCon or siAtf6, and either control or 147 for 24-hours. Medium was collected and luciferase activity was measured (n=3). **d,** NRVM were transfected with siCon or siAtf6, then treated with or without TM, control or 147 for 24h, after which viability was determined (n=4). **e, f,** NRVM were transfected with siCon or siAtf6, treated with or without control or 147 for 24h, then I/R, after which viability **(e)** and MDA **(f)** were measured. **g,** Viability of I/R-treated cultured adult cardiomyocytes isolated from WT (n=3) or ATF6 cKO (n=3) mice 24-hours post-treatment with control or 147. **h,i,** LVDP **(h)** and relative infarct sizes **(i)** of WT or ATF6 cKO mice treated 24h with control or 147 then ex vivo I/R. Data are represented as mean ± s.e.m. Two-group comparisons were performed using Student's two-tailed t-test, and all multiple group comparisons were performed using a one-way ANOVA with a Newman-Keuls post-hoc analysis. **P≤0.01, ***P≤0.001.

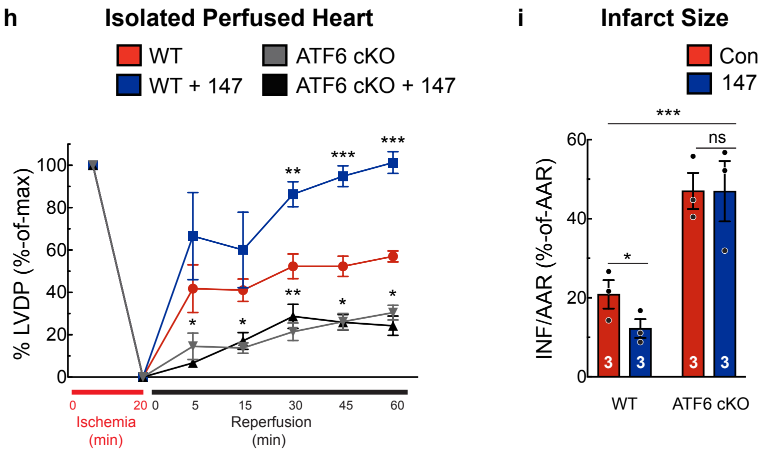

Figure 4.7 (continued)- Caption shown on previous page.

4.3.4. 147 in vivo protects cardiac myocytes and hearts *in vitro*

To determine whether **147** retained its ability to protect myocytes *in vivo*, mice were treated for 24h with either the negative control compound or **147**, after which cardiac myocytes were isolated and subjected to I/R in culture. Compared to the negative control, myocytes from **147**-treated WT mice exhibited increased viability when subjected to I/R *in vitro* **(Fig. 4.7g, left)**; however, this benefit was absent in myocytes from ATF6 cKO mice **(Fig. 4.7g, right)**. Thus, when administered *in vivo*, **147** retained its ability to protect cardiac myocytes from I/R damage in culture, and this protection was mediated through endogenous ATF6. To determine whether the protection seen in isolated cardiac myocytes had any effect in the intact heart, hearts from WT and ATF6 cKO mice that had been treated for 24h with **147** were examined in the *ex vivo* I/R model. Compared to control, hearts from **147-**treated WT mice had greater LVDP recovery and smaller infarct sizes **(Fig. 4.7h, blue vs red; 4.7i, left)**. Notably, **147** exhibited neither of these beneficial effects in hearts from ATF6 cKO mice **(Fig. 4.7h, gray and black; 4.7i, right)**. Thus, when administered to mice, **147** protected cardiac myocytes, and decreased I/R injury of the heart while preserving cardiac function. Furthermore, all of these beneficial effects of **147** were dependent upon endogenous ATF6 in cardiac myocytes.

4.3.5. 147 transiently activates ATF6 in the heart

To begin to understand the temporal dynamics of the function of **147** in mice, a time course of gene induction was performed. *Atf6* and its target genes were induced at the earliest time point examined, i.e. 8h, reaching a maximum 24h after administration and falling back to baseline values by 7d after administration **(Fig. 4.8a)**. Furthermore, pharmacokinetic studies in and revealed a relatively rapid clearance of **147** from plasma **(Fig. 4.8b),** supporting the further examination of multiple dosing strategies. Accordingly, several dosing strategies spanning 7 days were used to examine the temporal dynamics of the effects of **147** on ATF6 target gene induction in the hearts of mice that were not subjected to I/R were examined using several dosing protocols spanning 7 days **(Fig. 4.9a)**. Mice were injected with the negative control compound or **147** either twice, at days 0 and 4 (Experiments 1 and 2, respectively), or **147** was injected only once, at day 0 (Experiment 3). Compared to Experiment 1, Experiment 2 but not 3 resulted in increased the expression of the ATF6-regulated genes *Grp78* and *Cat* **(Fig. 4.9b, c, e)** but not the IRE1-regulated *Erdj4* or the PERK-regulated *Atf4* **(Fig 4.10a, b).** These results indicated that **147**-mediated induction of ATF6-target genes is transient, as gene expression was increased 3d after administration, but returned back to baseline 7d after administration.

Interestingly, Experiment 2 significantly enhanced cardiac performance **(Fig. 4.9d; Experiment 1 vs 2; Table 4.2)**, which could be partly due to **147**-dependent increases in *Atp2a2* expression **(Fig 4.10c)**. *Atp2a2* encodes SERCA2a, an adaptive SR/ER-localized calcium ATPase previously shown to be ATF6-inducible in the heart[25] and to improve contractility in heart failure patients[26]. None of the **147** dosing protocols resulted in cardiac pathological remodeling **(Fig 4.10d; Table 4.2)**, cardiotoxicity, as evidenced by no increased plasma cTnI **(Fig 4.10e)** or cardiac pathology-associated genes, such as *Nppa*, *Nppb*, *Col1a1* or *Myh7* **(Fig 4.10f)**. Furthermore, no apparent deficits were observed in any of the experiment upon inspection of the liver or kidneys when steatosis and glomerular filtration rate were assessed by hepatic triglyceride accumulation and creatinine clearance, respectively **(Fig 4.10f, g)**. These results indicate a time course of gene induction and no toxic side effects of **147** that support the efficacy of **147** when administered in the setting of an I/R injury, either as a single dose or as part of a serial dosing regimen.

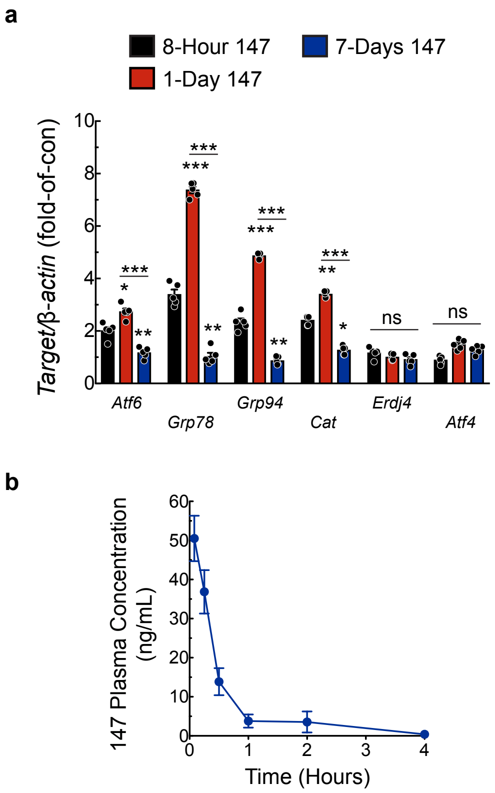

Figure 4.8– 147 acts transiently *in vivo*.

a, qPCR for Atf6 and ATF6 target genes Grp78, Grp94, and Cat in WT (n=5) mice either 8-hours, 1-day, or 7-days after a single bolus venous injection of 147 (2 mg/kg). **b,** 147 plasma concentration-time curve in mice receiving 2 mg/kg via venous injection. Blood was collected at baseline and 5-min, 15-min, 30-min, 1-hour, 2-hours, and 4-hours post injection (n=4 mice per timepoint). Data are represented as mean ± s.e.m. Two-group comparisons were performed using Student's two-tailed t-test, and all multiple group comparisons were performed using a one-way ANOVA with a Newman-Keuls post-hoc analysis. $^{*}P \leq 0.05$, $^{**}P \leq 0.01$, $^{***}P \leq 0.001$.

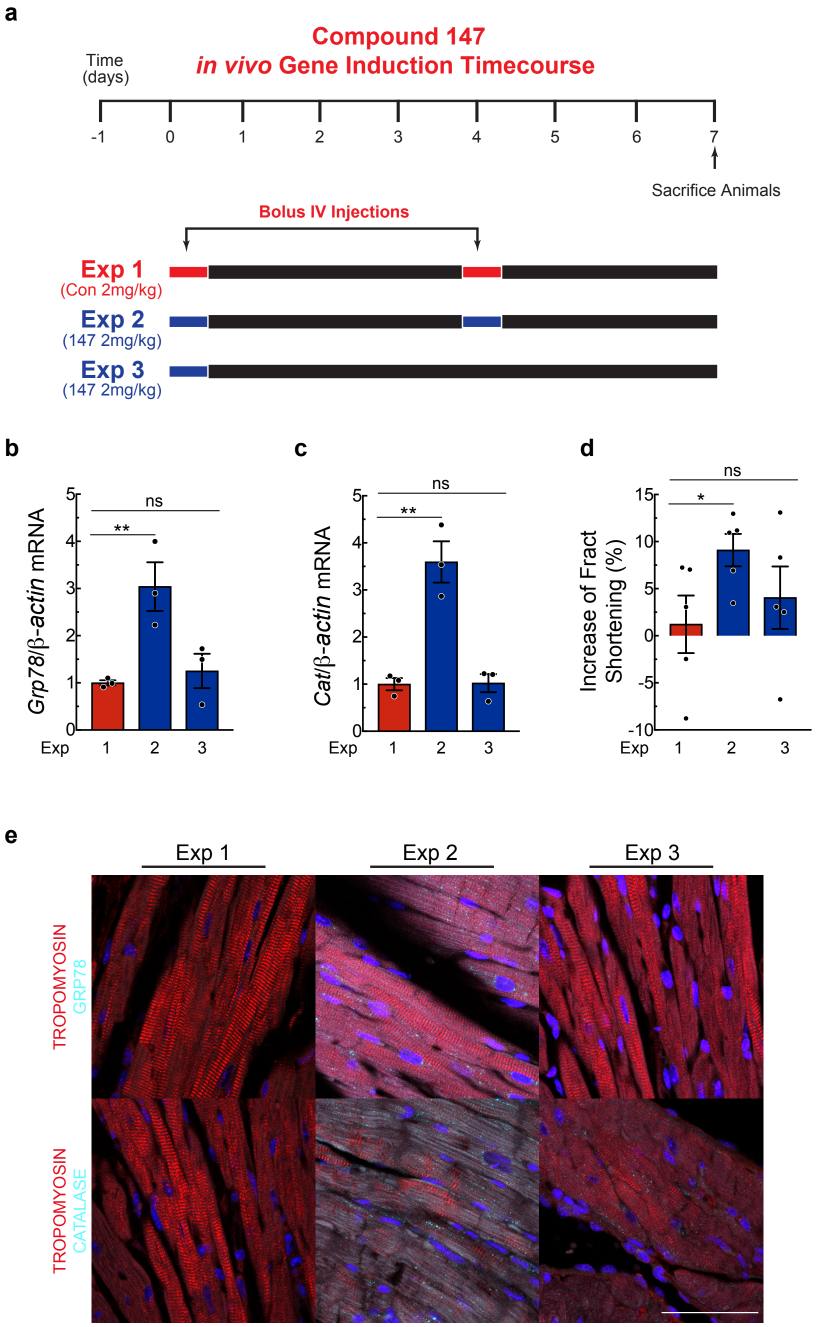

Figure 4.9– 147 gene induction timecourse *in vivo*.

a, Experimental design testing the effects of 147 in WT untreated mice. Red bars depict the bolus administration of the control compound, while blue bars depict the bolus administration of 147. **b, c,** qPCR for Grp78 **(b)** or Cat **(c)** in LV of mice from indicated experiments (n=3). **d,** Percent increase in fractional shortening. Detailed analyses of echocardiography parameters are in Table 4.2 (n=5). **e,** IHC staining of GRP78 or CAT (cyan), tropomyosin (red), and nuclei (TOPRO-3) in LV of mice from respective experiments. Tissue sections are representative images from one mouse per condition. Scale bar represents 50μm. Data are represented as mean ± s.e.m. Two-group comparisons were performed using Student's two-tailed t-test, and all multiple group comparisons were performed using a one-way ANOVA with a Newman-Keuls post-hoc analysis. *P≤0.05, **P≤0.01.

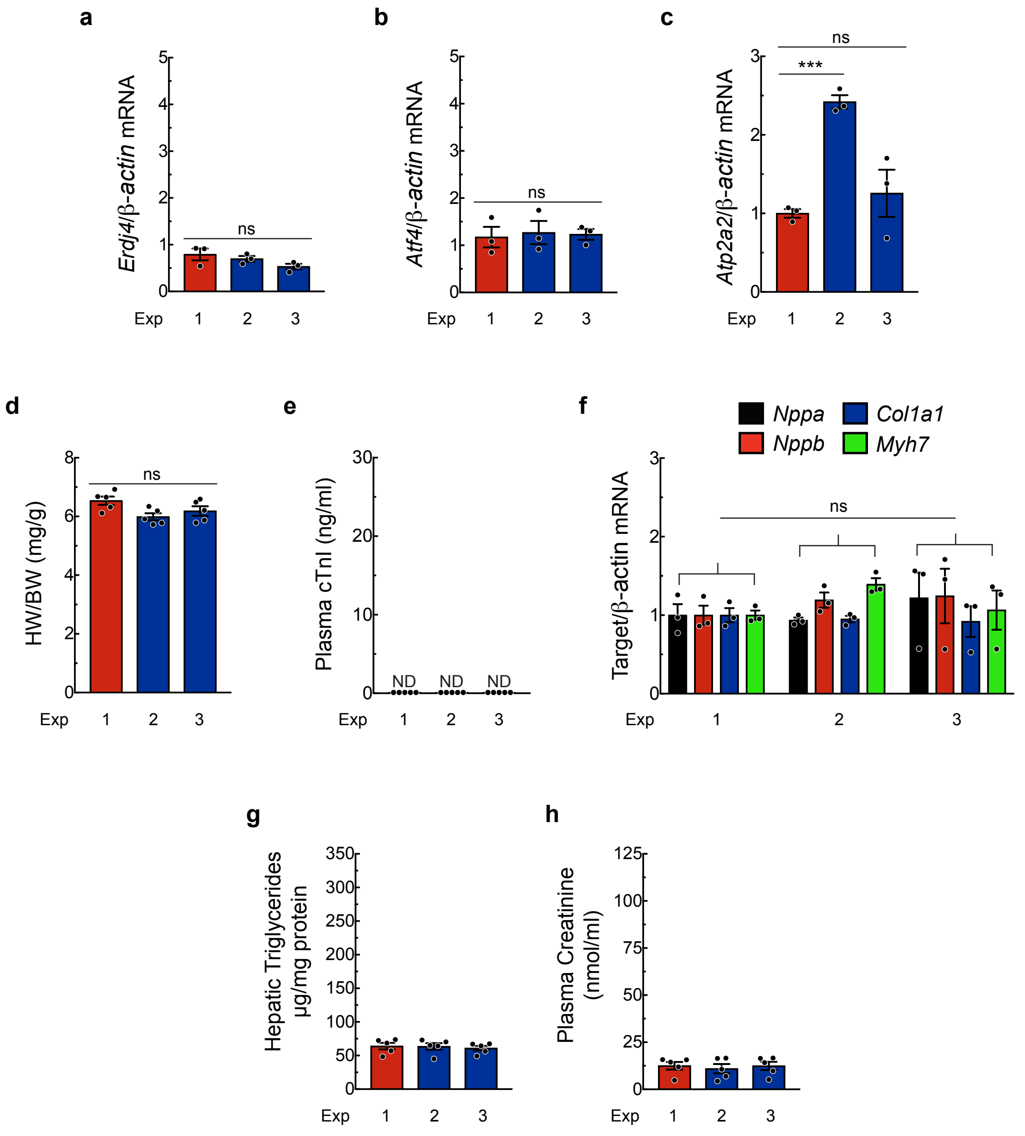

Figure 4.10– 147 exhibits no deleterious effects, *in vivo*.

a-c, qPCR for Erdj4 **(a)**, Atf4 **(b)**, and Atp2a2 **(c)** following experimental design in Fig. 4.9a. **d,** Ratio of heart weight to body weight (n=5). **e,** Plasma cTnI (n=5). **f,** qPCR for cardiac pathology genes: Nppa (black), Nppb (red), Col1a2 (blue), and Myh7 (green) following experimental design in Fig. 4.9a (n=3). **g,** Triglyceride levels in liver extracts from mice following experimental design in Fig. 4.9a (n=5). **h,** Plasma creatinine from mice following experimental design in Fig. 4.9a (n=5). Data are represented as mean ± s.e.m. Two-group comparisons were performed using Student's two-tailed t-test, and all multiple group comparisons were performed using a one-way ANOVA with a Newman-Keuls post-hoc analysis. ***$P \leq 0.001$.

Table 4.2- Compound 147 7-day Time Course echocardiographic parameters

	Trial 1 Baseline (n = 5)	Trial 2 Baseline (n = 5)	Trial 3 Baseline (n = 5)	Trial 1 7-day (n = 5)	Trial 2 7-day (n = 5)	Trial 3 7-day (n = 5)
FS (%)	34.00±2.56	25.34±1.58	27.68±1.90	35.21±2.17	34.44±2.11[1]	31.73±4.11
EF (%)	64.51±3.30	51.55±2.63	55.29±3.22	66.16±2.77	65.61±2.72[1]	60.51±5.83
LVEDV (μl)	30.40±6.89	33.83±6.27	32.46±5.61	30.01±2.98	21.61±1.47[1]	32.26±3.46
LVESV (μl)	10.22±1.50	16.30±3.03	14.89±3.16	10.27±1.39	7.30±0.32[1]	13.04±2.82
LVIDD (mm)	2.78±0.23	2.91±0.22	2.87±0.20	2.81±0.11	2.46±0.07[1]	2.88±0.13
LVIDS (mm)	1.82±0.11	2.17±0.16	2.08±0.18	1.82±0.11	1.61±0.03[1]	1.98±0.17
PWTD (mm)	1.66±0.08	1.40±0.19	1.37±0.14	1.17±0.11[1]	1.80±0.03[1]	1.40±0.26
PWTS (mm)	1.76±0.05	1.67±0.17	1.45±0.10	1.43±0.12[1]	2.01±0.09[1]	1.61±0.10
AWTD (mm)	1.01±0.04	1.02±0.08	0.98±0.02	0.91±0.03	0.88±0.01	0.95±0.04
AWTS (mm)	1.22±0.13	1.19±0.05	1.20±0.06	1.29±0.04	1.16±0.07	1.21±0.11
LV mass (mg)	105.21±4.51	107.38±6.23	93.15±5.72	80.24±3.78[1]	99.78±1.89	97.21±11.04
HR (bpm)	543±9.05	493±14.51	488±40.29	522±2.76[1]	515±10.32	520±5.38

FS = fractional shortening
EF = ejection fraction
LVEDV = left ventricular end diastolic volume
LVESV = left ventricular end systolic volume
LVIDD = left ventricular inner diameter in diastole
LVIDS = left ventricular inner diameter in systole
PWTD = left ventricular posterior wall thickness in diastole
PWTS = left ventricular posterior wall thickness in systole
AWTD = left ventricular anterior wall thickness in diastole
AWTS = left ventricular anterior wall thickness in systole
LV mass = left ventricular mass
HR = heart rate in beats per minute

Statistical analyses used a one-way ANOVA with a Newman-Keuls post-hoc analysis.

[1] = $p \leq 0.05$ different from respective Baseline

4.3.6. 147 protects the heart from I/R injury *in vivo*

Next, the effects of **147** were examined in an *in vivo* model of I/R damage in the heart 7d after reperfusion **(Fig. 4.11a)**. In Experiments 1 and 2, the negative control compound or **147**, respectively, were administered 24h prior to AMI, with a second dose at reperfusion and a third dose 4 days later. In Experiment 3, **147** was administered at reperfusion and again 4 days later. In Experiment 4, **147** was administered only one time, at reperfusion. Given the transient nature of **147**, we designed our multiple-dose strategy so that it mimics a therapeutic approach used for treating AMI patients as soon as possible after the infarction, to mitigate the initial reperfusion damage to the heart, as well as days later to ameliorate the detrimental effects of continued expansion of infarct damage and cardiac remodeling in the infarct and infarct border zones on heart pump function. Strikingly, cardiac performance was preserved to similar extents in all experiments involving **147 (Fig. 4.11b)**, as was the ability of **147** to reduce cardiac hypertrophy, which is a pathological response to I/R in this model **(Fig. 4.11c)**. **147** decreased plasma cTnI in all of the experiments, though somewhat less so in Experiments 3 and 4 **(Fig. 4.11d)**. Importantly, **147** preserved diastolic cardiac function and left ventricular volumes in all of the experiments **(Fig. 4.11e-g; Table 4.3)**, showing that **147** impeded the progression toward heart failure. In Experiments 2 and 3, the beneficial structural and functional effects were accompanied by increased expression of the ATF6-regulated genes, *Grp78* and *Cat* **(Fig. 4.11h-i; Fig. 4.12a)** but not *Erdj4* and *Atf4* **(Fig. 4.12b, c)**. However, in Experiment 4, the levels of *Grp78* and *Cat* were comparable to control treated animals, as expected, given the transient nature of **147**-mediated gene induction seen in a previous experiment **(see Fig. 4.9)**. Moreover, I/R induced cardiac pathology genes **(Fig. 4.12d, Sham vs Experiment 1)**, as expected; however, these effects were blunted by **147 (Fig. 4.12d, Experiments 2-4)**. In addition, decreased levels of pro-apoptotic cleaved caspase-3 were seen in Experiments 2-4 **(Fig. 4.12e)**, indicating that **147** protected myocytes from apoptosis during I/R. Thus, pharmacologic ATF6 activation at reperfusion ameliorated pathologic cardiac dysfunction in response to I/R injury.

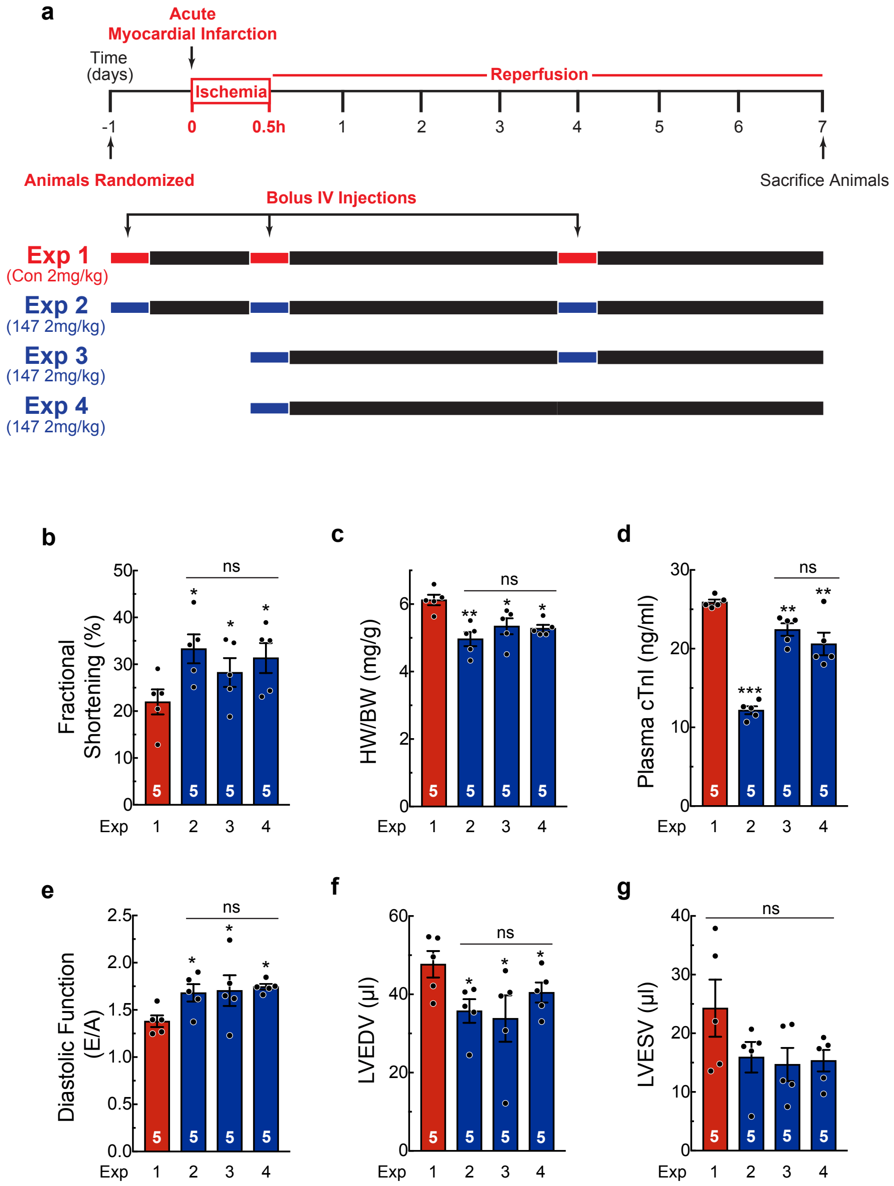

Figure 4.11– 147 improves cardiac performance 7d post-AMI.

a, Experimental design for testing the effects of 147 in the hearts of mice subjected to 30 min of myocardial infarction, then examined 7d after the initiation of reperfusion. Red bars depict the bolus administration of the control compound, while blue bars depict the bolus administration of 147. **b, f, g,** Echocardiographic parameters of fractional shortening **(b)**, LV end diastolic volume (LVEDV) **(f)** and LV end systolic volume (LVESV) **(g)** (n=5). Detailed analyses of echocardiography parameters are in Table 4.3. **c,** Ratio of heart weight to body weight (n=5). **d,** Plasma cTnI (n=5). **e,** Diastolic function as determined by pulse wave Doppler (PW) technique to analyze E and A waves (n=5). **h, i,** qPCR for Grp78 **(h)** or Cat **(i)** in LV of mice from indicated experiments at culmination of study (n=3). Data are represented as mean ± s.e.m. Two-group comparisons were performed using Student's two-tailed t-test, and all multiple group comparisons were performed using a one-way ANOVA with a Newman-Keuls post-hoc analysis. $^{*}P \leq 0.05$, $^{**}P \leq 0.01$, $^{***}P \leq 0.001$.

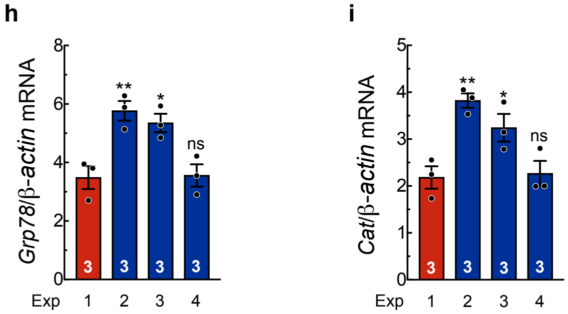

Figure 4.11 (continued)- Caption shown on previous page.

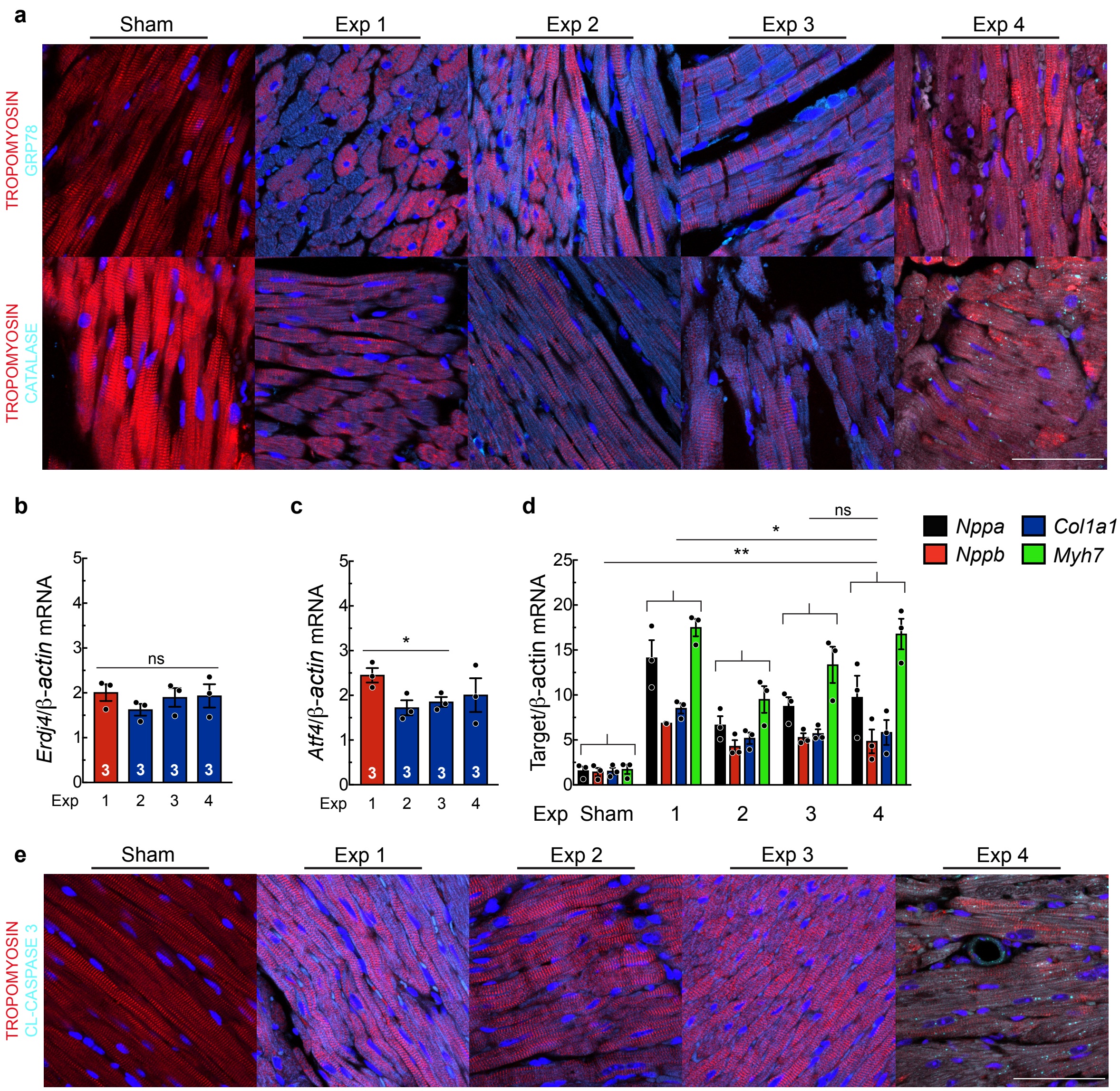

Figure 4.12– 147 decreases pathological remodeling 7d post-AMI.

a, IHC staining for GRP78 or CAT (cyan), tropomyosin (red), and nuclei (TOPRO-3) in left ventricular free wall of sham hearts or the border zone of hearts from respective trials of experimental design in Fig. 4.11a. Tissue sections are representative images from one mouse per condition. Scale bar represents 50μm. **b, c,** qPCR for Erdj4 **(b)** or Atf4 **(c)** in border zone of mice from Experiments 1-4 of the chronic I/R protocol shown in Fig. 4.11a (n=3). **d,** qPCR for cardiac pathology genes: Nppa (black), Nppb (red), Col1a2 (blue), and Myh7 (green) in border zone of mice from Experiments 1-4 of the chronic I/R protocol shown in Fig. 4.11a (n=3). Statistics represent significance of entire gene sets for each trial from that of separate experiments. **e,** IHC staining for cleaved caspase-3 (cyan), tropomyosin (red), and nuclei (TOPRO-3) in LV free wall of sham hearts or the border zone of hearts from indicated experiments of experimental design in Fig. 4.11a. Tissue sections are representative images from one mouse per condition. Scale bar represents 50μm. Data are represented as mean ± s.e.m. Two-group comparisons were performed using Student's two-tailed t-test, and all multiple group comparisons were performed using a one-way ANOVA with a Newman-Keuls post-hoc analysis. $^{*}P \leq 0.05$, $^{**}P \leq 0.01$.

Table 4.3- Compound 147 7-day AMI echocardiographic parameters

	Trial 4 Baseline (n = 5)	Trial 5 Baseline (n = 5)	Trial 6 Baseline (n = 5)	Trial 7 Baseline (n = 5)	Trial 4 Post-AMI (n = 5)	Trial 5 Post-AMI (n = 5)	Trial 6 Post-AMI (n = 5)	Trial 7 Post-AMI (n = 5)
FS (%)	33.08±2.45	34.91±5.58	32.22±1.39	33.58±4.77	22.60±2.39^{1}	33.29±3.09^{2}	28.05±1.57^{1,2}	31.34±3.19^{2}
EF (%)	63.42±3.64	65.05±7.21	62.21±2.18	62.24±6.29	50.40±3.75^{1}	62.74±4.37^{2}	57.07±4.23^{2}	60.03±4.74^{2}
LVEDV (µl)	25.65±2.70	31.06±4.20	31.12±4.54	46.15±3.44	45.69±2.58^{1}	33.81±2.33^{2}	29.44±5.22^{1,2}	40.46±0.561^{1,2}
LVESV (µl)	9.68±1.97	11.46±3.40	12.15±2.37	18.20±3.80	21.02±3.49^{1}	15.92±4.60	10.80±7.77	15.33±2.83
LVIDD (mm)	2.63±0.11	2.84±0.16	2.83±0.17	3.35±0.11	3.43±0.15^{1}	3.02±0.11^{2}	2.76±0.19^{2}	3.18±0.08^{2}
LVIDS (mm)	1.77±0.13	1.87±0.26	1.93±0.16	2.25±0.22	2.40±0.16^{1}	2.15±0.17^{2}	1.85±0.12^{2}	2.14±0.11^{2}
PWTD (mm)	1.47±0.10	1.34±0.08	1.43±0.11	0.91±0.15	1.55±0.07	1.42±0.14	1.17±0.28^{1,2}	0.99±0.15^{2}
PWTS (mm)	1.73±0.08	1.60±0.19	1.65±0.11	1.35±0.16	1.69±0.04	1.89±0.22	1.63±0.23	1.32±0.16
AWTD (mm)	0.88±0.02	1.02±0.08	0.88±0.03	1.01±0.04	0.87±0.04	1.04±0.09^{2}	0.83±0.08	1.16±0.15
AWTS (mm)	1.12±0.05	1.31±0.09	1.17±0.05	1.28±0.06	1.17±0.04	1.43±0.12^{2}	1.15±0.06	1.45±0.20
LV mass (mg)	90.82±1.26	97.68±3.33	94.12±5.52	91.03±12.18	126.30±7.43^{1}	113.39±2.43^{1,2}	118.22±4.96^{1}	125.57±5.74^{1}
HR (bpm)	522±10.54	517±20.40	545±6.88	535±11.80	507±11.32	529±9.45	492±24.50	527±7.10

FS = fractional shortening
EF = ejection fraction
LVEDV = left ventricular end diastolic volume
LVESV = left ventricular end systolic volume
LVIDD = left ventricular inner diameter in diastole
LVIDS = left ventricular inner diameter in systole
PWTD = left ventricular posterior wall thickness in diastole
PWTS = left ventricular posterior wall thickness in systole
AWTD = left ventricular anterior wall thickness in diastole
AWTS = left ventricular anterior wall thickness in systole
LV mass = left ventricular mass
HR = heart rate in beats per minute

Statistical analyses used a one-way ANOVA with a Newman-Keuls post-hoc analysis.

^{1} = $p \leq 0.05$ different from respective Baseline
^{2} = $p \leq 0.05$ different from Trial 4 Post-AMI

4.3.7. 147 is beneficial in a wide range of disease models *in vivo*

Next, we examined the effects of **147** following 24h of administration, an important time at which AMI patients are often treated by coronary angioplasty. Additionally, since ATF6 is expressed in all cells, we posited that it might be effective in tissues in addition to the heart. Accordingly, in addition to the heart, we determined the effects of **147** in the liver, kidney and brain. **147** activated ATF6 target genes in all four of the tissues, as evidenced by significant increases in of *Grp78* and *Cat* **(Fig. 4.13a, b)**, although the magnitude of the responses varied somewhat between tissues. The functionality of **147**-mediated activation of ATF6 in the liver was evident in that it significantly reduced ER protein misfolding, measured by XBP1 splicing, in mice that had been injected with tunicamycin; this beneficial effect was lost upon genetic deletion of ATF6 **(Fig. 4.13c)**. Additional evidence of the functionality of **147** in the liver was evident in its ability to reduce hepatic triglycerides, the latter of which are a hallmark of hepatic steatosis, which demonstrates improved ER proteostasis in the liver **(Fig. 4.13d, blue)**; this beneficial effect of **147** was also lost upon deletion of ATF6 **(Fig. 4.13d, black)**.

Next, to examine the functional effects of **147** in the various tissues, the control compound or **147** were administered, as shown in **Figure 4.13e**, and the effects were examined on tissue damage in the heart via the acute I/R model, the kidney via transient unilateral renal portal system occlusion, and in the brain via transient unilateral middle cerebral artery occlusion. Throughout the studies, the surgeon and the data analyst were blinded to the animal assignments, which were predetermined by a separate investigator. Remarkably, even when administered only at the time of reperfusion, **147** significantly decreased infarct sizes in all three tissues when measured 24h after I/R **(Fig. 4.13f-h; Fig. 4.14a)**. Moreover, **147** decreased plasma cTnI and creatinine, which are biomarkers of cardiac and kidney damage, respectively, and it improved behavioral indicators of post-ischemic neurological deficit **(Fig. 4.13i-k)**. As expected, since 24h after reperfusion is too short for structural remodeling there was no observable functional deficit on cardiac performance, chamber size, or pathological hypertrophy, as monitored by echocardiography **(Table 4.4)**. As further proof of concept, this experiment was replicated in female mice and, again, both Experiments 2 and 3 conferred protection as evidenced by reduced infarct sizes and plasma cTnI **(Fig. 4.14b, c)**. Importantly, these beneficial effects of **147** in response to myocardial acute I/R were not seen in ATF6 cKO mice, further emphasizing that **147**-mediated protection of the heart required ATF6 activation **(Fig. 4.14d, e)**. Interestingly, the beneficial effects of **147** were also seen in a different AMI model induced by acute administration of the β-adrenergic receptor agonist, isoproterenol, which is known to cause widespread oxidative damage and cardiac myocyte death in mice at this dose **(Fig. 4.14f-h)**.

Thus, when administered at the time of injury, 147 was able to protect a wide range of tissues from I/R damage, emphasizing the broad spectrum of potential applications for this compound as a transcriptional regulator of the ATF6 arm of the UPR and subsequent reprogramming of proteostasis, *in vivo.*

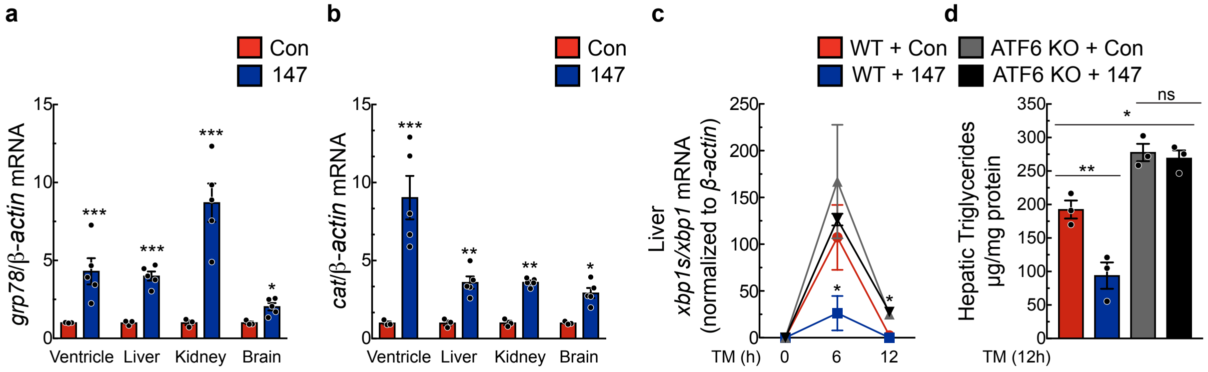

Figure 4.13– 147 exerts widespread protection in multiple organ systems.

a, b, qPCR for Grp78 **(a)** or Cat **(b)** in left ventricular, liver, kidney, and brain extracts from WT mice 24-hours post-treatment with control or 147 (n=3). **c,** Ratio of transcript levels of Xbp1s to Xbp1 as determined by qPCR in liver extracts from WT or ATF6 KO mice 24-hours post-treatment with control or 147 and then treated with 2mg/kg of TM for designated periods of time (n=3). **d,** Triglyceride levels in liver extracts from WT or ATF6 KO mice 24-hours post-treatment with control or 147 and then treated with 2mg/kg of TM for 12-hours (n=3). **e,** Experimental design for testing the effects of 147 in the hearts of mice subjected to 30 min of myocardial infarction, then examined 24h after the initiation of reperfusion. Red bars depict the bolus administration of the control compound, while blue bars depict the bolus administration of 147. **f-h,** Relative infarct sizes in the heart **(f)** (n=6-7 for each experiment, as shown), kidney **(g)**, and brain **(h)** (n=4-5 for each experiment, as shown) of male mice 24h after reperfusion. **i-k,** Plasma cTnI **(i)** (n=6-7 for each experiment, as shown), plasma creatinine **(j)**, and neurological score based on the Bederson system of behavioral patterns post-cerebral ischemic injury of male mice 24h after reperfusion of respective injury models (n=4-5 for each experiment, as shown). Data are represented as mean ± s.e.m. Two-group comparisons were performed using Student's two-tailed t-test, and all multiple group comparisons were performed using a one-way ANOVA with a Newman-Keuls post-hoc analysis. $^{**}P \leq 0.01$, $^{***}P \leq 0.001$.

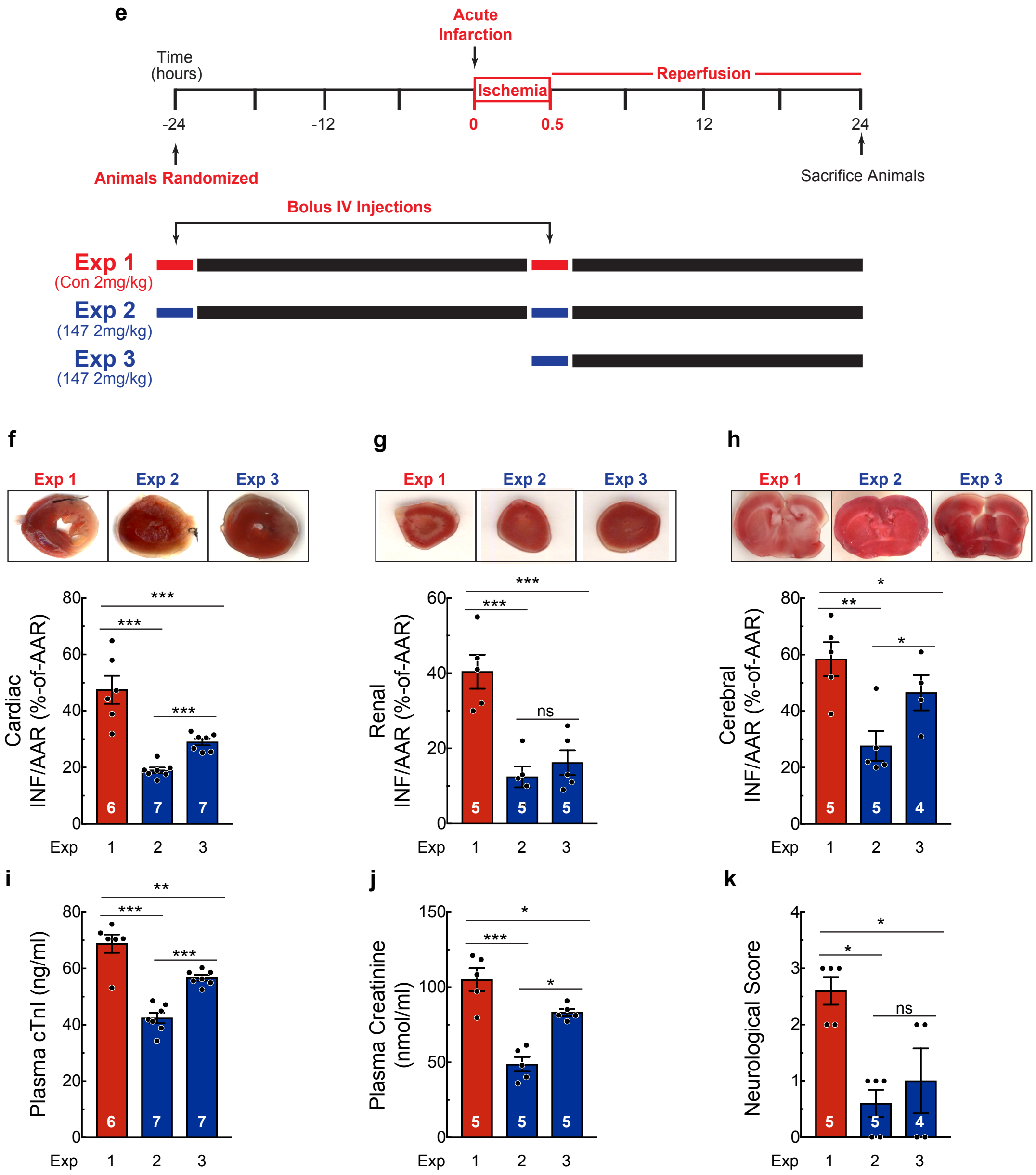

Figure 4.13 (continued)- Caption shown on previous page.

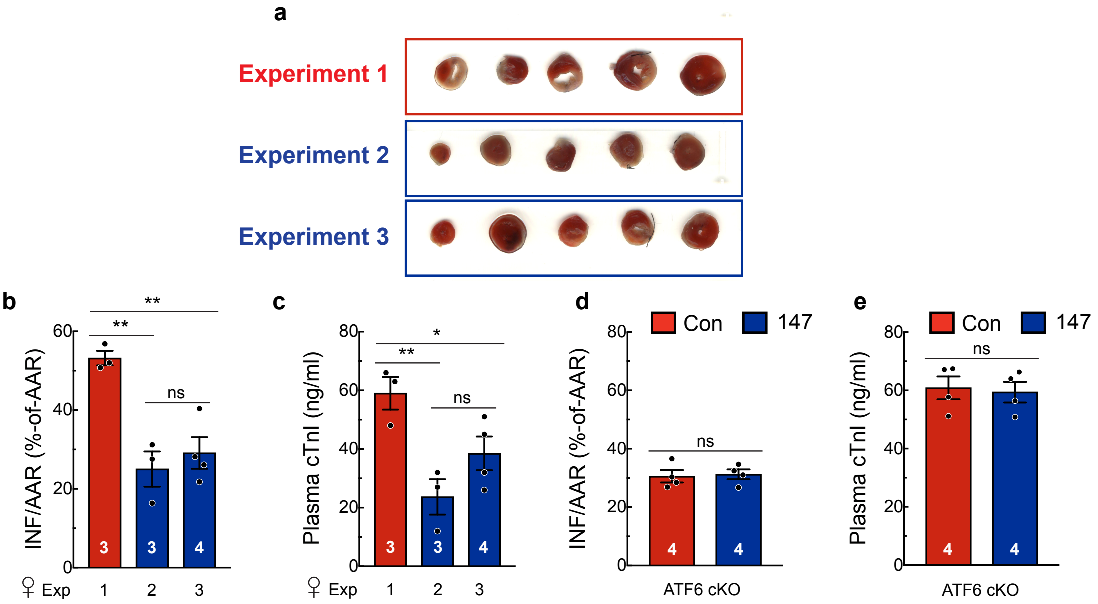

Figure 4.14– 147 is protective in multiple models of myocardial damage.

a, Representative images of TTC-stained post-I/R hearts from Experiments 1-3 of the acute I/R protocol shown in Fig. 4.13e. **b, c,** Relative infarct sizes **(b)** and plasma cTnI **(c)** of female mice 24-hours after reperfusion when following the acute I/R protocol shown in Fig. 4.13e (n=3-4 for each experiment, as shown). **d, e,** Relative infarct sizes **(d)** and plasma cTnI **(e)** of ATF6 cKO mice 24-hours post-I/R when following experimental Experiments 1 (Con) and 2 (147) of the acute I/R protocol (n=4). **f,** Experimental design for testing the effects of 147 in a different model of a AMI using isoproterenol. **g-h,** Relative infarct sizes **(g)**, and plasma cTnI **(h)** (n=4-5 for each experiment, as shown). Data are represented as mean ± s.e.m. Two-group comparisons were performed using Student's two-tailed t-test, and all multiple group comparisons were performed using a one-way ANOVA with a Newman-Keuls post-hoc analysis. *P≤0.05, **P≤0.01, ***P≤0.001.

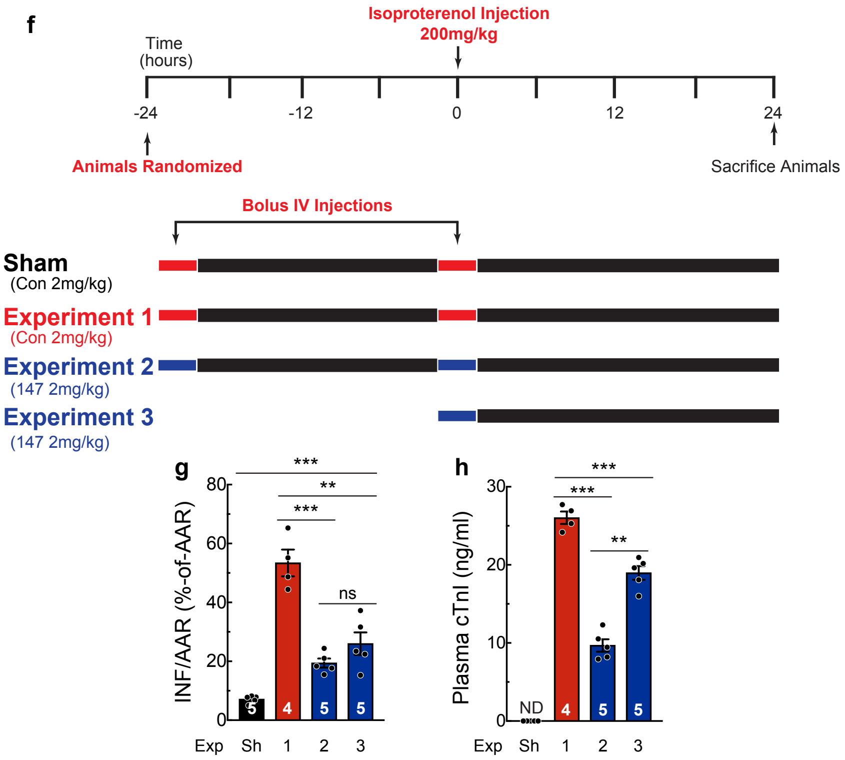

Figure 4.14 (continued)- Caption shown on previous page.

Table 4.4- Compound 147 24-hour AMI echocardiographic parameters

	Trial 8 Baseline (n = 3)	Trial 9 Baseline (n = 4)	Trial 10 Baseline (n = 4)	Trial 8 Post-AMI (n = 3)	Trial 9 Post-AMI (n = 4)	Trial 10 Post-AMI (n = 4)
FS (%)	35.07±1.61	33.01.91±2.75	30.94±2.75	34.06±2.41	34.70±1.13	30.27±1.86
EF (%)	66.14±2.43	63.07±4.04	60.61±4.18	64.60±3.49	65.61±1.35	58.99±2.88
LVEDV (μl)	32.00±8.38	30.74±3.75	23.34±2.70	29.22±3.21	32.17±3.63	39.03±5.67[1]
LVESV (μl)	11.32±3.68	11.70±2.38	9.40±1.93	10.73±2.34	10.92±0.81	16.46±3.14[1]
LVIDD (mm)	2.83±0.29	2.83±0.15	2.54±0.12	2.77±0.12	2.89±0.13	3.11±0.20[1]
LVIDS (mm)	1.85±0.23	1.91±0.16	1.76±0.15	1.84±0.14	1.88±0.05	2.18±0.19[1]
PWTD (mm)	1.40±0.16	1.38±0.25	1.60±0.08	1.30±0.13	1.27±0.04	1.31±0.07[1]
PWTS (mm)	1.61±0.13	1.78±0.17	1.77±0.10	1.66±0.13	1.61±0.08	1.53±0.09[1]
AWTD (mm)	1.07±0.03	0.95±0.07	0.97±0.12	1.10±0.03	0.97±0.04	0.97±0.11
AWTS (mm)	1.32±0.05	1.29±0.10	1.19±0.06	1.31±0.05	1.36±0.06	1.22±0.06
LV mass (mg)	129.50±7.91	120.70±17.09	122.45±6.31	125.02±5.62	119.03±11.24	136.04±4.34[1]
HR (bpm)	535±14.75	533±15.94	528±12.36	535±16.33	478±20.51	544±10.22

FS = fractional shortening
EF = ejection fraction
LVEDV = left ventricular end diastolic volume
LVESV = left ventricular end systolic volume
LVIDD = left ventricular inner diameter in diastole
LVIDS = left ventricular inner diameter in systole
PWTD = left ventricular posterior wall thickness in diastole
PWTS = left ventricular posterior wall thickness in systole
AWTD = left ventricular anterior wall thickness in diastole
AWTS = left ventricular anterior wall thickness in systole
LV mass = left ventricular mass
HR = heart rate in beats per minute

Statistical analyses used a one-way ANOVA with a Newman-Keuls post-hoc analysis.

[1] = $p \leq 0.05$ different from respective Baseline

4.4. Discussion

After an AMI, upon reconstituting blood flow reperfusion damage begins almost immediately and continues for at least 3 days[27]. The initial reperfusion damage is thought to be due ROS generation by mitochondria in the myocardium, while the longer term damage may be due to multiple mechanisms, including continued ROS generation by the infiltration of inflammatory cells into the infarct zone[13,28]. Therefore, an effective therapy for AMI should function over a timeframe spanning at least 3 days. While a number of potential therapies that act acutely to minimize reperfusion damage have been tested, many of them have failed to move through the drug development process and there is still no clinically available intervention[15]. At the outset of the current study we posited that this might be because most of the previous therapeutics function only during the initial stages of reperfusion, losing efficacy in the ensuing days. Furthermore, many of the initial trials performed in small animals have not tested therapies at times that accurately mimic typical clinical interventions (i.e. during coronary angioplasty) and have not adhered to the FDA's Good Laboratory Practices (GLP). Accordingly, in addition to addressing these points in the design of our animal experiments here, we examined the therapeutic function after both 1 and 7d of reperfusion. We also set out to develop a therapeutic approach that would exert beneficial effects through multiple mechanisms in various cellular locations, which we felt would broaden the potential utility to include different tissues and widen the scope to multiple proteostasis-based pathologies. In this regard, we focused on ATF6, since it adaptively reprograms ER proteostasis by inducing a wide range of protective response genes that encode proteins, such as catalase and grp78, which act to mitigate ROS-induced damage, as well as emending ROS-independent proteostasis pathways, respectively **(Fig. 4.15)**. Using this strategy, we found that selective pharmacologic activation of only the ATF6 arm of the UPR with **147** in mice acted within 1d to reduce reperfusion damage in the heart, although it is also possible that **147** might also reduce damage during ischemia. Moreover, we found that **147** acted after 7d to preserve cardiac function. This timing of these beneficial effects is consistent with the timing of adaptive ATF6-target gene induction and the reperfusion damage that takes place over this same time frame, although we cannot rule out an effect of **147** on reducing damage during ischemia. In addition to demonstrating its efficacy in the ischemic heart, we found that **147** protected the liver in a mouse model of dysregulated hepatic proteostasis, and it protected the kidneys and brain in models of renal and cerebral I/R damage. These findings, together with a recent report showing that **147** enhances the differentiation of human embryonic stem cells[29], support the broad therapeutic potential of pharmacologic activation of ATF6 for treating a wide range of proteostasis-based pathologies in various tissues.

In terms of its suitability as a pharmacologic agent, **147** exhibits many desirable properties. For example, **147** is highly specific, serving as the first example of a compound that selectively activates only one arm of the UPR, ATF6, which is well known for exerting mainly beneficial effects in many different cell types. **147** is highly efficacious *in vivo*, functioning at a dose similar to many other cardiovascular drugs and has the capacity to cross the blood brain barrier. Moreover, **147** does not exhibit any apparent toxicity or deleterious off-target effects *in vivo*. Both the efficacy and tolerance of **147** can be attributed in large part to the high-stringency, cell-based transcriptional profiling that was done in the initial screening to ensure that **147** specifically activates only the ATF6 arm of the UPR, instead of global UPR activation[20]. The relatively transient activation of ATF6 by **147** *in vivo* is also potentially advantageous, since many stress-signaling pathways, including the UPR, can be beneficial initially, but damaging upon chronic activation[30]. Since I/R only partially activates ATF6, the remaining inactive ATF6 provides a therapeutic reserve for **147** to activate, allowing it to boost adaptive ATF6 signaling pathways in multiple tissues, *in vivo.* Remarkably, we found that **147** exerted beneficial effects in the hearts of mice that were not subjected to any injury maneuvers, underscoring the safety, and perhaps even benefits of the compound in healthy tissues. Thus, while future pharmacokinetic and toxicology studies will address further details of **147** action, it is clear from the results presented here that **147** is easily administered, well tolerated, acts quickly, boosts an endogenous adaptive transcriptional stress signaling pathway, and has no apparent off-target or untoward effects, all of which are attributes of an excellent candidate for therapeutic development.

Impaired proteostasis contributes to numerous pathologies and even impacts aging[31]. Thus, global improvement of proteome quality through pharmacologic activation of defined transcriptional regulators of proteostasis should ameliorate a broad range of proteostasis-based diseases. Recent findings showing that the sphere of influence of the UPR, in particular, the ATF6 arm of the UPR, extends well beyond the ER to reprogram proteostasis in many cellular locations[10], support the potential broad spectrum of impact of pharmacologic compounds, like 147. The results presented here provide proof-of-principle that this type of pharmacologic correction can be achieved with well-characterized compounds, such as 147 that selectively activate a specific protective aspect of UPR signaling.

Chapter 4, in full, is a reprint of the material as it appears in Nature Communications in 2019. Blackwood, E.A., Azizi, K.M., Thuerauf, D.J., Paxman, R., Plate, L., Wiseman, L., Kelly, J., and Glembotski, C.C. Pharmacologic ATF6 activation confers global protection in widespread disease models by reprogramming cellular proteostasis. *Nat Commun*, 2019; 10:187. The dissertation author was the primary investigator and author of this paper.

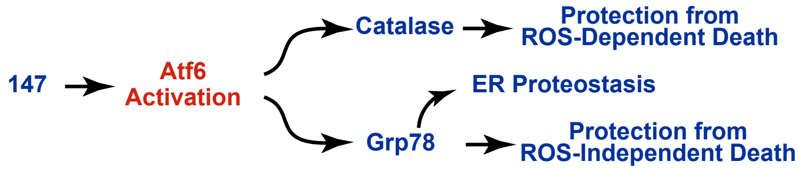

Figure 4.15– 147 mediates both ROS-dependent and ROS-independent protection globally.

Proposed mechanism whereby 147 confers widespread global protection within the cell through activation of ATF6 to act both in a canonical and non-canonical manner to protect against ROS-dependent and ROS-independent challenges to proteostasis.

4.5. References

1 Hartl, F. U., Bracher, A. & Hayer-Hartl, M. Molecular chaperones in protein folding and proteostasis. *Nature* **475**, 324-332, doi:10.1038/nature10317 (2011).

2 Labbadia, J. & Morimoto, R. I. The biology of proteostasis in aging and disease. *Annu Rev Biochem* **84**, 435-464, doi:10.1146/annurev-biochem-060614-033955 (2015).

3 Das, I. *et al.* Preventing proteostasis diseases by selective inhibition of a phosphatase regulatory subunit. *Science* **348**, 239-242, doi:10.1126/science.aaa4484 (2015).

4 Roth, D. M. & Balch, W. E. Modeling general proteostasis: proteome balance in health and disease. *Curr Opin Cell Biol* **23**, 126-134, doi:10.1016/j.ceb.2010.11.001 (2011).

5 Walter, P. & Ron, D. The unfolded protein response: from stress pathway to homeostatic regulation. *Science* **334**, 1081-1086, doi:334/6059/1081 [pii] 10.1126/science.1209038 (2011).

6 Smith, M. H., Ploegh, H. L. & Weissman, J. S. Road to ruin: targeting proteins for degradation in the endoplasmic reticulum. *Science* **334**, 1086-1090, doi:10.1126/science.1209235 (2011).

7 Chiang, W. C., Hiramatsu, N., Messah, C., Kroeger, H. & Lin, J. H. Selective activation of ATF6 and PERK endoplasmic reticulum stress signaling pathways prevent mutant rhodopsin accumulation. *Invest Ophthalmol Vis Sci* **53**, 7159-7166, doi:10.1167/iovs.12-10222 (2012).

8 Cooley, C. B. *et al.* Unfolded protein response activation reduces secretion and extracellular aggregation of amyloidogenic immunoglobulin light chain. *Proc Natl Acad Sci U S A* **111**, 13046-13051, doi:10.1073/pnas.1406050111 (2014).

9 Martindale, J. J. *et al.* Endoplasmic reticulum stress gene induction and protection from ischemia/reperfusion injury in the hearts of transgenic mice with a tamoxifen-regulated form of ATF6. *Circ Res* **98**, 1186-1193, doi:10.1161/01.RES.0000220643.65941.8d (2006).

10 Jin, J. K. *et al.* ATF6 Decreases Myocardial Ischemia/Reperfusion Damage and Links ER Stress and Oxidative Stress Signaling Pathways in the Heart. *Circ Res* **120**, 862-875, doi:10.1161/CIRCRESAHA.116.310266 (2017).

11 Yu, Z. *et al.* Activation of the ATF6 branch of the unfolded protein response in neurons improves stroke outcome. *J Cereb Blood Flow Metab* **37**, 1069-1079, doi:10.1177/0271678X16650218 (2017).

12 Roth, G. A. *et al.* Global, Regional, and National Burden of Cardiovascular Diseases for 10 Causes, 1990 to 2015. *J Am Coll Cardiol* **70**, 1-25, doi:10.1016/j.jacc.2017.04.052 (2017).

13 Frangogiannis, N. G. Pathophysiology of Myocardial Infarction. *Compr Physiol* **5**, 1841-1875, doi:10.1002/cphy.c150006 (2015).

14 Hausenloy, D. J. & Yellon, D. M. The evolving story of "conditioning" to protect against acute myocardial ischaemia-reperfusion injury. *Heart* **93**, 649-651, doi:10.1136/hrt.2007.118828 (2007).

15 Bulluck, H., Yellon, D. M. & Hausenloy, D. J. Reducing myocardial infarct size: challenges and future opportunities. *Heart* **102**, 341-348, doi:10.1136/heartjnl-2015-307855 (2016).

16 Hausenloy, D. J. & Yellon, D. M. Ischaemic conditioning and reperfusion injury. *Nat Rev Cardiol* **13**, 193-209, doi:10.1038/nrcardio.2016.5 (2016).

17 Kalogeris, T., Baines, C. P., Krenz, M. & Korthuis, R. J. Ischemia/Reperfusion. *Compr Physiol* **7**, 113-170, doi:10.1002/cphy.c160006 (2016).

18 Murphy, E. & Steenbergen, C. Mechanisms underlying acute protection from cardiac ischemia-reperfusion injury. *Physiol Rev* **88**, 581-609, doi:10.1152/physrev.00024.2007 (2008).

19 Yellon, D. M. & Hausenloy, D. J. Myocardial reperfusion injury. *N Engl J Med* **357**, 1121-1135, doi:10.1056/NEJMra071667 (2007).

20 Plate, L. *et al.* Small molecule proteostasis regulators that reprogram the ER to reduce extracellular protein aggregation. *Elife* **5**, doi:10.7554/eLife.15550 (2016).

21 Wang, J., Lee, J., Liem, D. & Ping, P. HSPA5 Gene encoding Hsp70 chaperone BiP in the endoplasmic reticulum. *Gene* **618**, 14-23, doi:10.1016/j.gene.2017.03.005 (2017).

22 Kumar, M. *et al.* Animal models of myocardial infarction: Mainstay in clinical translation. *Regul Toxicol Pharmacol* **76**, 221-230, doi:10.1016/j.yrtph.2016.03.005 (2016).

23 Dixon, J. A. & Spinale, F. G. Pathophysiology of myocardial injury and remodeling: implications for molecular imaging. *J Nucl Med* **51 Suppl 1**, 102S-106S, doi:10.2967/jnumed.109.068213 (2010).

24 Doroudgar, S. *et al.* Hrd1 and ER-Associated Protein Degradation, ERAD, are Critical Elements of the Adaptive ER Stress Response in Cardiac Myocytes. *Circ Res* **117**, 536-546, doi:CIRCRESAHA.115.306993 [pii] 10.1161/CIRCRESAHA.115.306993 (2015).

25 Thuerauf, D. J. *et al.* Sarco/endoplasmic reticulum calcium ATPase-2 expression is regulated by ATF6 during the endoplasmic reticulum stress response: intracellular signaling of calcium stress in a cardiac myocyte model system. *J Biol Chem* **276**, 48309-48317, doi:10.1074/jbc.M107146200 M107146200 [pii] (2001).

26 Gwathmey, J. K., Yerevanian, A. & Hajjar, R. J. Targeting sarcoplasmic reticulum calcium ATPase by gene therapy. *Hum Gene Ther* **24**, 937-947, doi:10.1089/hum.2013.2512 (2013).

27 Baines, C. P. How and when do myocytes die during ischemia and reperfusion: the late phase. *J Cardiovasc Pharmacol Ther* **16**, 239-243, doi:10.1177/1074248411407769 (2011).

28 Hernandez-Resendiz, S. *et al.* The Role of Redox Dysregulation in the Inflammatory Response to Acute Myocardial Ischaemia-reperfusion Injury - Adding Fuel to the Fire. *Curr Med Chem* **25**, 1275-1293, doi:10.2174/0929867324666170329100619 (2018).

29 Kroeger, H. *et al.* Induction of endoplasmic reticulum stress genes, BiP and chop, in genetic and environmental models of retinal degeneration. *Invest Ophthalmol Vis Sci* **53**, 7590-7599, doi:10.1167/iovs.12-10221 (2012).

30 Ron, D. & Walter, P. Signal integration in the endoplasmic reticulum unfolded protein response. *Nat Rev Mol Cell Biol* **8**, 519-529, doi:nrm2199 [pii] 10.1038/nrm2199 (2007).

31 Martinez, G., Duran-Aniotz, C., Cabral-Miranda, F., Vivar, J. P. & Hetz, C. Endoplasmic reticulum proteostasis impairment in aging. *Aging Cell* **16**, 615-623, doi:10.1111/acel.12599 (2017).

32 Engin, F. *et al.* Restoration of the unfolded protein response in pancreatic beta cells protects mice against type 1 diabetes. *Sci Transl Med* **5**, 211ra156, doi:10.1126/scitranslmed.3006534 (2013).

33 Charan, J. & Kantharia, N. D. How to calculate sample size in animal studies? *J Pharmacol Pharmacother* **4**, 303-306, doi:10.4103/0976-500X.119726 (2013).

34 Bedi, K. C., Jr. *et al.* Evidence for Intramyocardial Disruption of Lipid Metabolism and Increased Myocardial Ketone Utilization in Advanced Human Heart Failure. *Circulation* **133**, 706-716, doi:10.1161/CIRCULATIONAHA.115.017545 (2016).

35 Werfel, S. *et al.* Rapid and highly efficient inducible cardiac gene knockout in adult mice using AAV-mediated expression of Cre recombinase. *Cardiovasc Res* **104**, 15-23, doi:10.1093/cvr/cvu174 (2014).

36 Lynch, J. M. *et al.* A thrombospondin-dependent pathway for a protective ER stress response. *Cell* **149**, 1257-1268, doi:S0092-8674(12)00572-7 [pii] 10.1016/j.cell.2012.03.050 (2012).

37 Vekich, J. A., Belmont, P. J., Thuerauf, D. J. & Glembotski, C. C. Protein disulfide isomerase-associated 6 is an ATF6-inducible ER stress response protein that protects cardiac myocytes from ischemia/reperfusion-mediated cell death. *J Mol Cell Cardiol* **53**, 259-267, doi:S0022-2828(12)00182-4 [pii] 10.1016/j.yjmcc.2012.05.005 (2012).

38 Jin, J. K. *et al.* Localization of phosphorylated alphaB-crystallin to heart mitochondria during ischemia-reperfusion. *Am J Physiol Heart Circ Physiol* **294**, H337-344, doi:00881.2007 [pii] 10.1152/ajpheart.00881.2007 (2008).

39 Wei, Q. & Dong, Z. Mouse model of ischemic acute kidney injury: technical notes and tricks. *Am J Physiol Renal Physiol* **303**, F1487-1494, doi:10.1152/ajprenal.00352.2012 (2012).

40 Wallner, M. *et al.* Acute Catecholamine Exposure Causes Reversible Myocyte Injury Without Cardiac Regeneration. *Circ Res* **119**, 865-879, doi:10.1161/CIRCRESAHA.116.308687 (2016).

41 Xie, M. *et al.* Histone deacetylase inhibition blunts ischemia/reperfusion injury by inducing cardiomyocyte autophagy. *Circulation* **129**, 1139-1151, doi:10.1161/CIRCULATIONAHA.113.002416 (2014).

42 Bederson, J. B. *et al.* Rat middle cerebral artery occlusion: evaluation of the model and development of a neurologic examination. *Stroke* **17**, 472-476 (1986).

43 DeZwaan-McCabe, D. *et al.* ER Stress Inhibits Liver Fatty Acid Oxidation while Unmitigated Stress Leads to Anorexia-Induced Lipolysis and Both Liver and Kidney Steatosis. *Cell Rep* **19**, 1794-1806, doi:10.1016/j.celrep.2017.05.020 (2017).

44 Wu, J. *et al.* ATF6alpha optimizes long-term endoplasmic reticulum function to protect cells from chronic stress. *Dev Cell* **13**, 351-364, doi:S1534-5807(07)00266-3 [pii] 10.1016/j.devcel.2007.07.005 (2007).

45 Eckman, E. A. *et al.* Regulation of steady-state beta-amyloid levels in the brain by neprilysin and endothelin-converting enzyme but not angiotensin-converting enzyme. *J Biol Chem* **281**, 30471-30478, doi:10.1074/jbc.M605827200 (2006).

Chapter 5: Conclusions

5.1. Conclusions

Cardiac hypertrophy is an adaptive response to an increase in cardiac workload, either in a physiological or pathological manner. In order to maintain contractile function during growth, sarcomeric expansion in cardiac myocytes must be associated with proteostatic balance so as not to disrupt the integrity of the proteome with accumulation of toxic misfolded protein aggregates. ATF6 has been shown to be a primary adaptive sensor and responder to cardiac hypertrophy. In this setting, ATF6 induces both canonical and non-canonical gene panels associated with the balance of protein synthesis, folding, trafficking, and degradation. The recently demonstrated ability of ATF6 to be rapidly and transiently activated to induce adaptive genes specific to the stimulus or stressor has garnered great enthusiasm as a prime target for small molecule-based activators. Until recently, ATF6 has been a part of a class of proteins previously believed to be “undruggable”, but with research efforts detailing the mechanism of activation of ATF6 and stringent assays of small molecule library screening, the identification of ATF6-based therapeutics has taken great strides and shown promising efficacy in small animal models of CVD and other systemic proteostasis-based diseases (e.g., Compound 147).

Still, ongoing research efforts must be aimed at understanding the mechanism of activation and action of ATF6 during various etiologies of CVD, so as to better design small molecules and better predict possible untoward effects of chronic ATF6 activation. One of the biggest questions remaining is the mechanism by which ATF6 chooses the gene program it influences during various pathologies. All non-canonical genes discovered to date that ATF6 induces in a stimulus-specific manner possess canonical ATF6-binding motifs in the proximal promoter region (ERSEs). ATF6 has been known to dimerize with other transcription factors as part of its transcriptional engagement including: SRF (serum response factor), Nrf1 (nuclear respiratory factor 1), PGC1α and β (peroxisome proliferator-activated receptor gamma coactivator 1-alpha and -beta), and ERRγ (estrogen-related receptor gamma). It would be enlightening to understand the dynamics of the nuclear ATF6-interactome in response to these various pathophysiological stimuli.

Furthermore, the finding that the expression levels of ATF6 and other essential components of the adaptive UPR decrease as a function of age, while the propensity for developing cardiac pathology increases as a function of age has highlighted a glaring need for continued studies of ATF6 function. The age-dependent decline in ATF6 has led to the exploration of therapeutic approaches aimed at enhancing ATF6 activity in the aged, pathologic heart in hopes of improving proteostasis thereby enhancing cardiac myocyte contractility, and reducing the progression to heart failure characterized by the accumulation proteotoxic aggregates, fibrosis, and decreased cardiac compliance.

The development of proteostasis- and ATF6-based therapeutics is still in its infancy and reflecting on the incredible advancement in developing small molecule activators in a relatively short period of time provides a great deal of optimism as the field of proteostasis continues to develop. Hopefully, compounds like 147 will act as catalysts for the design of future studies aimed at targeting the UPR for treating CVD and other systemic diseases.